



الجامعة
UNIVERSITI
TEKNOLOGI
MARA

Jmeche

Journal of mechanical engineering

Regular Issue Apr 2021 | Volume No.18-2

ISSN : 1823 - 5514

e-ISSN : 2550 - 164X

jmeche.uitm.edu.my

JOURNAL OF MECHANICAL ENGINEERING

An International Journal

Vol 18 (2)	15 April 2021	ISSN 1823-5514	eISSN 2550-164X
------------	---------------	----------------	-----------------

1	Computational Analysis of Soft Polymer Lattices for 3D Wound Dressing Materials <i>Muhammad Hanif Nadhif, Muhammad Irsyad, Muhammad Satrio Utomo, Muhammad Suhaeri, and Yudan Whulanza*</i>	1
2	Sustainable Surface Water Dissolved Oxygen Monitoring at Lake 7/1F, Shah Alam, Selangor <i>Norashikin M. Thamrin*, Megat Syahirul Amin Megat Ali, Mohamad Farid Misnan, Nik Norliyana Nik Ibrahim, and Navid Shaghaghi</i>	13
3	Heat Transfer Simulation of Various Material for Polymerase Chain Reaction Thermal Cycler <i>Kenny Lischer*, Ananda Bagus Richky Digdaya Putra, Muhamad Sahlan, Apriliana Cahya Khayrani, Mikael Januardi Ginting, Anondho Wijanarko, Yudan Whulanza, and Diah Kartika Pratami</i>	27
4	COVID-19 and Effective Management of Public Transport: Perspective from the Philippines <i>G U Nnadiri, and N S Lopez*</i>	39
5	Microstructure and Microhardness Alterations of Inconel 718 under Cryogenic Cutting <i>Che Hassan Che Haron, Jaharah Abdul Ghani, Muammar Faiq Azhar, and Nurul Hayati Abdul Halim*</i>	51
6	Effect of Spindle Speed and Feed Per Tooth in Feed Rate Perspective on Inconel HX Cutting Force <i>N. A. Mohd Nor*, N. F. Kamarulzaman, N. A. S. Zakaria, and N. Awang, B. T. H. T. Baharudin, M. K. A. Mohd Ariffin, and Z. Leman</i>	65
7	Evaluation of Tabular Leg Structure of Mobile Offshore Production Unit (MOPU) Life Extension using Condition Assessment Method <i>Emi Hafizzul Jamaluddin, Azli Abd Razak*, Mohd Shahrman Adenan, and Mohd Faizal Mohamad</i>	77
8	Design for Additive Manufacturing and Finite Element Analysis for High Flexion Total Knee Replacement (TKR) <i>Solehuddin Shuib*, Mohammad Arsyad Azemi, Iffa Mohd Arrif, and Najwa</i>	97

	<i>Syakirah Hamizan</i>	
9	Comparative Investigation of Worm Positions for Worm Gear-box Performance under No-Load Condition <i>Hardik G Chothani*, and Kalpesh D Maniya</i>	111
10	Pressure Drop and Flow Characteristics in a Diffuser with a Dimpled Tube <i>Ehan Sabah Shukri Askari*, and Wirachman Wisnoe</i>	125
11	Heat Transfer and Pressure Drop Characteristics of Hybrid Al ₂ O ₃ -SiO ₂ <i>Muyassarah Syahirah Mohd Yatim, Irnie Azlin Zakaria*, Mohamad Fareez Roslan, Wan Ahmad Najmi Wan Mohamed, and Mohd Faizal Mohamad</i>	145
12	Optimization of Machining Parameters using Taguchi Coupled Grey Relational Approach while Turning Inconel 625 <i>Chinmaya Padhy*, and Pariniti Singh</i>	161
13	Effect of Fiber Misalignment on Mechanical and Failure Response of Kenaf Composite under Compressive Loading <i>M. F. Razali, S.A.H.A. Seman*, and T. W. Theng</i>	177
14	Flexible Pavement Crack's Severity Identification and Classification using Deep Convolution Neural Network <i>A. Ibrahim*, N. A. Z. M. Zukri, B. N. Ismail, M. K. Osman, N. A. M. Yusof, M. Idris, A. H. Rabian, and I. Bahri</i>	193
15	Severity Effect of Methanol Toxicity from High Pressure Reactor <i>Z A Rashid*, M A Subri, M A Ahmad, M F I Ahmad Fuad, and N S Japperi</i>	203
16	Artificial Neural Network Predictive Modelling of Laser Micro-Grooving for Commercial Pure Titanium (CP Ti) Grade 2 <i>Sivaraos*, A.K Zuhair, M.S. Salleh, M.A.M. Ali, Kadirgama, Satish Pujari, and L.D. Sivakumar</i>	217

Computational Analysis of Soft Polymer Lattices for 3D Wound Dressing Materials

Muhammad Hanif Nadhif^{1,2}, Muhammad Irsyad², Muhammad Satrio Utomo^{1,2}, Muhammad Suhaeri^{2,4}, Yudan Whulanza*^{5,6}

¹Department of Medical Physics, Faculty of Medicine,
Universitas Indonesia, Indonesia

²Medical Technology Cluster,
Indonesia Medical Education and Research Institute (IMERI), Indonesia

³Research Center for Metallurgy and Material,
Indonesia Institute of Science (LIPI), Indonesia

⁴Indonesia Unit of Education, Research, and Training,
Universitas Indonesia Hospital, Universitas Indonesia, Indonesia

⁵Department of Mechanical Engineering,
Faculty of Engineering, Universitas Indonesia

⁶Research Center on Biomedical Engineering (RCBE),
Faculty of Engineering, Universitas Indonesia

*yudan@eng.ui.ac.id

ABSTRACT

One of the wound treatments was negative pressure wound therapy (NPWT), which used wound dressings on the wound bed to ameliorate the wound healing. Unfortunately, most wound dressings were two dimensional (2D), lacking the ability to cover severe wounds with a straightforward procedure. The sheets needed to be stacked following the wound curvature, which might be problematic since improper stacking could hinder the wound healing. Regarding the mentioned problems, our group develop 3D wound dressings, which are made using 3D printers. The wound dressings are made of polycaprolactone (PCL), polyurethane (PU), and polyvinyl alcohol (PVA). As the initial stage, the mechanical integrity of the soft polymers was investigated

under uniaxial tensile and uniaxial compressive stress using computational methods. The polymers were defined as 3D lattices following the dimension of existing wound dressings. Based on the simulation results of displacement and von Mises stress, the three polymers are mechanically safe to be used as wound dressing materials.

Keywords: *Computational analysis; Lattice; Soft polymer; Wound dressing*

Introduction

Chronic ulcers affected 1% of the world population with various causes [1]. At least three types of chronic ulcer were known, venous leg ulcer, diabetic ulcer, and pressure ulcer. In Germany, 37% - 80% of leg ulcer cases had an aetiology of chronic venous insufficiency [2]. In the UK, venous ulcer prevalence could reach 1.2 – 3.2 per 1,000 people [3]. Apart from venous leg ulcers, diabetic foot ulcers also showed high prevalence. The incidence of diabetic foot ulcers also grown globally [4], along with the increase in the prevalence of diabetic mellitus all over the world. This type of ulcer was responsible for more hospitalization than other diabetic complications. This ulcer also increased the chance of the patient experiencing pressure ulcers [5]. Regardless of the diabetic co-factor, pressure ulcers also presented high prevalence, particularly in immobilized patients. It was reported that 18.1% of hospitalized patients in Europe were affected by pressure ulcers⁴. Both diabetic and pressure ulcers spent a high expenditure on national healthcare [4], [6].

The treatment of abovementioned ulcers varied. For the initial stage, the ulcer was cleansed using irrigation to remove debris and prevent premature surface healing [7]. The shallow ulcer usually only required wound dressing to close the ulcer and prevent contamination. However, higher-stage ulcers required a negative pressure wound therapy (NPWT) to accelerate the wound healing process by providing an electrically powered vacuum condition in the wound vicinity [8]. The vacuum condition enabled humidity maintenance, allowed for epithelization, and prevented tissue desiccation [9]. Due to the vacuum condition, the exudate could also be removed, thereby preventing contamination and lowering the risk of hematoma and seroma formation [10].

The selection of wound dressing for NPWT devices was crucial. Ulcers could react differently to different materials of wound dressing. To date, polycaprolactone (PCL), polyurethane (PU) dan polyvinyl alcohol (PVA) were regularly used as building blocks of wound dressings due to the biocompatibility [11]–[14]. Besides that, the use of materials was based on the softness since the materials interacted with damage skins (ulcers) [15], [16].

The available wound dressing materials, nonetheless, are mostly two dimensional (2D), in the form of sheet. For Stage III or Stage IV ulcers, the

2D wound dressing sheets have to be stacked to fill the gap in the wound cavity since every chronic ulcer had its own curvature. Sometimes, the wound dressing sheet was not able to fit properly in the wound bed, which caused the air leakage [17]. A loose stacking might cause a partially covered wound bed, while a tight stacking might induce pain to the wound bed. An improper stacking might also interfere with the vacuum perseverance of the NPWT. Regarding this problem, our group developed a three-dimensional (3D) wound dressing made of soft polymers. The 3D curvature of the wound dressing was extracted from medical imaging (i.e., magnetic resonance imaging, 3D scanning). The medical images were subsequently modified to generate a lattice pattern in the wound dressing, following the size of the existing wound dressing. The modified lattice-structured wound dressing was subsequently realized using rapid prototyping technology, as known as 3D printing.

Before the wound dressing realization, one of the crucial steps is the computational and experimental characterization of the wound dressing materials. This study aims to investigate the mechanical integrity of the materials using computational methods under several modes of stress. The materials were as 3D lattices made of soft polymers: PCL, PU, and PVA.

Methods

3D soft polymer lattice model

The model of the three lattices (PCL, PU, and PVA) was designed with the pore-strut configuration using an Autodesk Inventor Professional 2020 modelling software. The strut dimension was based on the maximum resolution of the 3D printer [18] and the setting in the slicer software. Low-cost fused deposition modelling (FDM) 3D printers commonly used a nozzle with a diameter of 0.4 mm [18]. The nozzle diameter determined the extrusion width (strut width), which had the same value as the nozzle diameter. The strut height, on the other hand, could be altered using a slicer software by choosing the 3D printing quality, which was the layer height per print. Commonly, the slightest dimension of the layer was 0.1 mm [18], thereby the strut height. From the mentioned considerations, the strut width and height were 0.4 mm and 0.1 mm, respectively. Different from the strut, which size was fixed, the pore dimension varied following the wound dressing specification applied in the NPWT device. There were three sizes of pore in literature: 0.4 mm [19], 0.5 mm [19], and 0.68 mm [20], thus generating three samples for each material, which had the same strut dimension, as well as the number of pores and struts. As a result, there were 9 samples: PCL0.68, PCL0.5, PCL0.4, PU0.68, PU0.5, PU0.4, PVA0.68, PVA0.5, and PVA0.4. The illustration of the 3D lattice is presented in Figure 1.

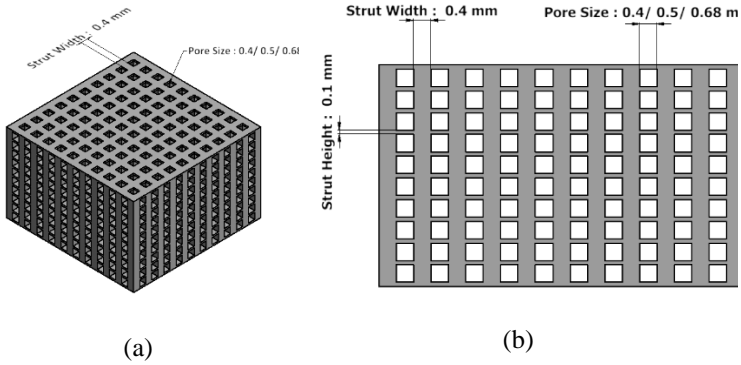


Figure 1: The computer-aided design (CAD) of the soft polymer lattice: (a) isometric projection, and (b) front view of the model.

Simulation parameters

COMSOL Multiphysics 4.5 was used to perform the computational simulations to determine the mechanical integrity of the 3D lattice [21]. The model that was built (Figure 1) was converted and exported to COMSOL. In this study, the uniaxial compressive and tensile stresses were applied on top of the lattice surface. The simulations were performed using a solid mechanics module in the stationary study. The mechanical properties of the three materials input in COMSOL were in the form of thermoplastics, following the form of the 3D printing filaments (presented in Table 1).

Table 1: Mechanical properties of PCL, PU, and PVA

Parameters	PCL	PU	PVA
Young's Modulus (MPa)	Compressive: 44 [22] Tensile: 27 [22]	55 [23]	44.7 [24]
Poisson's Ratio	0.442 [22]	0.48 [23]	0.45 [25]
Density (kg/m ³)	1,200 [26]	1,100 [27]	680 [28]
Tensile / Compressive Strength (MPa)	Compressive: 3.2 [22] Tensile: 1.4 [22]	24.8 [29]	40 [30]

The load boundary and fixed constraint were defined on two surfaces of the model. One was on top of the model, while the other one was applied on the bottom surface of the model, respectively. The load directed downward and upward along the z-axis placed on top of the model, recapitulated the compressive and tensile stress, respectively. To determine the value of the two forces, the working pressure of an NPWT device was used. On a clinical basis,

a 125-mmHg negative pressure was delivered to the wound bed [19]. Considering the safety factor of 10, the load used in this study was equal to 1250 mmHg (166,653 Pa). These simulations output resulted in the displacement and the von Mises Stress (vMS) of each material, model, and test used. The minimum-maximum value distribution of displacement was visualized by the colour scale (Figure 2). Following is the linear deformation equation:

$$\delta = \frac{PL}{EA} \quad (1)$$

where P, L, E, and A are the load (N), the original length of the lattice (mm), modulus elasticity of the material (N/mm²), and surface area (mm²), respectively. Meanwhile, the vMS calculation followed the below equation:

$$\sigma_v = \frac{1}{6} [(\sigma_{11} - \sigma_{22})^2 + (\sigma_{22} - \sigma_{33})^2 + (\sigma_{33} - \sigma_{11})^2] + \sigma_{12}^2 + \sigma_{23}^2 + \sigma_{31}^2 \quad (2)$$

where σ_{ij} is the stress tensor at the local coordinate system.

Results and Discussion

The displacement values were analysed using a COMSOL post-processing feature and evaluated from the top surface. Since the working force was on the z-axis, the displacement values along other axes were neglected. The simulation in COMSOL followed Equation 1. In all the samples, the lowest displacement values were distributed on all four corners on the bottom surface. Meanwhile, the higher displacement values were found on the middle surface, especially at the edges of the pores. The distribution values were visualized in Figure 2.

The resulted displacement values were obtained regarding the test method, pore size, and material were summarized in Figure 3a. The displacement increased along with the increase of the pore size. For both tensile and compressive tests, PU models had the lowest displacement among all materials in all pore sizes. The displacement values were 0.048 mm, 0.083 mm, and 0.129 mm for PU0.4, PU0.5, PU0.68, respectively. Meanwhile, the displacement values of the PVA0.4, PVA0.5, PVA0.68 model were 0.06 mm, 0.104 mm, and 0.161 mm, respectively. The PCL model for both test schemes had distinctive displacement values due to the difference of compressive and tensile strength. The compressive displacements of PCL0.4, PCL0.5, and PCL0.68 were 0.061 mm, 0.106 mm, and 0.164 mm, respectively. Meanwhile,

the tensile displacements of PCL0.4, PCL0.5, and PCL0.68 were 0.1 mm, 0.173 mm, 0.267 mm, respectively.

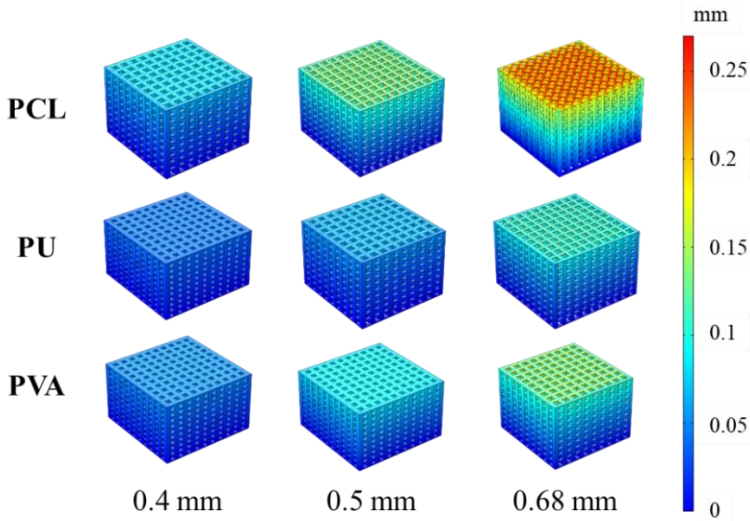


Figure 2: Displacement distribution on tensile test for each pore size and material.

Generally, the PU lattice has the lowest displacement in the compressive and tensile tests, followed by PVA and PCL ($d_{PU} < d_{PVA} < d_{PCL}$). The displacement results inversely corresponded to the elastic modulus of each material ($E_{PU} > E_{PVA} > E_{PCL}$), as shown in Table 1. The results also indicated that the PU lattice was more stable to preserve its shape compared with the PVA and PCL lattices. However, despite the highest displacement of PCL, the maximum tensile strain was only about 3.38%. This small strain can be considerably neglected during the implementation of NPWT.

The vMS values were also obtained from the simulation (Figure 3b), following Equation 2. The average vMS values were 1.21 ± 0.01 MPa, 2.02 ± 0.01 MPa, and 3.36 ± 0.06 MPa for the pore size of 0.4 mm, 0.5 mm, 0.68 mm, respectively. The simulation indicated that for the same strut size, the resulted vMS for each material was proportional to the pore size. The vMS values were lower than the respective ultimate tensile strength (UTS) values (shown in Table 1), except for the PCL lattice with the pore size of 0.5 mm and 0.68 mm. In terms of compressive stress, only vMS of PCL with the pore size of 0.68 mm exceeded the ultimate compressive strength (UCS). The three explained conditions were indeed problematic since the conditions indicated the failure

of materials. However, the safety factor used in the simulation was overestimated, 10. When the safety factor was lowered to 5 ($P = 83,326 \text{ Pa}$), the vMS of the PCL lattice with the pore size of 0.5 mm was lower than the UTS. When the safety factor was even decreased to 4 ($P = 66,661 \text{ Pa}$), the PCL lattice with the pore size of 0.68 mm did not experience failure due to either tensile or compressive stress. These results are of importance for the future design of 3D wound dressings made of PCL. Instead of 10, the safety factor used for PCL wound dressings can be 4. The safety factor of 4 is still tolerable.

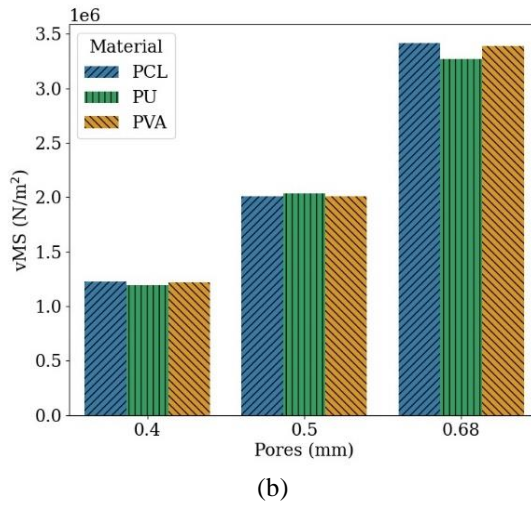
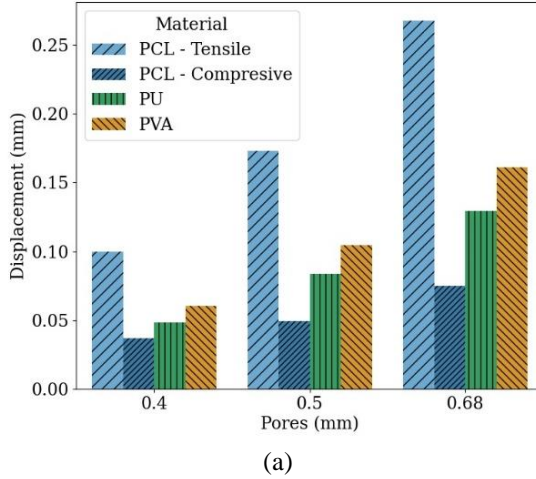


Figure 3: Displacement (a) von Mises Stress, and (b) along the z-axis.

Based on the mechanical simulation results, the 3D PU lattice was superior compared to the other two lattices. However, the strain of all lattices was very small (Table 2). The vMS of all materials was below the UTS, except for PCL with certain pore sizes. Nonetheless, when the safety factor was lowered to 4, PCL lattices were still safe and applicable for NPWT. It means that the other two materials (PVA and PCL) can still be considered as compatible materials for NPWT wound dressings. Therefore, three options of 3D wound dressing material are still available for plastic surgeons to use. For instance, if the surgeons would like to incorporate a biodegradable wound dressing, they can select 3D PVA-based and PCL-based wound dressings [31]–[33]. Meanwhile, when the surgeons want to keep the structural integrity of the 3D wound dressing material, they can choose 3D PU-based wound dressing since thermoplastic PU is not degradable in the body [13].

Table 2: The strain for each pore size and material

Material	Pore Size		
	0.4 mm	0.5 mm	0.68 mm
PCL (%)	1.95	2.84	3.39
PU (%)	0.95	1.37	1.64
PVA (%)	1.18	1.71	2.04

Conclusion

The computational analysis was successfully executed. From the results, it can be concluded that the 3D lattices made of PCL, PU, and PVA, were safe and feasible to be used as wound dressing materials. The von Mises stress resulted from the equivalent stress produced by NPWT devices on a wound bed did not exceed the ultimate tensile strength of all materials. The maximum strain rate due to the compressive and tensile stress was also considerably low. In terms of biodegradability, surgeons can take 3D PVA- and PCL-based wound dressings. On the other hand, the perseverance of 3D wound dressing structural integrity can be achieved using PU-based wound dressings. Finally, the results of this study provide the readers the finite element analysis of 3D lattices for wound dressing applications. However, this study hopefully will become a cornerstone of the development of 3D wound dressing materials, experimentally and clinically, since a one-piece dressing product was desired by burn wound specialists around the world [34].

Acknowledgement

This research was supported by the Universitas Indonesia through the PUTI Saintekes Grant NKB-2444/UN2.RST/HKP.05.00/2020.

References

- [1] L. Martinengo *et al.*, “Prevalence of chronic wounds in the general population: systematic review and meta-analysis of observational studies,” *Ann. Epidemiol.*, vol. 29, pp. 8–15, 2019.
- [2] K. Heyer, K. Protz, G. Glaeske, and M. Augustin, “Epidemiology and use of compression treatment in venous leg ulcers: nationwide claims data analysis in Germany: Compression treatment in venous leg ulcers,” *Int. Wound J.*, vol. 14, no. 2, pp. 338–343, 2017.
- [3] A. H. Davies, J. M. Mora, M. S. Gohel, F. Heatley, and K. Dhillon, “Early referral of venous leg ulcers: lessons from the EVRA trial,” *Nurs. Resid. Care*, vol. 22, no. 1, pp. 31–36, 2020.
- [4] P. Zhang, J. Lu, Y. Jing, S. Tang, D. Zhu, and Y. Bi, “Global epidemiology of diabetic foot ulceration: a systematic review and meta-analysis,” *Ann. Med.*, vol. 49, no. 2, pp. 106–116, 2017.
- [5] Z.-Q. Kang and X.-J. Zhai, “The Association between Pre-existing Diabetes Mellitus and Pressure Ulcers in Patients Following Surgery: A Meta-analysis,” *Sci. Rep.*, vol. 5, no. 1, pp. 13007, 2015.
- [6] B. K. Lal, “Venous ulcers of the lower extremity: Definition, epidemiology, and economic and social burdens,” *Semin. Vasc. Surg.*, vol. 28, no. 1, pp. 3–5, 2015.
- [7] J. C. Lawrence, “Wound irrigation,” *J. Wound Care*, vol. 6, no. 1, pp. 4, 1997.
- [8] A. Gabriel, “Integrated negative pressure wound therapy system with volumetric automated fluid instillation in wounds at risk for compromised healing,” *Int. Wound J.*, vol. 9, pp. 25–31, 2012.
- [9] N. A. Kantak, R. Mistry, D. E. Varon, and E. G. Halvorson, “Negative Pressure Wound Therapy for Burns,” *Clin. Plast. Surg.*, vol. 44, no. 3, pp. 671–677, 2017.
- [10] S. Gupta, “Optimal use of negative pressure wound therapy for skin grafts,” *Int. Wound J.*, vol. 9, pp. 40–47, 2012.
- [11] M. Mir *et al.*, “Synthetic polymeric biomaterials for wound healing: a review,” *Prog. Biomater.*, vol. 7, no. 1, pp. 1–21, 2018.
- [12] J. Kucińska-Lipka, “Polyurethanes Crosslinked with Poly(vinyl alcohol) as a Slowly-Degradable and Hydrophilic Materials of Potential Use in Regenerative Medicine,” *Materials*, vol. 11, no. 3, pp. 352, 2018.

- [13] R. R. M. Vogels *et al.*, “Biocompatibility and biomechanical analysis of elastic TPU threads as new suture material,” *J. Biomed. Mater. Res. B Appl. Biomater.*, vol. 105, no. 1, pp. 99–106, 2017.
- [14] D. Lupuleasa, “biocompatible polymers for 3d printing,” *FARMACIA*, vol. 66, no. 5, pp. 737–746, 2018.
- [15] A. Krishna, A. Kumar, and R. K. Singh, “Effect of Polyvinyl Alcohol on the Growth, Structure, Morphology, and Electrical Conductivity of Polypyrrole Nanoparticles Synthesized via Microemulsion Polymerization,” *ISRN Nanomater.*, vol. 2012, pp. 1–6, 2012.
- [16] D. Garcia-Garcia, J. M. Ferri, T. Boronat, J. Lopez-Martinez, and R. Balart, “Processing and characterization of binary poly(hydroxybutyrate) (PHB) and poly(caprolactone) (PCL) blends with improved impact properties,” *Polym. Bull.*, vol. 73, no. 12, pp. 3333–3350, 2016.
- [17] D. A. Hudson, K. G. Adams, A. Van Huyssteen, R. Martin, and E. M. Huddleston, “Simplified negative pressure wound therapy: clinical evaluation of an ultraportable, no-canister system,” *Int. Wound J.*, vol. 12, no. 2, pp. 195–201, 2015.
- [18] J. Cantrell *et al.*, “Experimental Characterization of the Mechanical Properties of 3D-Printed ABS and Polycarbonate Parts,” *Rapid Prototyp. J.*, vol. 23, no. 4, pp. 811–824, 2017.
- [19] T. O. H. Prasetyono, I. S. Rini, and C. Wibisono, “EASEPort NPWT System to Enhance Skin Graft Survival – A Simple Assembly,” *Int. Surg.*, vol. 100, no. 3, pp. 518–523, 2015.
- [20] V. Milleret, A. G. Bittermann, D. Mayer, and H. Hall, “Analysis of Effective Interconnectivity of DegraPol-foams Designed for Negative Pressure Wound Therapy,” *Materials*, vol. 2, no. 1, pp. 292–306, 2009.
- [21] M. S. Utomo, Y. Whulanza, F. P. Lestari, A. Erryani, I. Kartika, and N. A. Alief, “Determination of compressive strength of 3D polymeric lattice structure as template in powder metallurgy,” *IOP Conf. Ser. Mater. Sci. Eng.*, vol. 541, pp. 012042, 2019.
- [22] L. Lu *et al.*, “Mechanical study of polycaprolactone-hydroxyapatite porous scaffolds created by porogen-based solid freeform fabrication method,” *J. Appl. Biomater. Funct. Mater.*, vol. 12, no. 3, pp. 145–154, 2014.
- [23] H. J. Qi and M. C. Boyce, “Stress–strain behavior of thermoplastic polyurethanes,” *Mech. Mater.*, vol. 37, no. 8, pp. 817–839, 2005.
- [24] W. Zhang, X. Yang, C. Li, M. Liang, C. Lu, and Y. Deng, “Mechanochemical activation of cellulose and its thermoplastic polyvinyl alcohol ecomposites with enhanced physicochemical properties,” *Carbohydr. Polym.*, vol. 83, no. 1, pp. 257–263, 2011.
- [25] F. Chen, D. J. Kang, and J. H. Park, “New measurement method of Poisson’s ratio of PVA hydrogels using an optical flow analysis for a digital imaging system,” *Meas. Sci. Technol.*, vol. 24, no. 5, 2013.

- [26] M. Labet and W. Thielemans, "Synthesis of polycaprolactone: A review," *Chem. Soc. Rev.*, vol. 38, no. 12, pp. 3484–3504, 2009.
- [27] M. Al Minnath, G. Unnikrishnan, and E. Purushothaman, "Transport studies of thermoplastic polyurethane/natural rubber (TPU/NR) blends," *J. Membr. Sci.*, vol. 379, no. 1–2, pp. 361–369, 2011.
- [28] K. Wahyuningsih, E. S. Iriani, and F. Fahma, "Utilization of Cellulose from Pineapple Leaf Fibers as Nanofiller in Polyvinyl Alcohol-Based Film," *Indones. J. Chem.*, vol. 16, no. 2, p. 181, 2018.
- [29] Y. Kanbur and U. Tayfun, "Development of multifunctional polyurethane elastomer composites containing fullerene: Mechanical, damping, thermal, and flammability behaviors," *J. Elastomers Plast.*, vol. 51, no. 3, pp. 262–279, 2019.
- [30] V. Goodship and D. K. Jacobs, *Polyvinyl Alcohol: Materials, Processing and Applications*, vol. 16. Shrewsbury, Shropshire: Smithers Rapra Technology, 2009.
- [31] M. Sabino *et al.*, "In vitro biocompatibility study of biodegradable polyester scaffolds constructed using Fused Deposition Modeling (FDM)," *IFAC Proc. Vol.*, vol. 46, no. 24, pp. 356–360, 2013.
- [32] S. Mohanty *et al.*, "Fabrication of scalable and structured tissue engineering scaffolds using water dissolvable sacrificial 3D printed moulds," *Mater. Sci. Eng. C*, vol. 55, pp. 569–578, 2015.
- [33] N. Thuaksuban, R. Pannak, P. Boonyaphiphat, and N. Monmaturapoj, "In vivo biocompatibility and degradation of novel Polycaprolactone-Biphasic Calcium phosphate scaffolds used as a bone substitute," *Biomed. Mater. Eng.*, vol. 29, no. 2, pp. 253–267, 2018.
- [34] H. F. Selig, D. B. Lumenta, M. Giretzlehner, M. G. Jeschke, D. Upton, and L. P. Kamolz, "The properties of an 'ideal' burn wound dressing – What do we need in daily clinical practice? Results of a worldwide online survey among burn care specialists," *Burns*, vol. 38, no. 7, pp. 960–966, 2012.

Sustainable Surface Water Dissolved Oxygen Monitoring at Lake 7/1F, Shah Alam, Selangor

Norashikin M. Thamrin, Megat Syahirul Amin Megat Ali
College of Engineering, Universiti Teknologi MARA,
40450 Shah Alam, Selangor, Malaysia
norashikin@uitm.edu.my

*Mohamad Farid Misnan
Faculty of Electrical Engineering, Universiti Teknologi MARA,
Pasir Gudang, Johor, Malaysia*

*Nik Norliyana Nik Ibrahim
Department of Chemical and Environmental Engineering,
Universiti Putra Malaysia, Serdang, Selangor, Malaysia*

*Navid Shaghaghi
EPIC (Ethical, Pragmatic, and Intelligent Computing) Laboratory,
Departments of Mathematics and Computer Science (MCS) and
Computer Science and Engineering (CSE)
Santa Clara University (SCU), Santa Clara, USA*

ABSTRACT

Shah Alam is in Selangor, Malaysia and symbolized with several lakes that are popular among local communities and visitors for leisure and recreational activities. Among of these lakes, few lakes need management to look after its hygienic and well-being to serve its purpose as the recreational lake for the nearby community, such as Lake 7/1F, Shah Alam, Selangor. The secluded location of this water reservoir has made it unpopular, and improper management of it could invite an imbalance environment to its surrounding. Therefore, to initiate the effort, an Internet-of-Thing (IoT) water monitoring system is deployed at this lake to study the dissolved oxygen (DO) level in the water that could indicate the health status of this lake. The system consists of a DO sensor, embedded controller, self-charging power supply, wireless data transmission, and IoT dashboard for in-situ DO measurement. From the analysis, the lake has the normal cycle of DO production, but a

dangerous condition is detected when the concentrated DO in the lake water is mostly below the saturation value.

Keywords: *Water Quality; Surface Water; Dissolved Oxygen; IoT System; Lake Water*

Introduction

Recreational lakes are becoming increasingly popular with local communities for leisure and social activities. Shah Alam is a city and the state capital of Selangor, Malaysia and was the first planned city in this country after the Independence Day in 1957. This well-designed plan has set up a few recreational areas in a walking distance from surrounding residential areas, such as catchment ponds and artificial lakes. Furthermore, the presence of well-developed parks with ponds and lakes has a positive impact on the perception of the historical, cultural, environmental, and recreational functions that can surely develop the domestic and international tourism [1]. On top of that, these lakes' aquatic systems can improve the urban microclimate problem by absorbing solid pollutants, increasing air humidity, and reducing the adverse thermal radiation during the hot season [2-3]. Besides, with these aesthetic and scenic values, they are enticing the attractive water resources, which are capitalized into property prices [4-5].

However, climate change and rapid developments around the lake have modified the ecological character of the lake. Climate change affects the levels of dissolved oxygen level and aquatic species in lake water. With the increase in surface water temperature, the concentration of dissolved oxygen in the water decreased [6]. The prolonged dry season also reduces the volume of lake water that affects the health of Urmia Lake, Iran. When the climate has changed the character of this lake water over the last few decades, its use for irrigation should be supplemented by other groundwater sources, further reducing the depletion of that lake [7]. There is also environmental concern regarding the relationship between nutrient runoff and biological growth, including harmful algal blooms and hypoxic conditions caused by the entry of untreated wastewater into the water, littering, and eutrophication [1,5]. If lake water cannot be self-purified, it loses its recreation and may be unfit to be used by the local communities.

The excessive presence of nitrate and phosphate in the water may invite unwanted weeds to cover the lake, which leads to the lake eutrophication. This condition can pose a threat to the public with dangerous diseases such as malaria, dengue and cholera, and other parasitic infections [1,8]. Figure 1 shows the Lake 7/1F condition with the growing weeds in the water.



Figure 1: The growing weeds on the banks of the Lake 7/1F, Shah Alam, Selangor.

The vast majority of studies included in the review suggest that the concentration of the dissolved oxygen in the lake water can determine the health of its ecosystem [6-10]. The dissolved oxygen concentration needs regular monitoring to observe any sudden and extreme changes in the data. Traditional in-situ measurements have too limited time and spatial resolution to make such a numerical model accurate. Efforts needed to use innovative tools to solve these limitations [11]. Consequently, a faster approach in monitoring the concentration of the dissolved oxygen level in the lake water is desired. Previous researchers in the literature have proposed a range of techniques. This approach incorporates two essential techniques, namely (1) in-situ measurement of the dissolved oxygen concentration, and (2) remote monitoring access. In-situ measurement is the critical element of continuously monitoring the water parameter in the lake. The sensor is attached to a self-power embedded system that contains a controller for a sustainable water monitoring system. A continuous dissolved oxygen monitoring data allow prediction on the health of the lake water and fish habitats by integrating it with the numerical analysis and prediction algorithm [6,10,11]. The changes in the dissolved oxygen concentration assessed through the computers and smartphones by using the intelligent sensor network implementation or the Internet-of-Thing (IoT) approach, which is one of the advantages of the automated monitoring system can provide to the local authorities and community. For this purpose, the system equipped with the wireless data transmission by using several IoT protocols such as Message Queue Telemetry Transport (MQTT), Hypertext Transfer Protocol (HTTP), and others [12-15] to display the monitored dissolved oxygen concentration level in the IoT dashboard. The use of IoT technology supported by the data retrieval method using sensors, embedded systems and remote communication technology can, therefore, help to simplify the assessment of lake water quality.

Research Methodology

This project developed a Buoy water monitoring to gather a broad data set of the water parameter. This system involves the design and development of the floating Water Quality Monitoring Platform, Sustainable Power Supply System, Sensor Network, IoT Mobile Dashboard & Cloud Data Storage System. This system installed at Lake 7/1F, Shah Alam, Selangor, as shown in Figure 2.

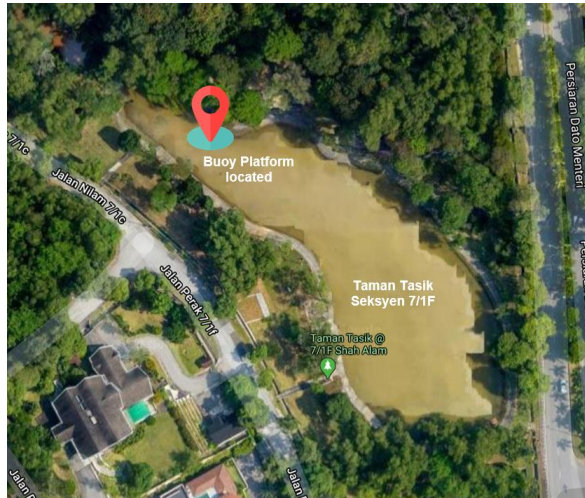


Figure 2: The research location at Lake 7/1F Shah Alam, Selangor.

Development of IoT-based water Qquality monitoring system

Five components involve in this development, namely, are the floating platform (buoy), sustainable power supply management unit, embedded controller unit, sensor network system, IoT dashboard, and physical data storage for the backup system during failure. Each component includes the mechanical and electrical/ electronic components, has been weatherproofed to be placed in the lake water. The overall architecture diagram of the system is shown in Figure 3 and Figure 4, respectively.

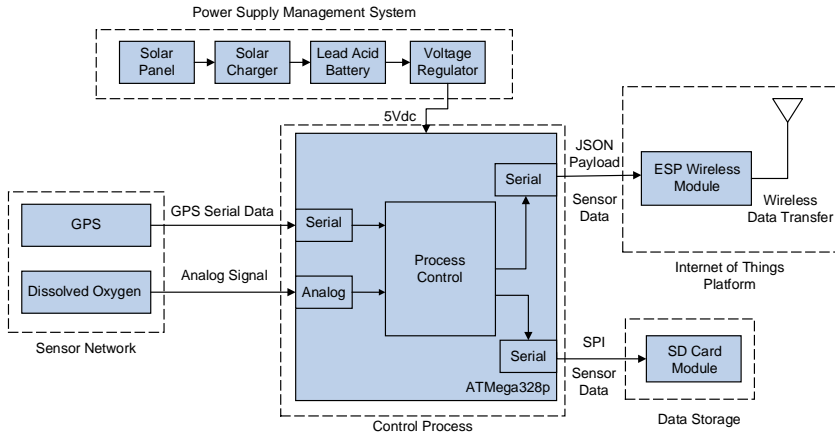


Figure 3: Block diagram of the floating water quality monitoring system.

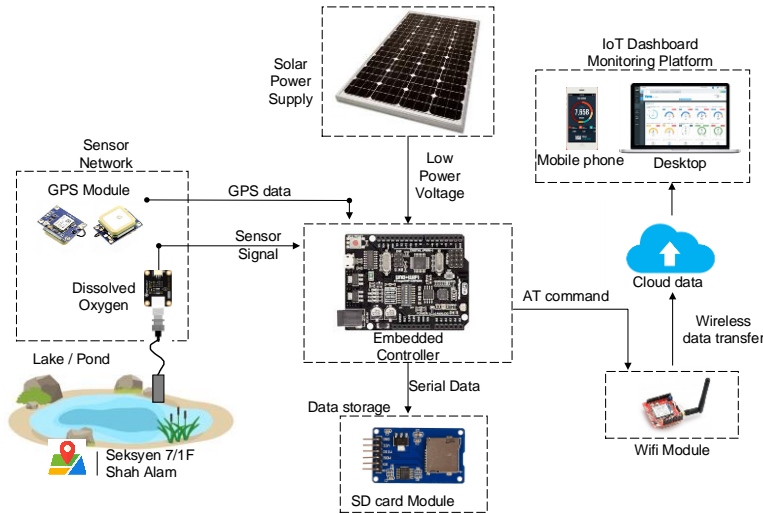


Figure 4: The architecture of the Floating Water Quality Monitoring using IoT System.

The Design of the Floating Platform for Water Monitoring System

The system used a buoy to float the water monitoring system platform on the lake while measuring the DO parameter. The size of the buoy used is approximately 750 mm outer diameter and 450 mm inner diameter with a load capacity of 14.5 kg above water, which is suitable to be used as the total weight of the water monitoring system is 4 kg as depicted in Figure 5(a). The required floating platform must then be larger than the hardware mounted on the platform. The buoy platform frame made of aluminium steel to prevent rust from occurring due to the oxidation process. An opening is made in the middle of the buoy platform to allow trouble-free water flow and exchange, and therefore, avoid the stagnant water which can interrupt the precise measurement. The buoy platform was anchored via the nylon cable on the lake to prevent it from drifting into the middle of the lake, as shown in Figure 5(b). The electrical/electronic components and sensor network are installed at this frame using the grey polycarbonate boxes fitted with a standard IP67 waterproof compliance [16]. The external dimensions of the IP67 boxes were about 300 mm (H) x 200 mm (L) x 80 mm (W) and were equipped with the stainless-steel screws to avoid corrosion. A solar panel is placed on top of the aluminium frame, as shown in Figure 5(a).



(a)



(b)

Figure 5: (a) Buoy monitoring system platform, (b) The floating buoy platform in the Lake 7/1F, Shah Alam, Selangor.

Sustainable solar power supply system

The buoy platform is fitted with 1000 mm x 670 mm solar panels which mounted horizontally on the buoy platform [16]. The installed system hardware powered by a solar power supply system with 30W small solar panel, 12V solar charger, 12V 7AH lead-acid rechargeable battery and a low voltage converter [17-19]. The voltage regulator is used to supply different

voltage to different components, which is 5Vdc to the embedded controller and 9Vdc to the sensor network. The solar panel is mounted facing higher solar exposure to get the optimum solar energy to charge the rechargeable battery. As an estimate, the power storage could provide enough for the entire system to operate with optimum voltage and current for 24 hours operation.

Embedded control unit

Embedded controller AtMega328p used as the central controller for this project to process all the sensor data parameters [19-20]. Appropriately, C program with Arduino IDE software used to read the analog sensor value data via the ADC at setup time intervals to digitize the required parameter value to the exact unit value. The controller also integrated with the offline data storage SD card module to gather all sensor data parameters via the Serial I2C data transfer. It is also integrated with the ESP wireless module for transmitting all the necessary parameter data to the cloud storage to the IoT dashboard platform for Big Data Analysis and data visualization [19-20]. All water parameters instantaneously and wirelessly updated in a requisite setup period, which can be monitored at anytime and anywhere by the authorized person [19].

Water sensors

The water parameter sensor network comprises two sensors, namely the DO sensor and Global Positioning System (GPS) as shown in Figure 6. The former is a sensor used to measure the chemical parameter, which is the dissolved oxygen in the water. The latter used to read the location of the water monitoring system at the lake [16, 21]. An Industrial DO sensor module used to obtain precise oxygen level information from the water [17, 22]. The DO sensor is immersed approximately 30 cm from the surface of the water, beneath the buoy platform [23]. The selected location of the sensors in the buoy is to keep them protected from shock and other problems. The integrated real-time clock (RTC) in the SD card module used to record data using pre-loaded sampling time.

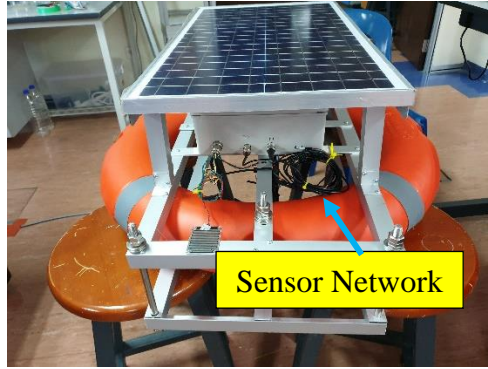


Figure 6: The sensors network.

Data storage

With the emerging of the IoT advancement nowadays, device-to-device and device-to-cloud are the two types of communication that regularly applied in this intelligent system [24]. The latter approach is the most adopted in the developed IoT-based systems for data storing and online monitoring [25]. Besides, this technology also provides a complete solution for system notification to the authorized person when unnecessary water condition occurs during the monitoring process. There are two types of data storage used to store the data obtained from the sensor network, namely the offline and online storage systems. An SD card used to store the data offline using the CSV file format through the serial 12C data transmission protocol. While on the other hand, an online data storage which using cloud storage through the MQTT protocol. These data transmitted to the IoT dashboard for real-time water monitoring system application using JSON payload data. Figure 7 shows the block diagram of the data visualization process through IoT dashboard.

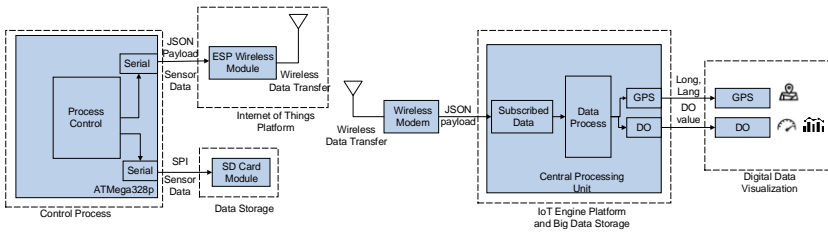


Figure 7: The IoT dashboard for data visualization.

Result and Discussion

In this section, the concentration of DO in Lake 7/1F, Shah Alam, is analyzed and summarized in Figure 8 and Figure 9. The data is sampled from 18 February 2020 to 3 March 2020 to monitor the DO concentration level pattern in this lake. Figure 8 shows the output trend obtained from the DO sensor for 24 hours. The concentration of the DO varies in the lake during the day, and night time is analyzed. The DO concentration level inclines after sunrise and approaching the noon. The minimum oxygen concentrations in the water occurred during sunrise (2.8 mg/L–3.0 mg/L) after a full respiration process by the aquatic life at night [26]. The Sediment denitrification in the shallowed vegetated lake water can also reduce the dissolved oxygen concentration, which can be the first sign of nitrogen pollution in the lake ecosystem [27]. The highest DO value of 7.11 mg/L obtained during the afternoon, around 4.40 PM. During the night, the DO level declines to 2.68 mg/L. When the DO level in the surface water is less than 5 mg/L, it indicates a distressed environment to the aquatic lives such as fish [28]. It also indicates the appearance of sediment oxygen demand (SOD) caused by the algae in the water as well [29]. This value indicates an alarming sign as growth of aquaculture will be slow due to low exposure of dissolved oxygen.

The broad range of DO value is indirectly proposing the lake has excessive algae and phytoplankton which high oxygen consumption by the photosynthetic organisms in the lake. However, more studies are needed to confirm this condition. Correlation between different parameters needs to be determined and measured for further studies. The temperature of the lake water also plays a prominent role in dissolved oxygen levels. During this monitoring period, the range of the water temperature at Lake 7/1F Shah Alam is from 29 °C to 33 °C, which is considered high [12]. The rain also contributes to the DO concentration level in the lake water. Figure 9 shows the scenario explained. A plausible and useful theory behind the situation is that the cloudy day affects the rate of photosynthesis by aquatic life. During the dry season, the DO concentration is higher compared to the wet season [30]. During rainy days, the highest DO concentration level at this lake ranges from 6.63 mg/L to 7.75 mg/L. Table 1 summarizes the percentage of the DO level distribution during the monitoring period. From this table, 62.4% of the DO concentration levels are below 5 mg/L, which is not a good sign for a healthy lake ecosystem. Only 2% obtain more than 8 mg/L during the peak of hot weather.

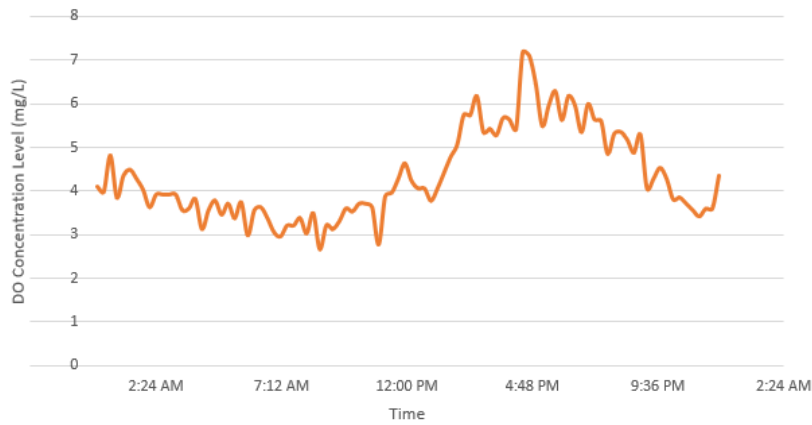


Figure 8: 24 hours DO concentration level measurement in the Lake 7/1F, Shah Alam, Selangor.

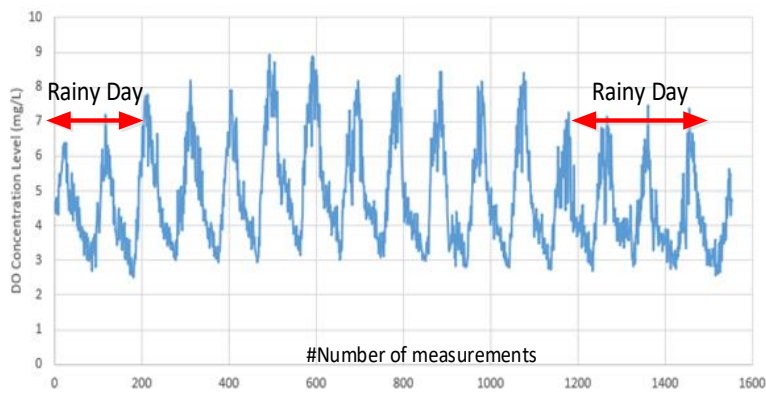


Figure 9: The pattern of DO concentration level at Lake 7/1F, Shah Alam, Selangor for 16 days of observations.

Table 1: DO Concentration Level Results at Lake 7/1F, Shah Alam, Selangor

	$x < 5\text{mg/L}$ (%)	$5\text{ mg/L} \leq x < 8\text{ mg/L}$ (%)	$x \geq 8\text{ mg/L}$ (%)
DO Concentration Level	62.4	35.6	2

This study was limited to the pattern monitoring of DO concentration level at Lake 7/1F for a short period before the COVID-19 pandemic and Movement Control Order by the Government of Malaysia. More studies are needed to address issues that are related to the obtained DO concentration level results. This study can be extended by observing other water parameters such as Biochemical Oxygen Demand (BOD), Chemical Oxygen Demand (COD), Turbidity, pH, Electrical Conductivity, Total Dissolved Solids, and others to confirm the quality and well-being of this recreational lake in more details.

Conclusion

In this paper, the design and development of the real-time monitoring system for DO concentration level at Lake 7/1F, Shah Alam, Selangor is presented. The deployed system consists of DO sensor, an embedded system with the Arduino board implementation, together with the ESP wireless module and SD card for physical back up data storage. The output of this experimentation leads to the conclusion that the pattern of the DO concentration level at this lake shows the vital sign of the photosynthesis appears in the lake water ecosystem. This shows a good indication of a healthy lake cycle, but the consumption of the oxygen in the water during night time is alarming as the DO level drops below the permitted value. This issue should be anticipated and addressed in future research work.

Acknowledgement

The study was performed in collaboration with the Faculty of Electrical Engineering, Universiti Teknologi MARA, Department of Chemical and Environmental Engineering, Universiti Putra Malaysia, Santa Clara University and Majlis Bandaraya Shah Alam (MBSA). The work is supported with the SDG-Lestari Grant (600-RMC/LESTARI SDG-T 5/3(131/2019)).

References

- [1] A. Ishbirdin, M. Ishmuratova, G. Gabidullina, & Z. Baktybaeva, "Ecological and Hygienic Assessment of the State of the Recreational Lake in the City of Ufa," in *Ecological-Socio-Economic Systems: Models of Competition and Cooperation (ESES 2019)*, pp. 104-109, 2020.
- [2] C.Y. Zhu "Effects of urban lake wetland on temperature and humidity: A case study of Wuhan City," *Acta Ecologica Sinica*, vol. 35, no. 16, pp. 5518-5527, 2015.
- [3] D. Zhu and X.F. Zhou, "Effect of urban water bodies on distribution characteristics of particulate matters and NO₂," *Sustainable Cities and Society*, vol. 50, pp. 101679, 2019.
- [4] S. Nicholls, & J. L. Crompton, "The contribution of scenic views of, and proximity to, lakes and reservoirs to property values," *Lakes & Reservoirs: Research & Management*, vol. 23, no. 1, pp. 63-78, 2018.
- [5] M. R. Moore, J. P. Doubek, H. Xu, & B. J. Cardinale, "Hedonic Price Estimates of Lake Water Quality: Valued Attribute Instrumental Variables, and Ecological-Economic Benefits," *Ecological Economics*, vol. 176, pp. 106692, 2020.
- [6] S. Missaghi, M. Hondzo, & W. Herb, "Prediction of lake water temperature, dissolved oxygen, and fish habitat under changing climate," *Climatic Change*, vol. 141, no. 4, pp. 747-757, 2017.
- [7] S. Shadkam, F. Ludwig, P. van Oel, Ç. Kirmit, & P. Kabat, "Impacts of climate change and water resources development on the declining inflow into Iran's Urmia Lake," *Journal of Great Lakes Research*, vol. 42, no. 5, pp. 942-952, 2016.
- [8] M. F. Khan, "Physico-Chemical and Statistical Analysis of Upper Lake Water in Bhopal Region of Madhya Pradesh, India," *International Journal of Lakes and Rivers*, vol. 13, no. 1, pp. 1-16, 2020.
- [9] R. Bhateria, & D. Jain, "Water quality assessment of lake water: a review," *Sustainable Water Resources Management*, vol. 2, no. 2, pp. 161-173, 2016.
- [10] T. Fukushima, T. Inomata, E. Komatsu, & B. Matsushita, "Factors explaining the yearly changes in minimum bottom dissolved oxygen concentrations in Lake Biwa, a warm monomictic lake," *Scientific reports*, vol. 9, no. 1, pp. 1-10, 2019.
- [11] Y. Hong, F. Soullignac, A. Roguet, F. Piccioni, P. Dubois, B. J. Lemaire, & B. Vinçon-Leite, "An automatic warning system for face al contamination in urban recreational lake," in *Novatech 2019*, pp. 3B82-274HON, 2019.

- [12] R. F. Rahmat, M. F. Syahputra, & M. S. Lydia, "Real time monitoring system for water pollution in Lake Toba," in *2016 International Conference on Informatics and Computing (ICIC)*, pp. 383-388, 2016.
- [13] L. F. M. Vieira, M. A. M. Vieira, J. A. M. Nacif, & A. B. Vieira, "Autonomous wireless lake monitoring," *Computing in Science & Engineering*, vol. 20, no. 1, pp. 66-75, 2018.
- [14] J. Huan, H. Li, F. Wu, & W. Cao, "Design of water quality monitoring system for aquaculture ponds based on NB-IoT," *Aquacultural Engineering*, vol. 90, pp. 102088, 2020.
- [15] R. P. N. Budiarti, A. Tjahjono, M. Hariadi, & M. H. Purnomo, "Development of IoT for Automated Water Quality Monitoring System," in *2019 International Conference on Computer Science, Information Technology, and Electrical Engineering (ICOMITEE)* pp. 211-216, 2019.
- [16] A. Hegarty, G. Westbrook, D. Glynn, D. Murray, E. Omerdic, & D. A. Toal, "Low-Cost Remote Solar Energy Monitoring System for a Buoyed IoT Ocean Observation Platform," in *2019 IEEE 5th World Forum on Internet of Things (WF-IoT)*, pp. 386-391, 2019.
- [17] T. Li, M. Xia, J. Chen, Y. Zhao, & C. de Silva, "Automated Water Quality Survey and Evaluation Using an IoT Platform with Mobile Sensor Nodes," *Sensors*, vol. 17, no. 8, pp. 1735, 2017.
- [18] R. Venkatesan, N. Vedachalam, M. A. Muthiah, B. Kesavakumar, R. Sundar, & M. A. Atmanand, "Evolution of Reliable and Cost-Effective Power Systems for Buoys Used in Monitoring Indian Seas," *Marine Technology Society Journal*, vol. 49, no. 1, pp. 71–87, 2015.
- [19] P. V. Vimal, & K. S. Shivaprakasha, "IoT based Greenhouse Environment Monitoring and Controlling System Using Arduino Platform," in *2017 International Conference on Intelligent Computing, Instrumentation and Control Technologies (ICICICT)*, pp. 1514 – 1519, 2017.
- [20] T. Perumal, M. N. Sulaiman, & C. Y Leong, "Internet of Things (IoT) Enabled Water Monitoring System," in *2015 IEEE 4th Global Conference on Consumer Electronics (GCCE)*, pp. 86-87, 2015.
- [21] H. Apel, N. G. Hung, H. Thoss, & T. Schöne, "GPS buoys for stage monitoring of large rivers," *Journal of Hydrology*, vol. 412-413, pp. 182–192, 2012.
- [22] R. Arridha, S. Sukaridhoto, D. Pramadihanto, & N. Funabiki, "Classification extension based on IoT-big data analytic for smart environment monitoring and analytic in real-time system," *International Journal of Space-Based and Situated Computing*, vol. 7, no. 2, pp. 82, 2017.
- [23] S. Sendra, L. Parra, J. Lloret, & J. M. Jiménez, "Oceanographic Multisensor Buoy Based on Low Cost Sensors for Posidonia Meadows

- Monitoring in Mediterranean Sea,” *Journal of Sensors*, vol. 2015, pp. 1–23, 2015.
- [24] A. N. Prasad, K. A. Mamun, F. R. Islam, & H. Haqva, “Smart Water Quality Monitoring System,” in *2015 2nd Asia-Pacific World Congress on Computer Science and Engineering (APWC on CSE)*, pp.1-6, 2015.
- [25] K. H. Kamaludin, & W. Ismail, “Water Quality Monitoring with Internet of Things (IoT),” in *2017 IEEE Conference on Systems, Process and Control (ICSPC)*, pp. 18-23, 2017.
- [26] M. R. Andersen, T. Kragh, & K. Sand-Jensen, “Extreme diel dissolved oxygen and carbon cycles in shallow vegetated lakes,” *Proceedings of the Royal Society B: Biological Sciences*, vol. 284, no. 1862, 20171427, 2017.
- [27] P. Hong, S. Gong, C. Wang, Y. Shu, X. Wu, C. Tian, & B. Xiao, “Effects of organic carbon consumption on denitrifier community composition and diversity along dissolved oxygen vertical profiles in lake sediment surface,” *Journal of Oceanology and Limnology*, vol. 38, pp. 733-744, 2020.
- [28] H. L. Koh, W. K. Tan, S. Y. Teh, & C. J. Tay, “Water Quality Simulation for Rehabilitation Of A Eutrophic Lake In Selangor, Malaysia,” in *IOP Conference Series: Earth and Environmental Science* vol. 380, no. 1, 012006, 2019.
- [29] L. D. Dien, S. J. Faggotter, C. Chen, J. Sammut, & M. A. Burford, “Factors driving low oxygen conditions in integrated rice-shrimp ponds,” *Aquaculture*, vol. 512, 734315, 2019.
- [30] R. Yang, H. Sun, B. Chen, M. Yang, Q. Zeng, C. Zeng, & D. Lin, “Temporal Variations In Riverine Hydrochemistry And Estimation Of The Carbon Sink Produced By Coupled Carbonate Weathering With Aquatic Photosynthesis On Land: An Example From The Xijiang River, A Large Subtropical Karst-Dominated River In China,” *Environmental Science and Pollution Research*, vol. 27, pp. 13142-13154, 2020.

Heat Transfer Simulation of Various Material for Polymerase Chain Reaction Thermal Cycler

Kenny Lischer, Ananda Bagus Richky Digdaya Putra, Muhamad Sahlan, Apriliana Cahya Khayrani, Mikael Januardi Ginting, Anondho Wijanarko*

*Department of Chemical Engineering, Faculty of Engineering,
Universitas Indonesia, Depok, West Java, 16424, Indonesia*

**lischer.kenny@ui.ac.id*

Yudan Whulanza

*Department of Mechanical Engineering, Faculty of Engineering,
Universitas Indonesia, Depok, West Java, 16424, Indonesia*

Diah Kartika Pratami

*Lab of Pharmacognosy and Phytochemistry, Faculty of Pharmacy,
Pancasila University, Jakarta 12640, Indonesia*

ABSTRACT

Medical diagnosis is the initial stage in identifying a person's condition, disease or injury from its signs and symptoms. The diagnostic method is carried out quantitatively by using a diagnostic kit which measures data such as blood pressure, heart rate frequency and blood cell concentration. These diagnostic kits are available in their respective capabilities and their activities require medical facilities and logistical readiness to function. Furthermore, Indonesia's geographical condition which consists of many islands and mountains causes uneven distribution of health facilities and laboratories in each region. Therefore, resulting in problems such as inadequate access and availability of these diagnostic kit in each region. Presently, one of the most widely used diagnostic methods is the Polymerase Chain Reaction (PCR) which allows the amplification of specific fragments from complex DNA. In PCR, only a small amount of DNA is needed to produce enough replication copies which were further analyzed by microscopic examination. This process begins with thermal cycling, which is the reactant's exposure to the heating cycle and repetitive repairs to produce reactions to different temperatures. This study aims to examine the material used for thermal cyclers which is an essential aspect of the heat transfer

needed by the PCR process. In this study, heat transfer from several materials were simulated and analyzed by COMSOL Multiphysics 5.3 Software. The following results were obtained from the simulation: the saturation time for heating aluminum, copper and nickel were 29,37 and 51 seconds, respectively. Meanwhile, the cooling time was 26, 35 and 55 seconds, respectively. In addition, the saturation time for heating and cooling silver and Polydimethylsiloxane (PDMS) were 26 and 1480 seconds, respectively.

Keywords: *COMSOL Multiphysics 5.3; Material; Heat Transfer Simulation; Polymerase Chain Reaction; Portable Thermal Cycler*

Introduction

Medical diagnosis is the initial stage in identifying a person's condition, disease or injury from its signs and symptoms. Furthermore, the diagnostic method is carried out quantitatively by using a diagnostic kit which measures data such as blood pressure, heart rate frequency and blood cell concentration. These diagnostic kits are available in various capabilities, ranging from blood pressure measuring devices to devices that require laboratory treatment such as blood cell checking devices. All of these diagnostic activities require the readiness of facilities and medical logistics to function.

Presently, one of the most widely used diagnostic methods is the Polymerase Chain Reaction (PCR) which allows the amplification of specific DNA fragments from complex DNA. In PCR, only a small amount of DNA is needed to produce enough replication copies which were further analyzed by microscopic examination [1]. It requires a thermal cycle or repeated temperature changes between two or three separate temperatures to amplify the specific nucleic acid target sequence [2]. Thermal cyclers with metal heating blocks powered by Peltier elements are widely used commercially by researchers in this field [3].

Furthermore, in making a thermal cycler machine, the material used as a container for heat transfer is of great importance because the use of PCR thermal cycler device material affects the time needed in the reaction process [4]. Some PCR thermal cycler devices are used commercially and have been patented using several materials such as Aluminum [5] – [8], Copper [9, 10], Nickel [8, 9, 11] and Silver [6, 12].

In general, the size of a commercial PCR machine is quite large and heavy therefore, it only allows PCR reactions to be carried out in a fully equipped laboratory [13]. However, the geographical condition of Indonesia, which consists of many islands and mountains, has resulted in an uneven

distribution of health facilities and laboratories in each region. There are 2820 hospitals spread across Indonesia which are unevenly distributed, with 1345 hospitals in region 1 (DKI Jakarta, West Java, Central Java, DI Yogyakarta, East Java, and Banten). This is inversely proportional to the number of hospitals in region 5 (NTT, Maluku, North Maluku, Papua, and West Papua), where the number of hospitals is 159 for the entire region [14]. This results in problems such as inadequate access and availability of health facilities for underdeveloped areas.

Modeling and simulation is one of the methods used in testing the effectiveness of a material as a conductor in the PCR reaction. In this study, several materials and thermal cycler designs will be simulated if used as heat transfer containers to carry out the PCR reaction.

The expected results were obtained by applying simulation and modeling the conduction heat transfer equation in order to obtain the heat transfer profile during the PCR reaction as well as the saturation time of each material and the heat transfer process.

Methods

In this study, Modeling discussed the uses and stages of work carried out using COMSOL Multiphysics 5.3. In the PCR reaction chamber, the heat comes from the heating element of the Al₂O₃ ceramic Peltier which experiences conduction passing through the material (PCR reaction chamber material). The geometry of the first model was done using a PCR tube, which became a container for placing samples for PCR reactions.

Determining models limitation and modeling

The modeling stages were carried out by the COMSOL Multiphysics 5.3 application using the HP 14-an002ax computer specifications with an AMD Quad-Core A8-7410 APU processor with Radeon™ R5 Graphics (2.2 GHz, up to 2.5 GHz, 2 MB cache) with 4 GB DDR3L memory -1600 SDRAM (1 x 4 GB) and AMD Radeon™ R5 M430 Graphics (2 GB DDR3 Video Memory) graphics card.

Conduction heat transfer equation:

$$\rho C_p \frac{\partial T}{\partial t} + \rho C_p u \cdot \nabla T + \nabla \cdot q = Q + Q_{ted} \quad (1)$$

where, $q = -k \nabla T$

Convection heat transfer equation:

$$\rho C_p \frac{\partial T}{\partial t} + \rho C_p u \cdot \nabla T + \nabla \cdot q = Q + Q_p + Q_v \quad (2)$$

where, $q = -kA \frac{dT}{dx}$

ρ is the density of the fluid in units (kg/m^3), C_p is the Heat Capacity in units (J.kg/K) and k is the Heat Conductivity in unit (W/m.K). Furthermore, Q is the heat source that comes from the heating carried out by the Peltier element in units (W/m^3). Meanwhile, Q_{ted} is thermoelastic damping which is the result of the irreversible heat flow across a temperature gradient produced by inhomogeneous compression and expansion of the resonating structure with units (W/m^3). In addition, Q_p is the pressure works in units (W/m^3).

There are also model limitations set as follows,
Thermal Insulation,

$$-n \cdot q = 0 \quad (3)$$

Temperature,

$$T = T_0 \quad (4)$$

Heat Source,

$$Q = Q_0 \quad (5)$$

Geometrical design

The heat transfer event that occurs in the PCR reaction using a PCR tube is conduction through the chamber material. The heat moves to the PCR tube and the convective heat is transferred to the PCR reagent solution. The size of the Peltier element used for heating was 80 mm x 40 mm x 4 mm figured in Figure 1.

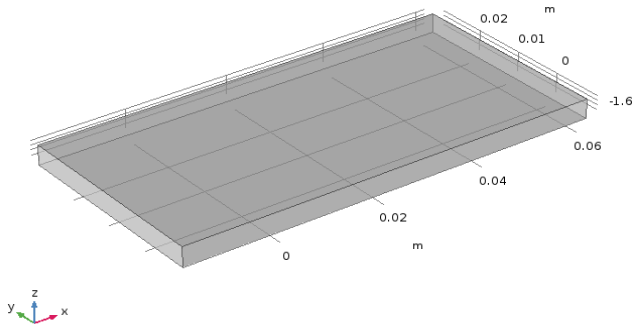


Figure 1: Geometry of Peltier element.

A geometry with the shape of a block was made for the PCR chamber having a size of 81 mm x 40 mm x 15 mm [15]. The chamber had an upper outer diameter of 10.7 mm, an inner diameter of 6.7 mm, a height of 10.5 mm and a radius of 1.5 mm. The distance between the chambers was designed to be 10 mm and 22 mm. This geometric shape was used as a material in the simulation stage until the PCR reaction stage figured in Figure 2.

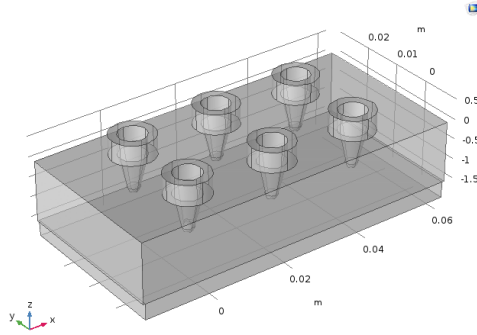


Figure 2: Geometry of PCR block.

The next step was to add the geometry of the PCR tube and the PCR reagent solution to the geometry of the Peltier element. The PCR tube was shaped like a chamber made with a height of 2 mm above the surface of the PCR chamber hole. This geometry was used to simulate heating in the PCR tube and the PCR reaction reagent solution figured in Figure 3.

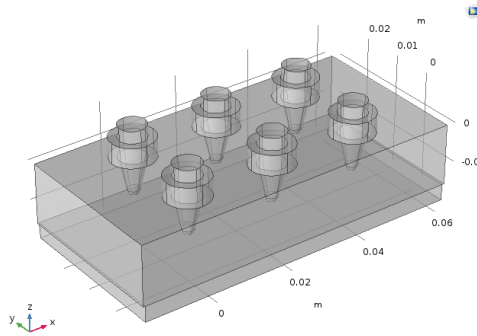


Figure 3: Geometry of PCR block, with PCR tube and reagents.

In this study, the time set for simulation was 60 seconds. Heat enters through the bottom of the Peltier element and moves towards the y-axis. The following is a heat transfer profile that occurs every 10 seconds for each material being simulated—the lowest and highest temperatures were set at 32.64°C and 105.06°C, respectively. The material properties for simulation used from COMSOL Application are shown in the Table 1.

Table 1: Material properties from COMSOL Multiphysics 5.3

Material	Thermal Conductivity (W/m.K)	Heat Capacity (J.kg/K)	Density (kg/m ³)
Aluminum	238	900	2700
Copper	400	385	8960
Nickel	90,7	445	8900
Silver	429	235	10500
PDMS	0.16	1460	970

As of July 2020, the prices of materials based on the IMF were 1621.25, 6328.37, 12179.61 and 1968.60 dollars per metric ton for aluminum, copper, nickel and silver, respectively. Furthermore, based on Alibaba.com as of July 2020, the price of PDMS was 2.75 dollars per kilogram.

Results and Discussion

Simulation results for various material

From Figure 4 below, it was observed that the saturation time for heating aluminum, copper and nickel were 29, 26 and 37 seconds, respectively. Meanwhile, the saturation time for cooling was 35, 51 and 53 seconds, respectively. In addition, the heating and cooling time for silver was 26 seconds.

In Figure 5 the heating and cooling values for the PDMS material were set to 60 seconds however, the material had not reached its saturation time at that simulation. The new PDMS material may reach its saturation time at 1480 seconds or around 24 minutes.

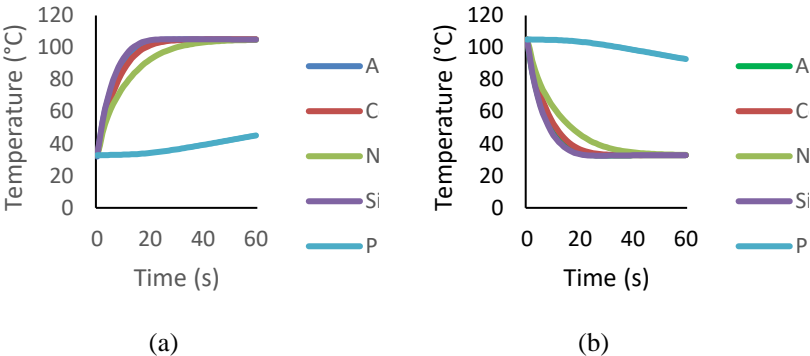


Figure 4: Temperature curve for each material for 60 seconds (a) heating (b) cooling.

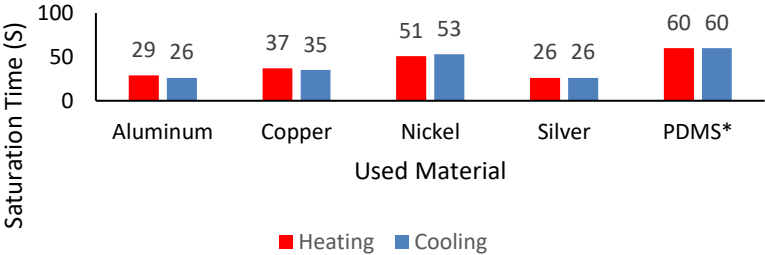


Figure 5: Saturation time for each material.

Considering that each type of material was tested in the same geometry, the factors affecting the time difference based on Equation (1) were density, thermal conductivity and thermal capacity values. The thermal conductivity value in Equation (1) also appeared in Equation (2) namely Fourier's law, where q is the heat transfer rate influenced by k which is the thermal conductivity and ∇T is the temperature gradient.

In Equation (1), the multiplication value of thermal density and capacity is also known as thermal mass. This is an energy requirement needed to increase the temperature at a specific volume [17]. Therefore, these two values have an effect on the heat transfer that will occur in the PCR thermal cycler [18].

Thermal conductivity is one of the crucial factors in the conduction of material. Therefore, a good thermal conductivity value determines the quality of a good conductor material [19]. It was observed that silver had the highest thermal conductivity value of 429 W/mK. Meanwhile, copper, aluminum,

nickel and PDMS had thermal conductivity values of 400, 238, 90.7 and 0.16 W/mK, respectively. Based on thermal conductivity alone, the order for selecting the best materials for producing a portable thermal cycler design is silver, copper, aluminum, nickel and PDMS.

However, study carried out by [16] used thermal mass as the basis for selecting a material to be developed as a portable thermal cycler design. Therefore, in addition paying attention to the conductivity value, it is necessary to pay attention to the value of the thermal mass of each material used. The higher the thermal mass value of a material, the higher the heat required for the material to raise the temperature. Therefore, much longer time would be required. Thermal mass is obtained by multiplying the density value of the material by its heat capacity. For materials with high thermal conductivity, aluminum had the smallest value of 2430000 J/K m³, silver, copper and nickel had values of 2467500, 344960 and 3960 500 J/K m³, respectively. Meanwhile, the PDMS material had a thermal mass of 1416200 J/K m³.

In the saturation time graph, it was observed that the combination of thermal capacity and thermal mass significantly affects the saturation time of each material. For example, although silver and copper have close thermal capacity values with differences in thermal mass values, the saturation times differ quite significantly. In addition, although aluminum has a low calorific capacity value compared to silver and copper, with a smaller heat mass the transfer of heat is faster than in copper but differs slightly when compared to silver. Aluminum benefits from its low density even though it has a high heating capacity and an average high thermal conductivity. Conversely, silver and copper have high thermal conductivity and low heat capacity. However, the density of the two materials is high enough that there is a little difference between these materials and aluminum.

For nickel and PDMS, with a conductivity value that is not too high, the results obtained were not very satisfying however, the nickel material still managed to reach its saturation time in 60 seconds. Meanwhile, the PDMS material was unable to reach its saturation time in 60 seconds at such a thickness condition. Therefore, the next study will focus on aluminum, copper and silver.

Furthermore, from the economic perspective, the market price of aluminum is low compared to copper and silver. This was reinforced by the statement of the company producing PCR, Eppendorf which stated that aluminum is widely used as a base material for commercial PCR thermal cycler blocks. In addition, they stated the use of other stuff as a coating on aluminum or as an alloy. However, there are also commercial PCR thermal cycler manufacturers that use pure silver as the primary material because of its effectiveness [20].

Aluminum is the best material that may be used as a portable design for thermal cycler PCR as a result of its low price and performance which is slightly different from silver. This material is also used by several methods of low-cost microfabrication [21].

Heat transfer to reagents

From the Figure 6, it was observed that the saturation time for heating the chamber material, PCR tube and PCR solution were 29, 30 and 32 seconds, respectively. Meanwhile for cooling, the saturation time was 26, 30 and 35 seconds, respectively.

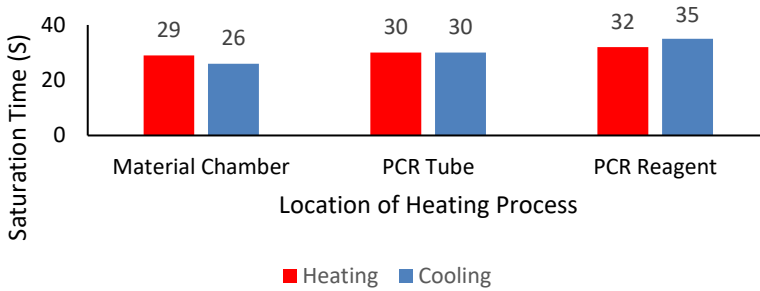


Figure 6: Saturation time for each heat transfer process.

The phenomenon that occurs is the transfer of heat to PCR tubes made of polypropylene [22]. The difference observed in saturation time was 1 second for heating and 4 seconds for cooling. This is the time required for conduction from aluminum to the PCR tube. The heat moves from the PCR tube to the PCR reagent and takes 2 seconds to warm up and 5 seconds to cool down. Therefore, with a total time of 32 seconds for heating and 35 seconds for cooling, the time required for heat to move from the metal to the reagent is 3 seconds for heating and 9 seconds for cooling. This is because a thermal cycler with static heater has more constant heat flux and gives good temperature uniformity [23].

Conclusions

From this study, the following conclusions were drawn. The heat transfer rate on a thermal cycler PCR machine may be influenced by the thermal conductivity and thermal mass values of the material used. The saturation time obtained in this design for heating was 29, 37 and 51 seconds for aluminum, copper and nickel, respectively. Meanwhile, the saturation time

obtained for cooling were 26, 35 and 53 seconds for aluminum, copper and nickel, respectively. In addition, the saturation time for heating and cooling were 26 seconds and 1480 seconds for silver and PDMS, respectively. In this design, the saturation time obtained to heat and cool the reagent when using aluminum was 32 seconds and 35 seconds, respectively after the heat had passed through the thermal block and the PCR tube

Acknowledgement

We acknowledge that the study is made as an output for PUTI Q2 with number NKB-1082/UN2.RST/HKP.05.00/2020.

References

- [1] L. Garibyan and N. J. T. J. Avashia, "Research techniques made simple: polymerase chain reaction (PCR)," *J. Investigative Dermatology*, vol. 133, no. 3, pp. 1 – 8, 2013.
- [2] H. Nagai, Y. Murakami, K. Yokoyama, and E. Tamiya, "High-throughput PCR in silicon based microchamber array," *Biosensor Bioelectronic*, vol. 133, no. 9, pp. 1015 – 1019, 2001.
- [3] S. Yamaguchi, T. Suzuki, K. Inoue, and Y. Azumi, "DC-driven thermoelectric peltier device for precise DNA amplification," *Japanese J. Applied Physics*, vol. 54, no. 5, pp. 057001, 2015.
- [4] S. Jeong, J. Lim, M. Y. Kim, J. Yeom, H. Cho, H. Lee, and J. H. Lee, "Portable low-power thermal cycler with dual thin-film Pt heaters for a polymeric PCR chip" *Biomedical microdevices*, vol. 2, no. (1), pp. 14, 2018.
- [5] T. Reid, R. Taylor, and L. Brown, *U.S. Patent No. 7,459,302*, Washington, DC: U.S. Patent and Trademark Office, 2 December 2008.
- [6] M. J. Mortillaro, and D. A. Cohen, *U.S. Patent No. 9,604,219*, Washington, DC: U.S. Patent and Trademark Office. 28 March 2017.
- [7] W. J. Bennett, J. T. Andreski, J. M. Dzenitis, A. J. Makarewicz, D. R. Hadley, and S. S. Pannu, *U.S. Patent No. 8,778,663*, Washington, DC: U.S. Patent and Trademark Office, 15 July 2014.
- [8] J. L. Danssaert, R. J. Shopes, and D. D. Shoemaker, *U.S. Patent No. 5,525,300*, Washington, DC: U.S. Patent and Trademark Office, 11 June 1996.
- [9] T. C. Gubatayao, K. Handique, K. Ganesan, and D. M. Drummond, *U.S. Patent No. 9,765,389*, Washington, DC: U.S. Patent and Trademark Office. 19 September 2017.
- [10] H. Koeda, *U.S. Patent No. 9,144,800*, Washington, DC: U.S. Patent and Trademark Office, 29 September 2015.

- [11] R. M. F. Jones, & E. T. McDevitt, *U.S. Patent No. 9,869,003*, Washington, DC: U.S. Patent and Trademark Office, 16 January 2018.
- [12] J. Courtney, *U.S. Patent No. 10,307,762*. Washington, DC: U.S. Patent and Trademark Office, 4 June 2019.
- [13] S. A. B. Hermesen, B. R. Roszek, A. W. van Drongelen, and R. E. Geertsma, “Lab-on-a-chip devices for clinical diagnostics: Measuring into a new dimension”, 2014.
- [14] O. O'Donnell, E. Van Doorslaer, R. P. Rannan-Eliya, A. Somanathan,, S. R. Adhikari, D. Harbianto, and G. M. Leung, “The incidence of public spending on healthcare: comparative evidence from Asia”, *The World Bank Economic Review*, vol. 21, no. (1), pp. 93-123, 2007.
- [15] K. S. Chong, K. B. Gan, and S. M. Then, “Development of a portable low-cost real-time PCR system”, In *2017 International Conference on Robotics, Automation and Sciences (ICORAS)* (pp. 1-5). IEEE, 2017.
- [16] S. Jeong, J. Lim, M. Y. Kim, J. Yeom, H. Cho, H. Lee, and J. H. Lee, “Portable low-power thermal cycler with dual thin-film Pt heaters for a polymeric PCR chip”, *Biomedical microdevices*, vol. 20, no. (1), pp. 14, 2018.
- [17] G. Wong, I. Wong, K. Chan, Y. Hsieh, and S. Wong, “A rapid and low-cost PCR thermal cycler for low resource settings” *PLoS one*, vol. 10, no. (7), pp. 0131701, 2015.
- [18] Q. Zou, Y. Miao, Y. Chen, U. Sridhar, C. S. Chong, T. Chai, and C. Heng, “Micro-assembled multi-chamber thermal cycler for low-cost reaction chip thermal multiplexing”, *Sensors and Actuators A: Physical*, vol. 102, no. (1-2), pp. 114-121, 2002.
- [19] K. S. Chong,, and K. B. Gan, “Portable polymerase chain reaction (PCR): thermal ramping rate performance evaluation”. In *2016 IEEE EMBS Conference on Biomedical Engineering and Sciences (IECBES)* (pp. 447-449). IEEE, 2016.
- [20] J. G. Atwood, A. Fawcett, K. S. Ferrara, P. M. Hetherington, R. W. Noreiks, D. E. Olsen, and C. M. Wittmer, *U.S. Patent No. 7,537,377*. Washington, DC: U.S. Patent and Trademark Office, 26 May 2009.
- [21] J. Charmet, R. Rodrigues, E. Yildirim, P. K. Challa, B. Roberts, R. Dallmann, & Y. Whulanza, Low-Cost Microfabrication Tool Box. *Micromachines*, vol. 11, no. (2), pp. 135, 2020.
- [22] X. Huang, L. Hou, X. Xu, H. Chen, H. Ji, and S. Zhu, “One-PCR-tube approach for in situ DNA isolation and detection”, *Analyst*, vol. 136, no. (20), pp. 4254-4259, 2011.
- [23] V. S. Duryodhan, S. G. Singh, & A. Agrawal. (2020). The Concept of Making On-Chip Thermal Cycler for RT-PCR Using Conjugate Heat Transfer in Diverging Microchannel. *Transactions of the Indian National Academy of Engineering*, 1.

COVID-19 and Effective Management of Public Transport: Perspective from the Philippines

*G U Nnadiri, N S Lopez**

*Mechanical Engineering Department, De La Salle University,
Manila, Philippines
neil.lopez@dlsu.edu.ph*

ABSTRACT

The fight of COVID-19 resulted to the suspension of main public transportation services in the Philippines to avoid the spread of the virus on March 16, 2020. This raised questions on how people can travel to access essential services. A study estimated that there can be 7 billion infections and 40 million deaths globally this year in the absence of interventions. Thus, in this paper, the authors reflect on key transport-related issues arising from the pandemic and analyse potential policy recommendations. Particularly, the paper provides a focus on public transport services. The authors recommend focusing on reducing virus transmission in surfaces found in public transport vehicles, use of digital technology to speed up information generation and distribution for contact tracing, and exertion of efforts to reduce transport demand by incentivizing and supporting telecommuting among companies. In conclusion, the authors believe that the central government should be on top of this COVID-19 response. Though delegating the management to local government units and various sectors has its benefits, one wrong decision from a certain unit can lead to a ripple of infections. Standards and protocols, especially on how public transport should operate, must be scientifically commissioned to avoid one big trial and error experiment considering the wealth of information already available in literature.

Keywords: Covid-19; Public transport; Philippines; Policy

Introduction

The intensity and speed Covid-19 spread vary by locations and is now planet-wide. A study [1] estimates 7.0 billion infections and 40 million death globally

this year in the absence of interventions. As of 25th of July 2020, there has been 15,581,009 confirmed cases, 635,173 deaths globally according to World Health Organization [2]. While the Centers for Disease Control and Prevention [3] claims that most coronaviruses will not survive high temperatures and humidity levels, the recent summer in Southeast Asia make it seem otherwise. This is explained in [4] where they estimated that the 2019-nCov only rapidly inactivated when exposed to 70 °C. In recent times, the hottest summer in the Philippines only reached a record high of 36.6 °C in April 2019 [5], while historically, the highest temperature recorded in the Philippines was 42.2 °C in Tuguegarao in 1969 [6].

To fight COVID-19, the Philippine government suspended public transportation on March 16, 2020. This decision has met significant disagreement from the public [7]. As a result of the travel ban, workers were forced to walk back to their homes outside of Metro Manila. Particularly, these were mostly the blue-collar workers who were not able to catch the last bus trips when the quarantine order was immediately raised. Without public transport, the public can only rely to private vehicles, bicycles, and when possible, walking. The vital role of public transport in the daily tasks of the public is undeniable and can never be met fully by private vehicles. People living in areas that are only accessible by tricycles and jeepneys are particularly affected the most [8].

Temporarily, the emphasis ought to be on demand control, and this will incorporate the exacting execution of physical distancing measures, regular transportation disinfection, implementation of safety rules in every single casual method of transport and control of travel demand. In the medium-term, there should be an emphasis on public transport improvement including interjurisdictional coordination of public travel and better administration of informal transport providers. This can be accomplished by acquiring multi-modular arrangements, for example, mass travel frameworks like Metro and bus transport and begin considering elective arrangements like bikes and e-vehicles to offer different versatility answers for individuals [9]. A study [10] reported the financial implications brought about by the pandemic. Manufacturing may lose PhP 82.1 billion to PhP 855.2 billion; wholesale and retail trade may suffer a loss of at least PhP 93.2 billion to PhP 724.8 billion; and transport, storage, and communication due to expected declines in tourism may lose between PhP 11.7 billion to PhP 124.3 billion. Those are among the expected worst-hit sectors. Philippines on the other hand is not expected to recover in the third quarter because of the long strict lockdown aimed to contain the outbreak of the virus. The country is the only country in the Asia-Pacific (APAC) region to implement the longest lockdown [11]. In addition, COVID-19 has become a devastating world-wide human catastrophe and has disrupted lives and livelihoods. The degree of change will affect the way people work and interact daily with several companies and organizations

imposing a telecommuting (work-from-home) setup for their employees who can still be productive while working from home. This new trend of mobility may present a unique opportunity to innovate for different sectors [12].

Given that mobility is almost front and centre in this pandemic, the authors recognize the need for governments to act swiftly and make key mobility-related decisions that would minimize further impacts to the economy and well-being of the people. Thus, in this paper, the authors reflect on key transport-related issues arising from the pandemic and analyse potential policy recommendations. Particularly, the paper provides a focus on public transport services. Moreover, the authors will be interchanging between COVID-19, SARS-CoV-2, and 2019-nCov throughout the manuscript as other published literature are cited. To clarify, 2019-nCov will be used to refer to the virus itself, COVID-19 to refer to the disease obtained from the virus, and SARS-CoV-2 to refer to the virus as part of a larger family of viruses.

Immediate issues for public transport

In this section, three key immediate issues are discussed: (1) the need to reduce virus transmission within the vehicles; (2) speeding up information generation and distribution in light of non-compliance reporting and contact tracing; and (3) keeping up with the demand.

Reducing virus transmission within the vehicles

Findings in literature about the transmission of the 2019-nCoV through aerosols vary. However, a computational fluid dynamics simulation by [13] showed that 85% to 100% of virus-carrying droplets deposit on surfaces or fall to the floor, instead of getting directly inhaled. Moreover, [14] noted that the residence of SARS-CoV-2 in the air is not long. [15] did not find SARS-CoV-2 in air samples obtained from the rooms of COVID-19 hospitalized patients. Furthermore, it has been observed that the disease is not transmitted to healthcare workers directly in contact with COVID-19 patients when they are wearing simple surgical masks [16]. Thus, the focus now should likely be on how the virus spreads through contact with infected surfaces. For public transport patrons, there is a huge chance that they can bring home the virus to unsuspecting family members through their clothing, bank notes (i.e. paper money) and unwashed arms or hands after getting into contact with various surfaces in public transport.

Most cases of COVID-19 are reported to be mild, but the infection tends to be transmitted quickly. Tiny droplets from coughing and sneezing can carry the virus by as far as one to two meters. If they happen to make it into another person's airways, they could become infected, but the virus can also live on surfaces where these droplets land [17].

A comprehensive report by [18] and [4] evaluated the survival of 2019-nCov on different sorts of surfaces (see Table 1). They analysed the aerosol

and surface stability of SARS-CoV-2 and contrasted it with SARS-CoV-1, the most firmly related human coronavirus. Results demonstrated that SARS-CoV-2 was more stable on plastic and stainless steel compared to copper and cardboard, and reasonable virus was recognized as long as 72 hours after application to these surfaces. Despite the fact that the infection (titer) was significantly diminished, it was still discernible in aerosol for as long as three hours, on copper for as long as four hours, on cardboard for as long as 24 hours and on plastic and stainless steel for up to a few days (two to three days) – proposing that individuals can be infected through the air and coming in contact with contaminated objects. Information on the stability of SARS-CoV on surfaces and in the environment can also be obtained from the World Health Organization (WHO) [19]. Starter discoveries have been summed up by the WHO multi-focus community-oriented system on SARS conclusion. Emergency clinic samples from a few locales, specifically from walls and the ventilation system, tested PCR positive in Canada.

Table 1: Stability of 2019-nCov on various surfaces [4], [17]

Type of Material	Length of stability of 2019-nCov on the surface
Plastic	3 to 7 days
Stainless Steel	3 to 7 days
Copper	Up to 4 hours
Paper (including paper money)	Up to 4 days
Glass	Up to 4 days
Cardboard	24 hours
Wood	Up to 2 days
Clothing	Up to 2 days

Common materials found on local public transport vehicles include plastic, steel, glass, and wood. In addition, the survival of the virus on clothing and paper would also be crucial, as it cannot be guaranteed that each seat will be sanitized every time a new passenger unboards, and his/her place is taken by a new passenger. Moreover, it is common practice in the Philippines to pass around money as fare payment from passenger to passenger to the conductor or driver. In addition to the challenges of physical distancing in crowded public transport vehicles and terminals, regular sanitation of a previously occupied seat and passing around fare payment are the primary threats to spreading the 2019-nCov inside public transport vehicles.

Speeding up information generation and distribution in public transport

The speed of information generation and distribution is crucial in controlling the spread of a virus like the 2019-nCov. Countries which have implemented strict contact tracing measures have been seen to beat COVID-19 faster than others [20]. Contact tracing, including case investigations, are part of the process of warning individuals who may have been exposed to the virus and have potentially contracted the disease as well. Countries such as South Korea and New Zealand [21] have shown that good contact tracing and case investigation strategies can stop chains of transmission of the virus. However, contact tracing is a specialized skill and time is of the essence [22].

The problem now is, how can contact tracing be implemented in public transport? A person would roughly get into close physical contact with at least 5 people in public transport. Additionally, these interactions are multiplied by the multi-modal nature of public transport. A person can take jeepney route A, and then transfer to rail route B, before finally taking jeepney route C to the final destination.

Recently, public transport operators in the Philippines have implemented their own approaches, such as requiring passengers to fill out information sheets before getting on board the vehicle [23]. However, though this is possible in terminal-based services, this will be challenging to implement in fast-paced services which implement road-side loading and unloading such as jeepneys. Moreover, given the paper-based system, how fast can contact tracing be done and who will be responsible to do the tracing? Will it be faster than the speed of transmission of the disease?

Furthermore, non-compliance among public transport operators and drivers must be promptly reported and acted on. Non-compliance to safety protocols put in place by policymakers carelessly spread the virus. Thus, the rapid generation and distribution of information among public transport stakeholders (i.e. operators, drivers, and commuters) would facilitate timely testing of potential virus carriers and stop random transmission of the virus. Contact tracing is the weakest link in the Philippine COVID-19 response. The adequacy of resources to identify people exposed to the virus, especially those who are asymptomatic can help manage the spread of the virus in public transport.

Keeping up with the demand

After the first phase of the quarantine order, the gradual reopening of shopping malls, public transit, and other selected services were proposed, should the government lift or extend the enhanced community quarantine (ECQ). The transportation department is looking into the possibility of allowing 30% capacity resumption of public transportation, mostly buses and trains, to allow the observation of physical distancing measures. In line with the resumption

and reduction of public transportation capacity, [24] reported the guidelines for public transportation in areas deemed at low risk for transmission of the virus (COVID-19). This guideline requires a special permit for public utility vehicles (PUV) to operate and the reduction of passenger capacity for buses, jeeps, and UV Express to 50% in adherence to a 1 meter physical distancing rule. A report retrieved from [25] on April 30, 2020 during the transition of Metro Manila from ECQ to general community quarantine (GCQ) stated that all allowed PUVs and transport terminals and administrators must stick to all three basic parts directed - Safety, Capacity and Coverage or Scope. Safety as expressed refers to the rules to decrease contact, transmission and spread of the virus through obligatory utilization of face cover and gloves by drivers, careful sanitation of vehicles, terminals, and even among travellers are likewise required. The admissible capacity is 50%, excluding driver and conductor to guarantee distancing in public utility buses (PUBs) and public utility jeepneys (PUJs). For utility vans and taxis, passengers ought to not surpass two persons for every row, aside from the driver's row where just a single passenger is permitted. Tricycles must not exceed one person in the sidecar, while back riding will not be permitted. With respect to private vehicle and motorcycle owners, they will be permitted to operate on essential purposes as approved by the Inter-Agency Task Force (IATF). Private vehicles will be permitted one person in the front row, while the rear seats should not surpass two persons for each row. Motorcycles are restricted from having back-riding travellers. The utilization of bicycles and comparative modes are likewise profoundly empowered, and local government units (LGUs) are additionally urged to identify dedicated bicycle paths or lanes.

This guideline was further amended, allowing motorcycles to have back-riding passengers with the use of barriers to demarcate the back-rider. While people are trying to observe physical distancing in public transport, there will be a rise on personal transport modes like bicycle, electric scooters, and other forms which are expected to gain popularity following this pandemic.

Possible issues of reducing transportation capacity by 50% will be the rise of more private vehicle trips thereby resulting to traffic congestion; stranded passengers at vehicles terminals; and loss of time. Similarly, the proposed barrier used for motorcycles may not be the best. This may lead to potential accidents and fatal injuries for both the motorist and the back-rider when driving on free roads where high speeds are inevitable.

On 11th and 14th of September 2020, the Philippine government planned the easing of physical distancing in public transports. This will be done with strict monitoring of the daily reported cases after its implementation to know the effects of the adjustments from the approved one-meter distance by WHO to a reduced distance of 0.75 meters. This will be further reduced to 0.5 meters and then 0.3 meters with two-weeks progressive monitoring of each

implemented reduced physical distancing, and if there are no issues then the policy will remain [26,27]. Furthermore, DOTr noted that with full compliance of the use of face masks and face shields in public transport, the one-meter distancing can successfully be reduced to 0.3 meters. A report from the International Union of Railways (UIC) further explained that the use of a face mask and face shield is 100 percent safe even if you come in contact with someone who is the carrier of the virus [28]. With this at hand, there has been complaints from the masses noting that the reduced physical distancing should only be encouraged when the number of reported cases and active cases flatten. With regards to this, there are a lot of oppositions to the implementation of reduced physical social distancing, mostly medical practitioners who have criticized and noted that the reduced spacing among commuters will further increase the spread of the virus [29]. Due to the strong opposition from the masses, the government decided to suspend this new policy on 17th September 2020 [30].

Policy Recommendations

Considering the key issues raised in the previous section, the authors would like to propose the following policy implications.

- *Provide standards.* The government should provide scientific and data-driven standards, rather than allowing local government units and sectors to implement their own strategies. The minimum requirements should at least come from the centralized government. For example, what safety features should be found in jeepneys at the minimum? Some operators are installing plastic sheets to shield passengers away from each other. Instead of helping, that can even help spread the virus further because it will add more surfaces for the virus to live on to. If the government does not publish standards about this, operators will just implement what they want, and our pandemic response will become one big experiment. There is enough information in literature now to narrow down the options and help the country develop minimum standards now. Standards should be developed scientifically and in consultation with academics.
- *Manage the demand.* You cannot expect a service to run smoothly when you decrease its capacity (supply) by half without creating a similar reduction in demand. To reduce demand, it is recommended that the government encourage companies to maintain their telecommuting (work-from-home) setups until after a viable vaccine becomes available. This can be done by providing fiscal and non-fiscal incentives to companies willing to do telecommuting. Without this kind of support, companies might be forced to risk their employees commuting or opt to suspend operations, which will be detrimental to the economy. In addition to the

said incentives, this is also prime time to improve the internet infrastructure of the country and strengthen our data security policies and protocols. It is also recommended to encourage schools capable of distance-learning to keep doing this until after a viable vaccine becomes available.

- *Improve the supply.* Supply can be improved by allowing modern jeepney fleets to operate and co-exist with conventional jeepneys. Modern jeepneys are more spacious, which could make physical distancing easier to implement. This can be a good opportunity to accelerate the implementation of the Public Utility Vehicle Modernization Program of the government. However, the welfare and livelihood of conventional jeepney operators and drivers should be put first and foremost. Social programs need to be set up for them.
- *Improve the services.* This can be done by leveraging and promoting digital technologies in transportation. The government should fund the development of fleet management systems, which would speed up information generation and distribution in public transport. This would manage non-compliance among operators and drivers. Also, the fleet management system should provide an efficient means to keep record of which vehicles each commuter takes and at which date and time to enable fast contact tracing in public transport. This can be done by creating an end-user app that commuters can use to book seats in advance, or just to log their vehicle boarding and unboarding activities.

Conclusions

In conclusion, the authors believe that the central government should be on top of this COVID-19 response. Though delegating the management to local government units and various sectors has its benefits, one wrong decision from a certain unit can lead to a ripple of infections. Standards and protocols, especially on how public transport should operate, must be scientifically commissioned. The country's COVID-19 response does not have to be a one big trial and error experiment considering the wealth of information already available in literature, especially when the lives of many people are on the line.

This is also a good time to embrace innovation, not only technologically but also on how certain business processes are carried out. The country should leverage on the telecommuting experience it has obtained during this time, including distance learning. These alternatives are better maintained even beyond the pandemic from a sustainability perspective.

Based on literature, the best protection for commuters, public transport operators and drivers are plain and simple wearing of face masks, good personal hygiene, and regular sanitation of surfaces which get into contact with

passengers. Thus, additional structures (e.g. shielding) might not be necessary after all. Proper management of supply and demand, the use of digital technology to speed up information generation and distribution, and the implementation of scientific safety standards should allow our commuters to use public transport safely and comfortably.

Acknowledgements

The authors would like to thank the ASEAN Foundation and USAID for their invaluable support to the ASEAN Science and Technology Fellows of the year 2019-2020. Gratitude is also expressed to the Office of the Vice Chancellor for Research and Innovation and the Science Foundation of De La Salle University for the financial support provided in the publishing of this work.

References

- [1] P. Walker, C. Whittaker, O. Watson, M. Baguelin, K. Ainslie, S. Bhatia and P. Z. Cucunuba, "The impact of COVID-19 and strategies for mitigation and suppression in low- and middle-income countries," *Science*, vol. 369, no. 6502, pp. 413-422, 2020.
- [2] World Health Organization, "*Coronavirus Diseases (COVID-19) Dashboard*," July 25, 2020. [Online]. Available: https://covid19.who.int/?gclid=Cj0KCQjwgo_5BRDuARIsADDEntSiBwc0wVE_m816mOuxm98W4of1C3PLXEZstZscG48yYBwVw6_1aZMaAueNEALw_wcB. [Accessed July 25, 2020].
- [3] Centers for Disease Control and Prevention, "*Coronavirus Disease 2019 (COVID-19)*," Frequently Asked Questions. [Online]. Available: <https://www.cdc.gov/coronavirus/2019-ncov/faq.html>. [Accessed July 30, 2020].
- [4] A. W. H. Chin, J. T. S. Chu, M. R. A. Perera, K. P. Y. Hui, H. Yen, M. C. W. Chan, M. Peiris and L. L. M. Poon, "Stability of SARS-CoV-2 in different environmental conditions," *The Lancet, Microbe*, vol. 1, no. 1, e10, 2020.
- [5] CNN Philippines, "*Metro Manila records highest temperature for 2019*," July 31, 2020. [Online]. Available: <https://www.cnnphilippines.com/news/2019/4/22/Metro-Manila-temperature-record-high-2019.html>. [Accessed July 31, 2020].
- [6] Inquirer, "*Tuguegarao City records hottest temperature–Pagasa*," April 26, 2014. [Online]. Available: <https://newsinfo.inquirer.net/597474/tuguegarao-city-records-hottest-temperature-pagasa>. [Accessed July 31, 2020].

- [7] R. De Silva, “COVID-19: Its Impact on the Philippines – FINAL,” *Europe Solidaire Sans Frontières*, July 25, 2020. [Online]. Available: <http://www.europe-solidaire.org/spip.php?article52772>. [Accessed July 25, 2020].
- [8] EcoMobility, “COVID-19: Focus on cities and transport responses—South East Asia,” July 25, 2020. [Online]. Available: <https://sustainablemobility.iclei.org/covid-19-focus-on-cities-and-transport-responses-south-east-asia/>. [Accessed July 25, 2020].
- [9] R. Madhu, “Building safer and more resilient cities in Philippines,” *World Bank Blogs*, May 14, 2020. [Online]. Available: https://blogs.worldbank.org/eastasiapacific/building-safer-and-more-resilient-cities-philippines?fbclid=IwAR0fJ4YXjW3VVBUwgLdl7LW_AjVHJ6Lbj9PXU2_JaHjVF3yo4RqyDJI9qtk. [Accessed July 25, 2020].
- [10] C. M. Ramos, “Covid-19 impact study: Losses may hit P2.5 trillion; ease economic restrictions,” *Inquirer*, April 17, 2020. [Online]. Available: <https://newsinfo.inquirer.net/1260203/ph-economy-may-lose-up-to-p2-5-trillion-due-to-covid-19-pandemic-pids-study>. [Accessed July 25, 2020].
- [11] S. Cochrane, “No growth for Philippines in Q3, says Moody’s unit,” *Philstar Global*, July 25, 2020. [Online]. Available: https://www.philstar.com/business/2020/07/25/2030363/no-growth-philippines-q3-says-moodys-unit?fbclid=IwAR2g_zL0JCBqRwsym4YVSnt2b26hgiXWRoGGGTCoQXfNrbe3Eyy0oFG94-0. [Accessed July 25, 2020].
- [12] L. Wright, “Let’s use the pandemic to expand our transport options,” *Asian Development Blog*, April 3, 2020. [Online]. Available: https://blogs.adb.org/let-s-use-the-pandemic-to-expand-our-transport-options?fbclid=IwAR0w4wXVhPudpo-kjNKCCceeES9_ThA7FLwbR6K2Dg7Uw1YKjXb5xGS6km8. [Accessed July 28, 2020].
- [13] X. Yang, C. Ou, H. Yang, L. Liu, T. Song, M. Kang, H. Lin and J. Hang, “Transmission of pathogen-laden expiratory droplets in a coach bus,” *Journal of Hazardous Materials*, vol. 397, pp. 122609, 2020.
- [14] J. H. Rubens, P. C. Karakousis and S. K. Jain, “Stability and Viability of SARS-CoV-2,” *The New England Journal of Medicine*, vol. 382, pp. 1962-1966, 2020.
- [15] S. W. X. Ong, Y. K. Tan, P. Y. Chia, T. H. Lee, O. T. Ng, M. S. Y. Wong and K. Marimuthu, “Air, surface environmental, and personal protective equipment contamination by severe acute respiratory syndrome coronavirus 2 (SARS-CoV-2) from a symptomatic patient,” *JAMA*, vol. 323, no. 16, pp.1610-1612, 2020.
- [16] K. Ng, B. H. Poon, T. H. Kiat Puar, J. L. Shan Quah, W. J. Loh, Y. J. Wong, T. Y. Tan and J. Raghuram, “COVID-19 and risk to health care workers: a case report,” *Annals of Internal Medicine*, vol. 172, no. (11), pp. 766-767, 2020.

- [17] K. E. Foley, “The novel coronavirus can likely live up to 96 hours on phone screens,” *Quartz*, February 29, 2020. [Online]. Available: <https://qz.com/1810508/covid-19-can-likely-live-up-to-96-hours-on-your-phone/>. [Accessed July 28, 2020].
- [18] N. Van Doremalen, T. Bushmaker, D. H. Morris, M. G. Holbrook, A. Gamble, B. N. Williamson and J. O. Lloyd-Smith, “Aerosol and surface stability of SARS-CoV-2 as compared with SARS-CoV-1,” *The New England Journal of Medicine*, vol. 382, pp. 1564-1567, 2020.
- [19] World Health Organization, “Consensus document on the epidemiology of severe acute respiratory syndrome (SARS) (No. WHO/CDS/CSR/GAR/2003.11),” May 17, 2003. [Online]. Available: <https://apps.who.int/iris/handle/10665/70863>. [Accessed July 28, 2020].
- [20] Bloomberg, “These elite contact tracers show the world how to beat COVID-19,” July 25, 2020. [Online]. Available: <https://www.bloomberg.com/news/articles/2020-07-25/these-elite-contact-tracers-show-the-world-how-to-beat-covid-19>. [Accessed July 31, 2020].
- [21] World Health Organization, “New Zealand takes early and hard action to tackle COVID-19,” July 15, 2020. [Online]. Available: <https://www.who.int/westernpacific/news/feature-stories/detail/new-zealand-takes-early-and-hard-action-to-tackle-covid-19>. [Accessed July 31, 2020].
- [22] Centers for Disease Control and Prevention, “Case investigation and contact tracing: Part of a multipronged approach to fight the COVID-19 pandemic,” December 3, 2020. [Online]. Available: <https://www.cdc.gov/coronavirus/2019-ncov/php/principles-contact-tracing.html>. [Accessed July 31, 2020].
- [23] Manila Times, “LTFRB: Commuters may be asked to give personal info to PUVs for virus contact tracing,” May 19, 2020. [Online]. Available: <https://www.manilatimes.net/2020/05/19/second-headline/ltfrb-commuters-may-be-asked-to-give-personal-info-to-puvs-for-virus-contact-tracing/725813/>. [Accessed July 31, 2020].
- [24] Philippine News Agency, “DOTr sets guidelines for public transport in GCQ areas,” May 1, 2020. [Online]. Available: <https://www.pna.gov.ph/articles/1101544>. [Accessed July 26, 2020].
- [25] Department of Transportation, “DOTr issued guideline for road transport sector in areas under GCQ,” May 1, 2020. [Online]. Available: <https://dotr.gov.ph/55-dotr-news/1315-dotr-issues-guidelines-for-road-transport-sector-in-areas-under-gcq.html>. [Accessed July 26, 2020].
- [26] CNN Philippines, “DOTr: Possible to recall new public transport distancing policy,” September 14, 2020. [Online]. Available: https://www.cnnphilippines.com/news/2020/9/14/DOTr-reduced-physical-distancing-public-transport-study.html?fbclid=IwAR2mon-aotP96nZd7FE_A9R4ABNpsPzJyYbul7l-wZFEl-pZLZEd9D9_gXM. [Accessed September 17, 2020].

- [27] CNN Philippines, “Gov’t approves easing of physical distancing rules in public transport,” September 11, 2020. [Online]. Available: https://cnnphilippines.com/news/2020/9/11/Public-transportation-physical-distancing-rules-Philippines.html?fbclid=IwAR1Q0-vuy9YnenkSWz2DHqFmj22jzFnNZz4YyldAYrV28uAgcu_jLT5os7LI. [Accessed September 17, 2020].
- [28] International Union of Railways, “Masks ventilation and social distancing,” September 17, 2020. [Online]. Available: https://uic.org/IMG/pdf/railsilience_masks_ventilation.pdf. [Accessed September 17, 2020].
- [29] M. Vacas, “Reduced commuter distancing up for review; DILG agrees more public transportation must be deployed,” *One News*, September 15, 2020. [Online]. Available: <https://www.onenews.ph/reduced-commuter-distancing-up-for-review-dilg-agrees-more-public-transportation-must-be-deployed>. [Accessed September 17, 2020].
- [30] P. Ranada, “Gov’t suspends reduced physical distancing in public transportation,” *Rappler*, September 17, 2020. [Online]. Available: <https://www.rappler.com/nation/government-suspends-reduced-physical-distancing-public-transportation>. [Accessed September 29, 2020].

Microstructure and Microhardness Alterations of Inconel 718 under Cryogenic Cutting

*Che Hassan Che Haron, Jaharah Abdul Ghani, Muammar Faiq Azhar
Centre for Engineering Materials and Smart Manufacturing (MERCU),
Faculty of Engineering and Built Environment,
Universiti Kebangsaan Malaysia, 43600 Bangi, MALAYSIA*

Nurul Hayati Abdul Halim
School of Mechanical Engineering, College of Engineering,
Universiti Teknologi MARA, 40450, Shah Alam, Malaysia.
hayatih@uitm.edu.my

*N. Badroush
Center of Human Resource Development and Quality,
Academy of Maritime Studies, Tripoli, Libya*

ABSTRACT

This paper presents the experimental investigations to identify the effect of different machining parameters on the microstructure and microhardness alterations beneath the machined surface of Inconel 718. The high-speed milling experiments were conducted using PVD multi-coated ball nose carbide inserts, under cryogenic CO₂ condition at controlled cutting speed of 120-140 m/min, feed rate of 0.15-0.25 mm/tooth, depth of cut of 0.3–0.7 mm and a fixed width of cut at 0.4 mm. The experimental results discovered that the formation of plastic deformation could only be observed when cutting with the highest value of feed rate and depth of cut, deepened until 8.87 μm from the machined surface. At the same time, those factors also significantly increased machined surface hardness, made the workpiece harder than its bulk hardness. However, the hardness values were found reduced towards the sub-surface and back to its bulk hardness approximately 250 - 300 μm from the top surface. This study suggests that the finishing milling process of Inconel 718 under cryogenic CO₂ condition and at predetermined parameters can be performed at a depth of cut less than 0.3 mm as its machined sub-surface microhardness and microstructure alteration were observed to be inconsequential. Thus, a more economical machining process can be performed.

Keywords: *Cryogenic Machining; Coated Tungsten Carbide; Inconel 718; Microstructure alteration; Microhardness*

Introduction

Super alloy Inconel 718 is one of the Nickel-based super-alloys. It is widely applied in aerospace industries due to its high strength at elevated temperatures and high resistance to corrosion. However, when cutting this difficult-to-machine material at high-speed, its low thermal conductivity caused the heat that inherently generated accumulating in the cutting zone to extreme levels. Researchers such as Musfirah et al. [1], Kasim [2], and Sonawane and Joshi [3] reported there were microstructure and microhardness changes beneath the machined surface when high-speed milling Inconel 718 under cryogenic, minimum quantity lubrication (MQL) and dry conditions, respectively. As reported, the combination of elevated cutting temperatures and the mechanical shock from the intermittent cutting of milling process accelerates wear rate which then facilitates sub-surface defects like plastic deformation and the tendency of the machined surface to work-harden [4]. These undesirable changes reduce its surface integrity while increasing its difficulty to be machined.

The correlation between different machining conditions and the levels of microstructure and microhardness alteration at machined sub-surface have been numerously examined by previous studies. Cutting speed, feed rate, depth of cut, tool type, geometry, as well as lubrication or cooling conditions, are some of the common factors that have been investigated [5]. The finding is important as the alterations affect the fatigue life, functionality, and durability of the final products, mainly the one serviced in high temperatures or stress loads and aggressive environments [6]. Meanwhile, Grzesik et al. [7] used terms abusive, conventional, and gentle machining processes which related to the level of heat and strain rates generated during cutting to demonstrate their influence on machined surface integrity.

Generally, the depth of plastic deformation below the machined surface to which it extends significantly influenced by the tool geometry, depth of cut, machining conditions as well as the absence or presence of coolant or lubricant during cutting [7]. For instance, Sharman et al. [8] found that the worn tool produced greater degree of grain boundary microstructural plastic deformation than the new tool in turning of Inconel 718. Meanwhile, a study by Musfirah et al. [1] revealed obvious grain structure deformation near the machined surface in dry milling of Inconel 718 rather than in cryogenic condition using liquid nitrogen (LN₂). This is apparently related to the elevated temperature of dry milling due to the absence of any coolant or lubricants during cutting [9]. However, the extremely low temperature of cryogenic LN₂ at -196 °C tends to work-harden Inconel 718, thus increase its microhardness. As also found by

Iturbe et al. [10], 160 – 200 μm below the machined surface of Inconel 718 were 50-130 HV harder than its base hardness after milled under cryogenic LN_2 . This finding proved the significant influence of the coolant on the cold hardening of the material. A similar finding was observed by Shokrani et al. [4] when milling titanium alloys under dry, flood and LN_2 cryogenic, where subsurface microhardness was found highest under cryogenic cooling compared others.

Meanwhile, a study by Kasim relates the increase of surface microhardness with the increase of cutting speed in the milling of Inconel 718 under MQL condition [2]. As explained by Liao et al. [11] and Halim et al. [12], cutting temperature is significantly increased with cutting speed, while below 650 °C, Inconel 718 tends to become harder and harder with the increase of cutting temperatures. However, in the case of titanium alloy, contradict finding reported by Ginting and Nouari [13] where the hardness of the machined surface was 8% less than the bulk hardness. They relate it with the thermal softening of the sub-surface region due to the ageing process during cutting.

Recently, the application of cryogenic carbon dioxide (CO_2) in metal cutting has been substantially increasing among researchers with the latest by Pereira et al. [14], Luka et al. [15] and Khanna et al. [16]. Promising results associated with cryogenic cutting of difficult-to-machine materials have been reported. Liquid CO_2 at -76 °C offered less cooling effect as compared to LN_2 . Thus, lower work hardening effect on the machined surface with better surface integrity is one of the targeted advantages from this approach. However, information regarding the microstructure and microhardness alterations when milling Inconel 718 under cryogenic CO_2 is scarce particularly pertaining the influence of cutting parameters.

Thus, this paper study the microstructure and micro-hardness changes of the machined surface layer of Inconel 718 after high-speed milling under cryogenic CO_2 condition affected by the different machining parameters. The microstructure alteration focuses on the grain deformation beneath the machined surface, while the microhardness alterations cover the relationship between the change in sub-surface hardness with the deepening of measurement points or distances from the machined surface. For the cryogenic CO_2 , it is also considered as a sustainable approach to substitute conventional cutting fluids, as it offers a clean and safe cutting environment. Once supplied to the cutting area; it automatically evaporates to the atmosphere without any residues [17].

Methodology

Experimental milling setup

The experimental high-speed milling processes were performed via a CNC milling machine. In total, five experiments were conducted according to the identified finishing process parameters as listed in Table 1. For the milling inserts, commercially available PVD carbide coated ball nose type from Sumitomo were applied. The diameter of the insert is 10 mm, and it is coated with the alternate layers of TiAlN and AlCrN at 3 μm thickness. Before cutting, the insert was attached to the 16 mm diameter of a BIG Hi-power milling cutter at radial rake angle of 0° , relief angle of 11° , approach angle of 90° , axial rake angle of -3° , and an overhang length of 30 mm. The workpiece for the experiments was an aged AMS5663 Inconel 718 in the form of a solid block, 170 mm in width, 100 mm in height and 50 mm in length. Its hardness is 42 ± 2 HRC with its chemical composition is as listed in Table 2. Before cutting, a thin layer of 0.3 mm was removed from its top surface prior to the experiments in order to get an even machined surface. The milling process was continued until the tool notch wear, V_{bmax} reaches 0.2 mm to avoid excessive temperatures, and severely worn tool that may affect the machined surface.

Table 1: Experimental milling parameters

Experiment	Milling parameters			
	Cutting speed, V_c (m/min)	Feed rate, f_z (mm/tooth)	Depth of cut, a_p (mm)	Width of cut, a_e (mm)
1	120	0.2	0.3	0.4
2	130	0.2	0.3	
3	130	0.25	0.7	
4	140	0.15	0.5	
5	140	0.2	0.3	

Table 2: Composition of the workpiece

wt. %	Ni	Cr	Fe	Nb	Ti	Al	B
	53.0	18.30	18.7	5.0	1.05	0.49	0.004
	C	Cu	Mn	Mo	Si	P	S
	0.051	0.04	0.0.23	3.05	0.08	< 0.005	< 0.002

For the cryogenic CO_2 coolant, a mixture of gaseous CO_2 , liquid CO_2 and compressed air was supplied directed into the cutting tip by using a nozzle as shown in Figure 1. The controlled minimum temperature of the cryogen was approximately $-55 \pm 5^\circ\text{C}$, which was confirmed using a K-type thermometer.

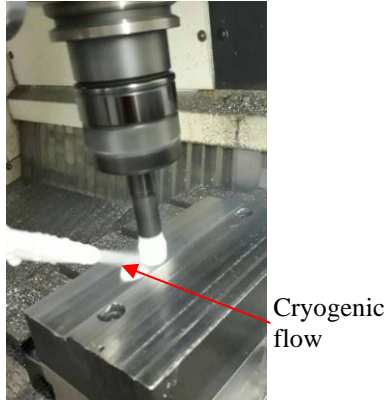


Figure 1: The milling process under cryogenic condition.

Samples preparation

The experimental samples over the cross-section of the workpiece were prepared according to the sequence shown in Figure 2. The workpiece was sectioned into pieces by using electrical discharge wire machining, before being hot mounted in Bakelite at 160 °C. The cross-section of the samples then underwent continuous grinding processes by using sandpapers and polishing processes to get a mirror-like finish, per ASTM E3-80/95. The process was followed by an etching process of 20 seconds using Kalling's reagent containing 100 ml hydrochloric acid (HCL), 100 cc ethyl alcohol and 5 g cupric chloride (CuCl_2) before being rinsed in water and dried by air [18].

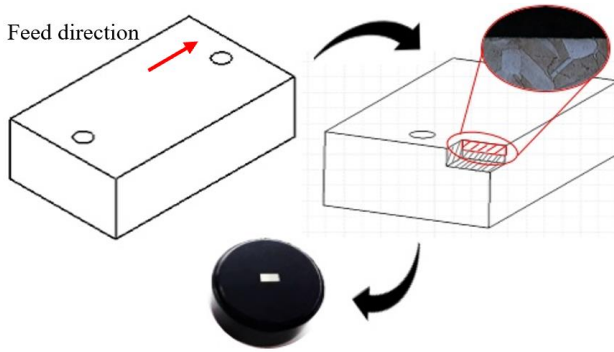


Figure 2: Experimental samples preparation.

Microstructure and microhardness observation

The changes in microhardness along the cross-section of the machined surfaces were measured using a Vickers microhardness tester. The measurements were conducted at depths of up to 600 μm with 100 μm intervals between successive readings from the edge of the sample. At each interval, three readings were taken from three different spots to get the average hardness for that particular depth. The indentation mark on the surface was generated by a diamond indenter in a pyramid form under a consistent load of 98.07 N (10 Kp) with 15 seconds dwell time. For the indentation mark, the angle between opposites was 136° . This approach was in parallel with that of researchers like Devillez et al. [19], Kenda et al. [5] and Kasim [2] which used 50-500 gf of indentation load and 10-15 seconds of holding time for Inconel 718. For microstructure observation, an Olympus optical microscope model BX51M at 10X magnification was used.

Results and Discussions

Figure 3 shows the microstructure of aged-hardened Inconel 718 before the machining process. As can be seen, the presences of micro-twinning structures known as annealing twins were found in the microstructure. These needle shapes were believed to have been created due to re-crystallization and growth of new grains during heat treatment process [20]. According to Ramirez [21], these structures made the material stronger in withstanding any plastic deformation due to the shearing force of the cutting process. Due that, the hardness of the aged-hardened Inconel 718 was found to be 65% higher as compared to its initial hardness before the heat treatment process. The heat-treated material is believed offer consistent thermal shock and creep properties at higher cutting temperatures as in high-speed machining.



Figure 3: Microstructure of Inconel 718 (before being machined).

Figure 4 depicts the microstructure of Inconel 718 after high-speed milling at different cutting parameters. Neither of the samples from Experiment 1 (Figure 4a) or Experiment 4 (Figure 4b) showed any plastic deformation. However, plastic deformation with a slip band was observed on the sample from Experiment 3, as shown in Figure 4c. As found, the length of the grain structure deformation was $8.87 \mu\text{m}$ from the machined surface. Slip band is the dislocation microstructure formed during the cyclic deformation of the cutting process. According to Antolovich [22], slip band is one of surface damage modes which tends to cause cracking on the machined surface.

Generally, these findings showed that cutting Inconel 718 at the highest value of feed rate (f_z) and depth of cut (ap) as applied in Experiment 3, altered its microstructure underneath the machined surface (as shown in Figure 4c). The findings are consistent with Griffiths [23], where it was found that factors related to the increase of cutting forces and temperatures increase the level of plastic deformation as well.

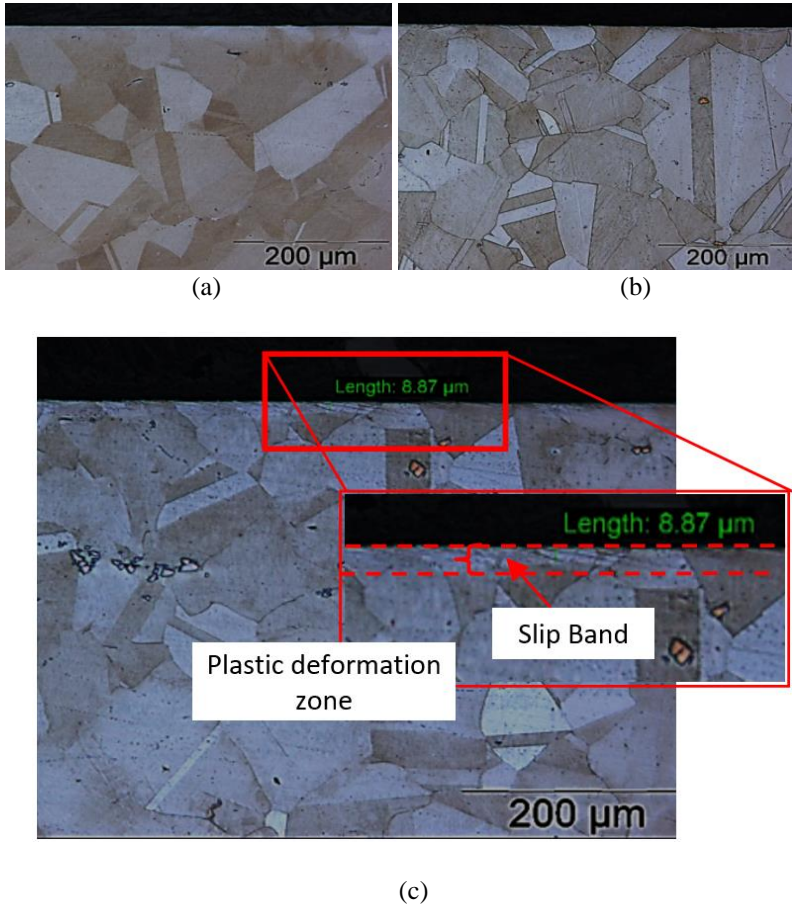


Figure 4: Microstructure alteration from; (a) experiment 1, b) experiment 4, and c) experiment 3.

To see the degree of work hardening experienced by the machined surface, the value of microhardness of each sample was measured from a depth of 25 μm until 600 μm beneath the machined surface. Figure 5 clearly shows that aged-hardening occurred during machining as the average hardness value of each sample was higher than its bulk hardness ($452.5 \pm 2.5 \text{ HV}_{0.1}$). Every sample resulted in a different value of hardness, with the highest value of each were at the depth closest to the machined surface. The values then were reducing as the profile go down beneath the surface. Regarding the work of Sadat and Reddy [24], this occurred because a massive amount of strain hardening was concentrated at the area nearest to the machined sub-surface as a result of high temperature and shearing force. This notable finding was

consistent with Hadi [25], Kasim [2] and Pusavec et al. [26], who were also concentrated on high-speed cutting of Inconel 718.

In this analysis, the highest value of hardness was obtained in Experiment 3 with an average value of 474 HV_{0.1}, 4.2% higher than its bulk hardness. In comparison, Hadi [25] and Kasim [2] recorded an increase in hardness of 8.9% and 8.8% in LN₂ cryogenic and MQL, respectively. Clearly, the effects of controlled cryogenic cooling and the use of a cutting tool with a maximum wear rate $Vb_{max} \geq 0.2$ mm helped to reduce the effects of heat and work hardening on the machined surface. The hardness values were found to decrease with the deepening of the measurement point from the sub-surface until it almost approached the bulk hardness approximately 0.3 mm from the machined surface. This was consistent with the findings of Devillez et al. [19], Hadi [25], Kasim [2], and Pusavec et al. [27]. The zone where age-hardening occurred is known as the machining affected zone, MAZ as proposed by Sonawane and Joshi [3]. MAZ results from work hardening during machining, which forms a plastic deformation layer at a certain distance from the machined surface. Ginting and Nouari [13] defined these two zones as the hard sub-surface region and the bulk material region as also adopted in Figure 5.

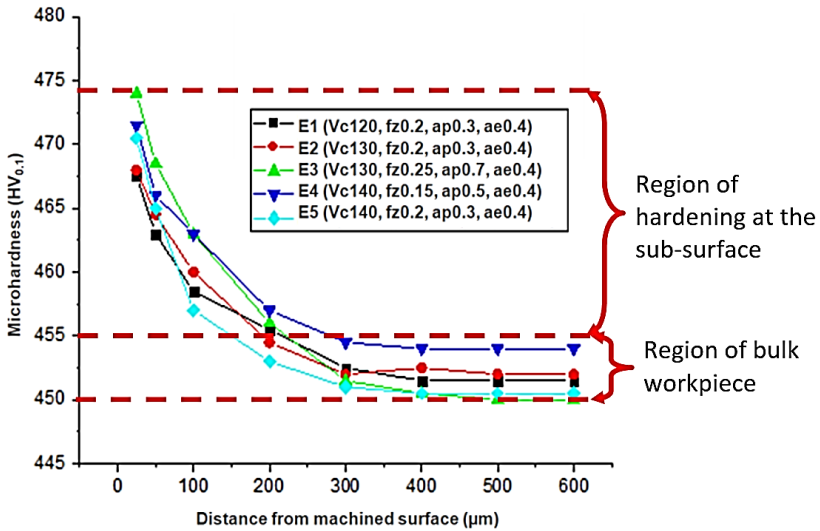
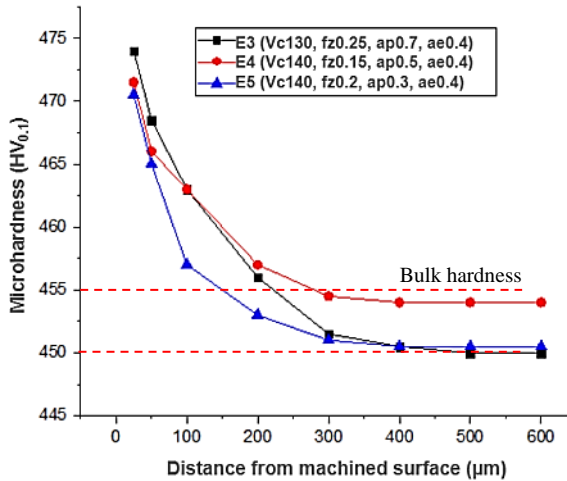


Figure 5: Micro-hardness at the sub-surface of the machined area.

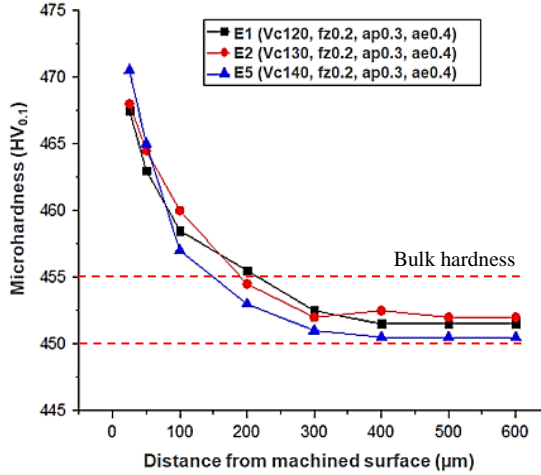
Figure 6a shows the effects of a feed rate (f_z) and depth of cut (ap) on micro-hardness in Experiment 3, Experiment 4 and Experiment 5. It is shown that the microhardness (starting at 50 μm beneath the machined surface) increased with the depth of cut. The highest value of feed rate also resulted with the highest microhardness. This result is consistent with the findings of

Kasim [2] and Hayati et al. [28] where they mentioned that the increase of feed rate and depth of cut increase not only the size of cut but also the cutting force that needed to be borne by the cutting tool. This condition resulted in a higher strain rate on the machined surface. Meanwhile, Tsirbas et al. [29] connected the increase of depth of cut with the increase in machining temperature.

The increase of cutting speed (V_c) also significantly increases the microhardness, as shown in Figure 6b. At the highest cutting speed (140 m/min) as in Experiment 5, the microhardness increases until 3.6% as compared to its bulk value. While Experiment 2 at cutting speed 120 m/min resulted with the lowest. This finding was consistent with Sonawane and Joshi [3] who also milled Inconel 718 but under dry condition. According to Thakur and Gangopadhyay [30], the increase of cutting speed tends to change the residual stress from compressive to tensile, which was related to the increase in machining temperature. This caused the workpiece exposes to higher temperature and pressure during cutting. The attribute of Inconel 718, its low thermal conductivity property was also believed to contribute to the increased machining temperature as well as affect the machined surface integrity. At temperatures lower than 650 °C, Inconel 718 tends to work harden along with the increase in machining temperature [11], [31].



(a)



(b)

Figure 6: Micro-hardness; (a) effects of feed rate (f_z) and depth of cut (ap); and (b) effects of cutting speed (V_c).

Conclusion

Microstructure and microhardness alterations on the sub-surface of Inconel 718 after high-speed cutting Inconel 718 under cryogenic CO₂ condition using PVD carbide coated ball nose milling insert were analyzed. It was found that the depth of plastic deformation depends greatly on the machining parameters. The highest value of feed rate and depth of cut resulted with obvious grain structure deformation, deepening until 8.87 μm from the machined surface. At the same time, those factors also significantly increase the sub-surface microhardness, made the machined surface harder and more difficult to be machined. Cutting speed also plays an important role in increasing the subsurface microhardness. At the highest cutting speed, the machined sub-surface microhardness was 3.6% harder than bulk hardness. Also found that the depth of machined affected zone was reduced as the profile goes down beneath the surface. The workpiece's hardness was back to its bulk hardness approximately 300 μm from the top surface. Thus, it can be suggested that the finishing process of Inconel 718 under cryogenic condition can be performed at a depth of cut lower than 0.3 mm to remove any hardening effect on the machined surface.

Acknowledgements

This research was founded by the UKM-DIP-2017-023 grant.

References

- [1] A. H. Musfirah, J. A. Ghani, and C. H. C. Haron, "Tool wear and surface integrity of Inconel 718 in dry and cryogenic coolant at high cutting speed," *Wear*, vol. 376–377, pp. 125–133, 2017.
- [2] M. S. Kasim, "Prestasi Perkakas Pemotong Karbida Bersalut Semasa Pengisaran Inkonel 718 Dalam Keadaan Kuantiti Pelincir Minimum," Universiti Kebangsaan Malaysia, Ph.D thesis, 2014.
- [3] H. A. Sonawane and S. S. Joshi, "Analysis of machined surface quality in a single-pass of ball-end milling on Inconel 718," *J. Manuf. Process.*, vol. 14, no. 3, pp. 257–268, Aug. 2012.
- [4] A. Shokrani, V. Dhokia, and S. T. Newman, "Investigation of the effects of cryogenic machining on surface integrity in CNC end milling of Ti-6Al-4V titanium alloy," *J. Manuf. Process.*, vol. 21, no. 1, pp. 172–179, 2016.
- [5] J. Kenda, F. Pusavec, and J. Kopac, "Analysis of Residual Stresses in Sustainable Cryogenic Machining of Nickel Based Alloy—Inconel 718," *J. Manuf. Sci. Eng.*, vol. 133, no. 4, pp. 041009-1-041009–7, 2011.
- [6] X. Liang, Z. Liu, and B. Wang, "State-of-the-art of surface integrity induced by tool wear effects in machining process of titanium and nickel alloys: A review," *Measurement*, vol. 132, pp. 150–181, 2018.
- [7] W. Grzesik, Z. Zalisz, S. Krol, and P. Nieslony, "Investigations on friction and wear mechanisms of the PVD-TiAlN coated carbide in dry sliding against steels and cast iron," *Wear*, vol. 261, no. 11–12, pp. 1191–1200, 2006.
- [8] A. R. C. Sharman, J. I. Hughes, and K. Ridgway, "Workpiece surface integrity and tool life issues when turning Inconel 718TM nickel based superalloy," *Mach. Sci. Technol.*, vol. 8, no. 3, pp. 399–414, 2004.
- [9] N. H. A. Halim, C. H. C. Haron, J. A. Ghani, and M. F. Azhar, "Tool wear and chip morphology in high-speed milling of hardened Inconel 718 under dry and cryogenic CO₂ conditions," *Wear*, vol. 426–427, 2019.
- [10] A. Iturbe, E. Hormaetxe, A. Garay, and P. J. Arrazola, "Surface integrity analysis when machining Inconel 718 with conventional and cryogenic cooling," *Procedia CIRP*, vol. 45, no. Table 1, pp. 67–70, 2016.
- [11] Y. S. Liao, H. M. Lin, and J. H. Wang, "Behaviors of end milling Inconel 718 superalloy by cemented carbide tools," *J. Mater. Process. Technol.*, vol. 201, no. 1–3, pp. 460–465, May 2008.
- [12] N. H. Abdul Halim, C. H. C. Haron, J. A. Ghani, and M. F. Azhar,

- “Machining-induced microstructure of Inconel 718 in cryogenic environment,” *Prog. Ind. Ecol. An Int. J.*, vol. 12, no. 3, p. 234, 2018.
- [13] A. Ginting and M. Nouari, “Surface integrity of dry machined titanium alloys,” *Int. J. Mach. Tools Manuf.*, vol. 49, no. 3–4, pp. 325–332, 2009.
- [14] O. Pereira, A. Celaya, G. Urbikain, A. Rodríguez, A. Fernández-Valdivielso, and L. Noberto López de Lacalle, “CO₂ cryogenic milling of Inconel 718: Cutting forces and tool wear,” *J. Mater. Res. Technol.*, vol. 9, no. 4, pp. 8459–8468, 2020.
- [15] L. Sterle, D. Mallipeddi, P. Krajnik, and F. Pušavec, “The influence of single-channel liquid CO₂ and MQL delivery on surface integrity in machining of Inconel 718,” *Procedia CIRP*, vol. 87, pp. 164–169, 2020.
- [16] N. Khanna, P. Shah, and Chetan, “Comparative analysis of dry, flood, MQL and cryogenic CO₂ techniques during the machining of 15-5-PH SS alloy,” *Tribol. Int.*, vol. 146, no. January, p. 106196, 2020.
- [17] T. Stefansson, “Application of Cryogenic Coolants in Machining Processes,” Royal Institute of Technology, 2014.
- [18] S. Kumar, G. Sudhakar Rao, K. Chattopadhyay, G. S. Mahobia, N. C. Santhi Srinivas, and V. Singh, “Effect of surface nanostructure on tensile behavior of superalloy IN718,” *Mater. Des.*, vol. 62, no. 3, pp. 76–82, 2014.
- [19] A. Devillez, G. Le Coz, S. Dominiak, and D. Dudzinski, “Dry machining of Inconel 718, workpiece surface integrity,” *J. Mater. Process. Technol.*, vol. 211, no. 10, pp. 1590–1598, 2011.
- [20] M. Moiz, “The influence of grain size on the mechanical properties of Inconel 718,” Linköping University, 2013.
- [21] A. C. Ramirez, “Microstructural Properties Associated with Adiabatic Shear Bands in Titanium-aluminum-vanadium Deformed by Ballistic Impact,” The University of Texas at El Paso, 2008.
- [22] S. D. Antolovich, “Microstructural aspects of fatigue in Ni-base superalloys,” *Philos. Trans. R. Soc. A Math. Phys. Eng. Sci.*, vol. 373, no. 2038, pp. 1–36, 2015.
- [23] B. Griffiths, *Manufacturing Surface Technology: Surface Integrity and Functional Performance (Manufacturing Engineering Modular)*, Ed. ke-4. New York: Elsevier, 2001.
- [24] A. B. Sadat and M. Y. Reddy, “Surface integrity of inconel-718 nickel-base superalloy using controlled and natural contact length tools. Part II: Unlubricated,” *Exp. Mech.*, vol. 33, no. 4, pp. 343–348, 1993.
- [25] M. B. A. Hadi, “Pencirian dan analisa pemesinan laju tinggi kriogenik menggunakan mata alat kisar hujung bebola bersalut karbida ke atas Inkonel 718,” Universiti Kebangsaan Malaysia, 2016.
- [26] F. Pusavec, H. Hamdi, J. Kopac, and I. S. Jawahir, “Surface integrity in cryogenic machining of nickel based alloy — Inconel 718,” *J. Mater. Process. Tech.*, vol. 211, no. 4, pp. 773–783, 2011.
- [27] F. Pusavec, H. Hamdi, J. Kopac, and I. S. Jawahir, “Surface integrity in

- cryogenic machining of nickel based alloy—Inconel 718,” *J. Mater. Process. Technol.*, vol. 211, no. 4, pp. 773–783, 2011.
- [28] N. Hayati, A. Halim, C. Hassan, C. Haron, J. A. Ghani, and M. F. Azhar, “Prediction of Cutting Force for Milling of Inconel 718 under Cryogenic Condition by Response Surface Methodology,” vol. 16, no. 1, pp. 1–16, 2019.
- [29] K. Tsirbas, G. Chryssolouris, and D. Mourtzis, “Grind-hardening modeling with the use of neural networks,” in *Conference: 5th International Conference on Advanced Manufacturing Systems and Technology (AMST)At: Undine, Italy*, 1999, pp. 197–206.
- [30] A. Thakur and S. Gangopadhyay, “State-of-the-art in surface integrity in machining of nickel-based super alloys,” *Int. J. Mach. Tools Manuf.*, vol. 100, pp. 25–54, 2016.
- [31] M. N. Sharif, S. Pervaiz, and I. Deiab, “Potential of alternative lubrication strategies for metal cutting processes : A review,” *Int. J. Adv. Manuf. Technol.*, vol. 89, no. 5–8, pp. 2447–2479, 2016.

Effect of Spindle Speed and Feed Per Tooth in Feed Rate Perspective on Inconel HX Cutting Force

N. A. Mohd Nor*, N. F. Kamarulzaman, N. A. S. Zakaria, N. Awang
Department of Mechanical Engineering, School of Engineering,
Manipal International University, 71800 Putra Nilai, Malaysia.

* noraznan.namn@gmail.com

B. T. H. T. Baharudin, M. K. A. Mohd Ariffin, Z. Leman
Department of Mechanical and Manufacturing Engineering,
Faculty of Engineering, Universiti Putra Malaysia,
43400 Serdang, Malaysia.

ABSTRACT

Reducing feed rate during end-milling of nickel-based superalloys for low-cutting force has always been a common approach. This is due to these alloys having superior properties, making them widely regarded as difficult-to-machine materials. As feed rate is tied to spindle speed and feed per tooth, it is crucial to comprehend whether spindle speed, feed per tooth or the interaction between spindle speed and feed per tooth has a significant factor on cutting force reduction when increasing the feed rate. Accordingly, this manuscript presents an effect of spindle speed and feed per tooth in feed rate perspective on Inconel HX cutting force. Half-immersion down-milling and full-immersion down-milling was conducted experimentally using solid ceramic end-mill cutter. The results indicate that cutting force decreases and then increases after further increase in spindle speed, while cutting force increases with an increase in feed per tooth. Optimum spindle speed and optimum feed per tooth for low-cutting force were 21,400 rpm and 0.013 mm/tooth. Furthermore, feed per tooth was the significant factor which influenced the cutting force, whereas spindle speed, and the interaction between spindle speed and feed per tooth were not significant.

Keywords: Spindle speed; feed per tooth; down-milling; Inconel HX; cutting force

Introduction

Cutting force or resultant force in end-milling is conveniently resolved into three cutting force components in the X, Y and Z axis. Firstly, the cutting force projection that acts along the feed direction or X-axis is defined as the feed force. Secondly, the cutting force projection in the Y-axis is called the normal force. Finally, the cutting force projection that acts in a perpendicular direction to the feed direction or Z-axis is called the axial force. On the other side, the findings from cutting force research have positively contributed to extending cutting tool life [1, 2], improved quality of machined material [2], reduction in production cost [3] and increase in production rate [4, 5]. Cutting force research findings are also key to curb carbon emissions due to climate change which is seen as top global threat. This is due to decrease in cutting force indirectly consumes less power for milling machine and can cause reduction in carbon emissions. As indicated by Hidayah et al. [6], approximately more than 70% of machining process is applied in the production sector in the world, and this sector has contributed about 36% of carbon emissions [7], thus reducing cutting force in end-milling can help in reducing the percentage of carbon emissions.

Apart from cutting force research findings, reducing feed rate and increasing cutting speed during end-milling of nickel-based superalloys have long been used for low-cutting force, as this difficult-to-machine material tends to be hard to end-mill [8, 9] which leads to high-cutting force due to its superior mechanical properties [8, 10]. The decrease in cutting force during reduction of feed rate is due to decrease in speed at which cutting tool engages the machined material [1]. Meanwhile, decrease in cutting force during increasing cutting speed is associated with increase in cutting temperature in the shear zone, and consequently softening the machined material due to drop in mechanical properties [11, 12]. In end-milling, feed rate is tied to spindle speed and feed per tooth, while cutting speed is tied to spindle speed. Decrease in feed per tooth indirectly decreases feed rate, and subsequently decreases cutting force. Whereas, increase in spindle speed not only increases cutting speed, but also increases feed rate. Therefore, a precise understanding whether spindle speed, feed per tooth or the interaction between spindle speed and feed per tooth is a significant factor on cutting force reduction when decreasing the feed rate is crucial.

In this manuscript, Inconel HX is selected as a specimen to study the effect of spindle speed and feed per tooth on cutting force in the feed rate perspective. It is one of the nickel-based superalloys and commonly used as a material for gas turbine engine applications [13] as it has high-strength at elevated temperatures [14] and outstanding oxidation resistance [15]. Besides, end-milling test performed experimentally by half-immersion down-milling and full-immersion down-milling as down-milling has been

recognised as the preferred method to end-mill difficult-to-machine materials compared to up-milling, since it reduces the load from the end-mill cutter edge, improves end-mill cutter life and leaves a better machined material surface quality. Solid ceramic end-mill cutter is used as it is an ideal solution to eliminate the role of cutting fluid due to its negative effect towards human health and environment [16], since this end-mill cutter has the ability to withstand high-cutting temperature during dry end-milling. The effect of spindle speed, feed per tooth and the interaction between spindle speed and feed per tooth are analysed systematically, therefore the optimum spindle speed and optimum feed per tooth for achieving low-cutting force is simultaneously proposed.

Experimental Setup

Experimental test for this research was carried out on a vertical machining centre model Mori Seiki NV 4000 DCG. Its maximum spindle speed is 30,000 rpm. The experimental set-up is illustrated in Table 1 where spindle speed and feed per tooth are divided into three levels. Since this research is focused on spindle speed and feed per tooth in feed rate perspective, there is no correlation between axial depth of cut and feed rate, thus axial depth of cut is held constant at 0.2 mm.

Table 1: Experimental setup

Cutting parameter	Level
Spindle speed (rpm)	16,000, 21,400 and 26,800
Feed per tooth (mm/tooth)	0.013, 0.016 and 0.019
Axial depth of cut (mm)	0.2

Dry end-milling of Inconel HX was performed by half-immersion down-milling and full-immersion down-milling using KYS40 solid ceramic end-mill diameter of 6 mm with 4 flutes from Kennametal. The dimension of Inconel HX specimen was 90 mm × 40 mm × 10 mm with original hardness 92 HR_B. Figure 1 and Figure 2 illustrate half-immersion down-milling and full-immersion down-milling performed in this experimental test. The cutting length was set at 22 mm per run. In addition, fresh KYS40 solid ceramic end-mill cutter was used at each run.

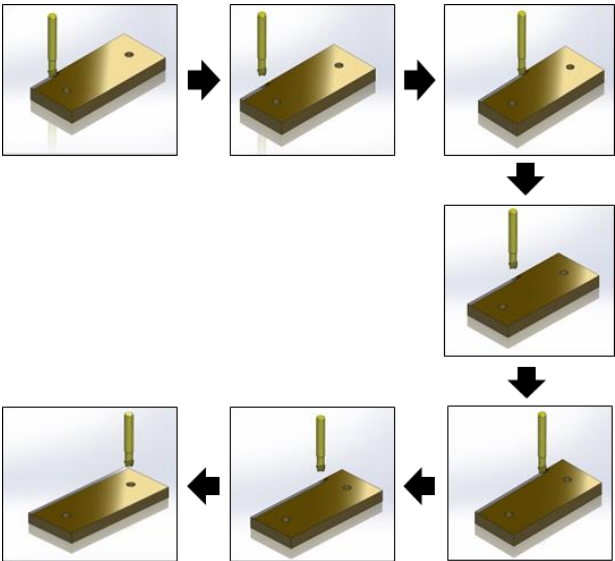


Figure 1: Half-immersion down-milling.

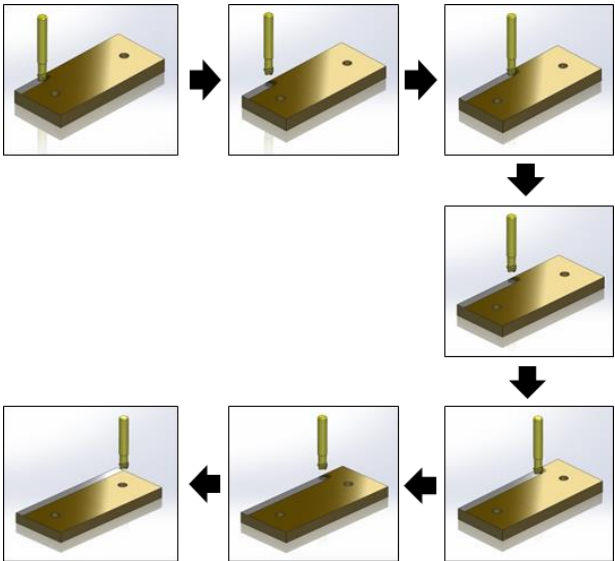


Figure 2: Full-immersion down-milling.

Cutting force components consisting of feed force (F_x), normal force (F_y), and axial force (F_z) were recorded using dynamometer type 9129AA from Kistler. The measurement was repeated three times at each run to find the average value. Figure 3 depicts the dynamometer measuring chain used in this experimental test.

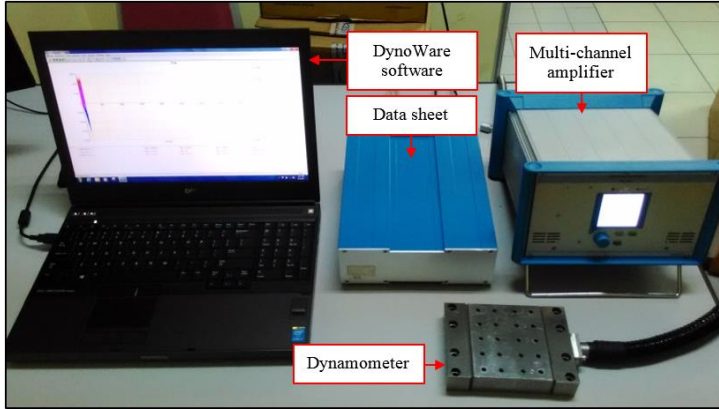


Figure 3: Dynamometer measuring chain.

The recorded cutting force components were then inserted into the Equation (1) [17] to compute the resultant force (F_r) or cutting force.

$$Fr = \sqrt{Fx^2 + Fy^2 + Fz^2} \quad (1)$$

From the computed cutting force, main effects plot and Pareto chart of the standardized effects in Minitab 19 were applied to perform analysis.

Results and Discussion

X-Y plots in Figure 4 and Figure 5 illustrate the overall results obtained after the recorded cutting force components were computed using Equation (1). X-axis and Y-axis represent spindle speed and cutting force respectively, while each trend-line represent feed per tooth at 0.013 mm/tooth (orange), 0.016 mm/tooth (lavender) and 0.019 mm/tooth (black). The effect of spindle speed and feed per tooth in feed rate perspective were discussed further based on the results obtained from main effects plot. Meanwhile, the factor that has significant effect on cutting force was discussed based on the results obtained from Pareto chart of the standardized effects.

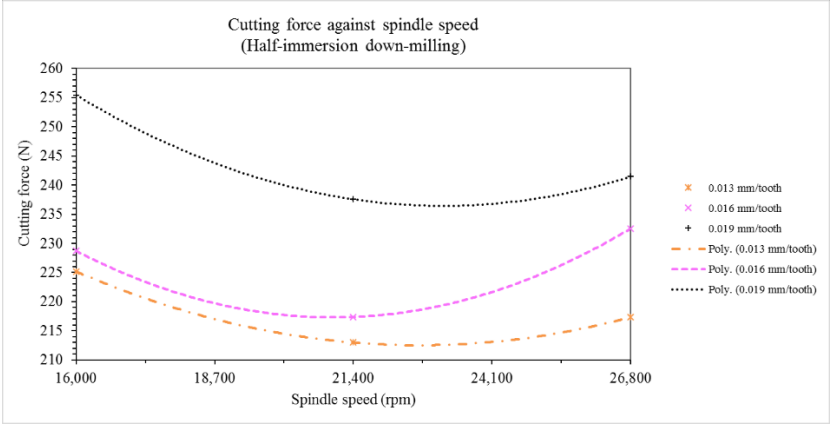


Figure 4: Cutting force against spindle speed for half-immersion down-milling.

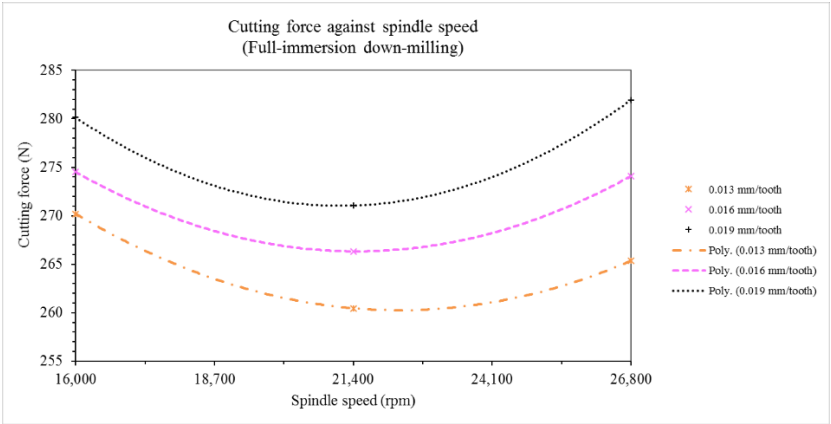


Figure 5: Cutting force against spindle speed for full-immersion down-milling.

Main effects in terms of mean cutting force (N) values for half-immersion down-milling and full-immersion down-milling were plotted in Figure 6 and Figure 7. It is evident from both plots that cutting force decrease when spindle speed increases from 16,000 rpm to 21,400 rpm, then start to increase when spindle speed increases higher from 21,400 to 26,800 rpm. This is contrary to [11, 18], which stated that the reduction of cutting

force is directly proportional to the increase in spindle speed. Furthermore, from both plots, it appears that spindle speed 21,400 rpm in half-immersion down-milling and full-immersion down-milling produced the lowest mean of cutting force, thus it can be claimed that increase in immersion amount or radial depth of cut does not influence the mean of cutting force. Following this, spindle speed 21,400 rpm can be classified as a critical spindle speed for both immersions due to the mean of cutting force drastically decrease before reaching 21,400 rpm and then increase again beyond this critical spindle speed. This can be related to the transition of machined material from ductile regime to brittle regime due to high-strain rate of the increased in spindle speed [19, 20]. In this scenario, Inconel HX undergoes brittle regime end-milling instead of ductile regime end-milling at spindle speed 21,400 rpm, whereby the chips of this end-milled material is removed due to brittle fracture that occurs at the point of tool-chip interface, and subsequently results in low mean of cutting force [21]. As expected, the mean of cutting force increases as the feed per tooth increases in both immersions. The observed increase in the mean of cutting force with increasing feed per tooth from 0.013 mm/tooth to 0.019 mm/tooth can be attributed to the probable increase in a shear amount of unwanted material at the end-mill cutter edge [1, 22]. Apart from this, feed per tooth 0.013 mm/tooth in both immersions are associated with the lowest mean of cutting force. From Figure 6 and Figure 7, it is observed that the optimum cutting parameters in achieving low cutting force are found to be at spindle speed 21,400 rpm and feed per tooth 0.013 mm/tooth, while the cutting force recorded were 213 N for half-immersion down-milling and 260 N for full-immersion down-milling.

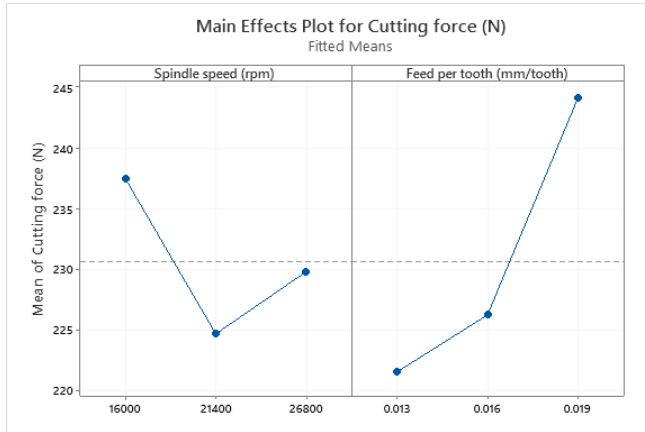


Figure 6: Main effects in terms of mean of cutting force (N) values for half-immersion down-milling.

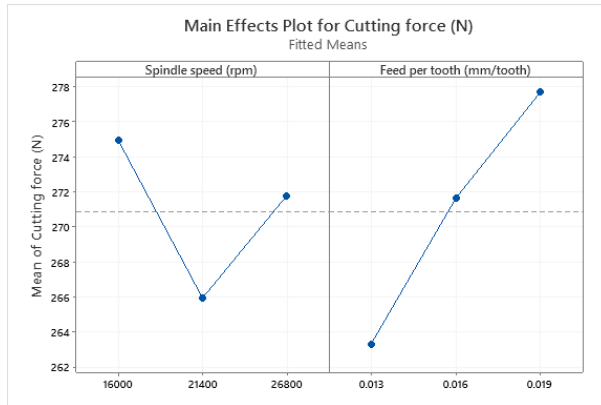


Figure 7: Main effects in terms of mean of cutting force (N) values for full-immersion down-milling.

Pareto chart of the standardized effects on cutting force were plotted in Figure 8 and Figure 9. The results show that B factor has the highest magnitude in half-immersion down-milling followed by A factor and AB factor. While in full-immersion down-milling, B Factor had the highest magnitude followed by AB factor and A factor. Furthermore, the reference line for both immersions was 2.571, therefore any factor that extended past this line was considered significant. It can be seen from Figure 8 and Figure 9 that feed per tooth is the significant factor in half-immersion down-milling and full-immersion down-milling. This is due to the increase in feed per tooth, whereas the mean of cutting force in both immersions also increases, as depict in Figure 6 and Figure 7. Meanwhile, spindle speed and the interaction between spindle speed and feed per tooth have effects on cutting force; however, both factors are not significant in half-immersion down-milling and full-immersion down-milling. In this scenario the mean of cutting force decreases and then increases after further increase in spindle speed, as can be seen in Figure 6 and Figure 7 this is the reason why spindle speed becomes insignificant factor on cutting force in both immersions. Since spindle speed has low magnitude and far from reference line as presented in Figure 8 and Figure 9, this scenario has led to interaction between spindle speed and feed per tooth to become insignificant factor on cutting force in half-immersion down-milling and full-immersion down-milling; although feed per tooth is the significant factor affecting cutting force in both immersions.

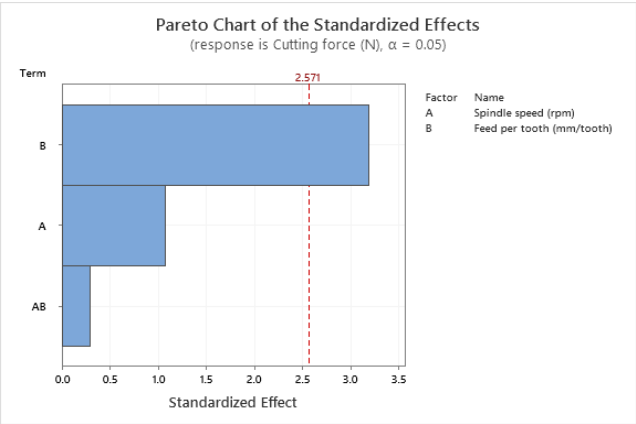


Figure 8: Pareto chart of the standardized effects on cutting force for half-immersion down-milling.

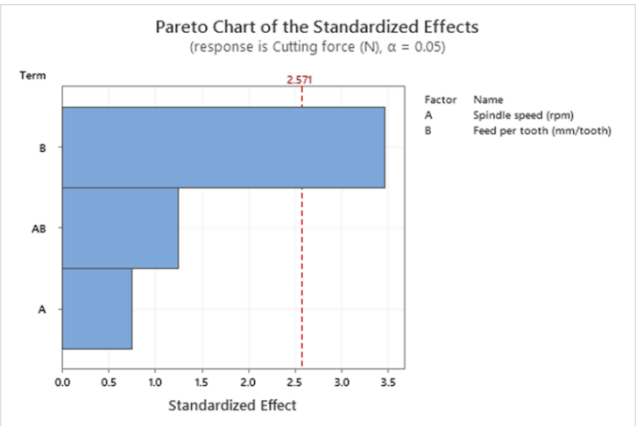


Figure 9: Pareto chart of the standardized effects on cutting force for full-immersion down-milling.

Finally, although spindle speed on cutting force is not a significant factor in feed rate perspective, spindle speed 21,400 rpm is enough to promote low-carbon manufacturing practices. This is due to spindle speed 21,400 rpm not being relatively high when considering Inconel HX as a machined material. Hence, low power consumption of machine tools can be obtained, and subsequently will curb carbon emissions [7]. In addition,

production sectors can reduce production cost due to low power consumption by using this spindle speed during end-milling of Inconel HX. Therefore, increasing spindle speed higher than 21,400 rpm or to its highest level for low-cutting force [11, 18], becomes unnecessary. Although Inconel HX had once been considered impractical to machine under dry condition, the use of KYS40 solid ceramic end-mill cutter in this experimental test proves that dry end-milling is practicable. Harmful effects of cutting fluid are becoming more apparent, mainly on human well-being and environment [23, 24]. Considering this issue, dry end-milling of Inconel HX using KYS40 solid ceramic end-mill cutter is the key for sustainable development.

Conclusion

In present research, the effects of spindle speed and feed per tooth in feed rate perspective on Inconel HX cutting force are studied. The following conclusions can be drawn from this research:

- Cutting force decreased when spindle speed is increased between 16,000 rpm and 21,400 rpm, and increased when using a spindle speed higher than 21,400 rpm.
- Cutting force increased with the increasing in feed per tooth.
- Spindle speed 21,400 rpm and feed per tooth 0.013 mm/tooth were an optimum cutting parameters as it was found to achieve low-cutting force.
- Feed per tooth was the significant factor affecting cutting force. Likewise, the effect of the spindle speed and the interaction between spindle speed and feed per tooth were not statistically significant.
- Future work should be focused on tool life and economical aspect of KYS40 solid ceramic end-mill cutter.

Acknowledgements

The results presented in this manuscript are part of the research project GP-IPS/2017/9539900 financed by Universiti Putra Malaysia. The authors would like to acknowledge Mr. Mohd Nor Bin Puteh, Mdm. Hatijah Binti Kassim, Mdm. Dyg. Siti Quraisyah Bt. Abg. Adenan and Mr. Nor Iman Ziqri Bin Nor Aznan for their support and encouragement.

References

- [1] G. Bolar, A. Das, and S. N. Joshi, "Measurement and analysis of cutting

- force and product surface quality during end-milling of thin-wall components,” *Meas. J. Int. Meas. Confed.*, vol. 121, no. November 2017, pp. 190–204, 2018.
- [2] J. Ma, D. Song, Z. Jia, G. Hu, W. Su, and L. Si, “Tool-path planning with constraint of cutting force fluctuation for curved surface machining,” *Precis. Eng.*, vol. 51, pp. 614–624, 2018.
- [3] Z. Xie, Y. Lu, and J. Li, “Development and testing of an integrated smart tool holder for four-component cutting force measurement,” *Mech. Syst. Signal Process.*, vol. 93, pp. 225–240, 2017.
- [4] M. Wan, W. Yin, and W.-H. Zhang, “Study on the Correction of cutting force measurement with table dynamometer,” *Procedia CIRP*, vol. 56, pp. 119–123, 2016.
- [5] M. Wan, W. Yin, W.-H. Zhang, and H. Liu, “Improved inverse filter for the correction of distorted measured cutting forces,” *Int. J. Mech. Sci.*, vol. 120, pp. 276–285, 2017.
- [6] M. T. Hidayah, J. A. Ghani, M. Z. Nuawi, and C. H. C. Haron, “A review of utilisation of cutting force analysis in cutting tool condition monitoring,” *Int. J. Eng. Technol. IJET-IJENS*, vol. 15, no. 28, pp. 150203–4848, 2015.
- [7] C. Tian, G. Zhou, J. Zhang, and C. Zhang, “Optimization of cutting parameters considering tool wear conditions in low-carbon manufacturing environment,” *J. Clean. Prod.*, vol. 226, pp. 706–719, 2019.
- [8] A. Pleta and L. Mears, “Cutting Force Investigation of Trochoidal milling in Nickel-based superalloy,” *Procedia Manuf.*, vol. 5, pp. 1348–1356, 2016.
- [9] D. Grguraš, M. Kern, and F. Pušavec, “Suitability of the full body ceramic end milling tools for high speed machining of nickel based alloy Inconel 718,” *Procedia CIRP*, vol. 77, no. Hpc, pp. 630–633, 2018.
- [10] D. Finkeldei, M. Sexauer, and F. Bleicher, “End milling of inconel 718 using solid Si3N4 ceramic cutting tools,” *Procedia CIRP*, vol. 81, pp. 1131–1135, 2019.
- [11] N. Masmiahi, A. A. D. Sarhan, M. A. N. Hassan, and M. Hamdi, “Optimization of cutting conditions for minimum residual stress, cutting force and surface roughness in end milling of S50C medium carbon steel,” *Meas. J. Int. Meas. Confed.*, vol. 86, pp. 253–265, 2016.
- [12] H. Çalışkan and M. Küçükköse, “The effect of aCN/TiAlN coating on tool wear, cutting force, surface finish and chip morphology in face milling of Ti6Al4V superalloy,” *Int. J. Refract. Met. Hard Mater.*, vol. 50, pp. 304–312, 2015.
- [13] Q. Han, Y. Gu, S. Soe, F. Lacan, and R. Setchi, “Effect of hot cracking on the mechanical properties of Hastelloy X superalloy fabricated by laser powder bed fusion additive manufacturing,” *Opt. Laser Technol.*,

- vol. 124, p. 105984, 2020.
- [14] A. R. K. Chennamsetty, J. Leblanc, S. Abotula, P. N. Parrikar, and A. Shukla, "Dynamic response of Hastelloy® X plates under oblique shocks: Experimental and numerical studies," *Int. J. Impact Eng.*, vol. 92, pp. 75–88, 2016.
 - [15] M. Esmailzadeh, F. Qods, H. Arabi, and B. M. Sadeghi, "An investigation on crack growth rate of fatigue and induction heating thermo-mechanical fatigue (TMF) in Hastelloy X superalloy via LEFM, EPFM and integration models," *Int. J. Fatigue*, vol. 97, pp. 135–149, 2017.
 - [16] A. Iturbe, E. Hormaetxe, A. Garay, and P. J. Arrazola, "Surface integrity analysis when machining Inconel 718 with conventional and cryogenic cooling," *Procedia CIRP*, vol. 45, no. Table 1, pp. 67–70, 2016.
 - [17] W. Shixiong, M. Wei, L. Bin, and W. Chengyong, "Trochoidal machining for the high-speed milling of pockets," *J. Mater. Process. Technol.*, vol. 233, pp. 29–43, 2016.
 - [18] A. Mebrahitom, W. Choon, and A. Azhari, "Side milling machining simulation using finite element analysis: *Prediction of Cutting Forces*," *Mater. Today Proc.*, vol. 4, no. 4, Part D, pp. 5215–5221, 2017.
 - [19] B. Wang, Z. Liu, G. Su, Q. Song, and X. Ai, "Investigations of critical cutting speed and ductile-to-brittle transition mechanism for workpiece material in ultra-high speed machining," *Int. J. Mech. Sci.*, vol. 104, pp. 44–59, 2015.
 - [20] N. A. Mohd Nor, B. T. H. T. Baharudin, J. A. Ghani, Z. Leman, and M. K. A. Mohd Ariffin, "Effect of chip load and spindle speed on cutting force of Hastelloy X," *J. Mech. Eng. Sci.*, vol. 14, no. 1, pp. 6497–6503, 2020.
 - [21] B. Wang, Z. Liu, G. Su, and X. Ai, "Brittle removal mechanism of ductile materials with Ultrahigh-speed machining," *J. Manuf. Sci. Eng. Trans. ASME*, vol. 137, no. 6, 2015.
 - [22] V. Gaikhe, J. Sahu, and R. Pawade, "Optimization of cutting parameters for cutting force minimization in helical ball end milling of inconel 718 by using genetic algorithm," *Procedia CIRP*, vol. 77, no. Hpc, pp. 477–480, 2018.
 - [23] N.A. Mohd Nor, S.S. Mohd Alisjabana, G. Seloraji, Y. M. Tee, J. X. Teh, B.T.H.T. Baharudin, M.K.A. Mohd Ariffin, and Z. Leman, "Effect and optimization of cutting speed and depth of cut in half-immersion up-milling of 6061 aluminium alloy," *J. Mech. Eng.*, vol. 16, no. 1, pp. 17–27, 2019.
 - [24] N. A. Mohd Nor, B. T. H. T. Baharudin, M. K. A. Mohd Ariffin, and Z. Leman, "Effect of compressed air and cutting speed on surface roughness of 6061 aluminium alloy," *J. Mech. Eng.*, vol. 16, no. 2, pp. 53–62, 2019.

Evaluation of Tabular Leg Structure of Mobile Offshore Production Unit (MOPU) Life Extension using Condition Assessment Method

Emi Hafizzul Jamaluddin, Azli Abd Razak, Mohd Shahriman Adenan,
Mohd Faizal Mohamad*

*Faculty of Mechanical Engineering, Universiti Teknologi MARA,
40450, Shah Alam, Malaysia*

**azlirazak@uitm.edu.my*

ABSTRACT

A Mobile Offshore Production Unit (MOPU) is any type of portable structure that can be reused when procuring oil and gas from the seabed. There are few reasons why MOPU is chosen over the conventional fixed offshore platforms, mainly due to its ability to be installed and relocated in a short period, low installation, and abandonment cost, and providing adequate time to evaluate new reservoirs properly. In certain circumstances, MOPU may be required to remain at the same location for a more extended period beyond its designed life. This paper explains the method of life extension (LE) assessment to extend the useful life of the MOPU. A MOPU with a three-legged jack-up rig in cruciform shape designed and constructed based on the American Bureau of Shipping (ABS) Classification requirement with a design life of 5 years, which currently in laid-up mode after 14 years in operation. The legs will be the focus of the condition assessment for the LE of the MOPU. The MOPU was constructed with 3 tabular legs with each 92200 mm length, 3500 mm diameter, and 55 mm thickness operate under tensile and shear stress, standing with simply supported at the one-end with hull hanged at the tabular using jacking-pin at the equal elevation of 77,600 mm. The method of assessment used is Non-destructive Tests (NDT). No severe defects or cracks were recorded at the identified stress concentration points. All NDT measurements were found within the acceptable ranges with no recorded anomalies.

Keywords: *Condition Assessment; Life Extension; MOPU; Tabular Leg; NDT*

Introduction

Mobile Offshore Production Unit (MOPU) is a primary candidate for shallow water early production applications. MOPU offer a cost-efficient solution for short life fields, compared with conventional jacket structure. Advantages in terms of mobility enable ease of installation, hook up, and commissioning and decommissioning costs, in comparison with a traditional jacket structure [1]. For a newly build MOPU, the cost must be weighed against the cost of installation, hook-up, commissioning, and decommissioning. For an existing jackups as a MOPU conversion candidate, the cost is not as much of an issue as the cost of acquisition. MOPU has the added advantage of relocation and re-use at less cost [2, 3].

MOPU has proven its ability to accelerate the monetization of the newly discovered oil field. The first MOPU was installed in the Ekofisk Field in Norway, utilizing the Gulftide type (Figure 1) jackups as an early production system. Production began in 1971, in just 18 months after discovery while permanent were being designed and build. The Gulftide remained a MOPU until the permanent production facilities were installed in 1975, at which time it returned to drilling [4].

Offshore structures are subject to very harsh marine environment [5]. Deterioration of offshore structure commonly caused by forces such as wind, ocean wave's buoyant forces, current loading, and marine growth [6]. The most critical component in MOPU to ensure it can stand at the location safely is the legs, where it can directly affect the overall performance of the unit. There are 2 types of leg construction, as shown in Figure 2 [7].

In offshore oil and gas operation, a temporary or permanent structure equipped with necessary operational equipment is required before the commencement of the production. The living quarter module is part of the facility attached to the structure to man the structure for operational and maintenance purposes. In certain cases, the unmanned structure was installed, which operates remotely. The design of the structure deployed is depending on the depth of the seawater and as per the requirement [8].

Offshore exploration and production require a massive amount of investment. An optimal solution is always a desirable option in making sure of a profitable investment. There are three main economic reasons that usually taken into consideration to decide the use of MOPU: schedule, cost, and risk [3, 9, 10]. MOPU has limitations in terms of operational conditions. It is suitable to operate only at shallow water with a water depth of less than 152.4 meters [6]. To optimize the useful life of the structure, it has to be maintained and inspected as per Class guideline such as American Bureau of Shipping (ABS), Bureau Veritas (BV), China Classification Society (CCS), Croatian Register of Shipping (CRS), DNV GL (DNV GL), Indian Register of Shipping (IRS), Korean Register of Shipping (KR), Lloyd's Register of Shipping (LR),

Nippon Kaiji Kyokai (NK/ClassNK), Polish Register of Shipping (PRS), Registro Italiano Navale (RINA), and Russian Maritime Register of Shipping (RS).



Figure 1: Gulftide MOPU [4].

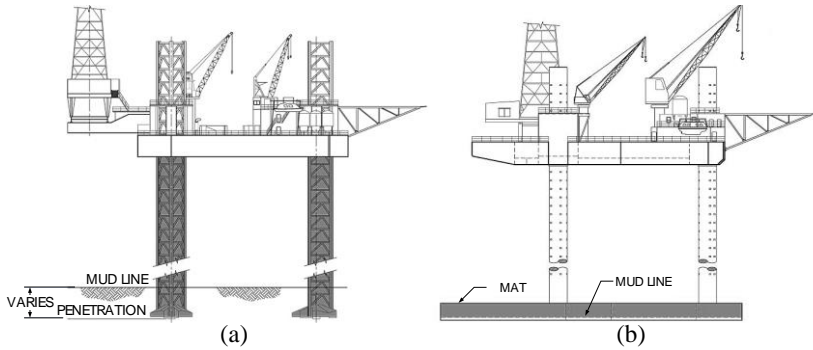


Figure 2: Type of jack-up legs [7]; (a) open-truss legs made of tabular steel sections that are crisscrossed and (b) open-truss legs made of huge steel tubes.

Generally, offshore structures must be able to safely function for a design lifetime of 25 years [5, 6]. Life extension (LE) program is commonly applied to offshore oil and gas installation. LE program is the lucrative end-of-life assets management strategy to extend the useful life (UL) of the assets beyond the design limit (DL) at the current installation location. Over half of the offshore assets at the North Sea and Mexico Gulf and it is more than 50%

of the offshore installation in UK Continental Shelf (UKCS) has exceeded its design life [11, 12]. The number of offshore installations that exceeded the design life expected to be continually increasing over time as most of the oil and gas offshore facilities are reaching their end-of-life period [13]. In China at the South China Sea, the first offshore installation that reached the original Design Life (DL) was in 2008, which still in operation. It is expected 43.8% of the offshore installation will reach its DL by 2021 [14].

LE program is also being well accepted in the other part of the world such as Malaysia [15] and Indonesia [16]. In Indonesia, Time Based Inspection (TBI) for offshore installations been regulated since 1977. The Indonesian government encourages for Risk-Based Underwater Inspection (RBUI) to be adapted over TBI. The risk will be the factor to determine the inspection interval, where the higher the risk is, the shorter the inspection interval will be [16, 17]. As been explained earlier, most of the offshore installation was designed conservatively, and RBUI opens up the opportunity for the extended useful life of the installations beyond Design Fatigue Life (DFL) provided the installation has never been exposed to the load exceeded the design envelope.

Life Extension

For this study, the MOPU as Figure 3, is a three-legged jack up rig with 3,000 tons holding capacity for each and constructed in cruciform shape assembled from 2 barges. It was designed and constructed based on the American Bureau of Shipping (ABS) Classification requirement with a design life of 5 years. The facility was commissioned in March 2006 and operated with a valid ABS Classification certificate society certificate until 2011. The class was renewed and transferred to the Russian Marine Register of Shipping (RS) Classification certificate prerequisite by executing Underwater inspection In-lieu of Dry-docking (UWILD) [18]. The renewal has enabled MOPU to be operated until March 2016. The MOPU operation was ceased in March 2016 due to unfavourable economic reasons. Before the Classification certificate expiry in March 2016, the MOPU has successfully being laid-up under RS Class, in which RS has granted MOPU Classification certificate under Laid-up mode until 2021, subjected to an annual verification survey.

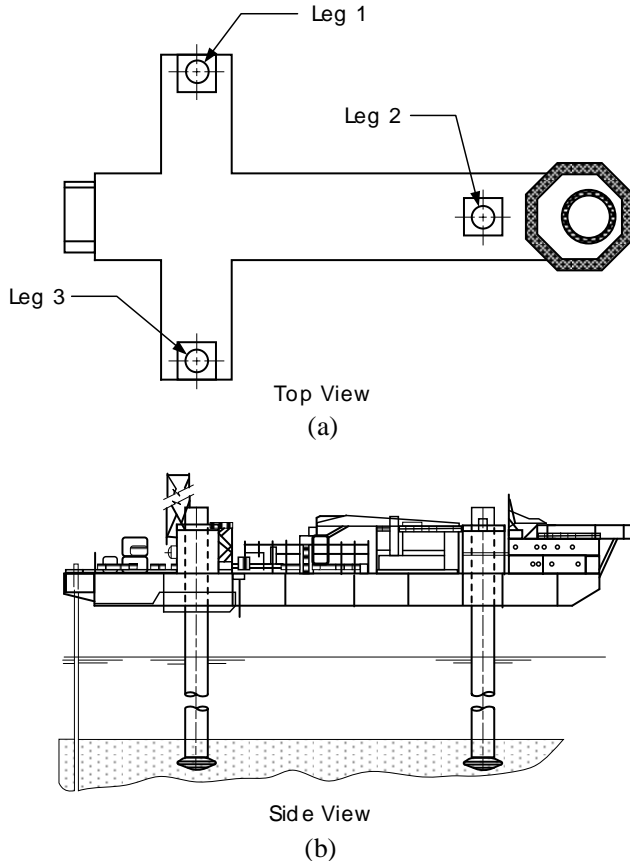


Figure 3: General arrangement of MOPU; (a) top view and (b) side view.

To maximize the asset useful life, LE exercise is a common method used in the industry. DFL normally developed by using conservative theoretical data. With that, there is always a chance to prolong the DFL by putting in the asset into a LE program. The concept of Life Time Extension (LTE) is that there is a time or an amount of duty when the installation would be normally considered for retirement, but where, certain processes and criteria, life can be extended without a reduction in margins below safe operating limit [8]. A typical operational timeline for an offshore oil and gas asset illustrated in Figure 4. Asset life begins at time $t=0$, where the asset commences for operation after successful of commissioning. The asset operates until time $t=t_0$, where t_0 denotes the end of DFL and marks the beginning of the LE. In order asset to be granted an extension of operational

period l_e ($>l_o$), the asset owner is obliged to meet some regulatory requirement [11]. Re-certification by Classification body is one of the main regulatory requirements that must be met. While many offshore structures exceed their original design life, the safety of the operations on these structures needs to be guaranteed. This safety is warranted during the re-certification process [19].

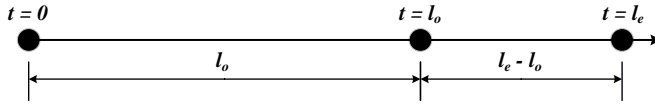


Figure 4: The original design life and the extended life of an asset.

The conventional end-of-life (EOL) asset management strategy; decommissioning or replacement gives a negative social impact as it closely relates to loss of jobs and a threat to the natural environment. LE program on EOL assets creates an added value to the economic, technical, social, and environmental. The decision to proceed with the LE program requires the asset owner to understand the existing processes and issues. Life extension processes include the definition of premises for the life extension program, assessment of asset condition, estimation of remaining useful life (RUL), evaluation of different strategies for life extension, obtaining regulatory approval, and implementation of the program [20].

Remaining useful life (RUL) is the critical elements that need to be predicted before the decision of life extension (LE) to be made. RUL can be estimated using the physic-based approached and data-driven approach [11]. Towards the end of the DFL, due to the constant exposure to the operational loadings, and environmental impact, the structure may suffer some form of material deterioration and damage (usually, but not necessarily, associated with time in service) with an increased likelihood of failure over the lifetime. Identified defects or damages require restoration such as strengthening, modification, and repair (SMR). Offshore restoration works are typically expensive. Inappropriate method selection will cause high cost and result in low effectiveness. SMR can be optimized to determine an appropriate activity for the restoration [21].

Effective LE requires input from all the stakeholders, including designers, system engineers, manufacturers, material specialists, operators and maintenance technicians, health and safety professionals, financial and economic analysts, and human factor researchers. Therefor LE should not only analyze the economic factor i.e., operating expenses (OPEX) & capital expenditures (CAPEX), but the availability and survivability of the Safety Critical Element (SCE) [22].

LE requires regular inspection, assessment and maintenance, which fatigue, and fracture degradation are the main elements that need to be well understood. RUL can be predicted with S-N Curve approach, which conducted during the design stage and Fracture mechanic (FM) approach can predict RUL when S-N Curve analysis gives a low RUL to components. Inspection interval developed based on the prediction to detect crack that grows to a critical level and caused a catastrophic failure [23].

Condition Assessment

Condition assessment is a vital part of the marine industry, regulated by the United Nation (UN) under the supervision of IMO and being adopted by the marine industry worldwide. As a specialized agency of the United Nations, IMO is the global standard-setting authority for the safety, security, and environmental performance of international shipping. Its primary role is to create a regulatory framework for the shipping industry that is fair and effective, universally adopted and universally implemented.

Inspection activity includes coverage above and underwater locations at specified points. It is focusing on the effectiveness of structure protection system, i.e., cathodic protection, coating system and measuring the deterioration of the legs. The inspection categorization:

- i. General visual inspection (GVI); As found visual inspection, video & photo.
- ii. Close visual inspection (CVI); Surface cleaning, Non-destructive Test (NDT) & measurement.
- iii. These surveys were conducted to find any defects and correctly and accurately record:
- iv. the type of defect
- v. the location of the defect
- vi. the dimension of the defect

The leg comprises of 3 main components; tabular, tabular-to-spud can flange, and spud can as shown in Figure 5. Critical hotspots or stress concentration points for MOPU has been pre-identified during the design stage as per below; however, the inspection location is not limited to the hotspot's points:

- i. Pin holes near lower guide
- ii. Lowest pin holes near to mud line
- iii. Welding connection at flange to the tubular pipe
- iv. Flange and bolt connection
- v. Spudcan

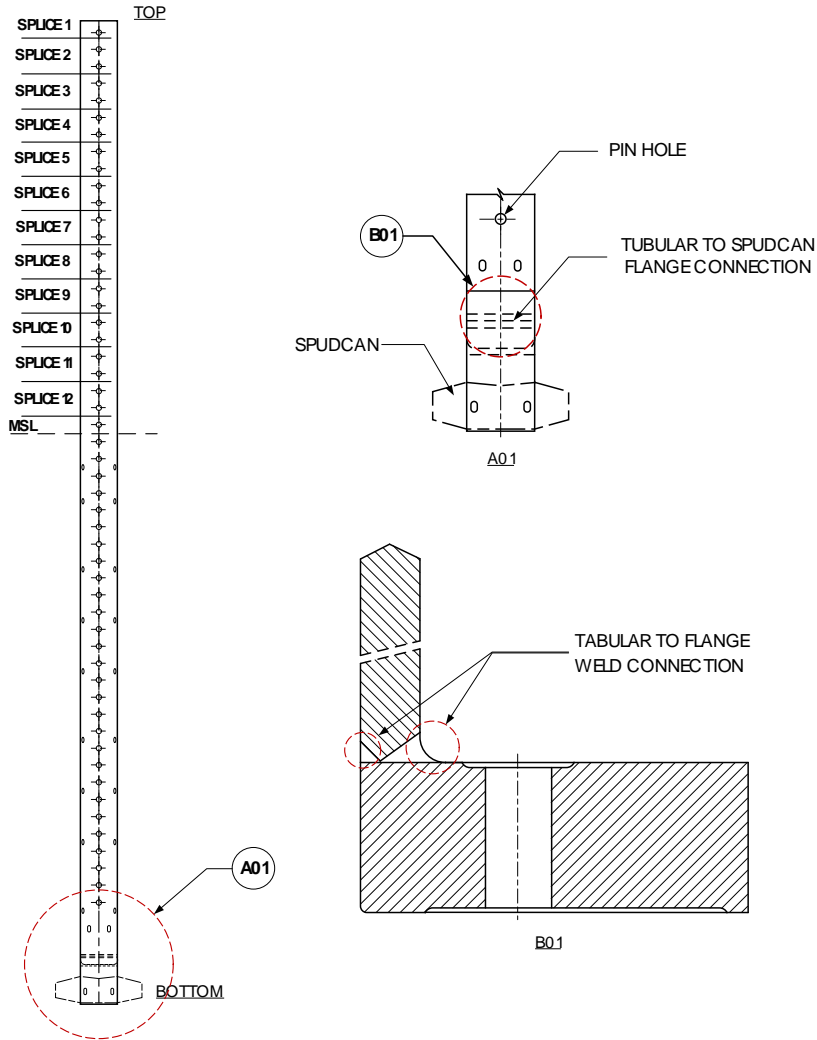


Figure 5: MOPU leg assembly.

Spud can be classified as uninspectable point and will be assess using numerical method. Location and method of inspection were categorised as listed below:

- i. Hybrid Acoustic Technology System (HATS) diagnostic testing of the three legs (subsea and above water) to inspect the overall structural condition.

- ii. General Visual Inspections (GVI), Close Visual Inspections (CVI), and Eddy Current Inspections (ECI) of above water weld joints and pinholes in all three of the MOPU's legs.
- iii. General Visual Inspections (GVI), Close Visual Inspections (CVI) inspections of the underwater weld joints and pinholes in all three MOPU's legs.
- iv. Alternating Current Field Measurement (ACFM) inspections of the underwater
 - v. Weld joints and pinholes in MOPU's legs number 2.
- vi. CVI or voltage measurement of the MOPU's Cathodic Protection (CP) System.

Assessment Method

The proposed method for life extension, as shown in Figure 6 comprises of 2 phases: 1) preparation and 2) implementation. The critical tasks in each of the three phases are described in the following subsections.

Phase 1: Preparation

The first phase in the LE process is the preparation stage which includes two tasks of data gathering and development of essential criteria.

Data gathering

The operational integrity of the MOPU legs LE depends on the accuracy and quality of the data from how it has been designed, constructed, commissioned, operated, and maintained over the original lifetime [22]. Design Fatigue Life (DFL) study carried out during the design stage used as a basis to determine the highest stress concentration points. Maintenance history of the MOPU inclusive of incident reports were analyzed to identify any significant incident that may have to the structural integrity and affects the stress concentration points. Pass inspection reports were analyzed to develop the inspection plan. Method of inspection determined by the defects that prone to be happening on the legs i.e., loss of metallic area, surface crack, sub-surface crack, and insufficient voltage for the Cathodic Protection for locations at above and underwater.

Development of essential criteria

Essential criteria developed based on the Classification guidelines. In this study the classification guideline used are from American Bureau of Shipping (ABS) and Russian Marine Register of Shipping (RS). Classification guideline provides the acceptance criteria such as allowable percentage of general metal loss, localized metal loss and coating breakdown [18].

Inspection specifications developed based on the anticipated defects at the stress concentration points. Suitability of the inspection method depends on the location of the stress concentration points either it will be above or underwater. Certified inspectors from various accredited examination body such as American Petroleum Institute (API), CSWIP and ASNT were used to carry out the inspection works at the points identified.

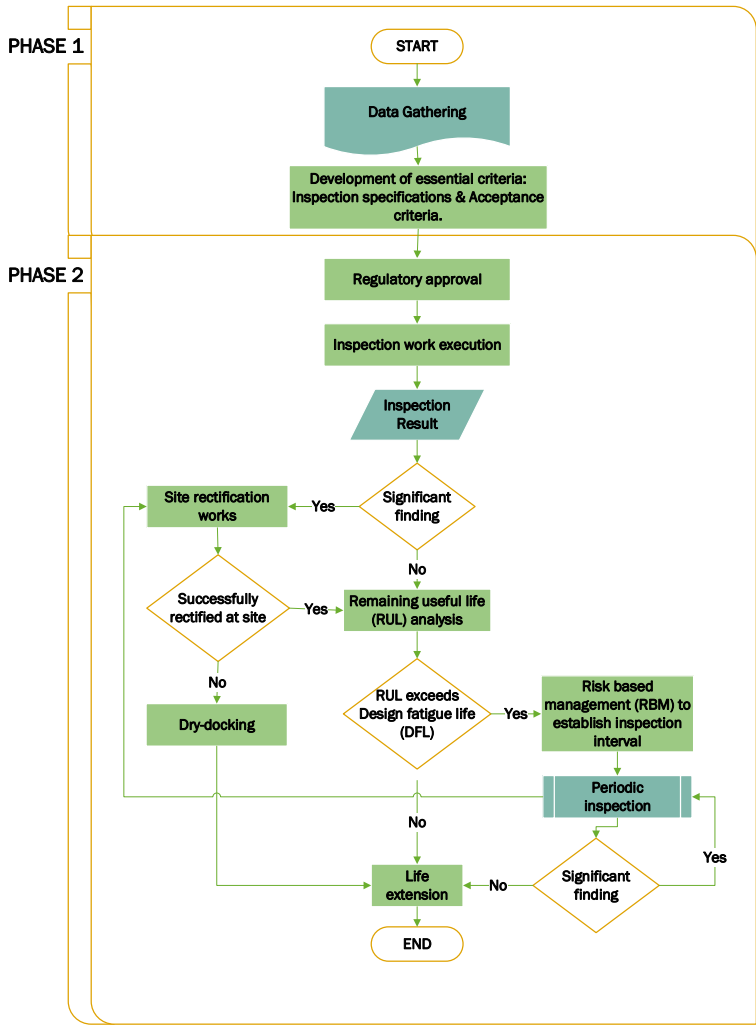


Figure 6: Assessment process flow.

Phase 2: Approval and implementation

The second stage of the LE process focuses on regulatory approval process and implementation measures.

Regulatory approval

Main regulatory body that oversees the marine activity is the Flag State Marine Administration (FSMA) who responsible to issue the final approval for the MOPU to operate within their water territory. Classification body is responsible to ensure the integrity of the MOPU is intact to continue operation.

Inspection work execution

All the surveys and inspections of the MOPU were conducted considering that the facility is in “Laid-Up” mode as classed by RS, non-operational and clear of hydrocarbons. The inspection divided to two; above water and underwater. Based on the anticipated defects and inspection parameter, method of inspection as shown in Table 1.

Table 1: Method of inspection

Anticipated Defect / Inspection Parameter	Method of Inspection	
	Above Water	Underwater
General metal loss	UT	UT
Localize metal loss	UT	UT
Coating breakdown	Visual	Visual
Surface crack	Visual, EC	ACFM
Sub-surface crack	EC	ACFM
Depletion of anode	Visual	Visual
CP voltage measurement	Voltmeter	N/A
Area/Surrounding survey	N/A	Visual/ROV
Overall thickness screening	HATS	HATS

Site rectification work

Found defects that exceeded the allowable limit require rectification. Rectification at the site is a preferred method aligned with the LE intention to maintain the MOPU location beyond design life.

Remaining useful life (RUL) analysis

There are few methods used to determine the remaining period for MOPU to safely stand at the existing location. RUL will be based on the DFL calculation where the safety factor may be reduced depending on the inspection result [24].

Risk-based management

Risk-Based Management (RBM) on assets consists of the execution of risk assessment and the development of an inspection plan. The assessment and the inspection may cover the whole assets or only focus on certain equipment or component. Risk ranking was developed to define the requirement of the inspection requirement and the intervals [25].

Dry-docking

Dry-docking is a term used for repairs or when a ship is taken to the service yard. During dry docking, the whole ship is brought to dry land so that the submerged portions of the hull can be cleaned or inspected. In the event where site rectification work is not doable, dry-docking is the only method for the rectification works to be executed.

Result and Discussion

The topsides and underwater leg surveys found minor weld bulges, anode depletion, and coating variations on all three legs. However, no severe defects or cracks were recorded at the jacking pinholes or indeed anywhere else. Ultrasonic Testing (UT) and Cathodic Protection (CP) surveys of each leg were carried out. All readings for ultrasonic thickness gauging and cathodic potential were found to be within acceptable ranges with no recorded anomalies.

Condition assessment

Critical hotspots or stress concentrations as identified by the analyses and recommended to be inspected have been inspected in accordance with the schedule of inspections and resulted in no significant findings other than corrosion. The hotspots remain unchanged due to no excessive load or forces being applied to the structure i.e.: collation with vessels, earthquakes, etc.

Hybrid acoustic technology system survey

Hybrid Acoustic Technology System (HATS) can detect and record an anomaly's size, severity, and number and then classifies it according to the type of anomaly, e.g., corrosion, metal loss, crack. HATS diagnostics were conducted to the entire length of the legs and recorded the relevant data.

Dormant cracks cannot be detected with the HATS diagnostics (such as fatigue cracks which have stopped propagating, i.e., remain the same in time, and therefore have no significant effect on the overall integrity of the structural member). However, active defects including fatigue cracks that are still developing in time can and would have been detected by this methodology.

According to HATS acoustic diagnostic results, external anomalies were detected on the inspected legs. A summary of the HATS diagnostic results as recorded for the inspected legs is presented in Table 2. All anomalies are less than 10% metal loss [18]. From observation of the defects recorded in Table 2, there is no fatigue cracks have been found.

Table 2: Summary of HATS defects per leg

Part	Anomalies				Metal Loss [%]
	Type	Number	Min. Depth [mm]	Max. Depth [mm]	
Leg 1	Corrosion	54	0.7	2.9	< 10
Leg 2	Corrosion	37	0.5	4.6	< 10
Leg 3	Corrosion	44	0.6	3	< 10

Above water inspection

The following findings from the above water surveys and inspections that were undertaken on each leg are summarized below:

- i. Inspections (GVI and CVI): Leg external visual inspection from the inside of the Jack House and from the top of the Jack House to leg top.
Findings: In general, during the external visual inspections of the legs, only minor coating damage, corrosion stains, and surface corrosion were recorded. There were no severe defects/flaws found.
- ii. Inspection (CVI): Internal visual inspection via abseil of all welds (circumferential and vertical) and pinholes from sea level to leg top.
Findings: During the internal visual inspection of the jacking legs, damage to the paint coating with surface corrosion of the exposed bare metal was observed together with some active corrosion, especially between splice zone no. 11 and 12 of leg number 3, just above the main sea level (MSL) as depicted in Figure 7 with tag no (45), (46), (47) and (48). No indication of weld flaws was observed on both, the circumferential and the longitudinal welds.

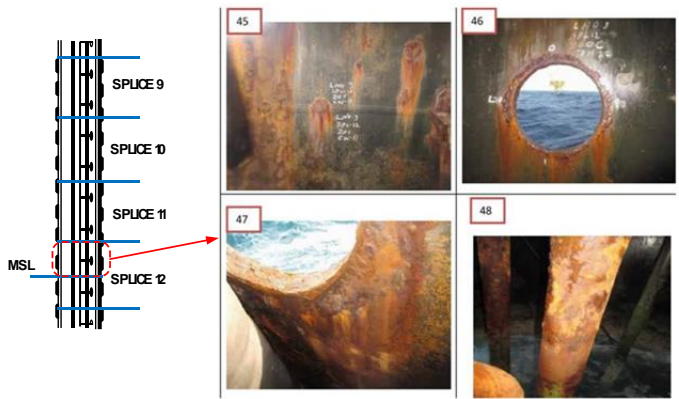


Figure 7: Observed paint damage and surface corrosion at leg 3.

- iii. Inspection: Ultrasonic thickness measurements of the legs were carried out at four main areas namely, within their splash zone area, at points below the shear pin location of leg 1 and 3, and areas above the shear pin location of leg 2.
Findings: No significant reductions of the wall thicknesses were observed during the measurements. Thickness measurements were within the range 53.9 mm to 56.2 mm. The design thickness is 55 mm. Table 3 provides the thickness measurements for all three legs.

Table 3: Leg thicknesses (above water)

Part	Thickness [mm]			
	Design Value	Min. Measured	Max. Measured	Average Measured
Leg 1	55.00	53.90	56.20	55.56
Leg 2	55.00	54.70	56.00	55.41
Leg 3	55.00	54.10	55.90	55.57

- iv. Inspection: Eddy Current Inspection of the legs at designated areas of the jacking holes circumferential and longitudinal welds.
Findings: No significant flaws/defects were observed during the ECI.
- v. Inspection (UFD): Ultrasonic Flaw Detection to be carried out on MOPU legs at designated areas of Jacking holes, circumferential and longitudinal welds.

Findings: No recordable Indications were observed during the inspection.

Under water inspection

The GVI to the subsea parts of the legs was carried out by divers aiming at inspecting the coating condition and at finding any abnormalities such as cracks and other defects. The following findings from the underwater surveys and inspections that were undertaken on each leg are summarized below:

- i. General Visual Inspection of the legs, the full leg length (from MSL to seabed) was reported to be covered with hard marine growth. No cracks/flaws were found. The CVI of the subsea parts of the legs has been carried out by divers on the jacking holes of the splash zone area all the way to the lowest reachable jacking holes (No 52) to identify cracks (if any present) on all three legs. Prior to the commencement of CVI, cleaning of all jacking holes was carried out using HP water jet, hand scraper, and wire brush. No crack initiation indications were reported during the Close Visual Inspection of the jacking pinholes. A considerable amount of metallic debris was found in close vicinity of leg 1 and 3 which can compromise the cathodic protection of the underwater leg structure by creating overprotection or under-protection voltages of the legs. This concern, however, has been assessed and eliminated on the grounds provided by the following facts:
 - a. The debris has been in the same location for several years as recorded from previous surveys.
 - b. The cathodic protection (CP) measurements recorded by the surveys of the years 2013, 2014, 2015 and 2017 have been consistent and with voltage values within the normal range of protection.
 - c. No active corrosion has been recorded at these locations.
- ii. Marine growth thickness was measured by a mechanical measurement technique which recorded an average thickness of 25 mm and 41 mm at depths of 48.5 m and 10 m below the MSL respectively.
- iii. Ultrasonic thickness measurements of the legs were carried out for four measurement points at specified underwater areas. No significant reduction in the wall thickness was observed during these measurements. Thickness measurements were within the range 53.9 mm to 56.0 mm. The design thickness is 55 mm. The thickness measurements for all the legs are given in Table 4.
- iv. Alternating current field measurement (ACFM) was employed on leg 2 to determine the weld presence in the joint as well as determine underwater crack sizing. The ACFM underwater survey of weldments and jacking pinholes was performed by divers. No crack initiation indications were recorded while carrying out ACFM.

Table 4: Leg thicknesses (underwater)

Part	Thickness [mm]			
	Design Value	Min. Measured	Max. Measured	Average Measured
Leg 1	55.00	55.10	55.90	55.35
Leg 2	55.00	55.70	55.90	55.62
Leg 3	55.00	55.20	56.00	55.18

Inspection of the MOPU's anode cathodic protection system

The Sacrificial Anode Cathodic Protection (SACP) system was checked with GVI as well as NDT methods by measuring the current voltage potential across the system. Twenty-seven sacrificial anodes (circular shape inscribed within the leg thickness) were inspected on each leg at various water depths confirming the anodes presence as per the original design. However, three sacrificial anodes on leg 3 were depleted with the depletion range of 90%-100%, and one sacrificial anode on leg 3 was depleted with the depletion range of 70%-80% (only the vertical bracket, designed to support the anode in place was visible). Except for these four anodes, no other serious depletions were reported during the remaining general visual inspection. The particulars of the over 70% depleted anodes are shown in Table 5. Voltage reading of Cathodic Protection (CP) taken (Table 6) on each leg suggesting the existing anode still giving an adequate protection to the structures.

Table 5: Summary of anode inspection findings

Part	Water Depth [m]	Jacking Hole Reference	No. of Anode >70%	Depletion Range [%]	Attachment
Leg 3	35.60	45/46	1	70-80	Firmly secured
Leg 3	6.00	26/27	2	90-100	Firmly secured
Leg 3	9.00	28/29	1	90-100	Firmly secured

Table 6: Voltage reading

Part	Voltage [mV]
Leg 1	-925
Leg 2	-917
Leg 3	-920

Conclusion

MOPU that designed for 5 years of design life was found intact after 14 years in operation. Based on the condition assessment result, there is an opportunity to extend the life of the structure as no anomalies found. Based on CP reading shown in Table 7, each of the legs are above the minimum voltage limit. This shown all the legs are protected against corrosion caused by the environment. It was also reported that the anode is depleted. Depletion of anode is a good sign that the CP system is in good working condition. It is recommended to replace the anode that depleted more than 70%. Table 7 also indicate that the overall wall thickness measurement and flaw detection using HATs on the tabular wall loss is less than 10% and there is no sign of active flaw at any of the legs.

Table 7: Overall inspection result

Part	Cathodic Protection System		Tabular Wall Loss (HATs)	
	Voltage, [mV]		[%]	
	Limit	Finding	Limit	Finding
Leg 1	> -850	-925	< 10	< 10
Leg 2	> -850	-917	< 10	< 10
Leg 3	> -850	-920	< 10	< 10

CVI for the above water and underwater is complementing HATs by utilizing different approach or method. Focus is given at the hotspot point and at the adjacent area. Table 8 depicted that none of the minimum thickness value recorded using Ultra-sonic Thickness Measurement (UTM) is beyond the minimum limit set. Eddy Current Inspection (ECI) was used for subsurface crack detection. No anomalies were found.

Table 8: Above water inspection result

Part	A/water Tabular Wall (UTM)		A/water Flaw Detection (ECI)	
	Thickness [mm]		No. of Anomalies	
	Limit	Finding	Limit	Finding
Leg 1	> 49.5	53.90	0	0
Leg 2	> 49.5	54.70	0	0
Leg 3	> 49.5	54.10	0	0

As per Table 9, none of the minimum thickness value recorded using Ultra-sonic Thickness Measurement (UTM) is beyond the minimum limit set. Alternating Current Field Measurement (ACFM) was used for subsurface crack detection. No anomalies was found. Based on the design, Leg 2 received the highest loads compared to others. Thus, only Leg 2 has been considered for ACFM. In case of any flaw detected at Leg 2, ACFM will be expand to the other legs.

Table 9: Underwater inspection result

Part	U/water Tabular Wall (UTM)		U/water Flaw Detection (ACFM)	
	Thickness [mm]		No. of Anomalies	
	Limit	Finding	Limit	Finding
Leg 1	> 49.5	55.10	N/A	N/A
Leg 2	> 49.5	55.70	0	0
Leg 3	> 49.5	55.20	N/A	N/A

Recommendation

For MOPU useful life to be extended, there is an engineering assessment that required to take place such as: i) Remaining Useful Life (RUL) Assessment and ii) Risk Assessment. RUL at each of the hotspot has to be calculated to establish the inspection interval based on the remaining years of life. Based on the condition assessment result that shows no significant anomalies, thus Reduced Fatigue Design Factor (FDF) can be applied in the RUL calculation [24]. Hotspots that have exceeded the RUL require further extensive engineering assessment i.e.: Finite Element Analysis to predict the deterioration rate or pattern. The risk on each hotspot has to be assessed to firm up the inspection interval. A risk-based structural assessment considers that structures of a higher risk require more frequent and more detailed levels of inspection than those with a lower risk.

Acknowledgement

The authors of this work would like to express their sincere gratitude to Faculty of Mechanical Engineering, Universiti Teknologi MARA (UiTM) for facilitating this research.

References

- [1] W. P. Stewart and M. Ooley, "The Maleo MOPU Project-Overview and Keynote Introduction to Session," in *Offshore Technology Conference*, 2008.
- [2] Z. Alwi, "Decommissioning of Kapal Wellbay Module, its Support Structure and MOPU Mobile Producer 1," in *SPE Symposium: Decommissioning and Abandonment*, 2018.
- [3] M. J. Kaiser and M. Liu, "Decommissioning cost estimation for deepwater floating structures in the US Gulf of Mexico," *Ships and Offshore Structures*, vol. 10, no. 4, pp. 436-455, 2015.
- [4] B. Crager, F. Shumaker, and C. McCabe, "Mobile Offshore Production Systems: An Analysis of Technical and Commercial Trends," in *Offshore Technology Conference*, 1996.
- [5] M. Abbas and M. Shafiee, "An overview of maintenance management strategies for corroded steel structures in extreme marine environments," *Marine Structures*, vol. 71, pp. 102718, 2020.
- [6] A. Kharade and S. Kapadiya, "Offshore engineering: an overview of types and loadings on structures," *International Journal of Structural and Civil Engineering Research*, vol. 3, no. 2, pp. 16-28, 2014.
- [7] Y. M. Welaya, A. Elhewy, and M. Hegazy, "Investigation of jack-up leg extension for deep water operations," *International Journal of Naval Architecture and Ocean Engineering*, vol. 7, no. 2, pp. 288-300, 2015.
- [8] A. Nezamian, D. Vuckovic, and R. J. Nicolson, "Integrity Assessment and Redeployment of Existing Mobile Offshore Production Unit for a Marginal Field Development," in *The 26th International Ocean and Polar Engineering Conference*, 2016.
- [9] J. Van Meter, "Deciding when to use a MOPU for field development," *Offshore*, vol. 55, no. 5) pp. 112-114, 1995.
- [10] M. Shafiee and I. Animah, "An integrated FMEA and MCDA based risk management approach to support life extension of subsea facilities in high-pressure-high-temperature (HPHT) conditions," *Journal of Marine Engineering & Technology*, pp. 1-16, 2020.
- [11] I. Animah and M. Shafiee, "Condition assessment, remaining useful life prediction and life extension decision making for offshore oil and gas assets," *Journal of loss prevention in the process industries*, vol. 53, pp. 17-28, 2018.
- [12] A. Stacey, M. Birkinshaw, and J. Sharp, "Life extension issues for ageing offshore installations," in *International Conference on Offshore Mechanics and Arctic Engineering*, 2008, pp. 199-215.
- [13] E. Tveit, H. Sivertsen, and S. Hernæs, "Experience from field life extension," in *Offshore Technology Conference*, 2014.

- [14] H. Liu, X. Shi, X. Chen, and Y. Liu, "Management of life extension for topsides process system of offshore platforms in Chinese Bohai Bay," *Journal of Loss Prevention in the Process Industries*, vol. 35, pp. 357-365, 2015.
- [15] S. M. Ng, R. Khan, B. Isnadi, L. A. Lee, and S. N. Saminal, "A Holistic Approach to Life Extension of Fixed Offshore Platforms in Malaysian Waters," in *International Petroleum Technology Conference*, 2019.
- [16] R. Tawekal et al., "Risk based underwater inspection (RBUI) for existing fixed platforms in Indonesia," *International Journal of Research in Engineering and Science (IJRES)*, vol. 5, no. 7, 2017.
- [17] R. L. Tawekal, F. D. Purnawarman, and Y. Muliati, "Development of Risk-Reliability Based Underwater Inspection for Fixed Offshore Platforms in Indonesia," in *MATEC Web of Conferences*, 2018, pp. 05002.
- [18] *Rules for the Classification Surveys of Ship in Service*, R. M. R. o. Shipping, St Petersburg, 2018.
- [19] B. Nagesh and I. Niranjana Kumar, "Investigation on the Overturning Stability of a Jack up Mobile Offshore Production Unit by Site-Specific Analysis to Find a Solution to Avoid the Failure of Its Leg Lattice Structure," *IJRASET*, vol. 10, 2016.
- [20] M. Shafiee and I. Animah, "Life extension decision making of safety critical systems: an overview," *Journal of Loss Prevention in the Process Industries*, vol. 47 pp. 174-188, 2017.
- [21] S. M. Samarakoon and R. C. Ratnayake, "Strengthening, modification and repair techniques' prioritization for structural integrity control of ageing offshore structures," *Reliability Engineering & System Safety*, vol. 135, pp. 15-26, 2015.
- [22] M. Shafiee, I. Animah, and N. Simms, "Development of a techno-economic framework for life extension decision making of safety critical installations," *Journal of Loss Prevention in the Process Industries*, vol. 44, pp. 299-310, 2016.
- [23] A. Keprate and R. C. Ratnayake, "Fatigue and fracture degradation inspection of offshore structures and mechanical items: the state of the art," in *International Conference on Offshore Mechanics and Arctic Engineering*, 2015, pp. V004T03A018.
- [24] *Guide for Fatigue Assessment of Offshore Structures*, A. B. o. Shipping, Houston, 2003.
- [25] F. Guédé, "Risk-based structural integrity management for offshore jacket platforms," *Marine Structures*, vol. 63, pp. 444-461, 2019.

Design for Additive Manufacturing and Finite Element Analysis for High Flexion Total Knee Replacement (TKR)

Solehuddin Shuib*, Mohammad Arsyad Azemi, Iffa Binti Mohd Arrif,
Najwa Syakirah Hamizan

Faculty of Mechanical Engineering, Universiti Teknologi MARA,
40450 Shah Alam, Selangor, Malaysia.

*solehuddin2455@uitm.edu.my

ABSTRACT

The patient from the Asian region always demanded a fully functional knee implant, which implied a high-flexion range of motion. Most of their daily life activities utilized the deep knee flexion which flexed until 165° such as the Japanese proper sitting style and Muslim prayer position. The problem of the study is extending the range of motion or achieving the high flexion of total knee replacement as the traditional total knee replacement was incapable to achieve more than 115°. Hence, the purpose of this study is to achieve a modified design of a knee implant that can flex up to 165° by carried out a static structural analysis in the ANSYS R16. There are 0°, 90°, 135°, and 165° angles of flexion with a different net force based on the percentage of body weight implemented on the knee implant. The analysis includes total deformation, Von Mises stress, shear stress, and contact pressure on knee implant were observed and compared to find better modification design. The total deformation had been decreased by about 69% at 0° flexion, 58.5% at 90° flexion, 90.93% at 135° flexion. The contact pressure also had been decreased by about 99.2%, 22.2%, 99.98% at angle flexion of 0, 90, and 135, respectively. The same declination happened to von Mises stress at about 85.05%, 9.52%, and 88.04% at the same angle of 0, 90, and 135, respectively.

Keywords: Total knee replacement; High flexion; Finite element analysis; Additive manufacturing

Introduction

The human knee joint is some of the most complex joints in the human body that can be divided into soft tissues and body structure. The soft tissues consist of tendons, menisci, muscles, and articular cartilages. While the bony structure includes the femur, tibia, fibula, and patella [1]. The knee joint bearing remarkably high loads as mostly human body weight are supported by it to do active movement such as walking, sitting, running, and kneeling for daily activities. Injury and damage to knee joints are bound to happen because of an accident and playing sports that can cause fractures, dislocations, and posterior cruciate ligament tears. Besides that, there is also disease due to inflammation of the knee joint namely arthritis. If nonsurgical treatment such as taking medications and walking using supports are no longer bearable, total knee replacement surgery should be considered [2].

Total knee replacement (TKR) is to replace a knee joint with artificial material by conducting a surgical procedure. This surgery and post-treatment are needed to relieve pain and to restore knee functionality. Squatting and kneeling are common activities that require normal flexion beyond 90°. As the development of surgical technique, implant designs, and available biomaterials have improved through the years, patients who undergo total knee replacement can achieve more than 100° of knee flexion and sometimes able to do squatting and kneeling [3]. However, the extent of the range of motion for deep flexion is required in young and active individuals in Asian countries. Besides, mostly Asian and Middle Eastern countries are required to bend their knee up to 165° for deep flexion to do their cultural and religious activities [4][5]. For instance, in Japanese culture, Seiza-sitting is a traditional practice of sitting in attending a tea ceremony. While for the Muslim religion, several positions required deep flexion to perform prayer.

Nevertheless, additive manufacturing (3D printing) is necessary to develop a knee joint with deep flexion as it is cost-effective and time-efficient to produce low volume and complex 3D implants [6]. This recent technology can assist in developing deep flexion of the knee joint with several modifications of designs and analysis. Besides that, additive manufacturing also helps to guide orthopedic surgeons to understand and plan their approach before beginning the operations as it can produce bone models rapidly [6].

Therefore, a suitable design of total knee replacement should be considered to fabricate and assist by additive manufacturing as well as to ensure the knee implant is fully functional in flexing to different angles. The main objective was to achieve a modified design of deep flexion of total knee replacement by implementing finite element analysis and fabricate the prototype of the 3D implant by using additive manufacturing such as fused deposition modeling (FDM).

Materials and Methods

A few types of knee implant designs were collected using the Pugh chart to acknowledge their range of motion referred to in Table 1 before started with the design modifications.

Table 1: Pugh chart

Description			Cruciate Retaining (CR)	Posterior Stabilized (PS)	Mobile Bearing
Criteria	Weight	Datum	Design 1	Design 2	Design 3
Range of Motion	3	0	+	+	+
Stability	2	0	+	+	-
Load Transfer	1	0	+	+	0
Biocompatibility	1	0	0	0	0
Wear Resistance	1	0	-	-	0
Ease of surgery	2	0	0	+	0
Risk of injury	2	0	-	-	0
	+		6	8	3
	0		2	1	5
	-		3	3	2
Net Score			3	5	1

Posterior Stabilized was chosen because it scored the highest compared to other designs. As well as contains an increased range of motion, a more stable component interface, and less technically demanding procedure [7]. The design of this project is modeled by using average dimensions of Chinese male that represent Asian knee male's community from Bing Yue et al. [8] study, that consists of femoral measurement and tibial measurement.

Design modifications

There were three designs to be analyzed consist of the first design was based on the standard total knee replacement that exists in the market as shown in Figure 1(1). The second and third designs were modified to achieve 165° flexion as shown in Figure 1(2) and Figure 1(3) respectively. These modifications were based on NexGen Legacy LPS-Flex Knee produced by Zimmer Incorporated in the year 2016 [9].

The second modification was an increase in cam height. The greater jump height is to prevent tibiofemoral disassociation during flexion from 120° to 155°. In some posterior stabilized knees, as the knee goes into deeper

flexion, the cam on the femoral component begins to move superiorly on the spine of the tibial articular surface. To address this, the shape of the cam on the LPS-Flex Femoral Component has been modified to contact the spine more inferiorly and thereby provide a greater jump height at flexion angles greater than 130° .

The third modification was the anterior flange of the femoral component has a larger deeper cut out to provide increased conformity for patella-femoral tracking and the anterior lip of the polyethene has a cut out for the patellar tendon. The difference between second and third design was the rotation in the tibial platform can significantly reduce contact stresses compare to fix the tibial platform. Furthermore, a study shows that there is a limited axial rotation during a setup motion, thereby giving advantages to mobile-bearing knee prostheses as it can be functional as an actual knee.



Figure 1: Three designs of total knee replacement.

Design analysis

These designs were modelled using SolidWorks 2017 software and imported to ANSYS R16.0 software. Titanium alloy was assigned for the femoral and tibial component. Ultra-High-Molecular Weight Polyethylene (UHMWPE) is the material for the tibial insert. The properties of these materials are shown in Table 2.

Table 2: Properties of material

Material	Poisson Ratio	Young Modulus (MPa)
Titanium Alloy	0.36	96000
Polyethylene	0.42	1100

Afterwards, the knee implant undergoes meshing set with adaptive size function, course relevance centre and element size of 1.50 mm as shown in Figure 2.

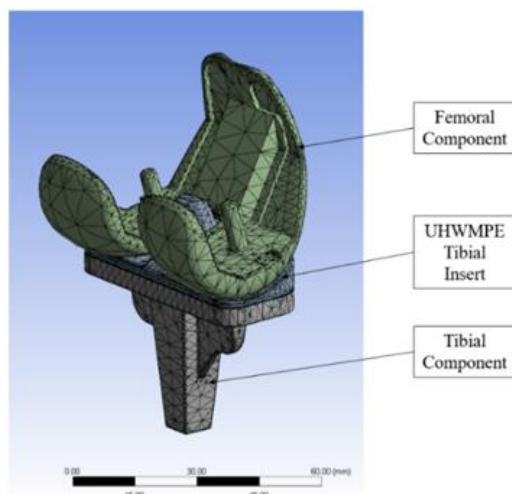


Figure 2: Meshing of the finite element model.

In this analysis, four different angles of flexion were used. The chosen angle is based on the most common daily activities done by Asian. The four angles of flexion are 0°, 90°, 135° and 165° of flexion that represent for standing, squatting, kneeling and sitting on feet position respectively. Each of these positions was applied with the force of certain magnitude.

The location of the applied force plays an important role in how it will affect the distributed forces and contact pressure around the femoral implant, and it is dependent on the angle of flexion used. The boundary condition is set as a fixed support feature at the base of the tibial tray. Then, the loading force applied vertically downward on the z-axis. The weight of 66.5 kg which equivalent to 652.365 N has been considered to apply during this analysis. This average weight (range 49-80 kg) is based on 100 patients with osteoarthritis who underwent knee replacement surgery in Malaysia [10]. Every position will have different net force produced in conjunction with the percentage of body weight [3]. Table 3 illustrates the position of the knee joint for different positions and Table 4 shows the net force applied on the knee joint with different flexion angle.

Table 3: Loading condition for each position

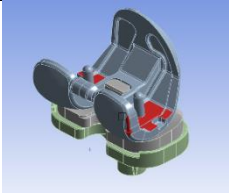
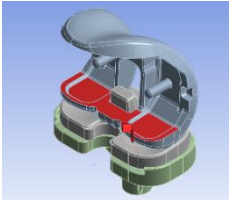
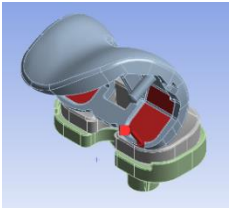
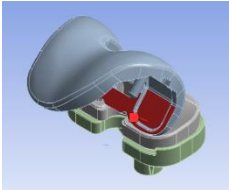
Angle (°)	Position	Loading of force
0	Stand	
90	Kneel	
135	Squat	
165	Sit on feet	

Table 4: The net force applied with different flexion angle

Angle (°)	0	90	135	165
Net force (N)	$0.5 \times 65.5 \text{ kg}$ = 326.18 N	$1.2 \times 65.5 \text{ kg}$ = 782.84 N	$5.3 \times 65.5 \text{ kg}$ = 3475.54 N	$6.0 \times 65.5 \text{ kg}$ = 3914.19 N

Design for additive manufacturing

Fused deposition modelling (FDM) was chosen to produce a prototype as this additive manufacturing is low-cost prototyping that considered more in form and fit rather than functionality. Moreover, FDM extrudes a thermoplastic one layer at a time onto a build plate. However, printed large parts can lead to large variations in temperature across the build platform as different areas of the part cool at different rates of internal stress [11]. This can cause the model printed to deform and leads to warping or shrinkage. The dimensional tolerance was determined to avoid shrinkage which is about ± 5 mm.

The chosen 3D FDM machine is Flashforge Guider II as shown in Figure 3. Its uniqueness is the closed surrounding box which allows the temperature to control more efficiently. The slicing software for Flashforge is called FlashPrint. This software is used to convert a 3D object model to specific instructions for the printer. In the slicing process, many additional features need to be determined. One of them is enabled to generate support when the model overhangs greater than 45° . Other features such as infill density and layer thickness affect the strength of the printed part [12]. Moreover, controlling the printing speed can manipulate the time but the quality will be affected too. Adhesion parameter such as brim, raft and skirt is used to prevent warping and helps in bed adhesion. Therefore, the total knee replacement must be strong enough without sacrificing the quality of the surface. Table 5 shows the features and parameters used in the slicer.



Figure 3: Flashforge Guider II [13].

Table 5: Slicer features and parameters

Features	Parameters
Infill density	30%
Infill pattern	Hexagon
Filament material	PLA
Printing speed	50%
Type of adhesion	Brim
Enable support	Enable when exceeding 45°
Layer height	0.2 mm
Printing time	9 hours 54 minutes
Estimated weight	112.81 g

Results and Discussion

This study proposes to achieve a modified design for deep flexion total knee replacement which can flex up to 165° by using finite element analysis. The results of the analysis are total deformation, Von Mises stress, shear stress in XY, and contact pressure. Total deformation can be defined as a change in length or shape depends on the type of material when the forces applied to the object. This parameter is used to show any change for femoral and tibial insert parts with two different materials when the forces were applied. Table 6 shows the analysis of total deformation for original design 1, and modification design 2 and design 3. The modification can be seen increases whenever the angle goes to deeper flexion. Thus, when the angle is deeper into flexion, the area decreases too. When the area is small, the deformation becomes bigger.

Table 6: Result analysis of total deformation (mm)

Angle (°)	Original design 1	Modification design 2	Modification design 3
0	0.007	0.0020443	0.043817
90	0.119	0.28785	0.4229
135	7.011	0.63615	3.9646
165	Cannot flex	2.55520	6.5570

The Von mises stress is a yielding criterion, widely used for metals and other ductile materials. It used to predict the materials yielding under loading applied to determine parameters such as Young's Modulus, yield

strength, ultimate strength, elongation at break and Poisson's ratio. It states that yielding will occur in a body if the stress components that affect it exceed the criterion [14]. Therefore, if the stress of Von Mises exceeds the basic tension yield limit stress, it is predicted that the material yields. Table 7 shows the analysis of Von Mises stress for original design 1, and modification design 2 and design 3.

Table 7: Result analysis of Von Mises stress (MPa)

Angle (°)	Original design 1	Modification design 2	Modification design 3
0	6.87	1.03	4.54
90	34.91	31.59	22.75
135	612.01	73.17	64.45
165	Cannot flex	206.20	180.80

Table 8: Yield strength of the materials

Material	Yield Strength (MPa)
Titanium Alloy	930
Polyethylene	25

Table 8 shows the yield strength for titanium alloy and polyethylene materials. When it reached 90°, the polyethylene starts to yield refer to Table 7. To what extent it will yield is based on the the total deformation values in Table 6. The titanium alloy's yield strength is far stronger, therefore no deformation occurred at the tibial and femoral components.

Table 9: Result analysis of shear stress in XY (MPa)

Angle (°)	Original design 1	Modification design 2	Modification design 3
0	1.11	0.42	2.058
90	9.08	10.26	10.024
135	95.44	26.66	14.583
165	Cannot flex	28398.00	64.794

Table 9 shows the analysis of shear stress in the XY plane for original design 1, and modification design 2 and design 3. Shear stress can be referred to as a force applied to tend to cause deformation to the object by slippage along planes parallel to the imposed stress. The infected areas show that they

become smaller when the angle reaches deeper flexion. Hence, the shear stresses are increases because the contact area is inversely proportional to the shear stress.

Table 10: Result of analysis of contact pressure (MPa)

Angle (°)	Original design 1	Modification design 2	Modification design 3
0	67.60	0.55	6.11
90	33.74	43.37	32.42
135	375000.00	90.30	136.36
165	Cannot flex	791.47	452.72

Table 10 shows the analysis of contact pressure for original design 1, and modification design 2 and design 3. The contact pressure created when two objects touch with force applied over the surface of the object. Hence, the higher the angle of flexion, the higher the values of deformation, stresses and pressure. These happen because, at 165° flexion, the surface area of femoral intact to the tibial insert is very small, thus produces very high pressure. Moreover, it obeys Pascal's law refer in Equation (1).

$$Pressure = \frac{Force}{Area} \quad (1)$$

As mentioned before, standard knee replacement (design 1) cannot achieve high flexion due to its design. Furthermore, at flexion angle of 135°, design 1 produces the highest values in total deformation = 7.011 mm, Von mises stress = 612.01 MPa, shear stress = 95.44 MPa and contact pressure = 37500 MPa. These happen due to short posterior femoral condyles or small contact area. It proves that the large posterior femoral condyles provide more contact area, hence reduces the deformation, stresses and pressure. Table 11 shows the percentage difference between the original design 1 and modification design 2. Majority of the values on the modification design 2 are lower than the original design 1.

Table 11: Percentage difference between original design 1 and modification design 2

Angle (°)	Total Deformation (%)	Von Mises Stress (%)	Contact Pressure (%)
0	69	85.05	99.2
90	58.5	9.52	22.2
135	90.93	88.04	99.98

Table 12: Percentage difference between modification design 2 and design 3

Angle (°)	Total Deformation (%)	Von Mises Stress (%)	Contact Pressure (%)
0	95	77.39	91.02
90	31.9	27.97	25.25
135	83.95	11.93	33.78
165	61.03	12.32	42.8

Table 12 shows the percentage difference for modification design 2 and design 3. Between design 2 and design 3, there are some tight competition but the differences between these two designs are unconstrained and constrained tibial platform. Moreover, results for design 3 are much better in most cases when comparing with design 1. However, comparing to design 1 and design 2, both results are divided into two sides and distributes equally with each other. The project was carried out in static analysis, so when comparing unconstrained and constrained tibial platform, it is more relevant to apply dynamic analysis since it involves movement in cylindrical motion. Also, there are many studies about comparing fix bearing and rotating bearing prosthesis that shows rotating bearing prosthesis increases the contact area, reduces load and improve in the motion of the knee [15][16][17]. Therefore, it is safe to say that design 3 is more practical and applicable than design 2 since design 3 constrain the rotation about 5° to 10°.

To achieve high flexion knee motion, some risks are suspected to happen such as post-fracture tibial inserts and polyethylene wear will increase whenever an overload occurs during high flexion knee motion [18]. Hence, carefully follow up of the patients are needed before more complications happen. The objective of this project can be achieved as it is to study the feasibility of high flexion knee using finite element analysis. However, the study has a few limitations which are first, the study was the only simulation and not in-real situation case. Secondly, the analysis considers only a few boundary conditions that are limited to software

capability [19]. Lastly, the analysis was done in static analysis whereas dynamic analysis is more practical. Therefore, further analysis needs to be done by considering real knee simulation, more boundary conditions and to implement the dynamic analysis.

Figure 4 shows from the left design 1, design 2 and design 3 printed using fused deposition modelling (FDM) which is Flashforge Guider II. The print settings from Table 5 produces fine TKR parts. They have a particularly good dimensional accuracy and high-quality surface. Post-processing such as rubbing with sandpaper is needed to remove the strings and smoothen some rough areas. The supports need to be removed by using scalpel and chisel. This method of additive manufacturing has the advantage of manufacturing objects with complex free form geometry, which is impossible using traditional methods of subtractive manufacturing [20][21]. In short, 3D printed patient-specific implant (PSI) is possible to be fabricated using FDM.



Figure 4: 3D printed of TKR using FDM.

Conclusion

This study aims to achieve a modified design of total knee replacement that able to extend the angle of flexion up to 165° . By implementing finite element analysis, the modified design of knee implant has been improved. The modified design has reduced total deformation, stresses and pressure successfully from the original design. This study proves that high flexion up to 165° of total knee replacement is still applicable and feasible by modifying the design at the crucial part of the knee implant.

Acknowledgement

This work is supported by the Strategic Research Partnership (SRP) under Research Grant 100-RMC 5/3/SRP PRI (022/2020).

References

- [1] R. Vaishya, V. Vijay, A. Vaish, and A. K. Agarwal, “Computed tomography based 3D printed patient specific blocks for total knee replacement,” *J. Clin. Orthop. trauma*, vol. 9, no. 3, pp. 254–259, 2018.
- [2] M. H. Seman, S. Shuib, M. Afzan, and A. A. Shokri, “Design and Analysis of High Flexion Femoral Component for Total Knee Arthroplasty (TKA),” *Int. Journal of Engineering and Technology*, vol. 7, no. October, pp. 381–385, 2018.
- [3] T. Nagura, C. O. Dyrby, E. J. Alexander, and T. P. Andriacchi, “Mechanical loads on the knee joint during deep flexion,” *Am. Soc. Mech. Eng. Bioeng. Div. BED*, vol. 50, pp. 393–394, 2001.
- [4] Y. Niki, Y. Takeda, K. Udagawa, H. Enomoto, Y. Toyama, and Y. Suda, “Is greater than 145 ° of deep knee flexion under weight-bearing conditions safe after total knee arthroplasty ?,” *Bone joint Journal*, no. March, pp. 782–787, 2010.
- [5] J. A. McClelland, J. A. Feller, H. B. Menz, and K. E. Webster, “Patients with total knee arthroplasty do not use all of their available range of knee flexion during functional activities,” *Clin. Biomech.*, vol. 43, pp. 74–78, 2017.
- [6] G. G. Jones, S. Clarke, M. Jaere, and J. Cobb, “3D printing and unicompartmental knee arthroplasty,” *EFORT Open Rev.*, vol. 3, no. 5, pp. 248–253, 2018.
- [7] F. R. Kolisek *et al.*, “Posterior-stabilized versus posterior cruciate ligament-retaining total knee arthroplasty,” *Iowa Orthop. J.*, vol. 29, pp. 23–27, 2009.
- [8] B. Yue, K. M. Varadarajan, S. Ai, T. Tang, H. E. Rubash, and G. Li, “Differences of Knee Anthropometry Between Chinese and White Men and Women,” *J. Arthroplasty*, vol. 26, no. 1, pp. 124–130, Jan. 2011.
- [9] G. Guild III, MD and S. Labib, MD, “Range of Motion In High Flexion Total Knee Arthroplasty vs. Standard Posterior Stabilized Total Knee Arthroplasty A Prospective, Randomized Study,” *Reconstr. Rev.*, vol. 3, no. 1, 2013.
- [10] A. H. Z, M. O, and G. Ruslan, “Total Knee Replacement: 12 Years Retrospective Review and Experience,” *Malaysian Orthop. J.*, vol. 5, no. 1, pp. 34–39, 2011.
- [11] “Dimensional accuracy of 3D printed parts | 3D Hubs.” [Online].

- Available: <https://www.3dhubs.com/knowledge-base/dimensional-accuracy-3d-printed-parts/>. [Accessed: 16-Jun-2020].
- [12] J. Fernandes, A. M. Deus, L. Reis, M. F. Vaz, and M. Leite, "Study of the influence of 3D printing parameters on the mechanical properties of PLA," *Proc. Int. Conf. Prog. Addit. Manuf.*, vol. 2018-May, no. August, pp. 547–552, 2018.
 - [13] "Guider IIs - FlashForge." [Online]. Available: <https://www.flashforge.com/product-detail/11>. [Accessed: 28-Oct-2020].
 - [14] H. Altenbach, "Book Review: Armenàkas, A. E., Advanced Mechanics of Materials and Applied Elasticity," *J. Appl. Mathematics Mech.*, no. 86(9), pp. 681–681, 2006.
 - [15] E. H. Garling, B. L. Kaptein, R. G. H. H. Nelissen, and E. R. Valstar, "Limited rotation of the mobile-bearing in a rotating platform total knee prosthesis," *J. Biomech.*, vol. 40, no. SUPPL. 1, 2007.
 - [16] G. Solarino, M. Carrozzo, G. Vicenti, and B. Moretti, "Joints Long-term outcome of low contact stress total knee arthroplasty with different mobile-bearing designs," *Joint*, vol. 2, no. 3, pp. 109–114, 2014.
 - [17] A. Causero, P. Di Benedetto, A. Beltrame, R. Gisonni, V. Cainero, and M. Pagano, "Design evolution in total knee replacement: which is the future?," *Acta Biomed.*, vol. 85, pp. 5–19, 2014.
 - [18] J. Victor, J. K. P. Mueller, R. D. Komistek, A. Sharma, M. C. Nadaud, and J. Bellemans, "In vivo kinematics after a cruciate-substituting TKA," *Clin. Orthop. Relat. Res.*, vol. 468, no. 3, pp. 807–814, 2010.
 - [19] C. K. Cheng *et al.*, "Biomechanical considerations in the design of high-flexion total knee replacements," *Sci. World J.*, vol. 2014, 2014.
 - [20] M. J. Rowe and M. Crane, "3D-printed patient-specific applications," *Orthop. Res. Rev.*, no. August, pp. 57–66, 2008.
 - [21] M. Javaid and A. Haleem, "Additive manufacturing applications in medical cases: A literature based review," *Alexandria J. Med.*, vol. 54, no. 4, pp. 411–422, 2018.

Comparative Investigation of Worm Positions for Worm Gear-box Performance under No-Load Condition

*Hardik G Chothani**

*Mechanical Engineering Department,
Government Engineering College, Bhavanagar, India
chothanihardik@yahoo.com

Kalpesh D Maniya

*Mechanical Engineering Department,
C.K.Pithawala College of Engineering & Technology,
Surat, Gujarat, India*

ABSTRACT

The Worm Gear drive is a gear arrangement where the worm shaft meshes with a worm wheel (gear). The worm shaft plays an important role in reduction ratio & efficiency. This worm shaft can be used at the top and the bottom in the gearbox. This technical research paper provides a comprehensive comparative evaluation of Input torque analysis & heating rate of lubricant inside the gearbox for two positions of the worm shaft in the worm gearbox under no-load condition. Worm shaft at the top and worm shaft at the bottom were assessed at variable speed (1000-1400 rpm), the different splashed volume of lubricant (1.5-2.7 liter), and variable temperature of lubricant (30-50 °C). Input torque was measured with the help of a direct torque measurement technique. Similarly, the heating rate of the lubricant was also measured with a temperature sensor for both orientations of the worm shaft. Full factorial experiments were performed on a specially designed and fabricated worm gear test rig. The experiments showed that the input torque requirement for the worm at the bottom position is 20 -25% higher than the worm at the top position at an

average speed. The heating rate remains almost the same for both orientations. This study aimed to find the suitable orientation of the worm shaft which reduces the power losses and increases efficiency.

Keywords: *Worm gear; Torque analysis; Worm orientation; Heating rate; Power loss*

Introduction

Worm Gear is used to transmit the motion and power from one shaft to another non-intersecting non-parallel shaft. The worm gear is used for limited space and a high reduction ratio. Worm gear consists of the main two parts, worm shaft, and worm wheel. The worm drives by its threads sliding into contact with the teeth of the worm wheel (gear). This constant sliding action generates heat due to friction and therefore adequate cooling and superior lubrication must be provided for gears [1].

Muminovic et al. [2] presented the results of an experimental method for determining the efficiency of worm gears. They also investigated the influence of lubricant type on the efficiency of worm gear. Mautner et al. [3] investigated the efficiency of worm gear by considering different gear ratios, worm wheel materials, lubricants, and contact patterns on efficiency and load-carrying capacity. They suggested that harden steel and copper-tin-bronze are the best material for worm shaft and worm wheel respectively to increase the efficiency. Magyar and Sauer [4] presented the calculation method to determine the efficiency of worm gear drives. This study showed how to increase the efficiency of worm gear drive by reducing the tooth friction power loss and reducing bearing power loss. Turci et al. [5] investigated the influence of center distance and reduction ratio on the efficiency of worm gear. They also showed the comparison of calculation of efficiency by various standards. Blaza et al. [6] worked on the influence of lubricant viscosity on the efficiency of worm gear. They concluded that the degree of efficiency is always higher for the high viscosity of the lubricant. Fontanari et al. [7] investigated the lubricated wear behavior of worm gear material. Many authors worked on the modification of worm gear geometry to increase the efficiency by increasing output [8]–[11].

The main aim of this work is to increase the efficiency of worm gear by considering various factors. Efficiency can be increased by increasing output power/torque or reducing input power/torque. Output power can be increased by reducing load-dependent losses while input power can be reduced by reducing non-load dependent losses. The non-load dependent losses are primarily related to viscous effects. These losses can be further subdivided into oil churning and windage losses that are the result of the interaction between the oil/air and the moving/rotating elements like gears and shafts, into pocketing/squeezing losses due to the pumping effect of the mating gears. Oil seal loss and bearing losses are part of non-load dependent losses. The non-load dependent losses are mainly dependent on input torque. The input torque may be reduced by considering various parameters such as lubricant type, lubricant viscosity, lubricant temperature tribological geometry, worm shaft position, and types of the worm shaft. The position of the worm shaft plays important role in worm gearbox performance [12]–[16].

Worm gears have an interesting property that no other gear set has: the worm shaft can easily turn the gear, but the gear cannot turn the worm shaft. This is because of the angle on the worm shaft. This feature is very important where a self-locking phenomenon is required. According to the orientation of worm shaft, it can be classified in mainly three categories that worm shaft at the top position, worm shaft at the bottom position, and worm shaft at the side position as shown in Figure 1. Similarly, according to the direction of rotation, it can be classified into the right-hand worm and the left-hand worm as shown in Figure 1. Among these, the worm shaft at the bottom and the worm shaft at the top were selected for the experiment. The aim was to investigate the effect of the orientation of the worm shaft on the input torque and heating rate of lubricant.

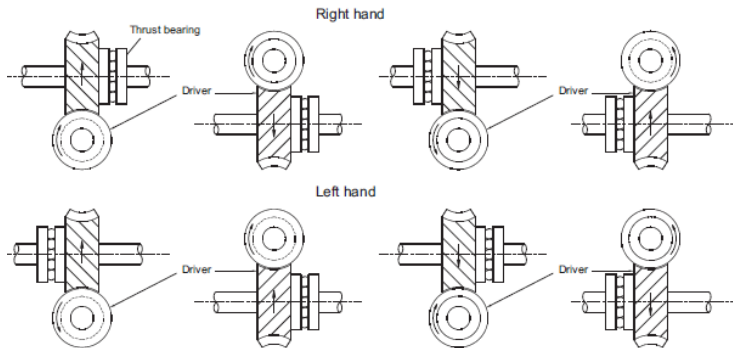


Figure 1: Classification of worm gear drive according to the position of worm shaft [17].

Material and Methodology

The experimental studies were performed on a specially designed torque measurement test machine. The schematic representation of this developed test machine is given in Figure 2. The test machine is composed of a motor, torque sensor, temperature sensor, variable frequency drive (VFD), shaft, Bearings, couplings, testbed, and data collector.

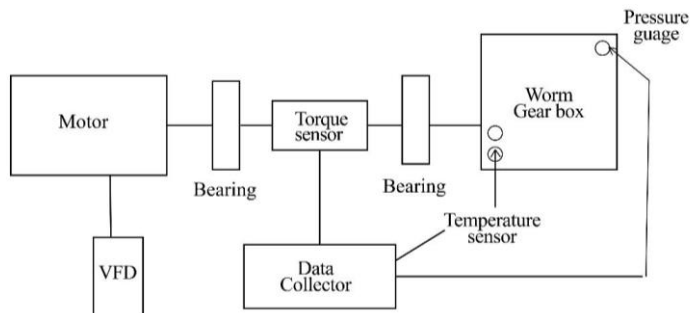
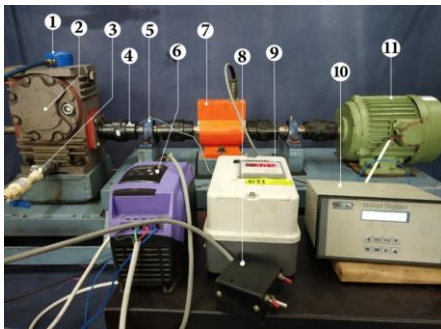


Figure 2: Schematic representation of the test machine for worm gear [18].

The test stand is built with an electric motor controlled by the variable frequency drive to enable the variation in rotational speed. The gearbox containing the test gear pair is connected to the motor through the shaft, torque sensor, and couplings. The gearbox is rigidly mounted at the end of the test-bed and similarly, the motor is mounted on the other end of the test-bed. The input torque of the test gear is measured with the torque sensor. The temperature of oil inside the gearbox and pressure of the air inside the gearbox can be measured with the help of a temperature sensor and pressure gauge respectively. This test rig is designed to perform the experiment based on the direct torque measurement technique. The same test rig is used for both orientations of the worm gearbox. The complete test rig with different views are shown in Figure 3(a) and (b). The selected test worm gearbox is shown in Figure 3(c) and its inside volume of the gearbox was kept constant (180 mm×180 mm×280 mm). In the same gearbox, the worm shaft can be used at the top and bottom positions.

The purpose of this study was to analyze the influence of the worm shaft of non-throated worm gearbox on input torque and heating rate of lubricant under the different speed, and different oil conditions. The range for control factors for various experiments was selected through various pilot experiments. The test matrix is given in Table 1.



- 1-Pressure Gauge,
- 2-Worm gearbox,
- 3-Provision for oil level indicator,
- 4-Jaw type coupling,
- 5-Foot mounted bearing,
- 6-Variable frequency drive (VFD),
- 7-Torque sensor,
- 8-VFD regulator,
- 9-Temperature indicator,
- 10-Digital controller for Torque sensor
- 11-AC motor

(a)

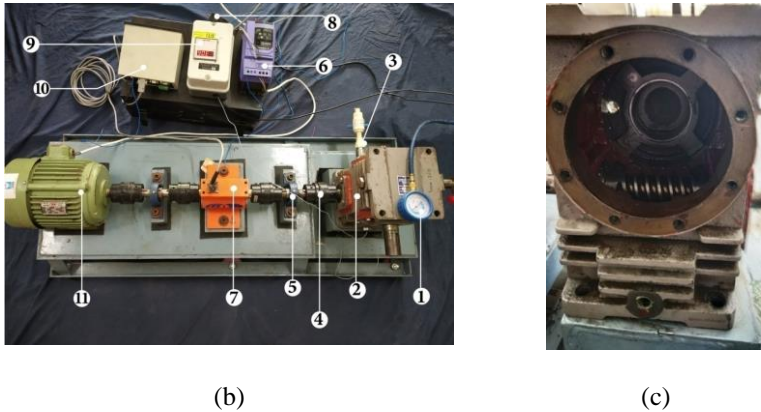


Figure 3: Test machine to measure the input torque and heating rate of worm gearbox. (a) Front view of the test rig, (b) Top view of test rig (c) Detailed arrangement of test gearbox.

Table 1: Test matrix

Control factors	Unit	Values
Speed of worm	rpm	1000, 1200, 1400
Oil volume	liter	1.5, 2.1, 2.7
Temperature	°C	30, 40, 50
Orientation of worm	-	The worm at the top, worm at the bottom

The speed of the driving shaft was selected as 1000 rpm minimum speed and 1400 rpm maximum speed [18]. Static oil levels were selected based on the capacity of the gearbox and worm gear manufacturer report [19]. The gearbox was operated at various lubricant volumes which are shown in Figure 4. The experiments were tested at three temperature levels of 30 °C, 40 °C and 50 °C [18].

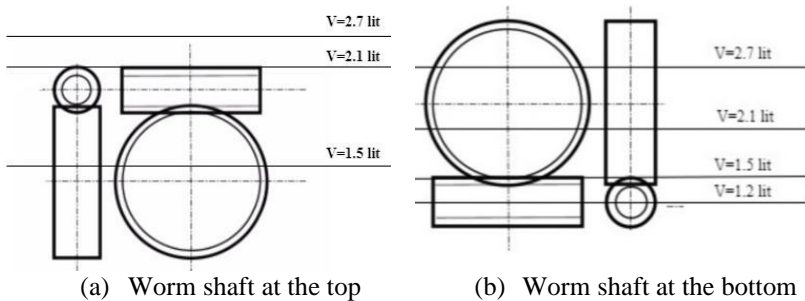


Figure 4: Lubricant level of worm gearbox for the various position of the worm shaft.

When worm gear operated at a 1.5-liter volume only the worm is fully immersed in lubricant and it operated at 2.7-liter volume both worm shaft and worm wheel are almost immersed in lubricant for worm at the bottom position as shown in Figure 4(b). For the worm at the top position, Volume 2.1 liter immersed both gears fully in lubricant as shown in Figure 4(a). For this experiment as a test gearbox, a single start worm gearbox was selected. The details of the selected worm gearbox are given in Table 2.

Table 2: Worm gear geometric properties

Gear	No. of teeth	Material	Module (mm)	Pressure angle	Center distance (mm)	Outer diameter (mm)	Reduction ratio
Worm Wheel	30	CuSn12	3	20	75	132	30:1
Worm Shaft	Single start	16MnCr5				40	

The most commonly used lubricant for worm gears is compounded mineral oils and synthetics oil. The synthetic lubricant was select for this experiment, detailed properties of the lubricant are given in Table 3.

Table 3: Lubricant properties

Sr. No	Name of oil	Kinematic Viscosity (cSt) @ 40 °C	Kinematic Viscosity (cSt) @ 100 °C	Viscosity Index	Density (Kg/m ³) @ 15 °C
1	Synthetic oil	330	35.50	162	790

Before any test, the machine was operated for at least 30 minutes with heated lubricant in circulation to bring the entire gearbox up to the steady-state test temperature. The experiments were operated from 2 °C to 5 °C before the starting temperature to avoid the previous experiment effect. The test machine was operated with different positions of the worm shaft at various controlling factors as per the test matrix. The input torque and temperature of the lubricant were measured at every interval of time.

Results and Discussion

According to the orientation of a worm, it can be classified in mainly three categories: worm on the top, worm on the bottom, and worm on the side. Among these three categories, two categories were tested on the designed test rig, worm at the bottom and worm at the top. The experiment test was conducted for at least a prior 5 °C temperature of the basic starting temperature of the test. Time was not bounded for the test but the test was going on till the desired temperature was reached. This test was designed to describe the influence of the orientation of the worm shaft on multiple responses: 1) influence of Position of worm shaft on input torque, and 2) influence of position of worm shaft on lubricant heating rate.

Influence of worm orientation on input torque

The input torque at various operating conditions was recorded in the digital controller of the torque sensor. To investigate the effect of the position of the worm shaft on input torque, the input torque obtained from the experiments was plotted in the form of a graph. The influence of worm position on input torque at different volume for speed 1000 and temperature 40 °C is shown in Figure 5. At 1.5-liter volume, there is no

dragging of lubricant for worm at the top position therefore the input torque was very small. For the worm shaft at the bottom position at 1.5-liter volume, the worm shaft was fully immersed so there is dragging of lubricant therefore comparatively large input torque was noted [18]. Once the volume of lubricant increased to the next level, dragging of lubricant faced by the worm shaft at the top position so the gap in input torque between both positions was reduced. The worm shaft at the top position is better at the lower level of lubricant. The input torque for the worm shaft at the bottom is 24%, 8%, and 7% higher than the worm shaft at the top for lubricant volume 1.5 liter, 2.1 liter, and 2.7 liter respectively as shown in Figure 5. It shows that the lubricant volume/static head significantly affects the non-load-dependent losses, however, it hardly affects the load-dependent losses [21].

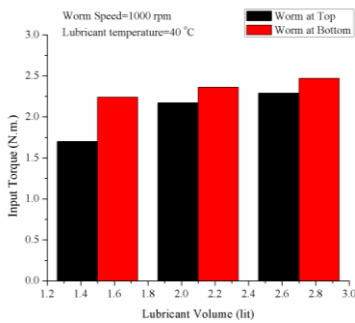


Figure 5: Influence of worm positions on input torque at different volume.

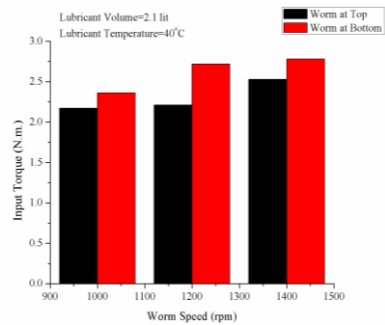


Figure 6: Influence of worm positions on input torque at a different speed.

The influence of worm position at various speeds is shown in Figure 6. As speed increases the input torque always increases for both positions, however, the difference is higher for worm at the bottom position due to higher dragging force comparatively at worm at the top position. At lower speed, the gap between input torques for both positions of the worm shaft is very small. As speed increases the gap of input torque for the worm at the top and the bottom position increased however, after a certain speed this gap again reduces. The input torque for the worm at the

bottom position is 0.2 Nm, 0.5 Nm, and 0.25 Nm higher than the worm at the top position for worm speed 1000, 1200, and 1400 respectively. The theoretical reason behind it, When the worm shaft at the top, the least amount of oil is likely to be forced compared to the worm at the bottom [14]. It reduces the churning power loss.

Figure 7 shows the influence of worm position on input torque at different lubricant temperature. The temperature range is selected from 30 to 50 °C. As temperature increases viscosity of lubricant goes down, this reduces the dragging force of lubricant [14]. Due to static head, dragging forces are high for worm shaft at the bottom and less for worm at the top so input torque for worm at top position is less for every temperature condition [18]. Input torque required for the bottom position of the worm shaft reduces as temperature increases, however, the gap was remained almost the same for temperature range from 30 °C to 50 °C. The constant gap suggests that there is no influence of the worm shaft position on input torque based on lubricant temperature.

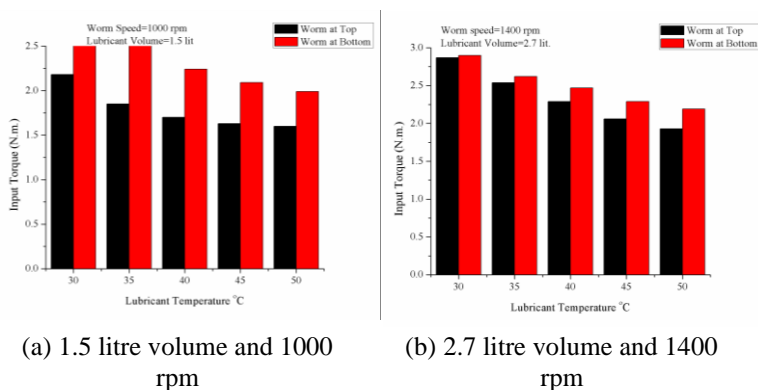


Figure 7: Influence of worm position on input torque at different temperature.

Influence of worm orientation on heating rate of lubricant

Lubricant is not essential only for the friction of gear and bearing but it is also useful to dissipate the heat during the operating condition [18]. Figure 8(a) shows the heating rate of lubricant for both operating conditions at volume 2.1 liter and speed of worm 1000 rpm. The lubricant heating rate

was observed based on time. The experiment was started at room temperature. This work aimed to compare the position of the worm shaft so only one lubricant was used as mentioned in Table 2. Theoretically if the lubricant is not sufficient, the heat generated due to friction and if lubricant is excessive, the heat generated due to dragging [20]. However, the aim was to select the best position of the worm shaft by considering the heating rate of lubricant and input torque. Figure 8(a) shows that there were good agreements for the heating rate between the orientations of the worm shaft. The average heating rate at 1000 rpm and 2.1-liter oil volume for the worm shaft at the bottom position is only 3% higher than the heating rate for the worm shaft at the top position. As speed and immersion depth increases, this gap is negligible as shown in Figure 8(b). The gap/difference of input torque or heating rate between both orientations shows the comparison and helps to select the better one. If the gap is minimum, it does not have much effect on power loss, in this situation anyone (either top position or bottom position) can be selected.

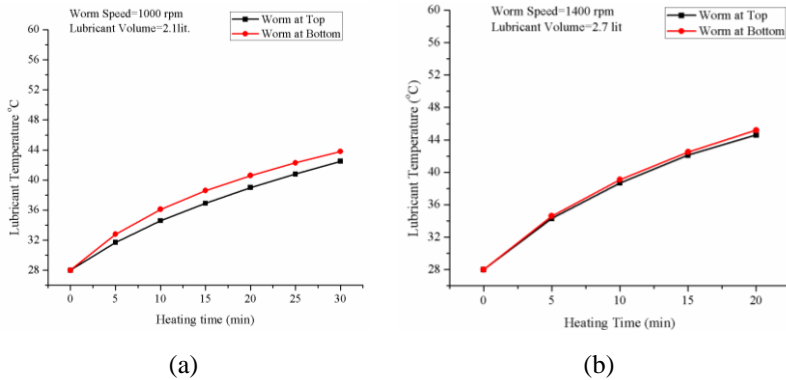


Figure 8: Influence of heating rate at (a) Volume 2.1-liter and 1000 rpm
(b) Volume 2.7-liter and 1400 rpm.

Conclusion

The research tries to analyze the best position of the worm shaft in the worm gearbox at different speeds, lubricant level conditions, and lubricant temperature under no-load conditions. The experimental setup was

pecially developed for the research study. Various experiments were conducted with the worm shaft at the top position and the worm shaft at the bottom position. Input torque and heating rate of lubricant were noted and plotted to understand the variations concerning worm positions. With the increase in the volume of lubricant, gear gets more dragged which increases the input torque. At 1.5 liter volume, 23.31% higher input torque is required for the worm at the bottom position, similarly, 10.9% and 7.9% higher input torque is required at 2.1 liter and 2.7 liter volume for the worm at the bottom position compares to the worm at the top position. As volume increases the gap between input torque for both positions reduces. The worm at the top condition for lower volume is quite preferable. With the increase in the temperature of the lubricant, input torque reduces. As volume increases at the same speed heating rate of lubricant reduce and as speed increases at the same volume heating rate of lubricant increases. However, it was applicable for both conditions of the shaft so the Influence of the position of the worm shaft cannot be evaluated based on lubricant temperature only. With the increase in speed, higher input torque was noted for both positions of the worm shaft however increasing input rate is quite higher for the worm at the bottom position. For worm at bottom position at 1000 rpm 12% input torque is more compare to worm at the top position. Based on the speed, the worm shaft at the top position required less input torque compare to the worm at the bottom position. It is concluded that the worm shaft at the top position is more preferable to the bottom position for non-load dependent losses.

References

- [1] V. Fontanari, M. Benedetti, G. Straffelini, C. Girardi, and L. Giordanino, "Tribological behavior of the bronze-steel pair for worm gearing," *Wear*, vol. 302, no. 1–2, pp. 1520–1527, 2013.
- [2] Muminovic Adil, R. Nedzad, and D. Zezelj, "The Efficiency of Worm Gears Lubricated with Oil of Mineral and Synthetic Bases," *Transactions of Famena*, vol. 70, no. 4, pp. 65–72, 2013.
- [3] E.-M. Mautner, W. Sigmund, J.-P. Stemplinger, K. Stahl, and Experimental, "Investigations on the Efficiency of Worm Gear Drives," *Gear Solution*, pp. 33–45, 2016.
- [4] B. Magyar and B. Sauer, "Calculation of the efficiency of worm gear

- drives,” in *International Gear Conference 2014: 26th–28th August 2014, Lyon*, 2014, no. June, pp. 15–23.
- [5] M. Turci, E. Ferramola, F. Bisanti, and G. Giacomozzi, “Worm Gear Efficiency Estimation and Optimization,” *Gear Technology*, vol. 92, pp. 46–53, 2016.
- [6] Blaza Stojanovic, Sasa Radosavljevic, V. Sandra, and M. Slavica, “The influence of lubricant viscosity on the efficiency of worm gear reducer,” in *8th International Scientific Conference IRMES*, 2017, no. September, pp. 219–224.
- [7] V. Fontanari, M. Benedetti, C. Girardi, and L. Giordanino, “Investigation of the lubricated wear behavior of ductile cast iron and quenched and tempered alloy steel for possible use in worm gearing,” *Wear*, vol. 350–351, pp. 68–73, 2016.
- [8] A. T. Alexandru, “Worm gears with optimized main geometrical parameters and their efficiency,” *Mechanika*, vol. 81, no. 1, pp. 62–65, 2010.
- [9] H. Winter and H. Wilkesmann, “Calculation of Cylindrical Worm Gear Drives of Different Tooth Profiles.,” *Journal of Mechanical Design*, vol. 103, no. 4, pp. 73–82, 1981.
- [10] K. Yukishima, I. Gonzalez-perez, A. Fuentes, and F. L. Litvin, “Geometry and Investigation of Klingelnberg-Type Worm Gear Drive,” *Journal of Mechanical Design*, vol. 129, no. January 2007, pp. 17–22, 2017.
- [11] V. V. Simon, “Influence of tooth errors and shaft misalignments on loaded tooth contact in cylindrical worm gears,” *Mechanism and Machine Theory*, vol. 41, no. 6, pp. 707–724, 2006.
- [12] S. Seetharaman and A. Kahraman, “Load-Independent Spin Power Losses of a Spur Gear Pair: Model Formulation,” *Journal of Tribology*, vol. 131, no. 2, pp. 022201, 2009.
- [13] P. Luke and a. V. Olver, “A study of churning losses in dip-lubricated spur gear,” *Proceedings of the Institution of Mechanical Engineers, Part G: Journal of Aerospace Engineering*, vol. 82, no. 1, pp. 337–346, 1999.
- [14] J. Polly, D. Talbot, A. Kahraman, A. Singh, and H. Xu, “An Experimental Investigation of Churning Power Losses of a Gearbox,” *Journal of Tribology*, vol. 140, no. 6, pp. 1–8, 2018.
- [15] C. Changenet and P. Velex, “Housing Influence on Churning Losses in Geared Transmissions,” *Journal of Mechanical Design*, vol. 130,

- no. June 2008, pp. 062603, 2008.
- [16] H. G. Chothani and K. D. Maniya, "Experimental investigation of churning power loss of single start worm gear drive through optimization technique," *Materials Today: Proceedings-Journal-Elseiver*, vol. 28, pp. 2031-2038, 2020.
- [17] O. Mohammed, *Mechanical Design Engineering Handbook.*, no. July. 2014.
- [18] H. G. Chothani and K. D. Maniya, "Determination of optimum working parameters for multiple response characteristics of worm gearbox," *International Journal of Recent Technology and Engineering*, vol. 8, no. 3, pp. 1858–1862, 2019.
- [19] KHK Stock gears, "Lubrication of Gears," *KHK Stock gears*, 2015. [Online]
- [20] M. C. Brown, "Machinery Lubrication," *Noria corporation*, 2011.
- [21] B. R. Höhn, K. Michaelis, and H. P. Otto, "Influence of Immersion Depth of Dip Lubricated Gears on Power Loss, Bulk Temperature and Scuffing Load Carrying Capacity," *International Journal of Mechanics and Materials in Design*, vol. 4, no. 2, pp. 145–156, 2008.

Pressure Drop and Flow Characteristics in a Diffuser with a Dimpled Tube

Ehan Sabah Shukri Askari*

Institute of Technology Baghdad, Middle Technical University (MTU),
Baghdad, Iraq,

*ehansabah@yahoo.com

Wirachman Wisnoe

Faculty of Mechanical Engineering, Universiti Teknologi MARA (UiTM),
Shah Alam, Selangor, Malaysia

ABSTRACT

The pressure drops and flow characteristics in a diffuser fitted with a semi-dimpled tube are numerically studied. Air is selected as a working fluid and its physical properties are modelled using pressure and velocity distribution. The study reveals that every semi-dimple act as a vortex generator. They provide the flow with intensive vortices between the dimpled surface and the diffuser wall. Therefore, they cause an enhancement in the pressure drop inside the diffuser. The performance of the dimples consisting of sphere type dimples with 5 mm in diameter. Three Reynolds number operated in the range of $25000 < Re < 50000$ that is based on the hydraulic diameter of the diffuser D_h . The variation in Reynolds number is examined to further investigations of the pressure drop and flow characteristics of the diffuser. The numerical simulations are conducted using incompressible steady-state Reynolds Averaged Navier Stokes equations and the turbulence model RNG k- ϵ is utilized in the current study. The flow characteristics of the diffuser with semi-dimpled tube are analysed and compared in terms of pressure contour, velocity profile, and velocity vectors, at the operating range of Reynolds numbers. The results are discussed to point out the flow structure mechanisms. It is found that equipping the diffuser with a semi-dimpled tube leads to an increase in the recirculation and vortices inside and near the dimples area. Therefore, they have a considerable influence on the flow field. For the diffuser equipped with a semi-dimpled tube, it is noted that the flow characteristics depend on the Reynolds number. The pressure drop in the flow direction becomes lower with increasing Reynolds number. The findings

indicate that for the semi-dimples, increasing Reynolds number increases the velocity distribution significantly due to better mixing of the air.

Keywords: CFD; annular diffuser; dimpled tube; pressure drop; velocity distribution

Nomenclature		Greek Symbols	
D_i	Inlet diameter of the diffuser, mm		
D_o	Outlet diameter of the diffuser, mm		
L	Length of the diffuser, mm	k	Turbulent kinetic energy
d_t	The diameter of the tube, mm	ε	Turbulence. dissipation
L_t	Length of the tube, mm	l	Turbulence. length scale
d_m	The diameter of the dimple, mm	I	Initial turbulence intensity
P	The pressure at the inlet, bar	C_μ	k - ε model parameter
u	The velocity at the inlet, m.s ⁻¹	λ	Thermal conductivity
ρ	Air density, kg.m ⁻³	C_p	Specific heat capacity, kJ.kg ⁻¹ K ⁻¹
Re	Reynolds Number		

Introduction

There are many engineering applications where flow mixing, and recirculation is a necessary part. The classic types of flow characteristics enhancements such as fins, helical screw tape, dimples, etc., always increase turbulence and recirculation. Gas turbine engines are one of the most popular kinds of applications. In such engines, the product of power and efficiency increases as these types of enhancement is added. One of the important gas turbine engine components is the combustor. It directly affects engine performance. The most serious problems of the combustors are the high-pressure air coming from the compressor and the other highlighted problem how good is the mixing between the fuel and the compressed air. These two facts may cause serious problems on combustion uniformity and total pressure loss coefficient. Utilizing pre-diffuser can reduce the effects of previous problems. It is used to decelerate the flow and distribute the air around the combustor uniformly and stably. This process should be completed with a minimum total pressure loss.

To enhance efficiency and save energy with less loss, enhancement techniques are required to improve mixing and increase turbulence. Dimples are selected to generate turbulence and surfaces with dimples are easy to fabricate. The existence of dimples enhances the character of the flow. In recent years, numerous studies with numerical and experimental methods have been carried out to improve the mixing and the performance of the heat transfer by using different types of turbulence generators systems such as

helical screw tapes [1]-[6], pin-fins [7]-[9], and dimples [10]-[18]. In the recent decade, many researchers used pimples as a mixing method and it could enhance the characteristics of the flow including temperature, velocity profile, etc. Zhou et al. [18] pointed out that the performance of the heat transfer in a dimpled surface is affected by the dimple geometries, including dimple shape, dimple depth ratio, and dimple diameter. They completed an experimental enquiry to search about the turbulent boundary layer characteristics when it flows over a dimpled surface and compares the results with a plain flat plate. The results found that the flow characteristics of the turbulent boundary layer flow over the dimpled surface were more complicated with much stronger near-wall Reynolds stress and higher turbulence kinetic energy, especially in the region near the back rims of the dimples.

Aroonrat and Wongwises [19] investigated the advantage of the refrigerant (R-134a) on the heat transfer and pressure drop characteristics. In a double-tube heat exchanger, the refrigerant (R-134a) was flowing into the inner tube and in the annulus, the cold water was flowing. The study focused on the inner tube with a dimpled tube and a plain tube. At the results, they found that with the dimpled tube, the heat transfer coefficient and frictional pressure drop were higher than that of the plain tube and as the Reynolds number increases, it increased Nusselt number.

To improve heat transfer by using dimples and protrusions, Xie et al. [20] suggested a modern design of an enhanced tube with dimples and protrusions to induce swirl flow. From this investigation, it is found that the geometries parameters of the dimples and the protrusions play an important role to improve the thermal-hydraulic characterizes and heat transfer rate compared with the plain tube, due to improved flow mixing. Xie et al. [21] carried out numerical research using cross-ellipsoidal dimples inside an enhanced tube to construe the mechanisms of the flow field method and heat transfer. In their research, they used longitudinal and transverse dimples. The effects of the dimple geometries (depth pitch and axis ratio) on thermal-hydraulic performance were discussed and the simulations were employed with the Re range from 5000 to 30,000. The results got that the flow mixing was improved by the downward flow of the transverse and longitudinal dimples. And the geometric parameter had been affected by the thermal-hydraulic performance significantly.

Recently, many industrial and thermal applications required new techniques to enhance heat transfer and increased thermal efficiency Wang et al. [22] applied a numerical study in a square channel with dimples. The aim was to test the bleed hole installation angle effect on the heat transfer and the flow structure. They found that utilizing a bleed hole in this channel significantly improved the thermal performance of the flow. Recently, dimples were utilized as one kind of concavity that has a significant effect on energy conservation augmentations. Qu et al. [23] investigated heat transfer

and flow features in arrays of dimples inside a rectangular channel at a transitional Reynolds number. In this investigation, they used the SST turbulent model coupled with the Gamma-Theta transition model to indicate the effect of different dimple depth and different Reynolds numbers on the heat transfer performance and Nusselt number. The results displayed that under the laminar condition the average Nusselt number decreases in the flow direction while it increased when the flow became turbulent. Moreover, the study obtained heat transfer enhancement during the turbulent flow and became worse during the laminar flow. The numerical findings showed that the heat transfer performance increased with the dimples depth increases because of the induction of the turbulence kinetic energy into the main flow.

Abdulwahid et al. [24] studied the effect of an oval cross-section tube with an oval dimpled surface in a laminar flow experimentally. The non-Newtonian fluid was assumed with a constant heat flux condition and water as a working fluid. This kind of passive technique showed good results in terms of Nusselt number enhancement.

Most of the above works investigated flow features and heat transfer improvement in channels and pipes with dimples. The present research conducts numerical simulations to study pressure drop and flow characteristics in a diffuser with a dimpled tube. The study is employed sphere type dimples of 5 mm diameter and different Reynolds numbers based on the diffuser hydraulic diameter in the range of $25000 < Re < 50000$. The pressure contour, velocity streamlines, and velocity vectors are numerically investigated to indicate the flow mixing mechanisms.

Setup Design Methods

Model mechanism descriptions

In the present research, a numerical method is used to be carried out to learn about the impact of dimples on the flow attribute and pressure drop in a diffuser geared up with a dimpled tube. Air is used as the working fluid in this investigation to show the effect of dimples insert. The study considers all the numerical simulations under the same inlet condition. In this research, ($L=80$ mm) is the diffuser length, ($D_i=20$ mm) is the diffuser inlet diameter, and ($D_o=40$ mm) is the diffuser outlet diameter. The tube diameter (d_t) is (10 mm) and a length (L_t) is (60 mm), [25]. The spherical dimples have a diameter ($d_s=5$ mm). The model geometries are illustrated in Figure 1.

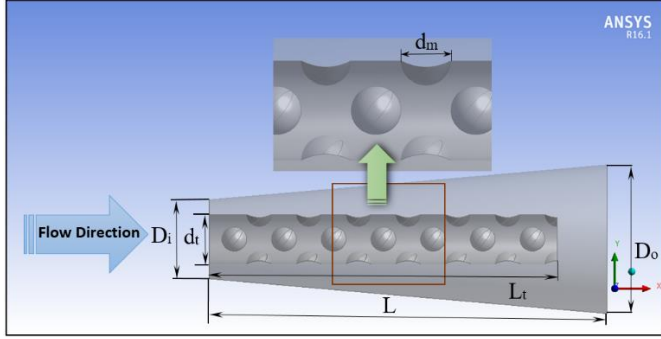


Figure 1: Model design geometries.

Boundary conditions arrangements

Some assumptions are made to design the pressure drop and flow structure of air flowing around a dimpled tube in a diffuser. They are as follows:

- i. Turbulent flow with Reynolds number ranged from 25,000 to 50,000, in a steady and incompressible flow.
- ii. The hydraulic diameter that is used in the Reynolds number is defined as the inlet diameter of the diffuser. The hydraulic diameter is calculated as follows, [26].

$$D_h = \frac{4\pi(D_i^2 - d_t^2)/4}{\pi(D_i + d_t)} = D_i - d_t \quad (1)$$

- iii. Air physical properties are considered as the dynamic viscosity (1.849×10^{-5} kg/m.s) and the density (1.184 kg/m³), [27].
- iv. At the inlet, the temperature is 870 K°. The Reynolds number is ranged from 25,000 to 50,000 according to the changes of the air specified mass flow rate. The study presumes the temperature of the wall constant.
- v. At the inlet of the diffuser, all the physical properties of the air are given constant.
- vi. In the outlet, the static pressure is set as zero.

Computational setup

Turbulence model

The pressure drops and the flow structure for a dimpled tube and a diffuser are studied in the current investigation. The research used the

RNG k - ε as a turbulence model. It is significantly important to pick a turbulence model for a particular simulation. The turbulence model is based on the computational demands and how carefully predicted flow phenomenon. Then, the RNG k - ε turbulence model is adopted in the present study because it can provide excellent performance for flow, including recirculation and rotation [27]. The finite quantity technique is used to solve the time-independent incompressible Navier Stokes equations. The finite modeling is achieved utilizing the commercial CFD (Computational fluid dynamics) software ANSYS 16.1. The simulations are completed in three-dimensional domains employing the RNG k - ε model as a turbulence model for studying the pressure and velocity fields. Moreover, the commercial software ICEM version 16.1 is used to generate the grid method for the dimpled tube and the diffuser. This meshing tool was utilized to mesh the fluid computational domain with the unstructured tetrahedral grid as shown in Figure 2. The predictable velocity profile for five extraordinary grid independence has been compared to estimate the effect of the grid sizes on the accuracy of the numerical options results. It has been determined that 21599 factors grid is convenient for the simulation. The following transport equations were used to create the turbulence kinetic energy k and its rate of dissipation ε , [28].

$$K = \frac{3}{2}(VI)^2 \quad (2)$$

where I is the initial turbulence intensity, and V is the inlet velocity magnitude, [28].

$$\varepsilon = \left(C_\mu^{\frac{3}{4}} \cdot K^{\frac{3}{2}}\right) l^{-1} \quad (3)$$

Here l is the turbulence length scale, and C_μ is a k - ε model parameter. Its value is given as 0.09, [28]. Then the initial turbulence intensity is given as below, [28]:

$$I = 0.16(Re)^{-\frac{1}{8}} \quad (4)$$

And the turbulence length scale, [28]:

$$l = 0.07 L \quad (5)$$

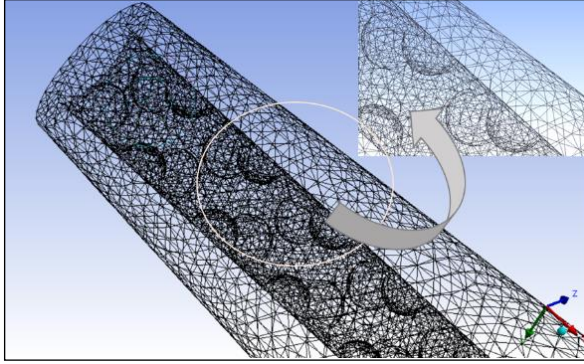


Figure 2: Schematic of the meshing generation.

Governing equations

The incompressible steady Navier-Stokes equations were solved by conservation Equations of mass, momentum, and energy. These equations mainly depict the flow characteristics and they are given by [29]:

- Continuity Equation

$$\frac{\partial}{\partial x_i} (r \rho u_i) = 0 \quad (6)$$

- Momentum Equation:

$$\frac{\partial}{\partial x} (r \rho u_i u_j) = -r \frac{\partial P}{\partial x_i} + \frac{\partial}{\partial x_j} \left[r \left(\mu \frac{\partial u_i}{\partial x_j} - \overline{\rho u_i u_j} \right) \right] \quad (7)$$

- Energy Equation:

$$\frac{\partial(\rho \bar{T})}{\partial x_i} + \frac{\partial(\rho \bar{u}_i \bar{T})}{\partial x_i} = \frac{\partial}{\partial x_i} \left(\frac{\lambda}{C_p} \frac{\partial(\bar{T})}{\partial x_i} \right) \quad (8)$$

Where the quantity $-\overline{\rho u_i u_j}$ in Equation (3) is symbolized the turbulent Reynolds stresses generated by velocity fluctuations, the thermal conductivity is λ , and the specific heat at constant pressure is C_p [29].

Validation methods

The numerical work results accuracy is an important aim. The numerical findings of the turbulent flow through the diffuser with semi-dimpled tube were validated with the experimental data of Arora [30] and Djebedjian [28]

as shown in Figure 3 and Figure 4, respectively. The validation is performed by two methods to support the reliability of the numerical work. Both the static pressure coefficient C_p and flow velocity are compared with the experiment results of the previous researchers. From Figure 3, it can be displayed that the numerical results of the static pressure coefficient C_p are in good agreement with the experimental of Arora [30], and the percentage error is within $\pm 2\%$. While Figure 4 displays a comparison of the velocity profile in the flow direction. The validation confirms the agreement of the numerical results with the experimental work of the Djebedjian [28] that presents the reliability of the adopted method within percentage error $\pm 4\%$.

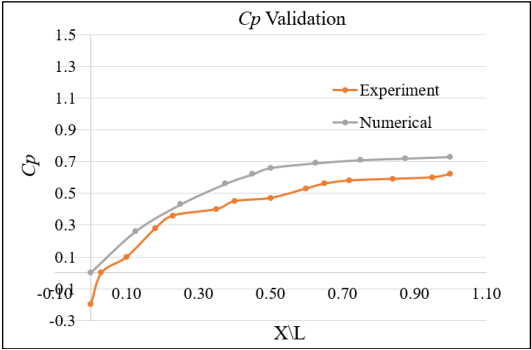


Figure 3: Numerical results validation of the static pressure loss coefficient C_p with the experimental data from Arora [30].

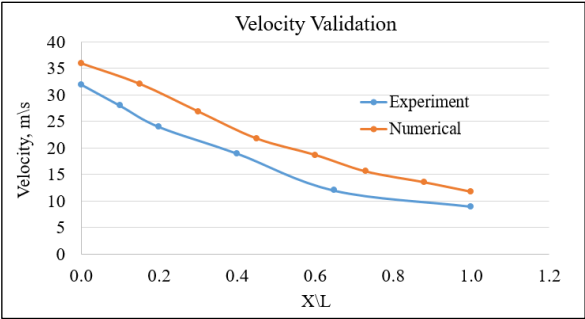


Figure 4: Comparison validation of numerical results with experimental work of Djebedjian et al. [28].

Results and Discussion

Pressure drop characteristics discussions

Based on the CFD simulations completed in the current study, the pressure drop characteristics for the airflow around the dimpled tube have been measured within the Reynolds Number range of $25000 < Re < 50000$. Due to the different Reynolds numbers that are studied, the pressure contours differed clearly. Figures 5 and Figure 6 show comparison of pressures in contour and in profile, respectively versus flow direction in the dimpled tube with three various Reynolds number (Re).

By comparison, it is found that in (a) with Re (2.5×10^4), the pressure is the highest. Besides (b) with Re (3.8×10^4), the pressure will be less. Higher Reynolds Number like in (c) with Re (5.0×10^4), the pressure is decreased. The flow characteristics related to pressure is better with Re (2.5×10^4), where the pressure is highest which means the pressure drop is lowest. The figures show the increase of pressure following the increase of passage area of the diffuser.

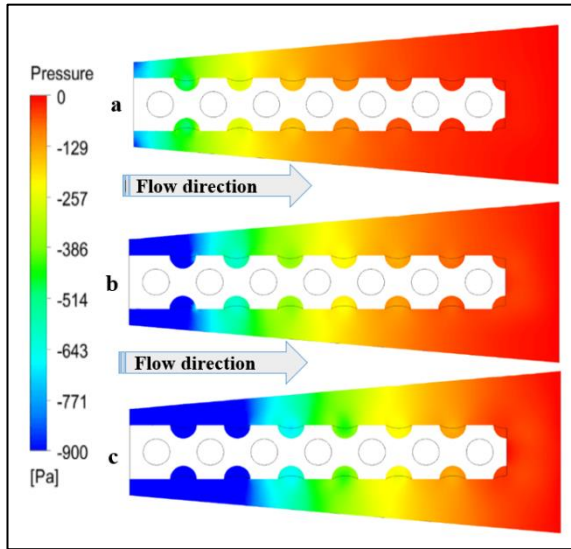


Figure 5: Comparison of pressure drop contours versus flow direction in the dimpled tube with various Reynolds number (a) $Re = 2.5 \times 10^4$, (b). $Re = 3.8 \times 10^4$ and (c) $Re = 5.0 \times 10^4$.

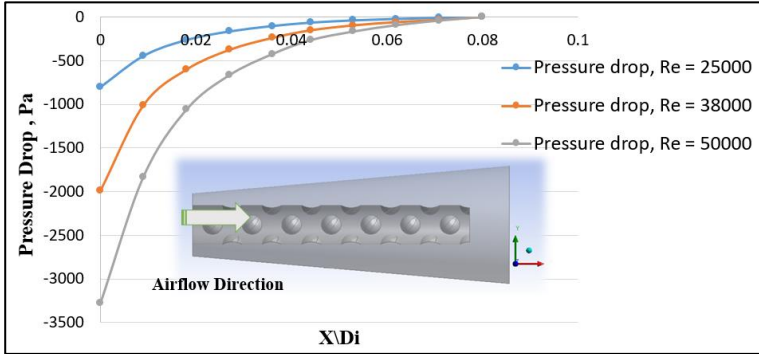


Figure 6: Comparison of pressure drop profile versus flow direction in a dimpled tube with various Reynolds number ($Re = 2.5 \times 10^4$, 3.8×10^4 and 5.0×10^4).

Velocity distribution characteristics discussions

The following simulations are utilized to study the velocity profile characteristics in a dimpled tube during turbulence flow. The effect of Reynolds number on the velocity profile through the dimpled tube is examined. Figures 7, 8 and 9 show the velocity vectors for three different Reynolds numbers (2.5×10^4 , 3.8×10^4 , and 5.0×10^4) along the flow direction.

In terms of the effect of Reynolds number on the velocity feature, the recirculation and the tangential velocity component near the dimples area increases as the Reynolds number increased. The figures reveal that the air near the dimples area is mixed with the additional air that flowing around the dimpled tube and enhances the distributions of the velocity.

More explanations for the effect of dimples on the flow characteristics can be depicted in Figure 10, Figure 11, and Figure 12. The figures show clearly the presence of flow recirculation at the dimples area. The colour of the blue balls shows the velocity magnitude. For the three tested Reynolds numbers, recirculation and vortices are conducted at the dimples area but in different manners. The recirculation remains at the three tests but became weak with Reynolds number (5.0×10^4). This means that dimples can produce tangential velocities and provide the flow with high distribution intensity. However, the high distribution intensity also increases the pressure drop. It is obvious that the dimple hole cause to change the direction of the velocity inside the dimple. Thus, the cross-sectional area of the flow is increased. Songtao Wang explained this fact, as when the main flow accesses the dimple, it will be divided into two parts. The flow in some parts of the dimple has a high velocity and it makes a low velocity recirculation-zone in other parts. When the flow impinging the dimples area, the flow streamlines

separate from the dimpled surface and reattach on the end wall downstream of the dimple. Then, the turbulent kinetic energy in the free shear layer is created between these two parts of the flow (the main and the reverse flow) [31].

The variation of velocity distribution in the flow direction around the dimpled tube is compared in Figure 13 for three various Reynolds numbers ($Re = 2.5 \times 10^4$, 3.8×10^4 and 5.0×10^4). In this direction, it can be noticed that the velocity distribution decreases as the Reynolds number increased.

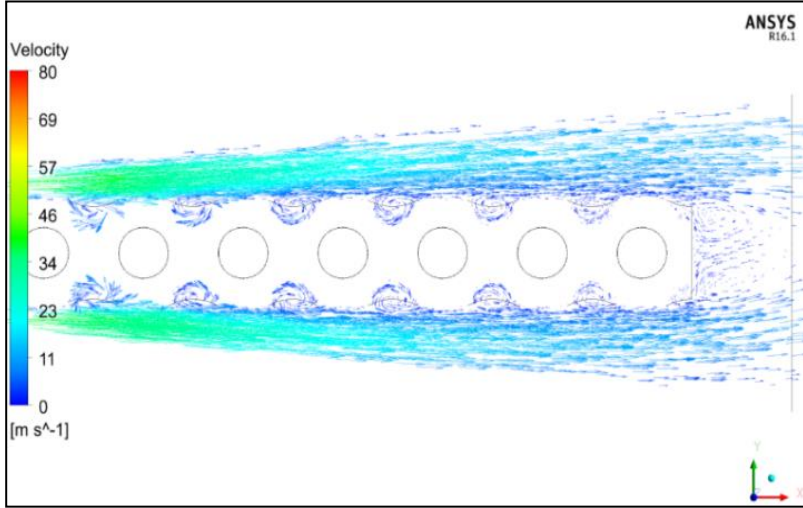


Figure 7: Velocity vectors around a dimpled tube with Reynolds number $Re = 2.5 \times 10^4$.

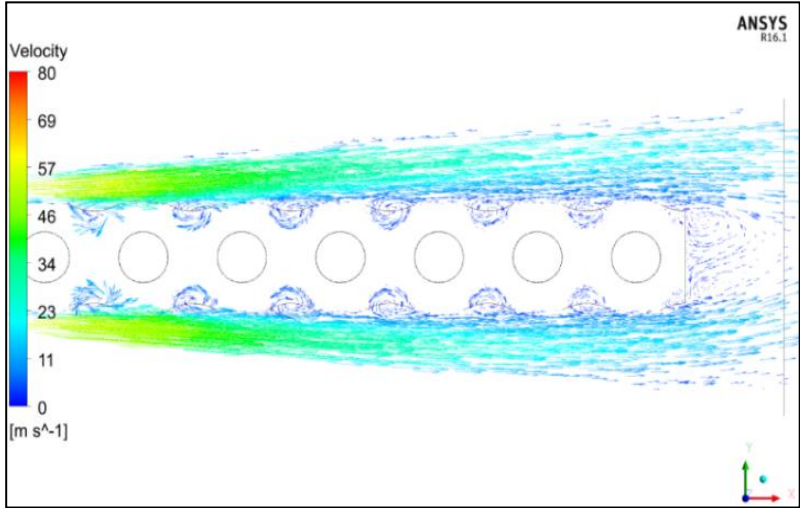


Figure 8: Velocity vectors around a dimpled tube with Reynolds number $\text{Re} = 3.8 \times 10^4$.

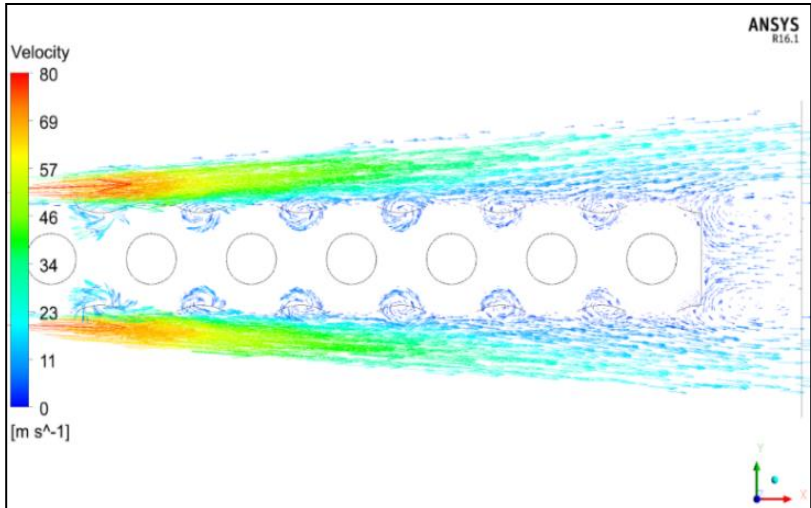


Figure 9: Velocity vectors around a dimpled tube with Reynolds number $\text{Re} = 5.0 \times 10^4$.

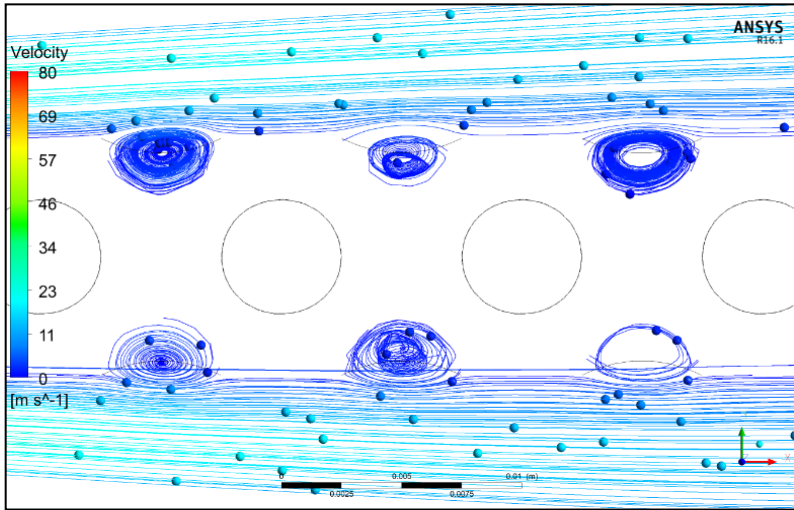


Figure 10: Velocity streamlines around a dimpled tube with $Re = 2.5 \times 10^4$.

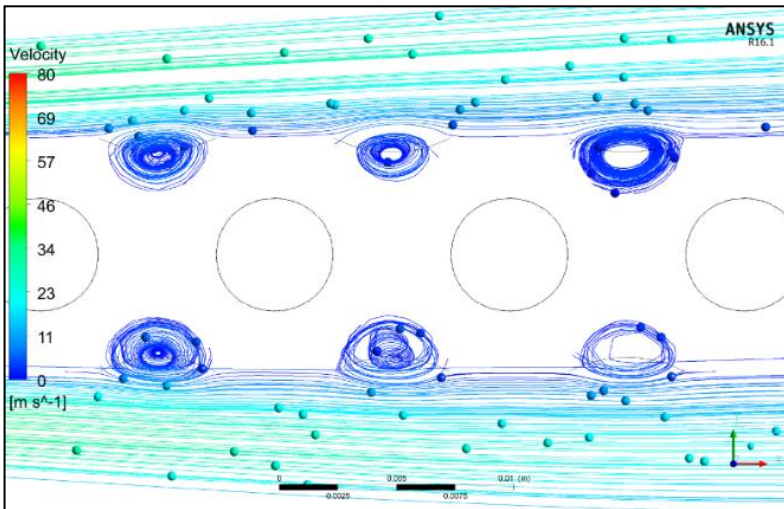


Figure 11: Velocity streamlines around a dimpled tube with $Re = 3.8 \times 10^4$.

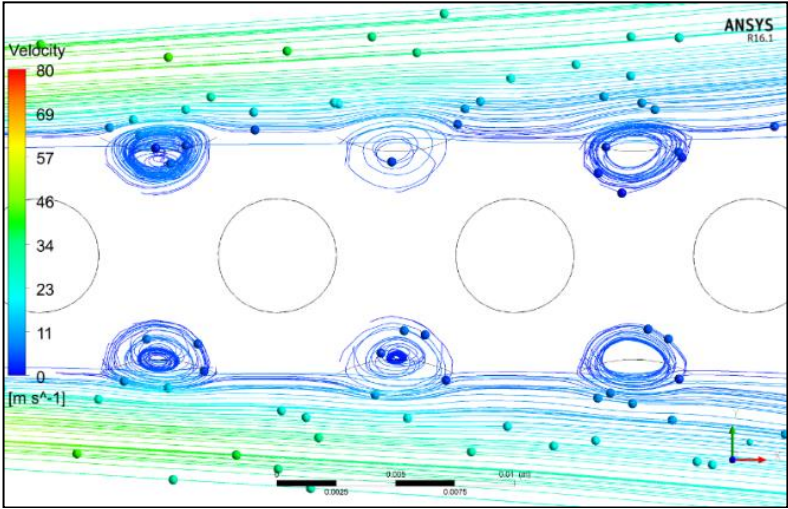


Figure 12: Velocity streamlines around a dimpled tube with $Re = 5.0 \times 10^4$.

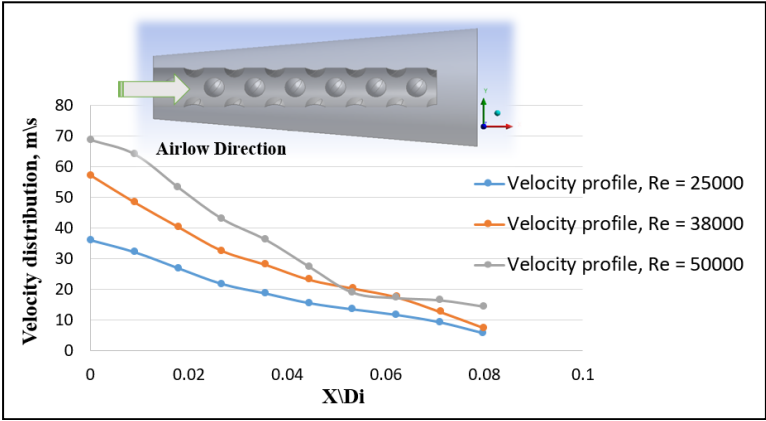


Figure 13: Comparison of velocity distribution versus flow direction in a dimpled tube with various Reynolds number ($Re = 2.5 \times 10^4$, 3.8×10^4 and 5.0×10^4).

Velocity and pressure profile comparison in the outlet

To test the effect of dimples insertion on the outlet flow characteristics, an outlet plane is used.

The streamline velocity, the velocity profile and the pressure variation comparison with three different Reynolds numbers ($Re = 2.5 \times 10^4$, 3.8×10^4 , and 5.0×10^4) are depicted in Figure 14, 15 and 16, respectively. Figure 14 presents the velocity streamlines for different Reynolds numbers (Re) near the outlet of the diffuser. For a plane at the outlet of the annular diffuser behind the dimpled tube, the distribution of the velocity increased with higher Reynolds numbers. In Figure 15, it is displayed that the distribution of the velocity increases at the outlet as the Reynolds number increases because that increase disturbs the entire flow and cause more swirl flow and recirculation. At the same time, the pressure variation decreases with a high Reynolds number as shown in Figure 16.

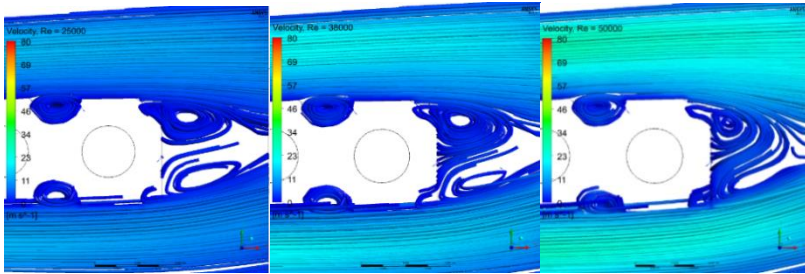


Figure 14: Streamline velocity comparison in the flow direction around a dimpled tube with various Reynolds number ($Re = 2.5 \times 10^4$, 3.8×10^4 and 5.0×10^4).

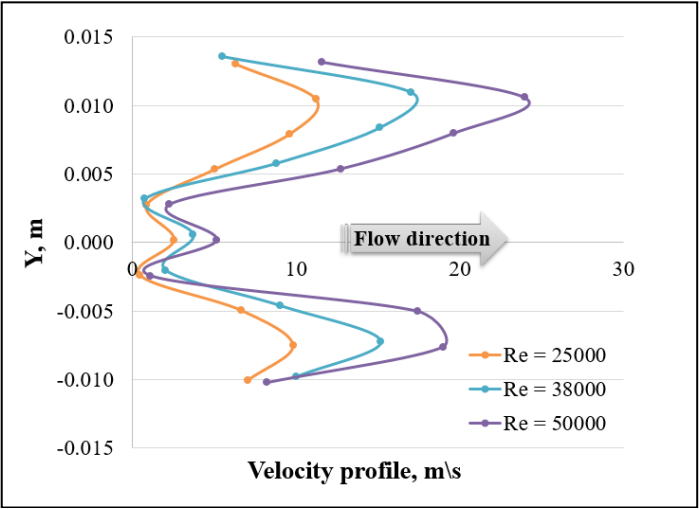


Figure 15: Comparison of velocity distribution versus radial flow direction around a dimpled tube with various Reynolds number ($Re = 2.5 \times 10^4$, 3.8×10^4 and 5.0×10^4).

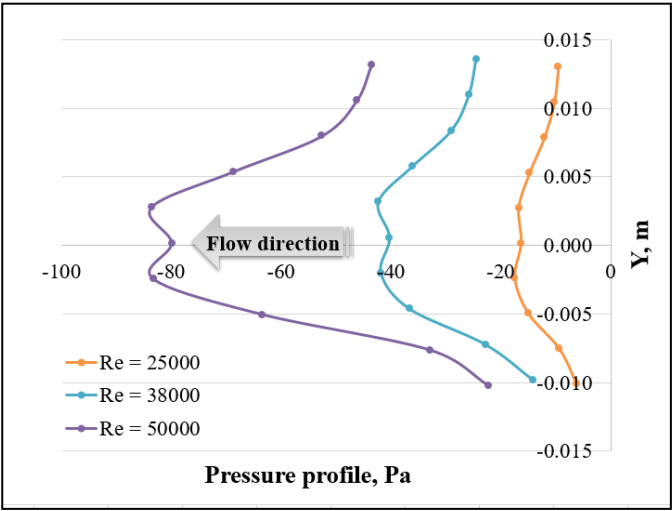


Figure 16: Comparison of pressure variation versus radial flow direction around a dimpled tube with various Reynolds number ($Re = 2.5 \times 10^4$, 3.8×10^4 and 5.0×10^4).

Conclusions

In this paper, a numerical analysis was performed to investigate the pressure drop and flow structure of air flowing around a dimpled tube in an annular diffuser. The research is considered the boundary condition as a steady and incompressible flow. The results were obtained by using different Reynolds numbers ranging as $25000 < Re < 50000$. Based on these assumptions, the following conclusion is made.

1. The numerical analyses were performed to differ the pressure drop around the dimpled tube. From the comparative analysis of pressure drop contours versus flow direction, the air pressure decreases with the increase of Reynolds number because of the increases in the flow passage area in the diffuser and the pressure losses increases due to the existence of the dimples that create recirculation and vortices causes to increase the losses.
2. Velocity simulations are utilized to study the velocity profile characteristics in a dimpled tube during the turbulent flow. It is found that the air near the dimples area is mixed with the additional air that flowing around the dimpled tube and enhances the distributions of the velocity that means more tangential velocity components. This fact leads to enhance the flow mixing through the diffuser area.
3. The recirculation and the tangential velocity component intensity near the dimples area increase as the Reynolds number increase.
4. In the flow direction, it can be noticed that with the increase of Reynolds number, the velocity profile decreases.
5. At the outlet, the velocity distribution increases as the Reynolds number increases and the pressure rate decreases with the increase of Reynolds number. The increase in Reynolds number disturbs the flow and creates more swirl flow and recirculation.

References

- [1] P. R. Ingole and S. L. Kolhe, "Analysis of coiled-tube heat exchangers to improve heat transfer rate with spirally corrugated wall," *International Journal of Modern Engineering Research (IJMER)*, vol. 4, pp. 196-175, 2014.
- [2] S. Naga Sarada, A.V. Sita Rama Raju, K. Kalyani Radha and L. Shyam Sunder, "Enhancement of heat transfer using varying width twisted tape inserts," *International Journal of Engineering, Science and Technology*, vol. 2, pp. 107-118, 2007.

- [3] F. A. Saleh, "Computational and experimental investigations on thermal and fluid flow characteristics for different models of tapes inserts with TiO₂/water nanofluid under turbulent conditions," *International Journal of Mechanical & Mechatronics Engineering IJMME-IJENS*, vol. 18, pp. 1-14, 2018.
- [4] E. S. Shukri and W. Wisnoe, "Temperature distribution enhancement in a conical diffuser fitted with helical screw-tape with and without center-rod," *International Journal of Mechanical, Aerospace, Industrial, Mechatronic and Manufacturing Engineering*, vol. 10, pp. 439-444, 2016.
- [5] E. S. Shukri, "Numerical comparison of temperature distribution in an annular diffuser fitted with helical screw-tape hub and pimpled hub," *4th International Conference on Power and Energy Systems Engineering, CPSE 2017, 25-29 September 2017, Berlin, Germany, Procedia Engineering*, vol. 141, pp. 625-629, 2017.
- [6] V. Arunprasad, P. Murugesan and S. Jaisankar, "Experimental studies on natural circulation solar water heating system fitted with helical screw tape inserts," *Asian Journal of Research in Social Sciences and Humanities*, vol. 6, pp. 1703-1716, 2016.
- [7] A. Soni, "Study of thermal performance between plate-fin, pin-fin and elliptical fin heat sinks in closed enclosure under natural convection," *International Advanced Research Journal in Science, Engineering and Technology, ISO 3297:2007 Certified, ISSN 2394-1588*, vol. 3, no. 11, pp. 133-139, 2016.
- [8] Y. S. Tomar and M. M. Sahu, "Comparative study of performance of pin fin under forced convection heat transfer," *International Journal of Engineering Research & Technology (IJERT)*, ISSN: 2278 – 0181, vol. 2 no. 9, pp. 364-374, 2013.
- [9] R. J. Moitsheki and C. Harley, "Steady thermal analysis of two-dimensional cylindrical pin fin with a nonconstant base temperature," *Hindawi Publishing Corporation Mathematical Problems in Engineering*, 2011, Article ID 132457, DOI:10.1155/2011/132457, 2011, pp. 1-17.
- [10] F. Sangtarash and H. Shokuhmand, "Experimental and numerical investigation of the heat transfer augmentation and pressure drop in simple dimpled and perforated dimpled louver fin banks with an in-line or staggered arrangement," *Applied Thermal Engineering*, vol. 82, pp. 194-205, 2015.
- [11] A. A. Tsynaeva and M. N. Nikitin, "Study of the flow in a channel with dumbbell-shaped dimples," *International Conference on Industrial Engineering, ICIE 2016, Procedia Engineering*, vol. 150, pp. 2340-2344, 2016.

- [12]J. Abraham and R. Maki, "Hydrodynamics of laminar flow through dimpled pipes," *MOJ Civil Engineering*, vol. 4, no. 3, pp. 150-154, 2018.
- [13]K. A. Amsha, "Turbulence modelling of the flow and heat transfer in dimpled channels," *A thesis submitted to The University of Manchester for the degree of Doctor of Philosophy (Ph.D.) in the Faculty of Science and Engineering, School of Mechanical, Aerospace and Civil Engineering*, 2017.
- [14]S. Shin, K. S. Lee, S. D. Park and J. S. Kwak, "Measurement of the heat transfer coefficient in the dimpled channel: effects of dimple arrangement and channel height," *Journal of Mechanical Science and Technology*, vol. 23, pp. 624- 630, 2009.
- [15]E. S. Shukri, "Thermal flow analysis for annular diffuser equipped with pimpled hub," *Journal of Mechanical Engineering, JMechE*, vol. 15, no. 1, pp. 115-134, 2018.
- [16]J.Sathees Babu, "Analysis of heat transfer and fluid flow characteristics of concentric tube heat exchanger with dimpled tube," *Journal of Xi'an University of Architecture & Technology*, vol. 13, pp. 508-516, 2020.
- [17]E. S. Shukri, "Performance analysis of annulus diffusing area with divergent dimpled tube," *The 6th International Conference on Power and Energy Systems Engineering (CPESE 2019), September 20 – 23, 2019, Okinawa, Japan*, vol. 6, pp. 11-18, 2020.
- [18]W. Zhou, Y. Rao and H. Hu, "An experimental investigation on the characteristics of turbulent boundary layer flow over a dimpled surface," *Journal of Fluids Engineering ASME*, vol. 138, pp. 021204-1-021204-13, 2016.
- [19]K. Aroonrat and S. Wongwises, "Experimental study on two-phase condensation heat transfer and pressure drop of R-134a flowing in a dimpled tube," *International Journal of Heat and Mass Transfer*, vol. 106, pp. 437-448, 2017.
- [20]S. Xie, Z. Liang, L. Zhang, Y. Wang, H. Ding and J. Zhang, "Numerical investigation on heat transfer performance and flow characteristics in enhanced tube with dimples and protrusions," *International Journal of Heat and Mass Transfer*, vol. 122, pp. 602- 613, 2018.
- [21]S. Xie, Z. Liang, L. Zhang and Y. Wang, "A numerical study on heat transfer enhancement and flow structure in enhanced tube with cross ellipsoidal dimples," *International Journal of Heat and Mass Transfer*, vol. 125, pp. 434- 444, 2018.
- [22]S. Wang, W. Du, L. Luo, D. Qiu, X. Zhang and S. Li, "Flow structure and heat transfer characteristics of a dimpled wedge channel with a bleed hole in dimple at different orientations and locations," *International Journal of Heat and Mass Transfer*, vol. 117, pp. 1216-1230, 2018.
- [23]H. Qu, Z. Shen and Y. Xie, "Numerical investigation of flow and heat transfer in a dimpled channel among transitional Reynolds numbers,"

- Hindawi Publishing Corporation Mathematical Problems in Engineering*, 2013, pp. 1-10.
- [24] Ammar F. Abdulwahid, Hyder H. Balla and Reyadh Ch. Al-Zuhairy, "Experimental heat transfer enhancement in oval dimpled tube," *Journal of Mechanical Engineering Research and Developments*, ISSN: 1024-1752, vol. 43, pp. 400-408, 2020.
- [25] Y. Eldrainy, J. Jeffrie and M. Ridzwan, "Prediction of the flow inside a micro gas turbine combustor," *Jurnal Mecchanikal*, no. 25, pp. 50–63, 2008.
- [26] P. Promvonge, S. Suwannapan, M. Pimsarn and C. Thianpong, "Experimental study on heat transfer in square duct with combined twisted-tape and winglet vortex generators," *International Communications in Heat and Mass Transfer*, vol. 59, pp. 158-165, 2014.
- [27] E. S. Shukri, B. H. Abdullah, O. M. Ali, "Velocity distribution in an annular diffuser fitted with twisted hub for different area ratios," *4th International Conference on Power and Energy Systems Engineering, CPES 2017, 25-29 September 2017, Berlin, Germany*, vol. 141, pp. 639-643, 2018.
- [28] B. Djebedjian, M. Giat, J. P. Renaudeau and M. A Rayan, "Numerical study of turbulent flow through equiangular annular diffusers," *Proceeding of Fifth International Conference of Fluid Mechanics*, Cairo, pp.719-729, 1995.
- [29] D. Flórez-Orrego, W. Arias, D. López, and H. Velásquez, "Experimental and CFD study of a single-phase cone-shaped helical coiled heat exchanger: an empirical correlation," *Proceedings of the 25th International Conference on Efficiency, Cost, Optimization, Simulation and Environmental Impact of Energy Systems*, pp. 375-394, 2012.
- [30] B. B. Arora and B. D. Pathak, "Effect of geometry on the performance of annular diffuser," *International Journal of Applied Engineering Research*, vol. 4, pp. 2639-2652, 2009.
- [31] S. Wang, W. Du, L. Luo, D. Qiu, X. Zhang and S. Li, "Flow structure and heat transfer characteristics of a dimpled wedge channel with a bleed hole in dimple at different orientations and locations," *International Journal of Heat and Mass Transfer*, vol. 117, pp. 1216-1230, 2018.

Heat Transfer and Pressure Drop Characteristics of Hybrid $\text{Al}_2\text{O}_3\text{-SiO}_2$

Muyassarrah Syahirah Mohd Yatim, Irnie Azlin Zakaria*,
Mohamad Fareez Roslan, Wan Ahmad Najmi Wan Mohamed,
Mohd Faizal Mohamad

Faculty of Mechanical Engineering, University Teknologi MARA (UiTM),
40450 Shah Alam, Selangor, Malaysia

*irnieazlin@uitm.edu.my

ABSTRACT

The emergence of Proton Electrolyte Membrane Fuel Cell (PEMFC) is seen as one of the greener alternatives to internal combustion engine (ICE) in automotive industry nowadays. However, the sensitivity of a PEMFC membrane needs to be further improved for the optimum performance. In this study, single and hybrid nanofluids are used as an alternative coolant in a single channel of PEMFC. The study was conducted in a channel with the adoption of single and hybrid nanofluids to observe the effect of the heat transfer and pressure drop in the set up. A heater pad was kept at constant heat load of 100 W, reflecting the actual heat load of a single cell. The study focuses on 0.5% volume concentration for single and hybrid nanofluids of Al_2O_3 and SiO_2 in water. The numerical study was conducted via ANSYS FLUENT 16.0. The 0.5% hybrid $\text{Al}_2\text{O}_3\text{:SiO}_2$ nanofluids of 10:90 and 30:70 in Re range of 300 to 1000 were compared to the base fluid. The heat transfer increment of 9.1% and 9.85% was observed. However, the pressure drop was also increased in the range of 22 Pa to 26 Pa for 0.5 % of $\text{Al}_2\text{O}_3\text{:SiO}_2$ of 10:90 and 30:70 consecutively as compared to the base fluid. The advantage ratio was then analyzed to show the feasibility of both ratios of 0.5 % hybrid nanofluid of $\text{Al}_2\text{O}_3\text{:SiO}_2$ at 10:90 and 30:70. It shows that both have advantage ratio higher than 1, thus feasible for the adoption in a PEMFC.

Keywords: Alumina oxides; Heat transfer; Hybrid; Pressure drop; Silicone dioxide

Introduction

The Proton-exchange membrane fuel cells (PEMFC) is one of the fuel cells categories which is favorable for automotive sector. The PEMFC has an advantage of high-power density, rapid response to change in loads, low operating temperature of 60 to 80 °C and its rapid start up [1]. The effective cooling is important to ensure that the proton exchange membrane fuel cell (PEMFC) is safe and operate efficiently, particularly when it comes to the higher fuel cell stack capacity. However, there are still some issues in the thermal management of PEMFC adoption which need to be resolved critically due to the sensitivity of its membrane as one of the vital components in its operation [2]. Besides the improvement in thermal management, many researchers nowadays are exploring possibilities to miniaturize the PEMFC cooling system in order to make it more attractive for commercialization [1]. Among the advancement are optimizing the design of the cooling path, the flow field and enhancing the heat transfer coefficient of its cooling medium [2]. The passive way of improving the PEMFC cooling medium property is through the adoption of nanofluids which seems to be a better way of thermal management without having to sacrifice the size of the cooling system of fuel cells [2-3].

Nanofluids is an engineered fluid which comprises of nano sized particles dispersed in its base fluid [3]. Nanofluids are primarily a dispersion of both metallic and non-metallic solids which is magnitudes higher in thermal conductivity as compared to base fluid [4]. Nanofluids is also capable of increasing the thermal conductivity of its base fluid due to increase in the total surface area of the nanoparticles [5]. In comparison to distilled water, a significant heat transfer coefficient improvement of 18 % was achieved through the nanofluids [6]. However, unlike adoption of nanofluids in other heat transfer application, PEMFC cooling fluids not only has to be high in thermal conductivity but at the same time maintaining the strict limit of its electrical conductivity value of 5 $\mu\text{S}/\text{cm}$ [4]. This is required as to avoid shunt current while operating the stack and also power leakage to the conductive coolant [7]. There are a lot of heat transfer improvement performed utilizing different types of nanofluids such as ZnO , TiO_2 , SiO_2 and Al_2O_3 [8–10].

A lot of research works has been established in the adoption of nanofluids to PEMFC. Zakaria et al. [11] was among the pioneer in the study and managed to established a correlation between thermal conductivity and electrical conductivity of Al_2O_3 in PEMFC. The study reported that there was an increment of 12.8 % in thermal conductivity and 14.8 % increment in electrical conductivity. There are various numerical and experimental works conducted to justify the feasibility of nanofluids adoption in PEMFC [10-12]. The performance of nanofluids was also studied in both plate and stack level of PEMFC [12–15]. It was reported that nanofluids has managed to improve

the heat transfer in a 1.5 kW_e Ballard PEMFC with almost negligible power drop with due to higher value in electrical conductivity nanofluids but is still acceptable with respect to overall stack output [14].

Research in nanofluids has evolved from a single nanofluids to both hybrid and tri-hybrid nanofluids in which the thermal conductivity was observed to be further improved [16-17]. Nabil et. al [20] has reported an increase of 22.8 % in thermal conductivity of TiO₂-SiO₂ hybrid nanofluids as compared to the base fluid. Saifudin et. al [5] on the other hand has managed to establish a performance enhancement ratio termed as PER for Al₂O₃-SiO₂ hybrid nanofluids in both thermal conductivity enhancement over electrical conductivity and viscosity penalty in PEMFC application. The study reported that the most feasible Al₂O₃-SiO₂ hybrid nanofluids mixture ratio was 10:90 and 30:70 for PEMFC application.

In this study, the established work of Saifudin et. al [5] is further investigated numerically. This work complemented the thermo-physical properties level of the study through the adoption of the Al₂O₃-SiO₂ hybrid nanofluids in a channel. This study add application value to the thermo-physical characterization done by Saifudin et. al [5]. The stainless steel channel was used to simulate a single channel in the PEMFC cooling plate. The channel was then subjected to a constant heat flux to replicate the heat released during the reaction in the bipolar plates of PEMFC. Two recommended mixture ratios as proposed in the previous work was studied which were 10:90 and 30:70 Al₂O₃-SiO₂ hybrid nanofluids in water. The base fluid of water, single nanofluids of Al₂O₃ and SiO₂ were also simulated as a cooling medium in the channel. At the end of the study, an advantage ratio was established to justify the feasibility of the adoption in PEMFC channel.

Methodology

Nanofluid thermo physical properties measurements

Thermal conductivity and viscosity of the nanofluid and base fluid used in this simulation were calculated at 30°C.

The density of nanofluid is calculated by using Equation (1):

$$\rho_{nf} = (1 - \phi)\rho_f + \phi\rho_p \quad (1)$$

The density of hybrid nanofluid is calculated by using Equation (2):

$$\rho_{nf} = (1 - \phi)\rho_f + \phi\rho_{p1} + \phi\rho_{p2} \quad (2)$$

The specific heat of nanofluid is calculated by using Equation (3):

$$C_{p,nf} = \frac{(1-\phi)\rho_f C_f + \phi \rho_p C_p}{\rho_{nf}} \quad (3)$$

The specific heat of hybrid nanofluid is calculated by using Equation (4):

$$C_{p,hnf} = \frac{(1-\phi)\rho_f C_f + \phi_{p_1}\rho_{p_1}C_{p_1} + \phi_{p_2}\rho_{p_2}C_{p_2}}{\rho_{hnf}} \quad (4)$$

Where ϕ was alluded as the proportion of particles by volume and the addendums f, p₁, p₂, b_f and h_{nf} were alluded as base liquid (water), Al₂O₃ and SiO₂ nanofluids and mixture nanofluid. Table 1 lists the nanofluid properties that were measured and determined.

Table 1: Nanofluid and base fluid properties used in numerical analysis

Fluid Name	Thermal Conductivity,K (W/mk)	Specific Heat,Cp (J/kg.k)	Viscosity,μ (Pa.s)	Density,ρ (kg/m ³)	References
Al ₂ O ₃ 0.5% conc.	36	765	-	4000	[11]
SiO ₂ 0.5% conc.	1.4	745	-	2220	[12]
Water	0.615	4180	0.000854	999	[11]

PEMFC channel mathematical model

A 3D Computational Fluid Dynamic (CFD) was established on the basis of a channel dimension as shown in Figure 1. As for the channel, the material used is stainless steel to imitate the channel of PEMFC. The dimension of channel is 20 mm x 10 mm x 380 mm. A consistent heat source of 100 W was implemented to the channel. There have only been a few assumptions [21]:

- i. Incompressible, laminar and steady state flow.
- ii. Body force effect is neglected.
- iii. Viscous dissipation is neglected.
- iv. With a relative velocity of zero, the fluid and nanoparticles are thermally balanced.

For computing in modelling, the channel has the same heat transfer and fluid flow characteristics.

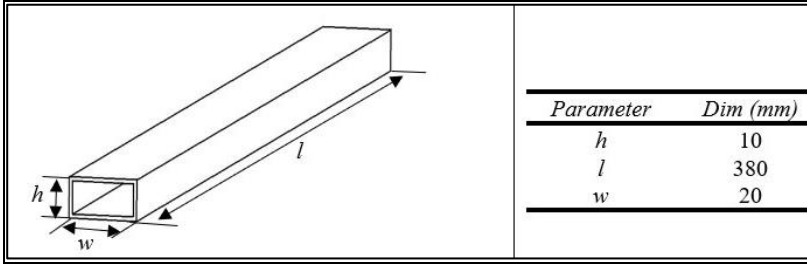


Figure 1: The schematic diagram of channel in PEMFC.

The following are the governing equations for the assumptions:

Equation for continuity:

$$\nabla \cdot (\rho_{nf} \cdot V_m) = 0 \quad (5)$$

Equation for momentum:

$$\nabla \cdot (\rho_{nf} \cdot V_m \cdot V_M) = -\nabla P + \nabla (\mu_{nf} \cdot \nabla V_m) \quad (6)$$

Coolant energy equation:

$$\nabla \cdot (\rho_{nf} \cdot C \cdot V_m \cdot T) = \nabla \cdot (k_{nf} \cdot \nabla T) \quad (7)$$

Conduction of heat through a solid wall:

$$0 = \nabla \cdot (k_s \cdot \nabla T_s) \quad (8)$$

At the wall, there is a no-slip boundary:

$$\vec{V} = 0 \text{ (Walls)} \quad (9)$$

The following boundary conditions were assumed at the channel inlet:

$$\vec{V} = V_m \text{ (inlet)} \quad (10)$$

$$P = \text{atmospheric pressure (outlet)} \quad (11)$$

Heat is transmitted through the solid and distributed through the channel by forced convection of cooling liquid.

$$-k_{nf} \cdot \nabla T = q \text{ (Bottom of channel)} \quad (12)$$

$$-k_{nf} \cdot \nabla T = 0 \text{ (Top of channel)} \quad (13)$$

The analysis of heat transfer and fluid flow

Using this equation, heat transfer coefficient can be determined (14):

$$h = \frac{q}{\Delta T} \quad (14)$$

The Nusselt number can be calculated by using this Equation (15):

$$Nu = \frac{hl}{k} \quad (15)$$

The pressure drop can be calculated by using this Equation (16):

$$\Delta P = P_i - P_o \quad (16)$$

The pumping power can be calculated by using this Equation (17):

$$W_p = \dot{Q} \cdot \Delta P \quad (17)$$

The advantage ratio can be calculated by using this Equation (18):

$$AR = \frac{h}{\Delta P} \quad (18)$$

Results and Discussion

Validation of the study

Prior to analysing the heat transfer and pressure drop effect of hybrid nanofluids, the simulation was first validated to ensure its accuracy against experimental data. The simulation data shows an acceptable accuracy value which was in the range of 2.47 % 2.82 % as shown in Figure 2. The small deviation shows that the simulation was reliable and further analysis then can be carried out.

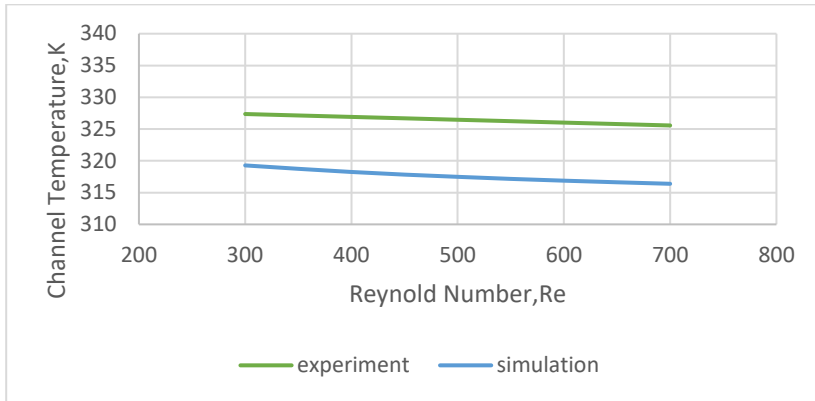


Figure 2: Base data validation.

Average channel temperature

When opposed to water as the base fluid, nanofluids also reduced total channel temperature. The highest improvement in the average channel temperature is given by the hybrid nanofluid with the ratio of 30:70 ($\text{Al}_2\text{O}_3\text{:SiO}_2$) with 2.57 % improvement as compared to base fluid of water as exhibited in Figure 3. This is followed by hybrid nanofluid of 10:90 ($\text{Al}_2\text{O}_3\text{:SiO}_2$), single nanofluid SiO_2 with the 0.276% lower compare to base fluid while the lowest average temperature is lower compared to the base fluid. This is due to the accumulation of nanoparticles in the fluids, which vastly enhance thermal conductivity while compared to the base fluid [22]. The use of two different nanoparticles in a fluid seeks to enhance thermal conductivity even more. This was proven by the improvement obtained in hybrid nanofluids with the ratio of 30:70 which has the lowest average channel temperature as compared to the rest of the fluids studied. The lower heat transfer in hybrid nanofluids is caused by the Brownian motion of both 13 nm Al_2O_3 and 30 nm SiO_2 nanoparticles [3]. The contact surface area of hybrid nanofluids has increased as a result of the smaller nano-sized particles, which has enhanced heat transfer. It was also discovered that as the number of Re grows, the average temperature of the channel decreases.

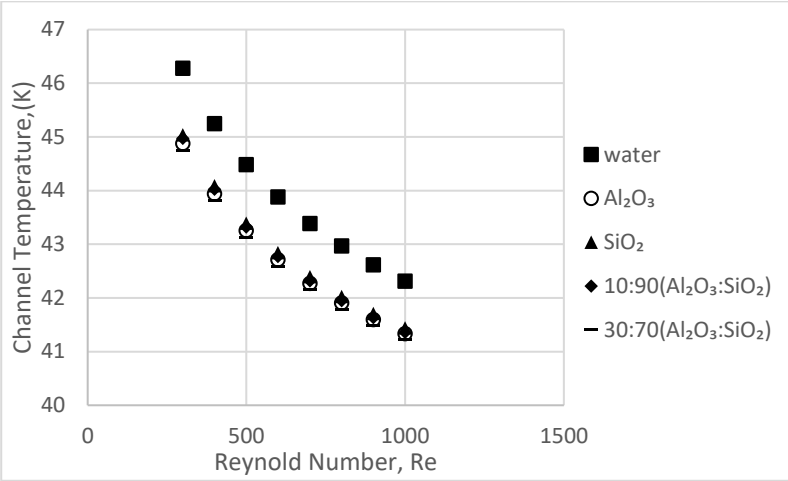


Figure 3: Average channel temperature with the adoption of nanofluids.

Heat transfer coefficient effect

The channel temperature was then converted to a heat transfer coefficient to determine a moving fluid's convective heat transfer ability. The higher convective heat transfer will give better heat transfer result. The highest heat transfer coefficient at Re 1000 is shown in Figure 4, was given by 0.5% of hybrid 30:70 Al_2O_3 : SiO_2 nanofluid with 9.851% higher than the base fluid. As the ratio of nanofluids changed and Reynold number increased for all hybrid Al_2O_3 : SiO_2 nanofluids, the heat transfer coefficient also increases. The addition of two nanofluids between Al_2O_3 and SiO_2 has enhanced thermophysical properties such thermal conductivity, specific heat capacity and others [6].

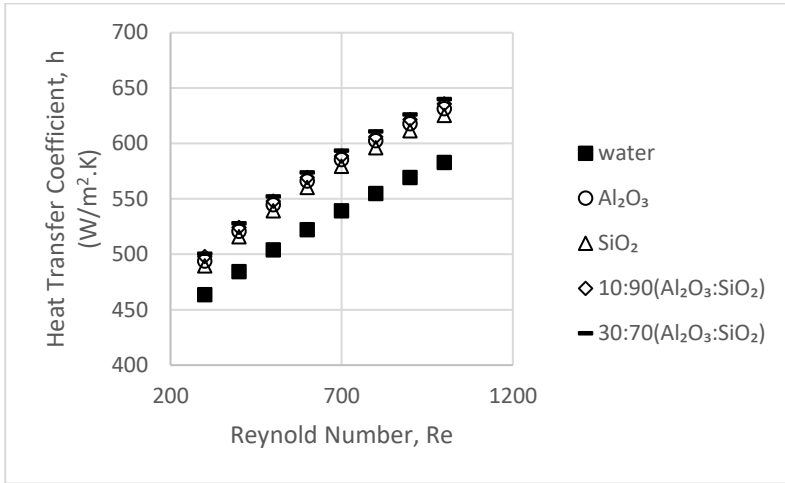


Figure 4: The graph of heat transfer coefficient against reynold number.

Nusselt number

Figure 5 indicates that as the Reynold number increases, the Nusselt number increased with it. To calculate the Nusselt number, convective heat transfer is necessary. There is a trend of lower Nusselt numbers for both hybrid nanofluids than single Al_2O_3 and SiO_2 nanofluids. This is because the hybrid nanofluids have lower thermal conductivity value compared to single Al_2O_3 and SiO_2 nanofluids. The highest Nusselt number for 0.5% concentration hybrid 10:90 $\text{Al}_2\text{O}_3:\text{SiO}_2$ nanofluids with 3.945% compared to the base fluid.

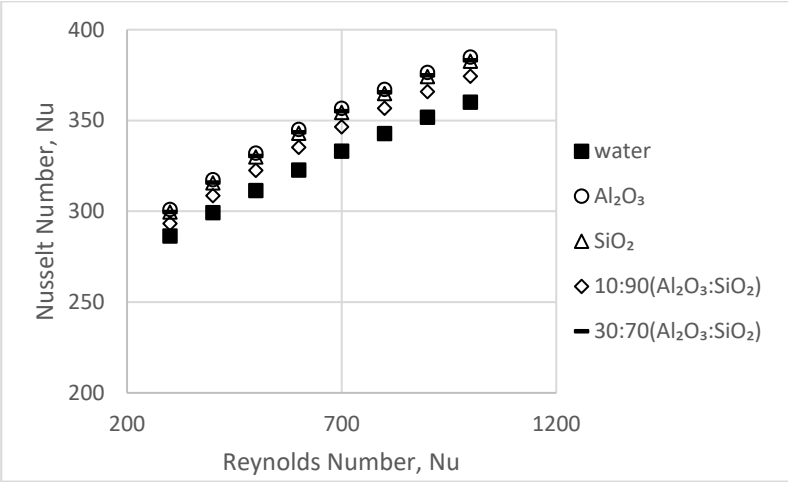


Figure 5: The graph of nusselt number against reynold number.

Pressure drop

The use of nanofluids in the channel, as seen in Figure 7, has an impact on the pumping power result. The pressure drop graph was plotted against the Reynold number is shown in Figure 6. The high-pressure will force the fluid to pass through the channel. The result of the pressure is as expected due to the need of fluid to flow in channel [13]. At a Re number of 1000, the highest pressure drop was measured at 0.5% Al₂O₃ with a 30:70 ratio, which was 26.468913 Pa higher than the base fluid. The single nanofluid of 0.5% concentration Al₂O₃ shown as the second highest pressure drop at Re number of 1000 which was 25.546417 Pa. The higher increment in pressure drop of hybrid nanofluid is shown compared to single nanofluids.

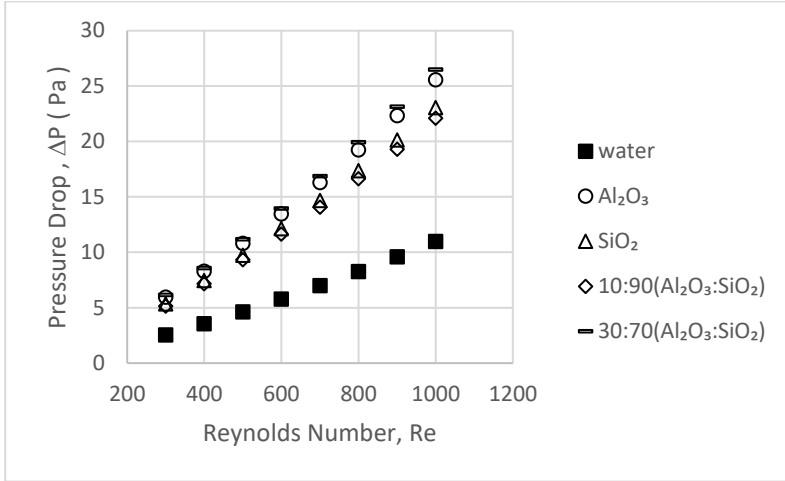


Figure 6: The graph of pressure drop against reynold number.

Pumping power

The higher pumping capacity is due to higher density and higher viscosity, resulting in a greater decrease in pressure [13]. As for single nanofluids, the pumping power was 0.5% concentration of Al₂O₃ at Reynold number of 1000 with w.564 times increment compared to the base fluid. Meanwhile, for hybrid nanofluid, the highest pumping power was 0.5% concentration Al₂O₃:SiO₂ with a ratio of 30:70 at Reynold number of 100 with 3.756 times increment compared to the base fluid. Figure 7 illustrates the use of nanofluids in the channel, which has an effect on the pumping power result.

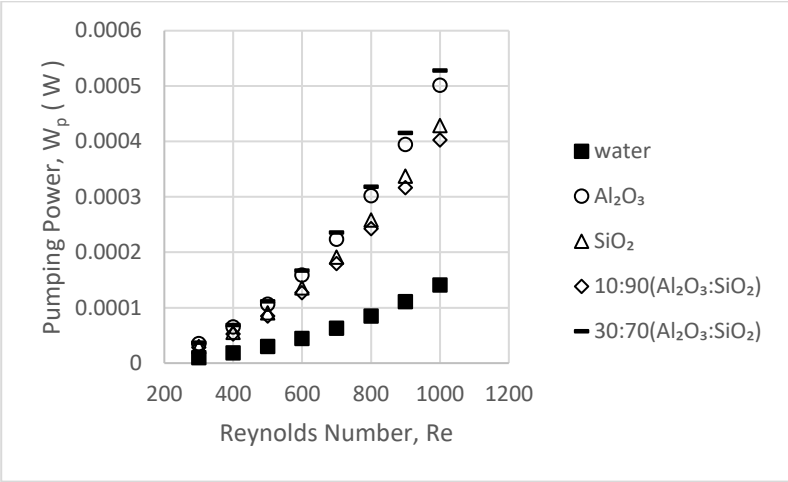


Figure 7: The graph of pumping power against reynold number.

Advantage ratio

The advantage ratio was calculated and shown in Figure 8 to ensure the feasibility of both single and hybrid nanofluid adoption in the channel of PEMFC. The advantage ratio was found to be highest at the lowest Reynold number for all coolants tested. This is due to decreased pressure encountered at a lower Reynold number, as opposed to the higher Reynold number. Compared with nanofluids, the base fluid was shown to have a higher advantage ratio. The advantage ratio for hybrid nanofluids used were greater than 1 at the whole Reynold number range from 300 to 1000. Azmi et al. claim that [7], for both improvements in the application of heat transfer and pressure drop factors, an advantage ratio greater than one should be conceivable.

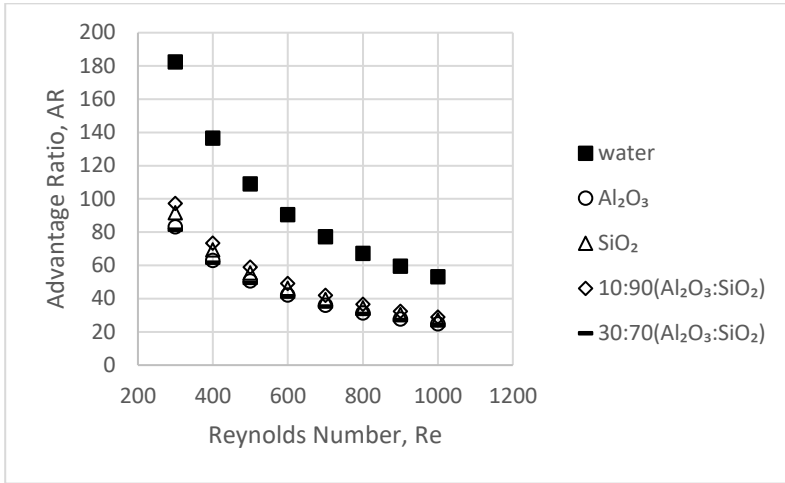


Figure 8: The graph of advantage ratio against Reynold number

Conclusion

The heat transfer and pressure drop characteristics of $\text{Al}_2\text{O}_3:\text{SiO}_2$ nanofluids in water were presented in this numerical analysis. The results showed there is an enhancement in all hybrid nanofluids compared to the base fluid. The improvement demonstrates this enhancement in terms of heat transfer coefficient and pressure drop. Since hybrid nanofluids in the channel undergo a higher pressure drop, the pumping capacity increases. Further correlation was then established which was termed the advantage ratio. This ratio, which includes both heat transfer enhancement parameters and increased pressure drop, justifies the viability of using hybrid nanofluids as a channel coolant. All hybrid nanofluids used in this study found advantageous adoption in PEMFC with advantage ratio values greater than 1 in all Reynold numbers.

Acknowledgement

This research was funded by a grant from Ministry of Higher Education of Malaysia 600-IRMI/FRGS 5/3 (375/2019).

References

- [1] H. Tamura and M. Matsumoto, "Fuel Cell Vehicles: Technology Development Status and Popularization Issues," *Converg. Int. Congr. Expo. Transp. Electron.*, no. 2002-21-0036, pp. 1-8, 2002.
- [2] M. Imazeki and T. Ushio, "Cooling system for fuel cell," *ed Google Patents*, 2004.
- [3] U. C. and T. Tran, "Experimental studies of the effects of non-Newtonian surfactant solutions on the performance of a shell-and-tube heat exchanger," in *American Society of Mechanical Engineers, Fluids Engineering Division (Publication)*, pp. 47-52, 1991
- [4] E. D. P. McMullen, S. Mohapatra, "Advances in PEM Fuel Cell Nano-Coolant," in *Fuel Cell Seminar & Energy Exposition*, pp. 344, 2013
- [5] S. Khalid, I. Zakaria, W. H. Azmi, and W. A. N. W. Mohamed, "Thermal-electrical-hydraulic properties of Al₂O₃-SiO₂ hybrid nanofluids for advanced PEM fuel cell thermal management," *J. Therm. Anal. Calorim.*, 2020.
- [6] M. R. Sohel, S. S. Khaleduzzaman, R. Saidur, A. Hepbasli, M. F. M. Sabri, and I. M. Mahbulul, "An experimental investigation of heat transfer enhancement of a minichannel heat sink using Al₂O₃-H₂O nanofluid," *Int. J. Heat Mass Transf.*, vol. 74, pp. 164-172, 2014.
- [7] H. Egawa, "Fuel Cell Coolant," US 8187763B2, May 29, 2012.
- [8] A. Abdollahi, H. A. Mohammed, S. M. Vanaki, A. Osia, and M. R. Golbahar Haghighi, "Fluid flow and heat transfer of nanofluids in microchannel heat sink with V-type inlet/outlet arrangement," *Alexandria Eng. J.*, vol. 56, no. 1, pp. 161-170, 2017.
- [9] R. Islam and B. Shabani, "Prediction of electrical conductivity of TiO₂ water and ethylene glycol-based nanofluids for cooling application in low temperature PEM fuel cells," *Energy Procedia*, vol. 160, no. 2018, pp. 550-557, 2019.
- [10] N. M. Muhammad, N. A. C. Sidik, A. Saat, and B. Abdullahi, "Effect of nanofluids on heat transfer and pressure drop characteristics of diverging-converging minichannel heat sink," *CFD Lett.*, vol. 11, no. 4, pp. 105-120, 2019.
- [11] I. Zakaria, W. H. Azmi, W. A. N. W. Mohamed, R. Mamat, and G. Najafi, "Experimental Investigation of Thermal Conductivity and Electrical Conductivity of Al₂O₃ Nanofluid in Water - Ethylene Glycol Mixture for Proton Exchange Membrane Fuel Cell Application," *Int. Commun. Heat Mass Transf.*, vol. 61, pp. 61-68, 2015.
- [12] I. Zakaria et al., "Thermal analysis of Al₂O₃-water ethylene glycol mixture nanofluid for single PEM fuel cell cooling plate: An experimental study," *Int. J. Hydrogen Energy*, vol. 41, no. 9, pp. 5096-5112, 2016.
- [13] I. A. Zakaria, W. A. N. W. Mohamed, A. M. I. Mamat, K. I. Sainan, and

- S. F. A. Talib, "Thermal performance of Al₂O₃ in water - Ethylene glycol nanofluid mixture as cooling medium in mini channel," *AIP Conf. Proc.*, vol. 1674, 2015.
- [14] I. Zakaria, W. A. N. W. Mohamed, W. H. Azmi, A. M. I. Mamat, R. Mamat, and W. R. W. Daud, "Thermo-electrical performance of PEM fuel cell using Al₂O₃ nanofluids," *Int. J. Heat Mass Transf.*, vol. 119, pp. 460–471, 2018.
- [15] I. A. Zakaria, W. A. N. W. Mohamed, M. B. Zailan, and W. H. Azmi, "Experimental analysis of SiO₂-Distilled water nanofluids in a Polymer Electrolyte Membrane fuel cell parallel channel cooling plate," *Int. J. Hydrogen Energy*, vol. 44, no. 47, pp. 25850–25862, 2019.
- [16] R. Islam, B. Shabani, J. Andrews, and G. Rosengarten, "Experimental investigation of using ZnO nanofluids as coolants in a PEM fuel cell," *Int. J. Hydrogen Energy*, vol. 42, no. 30, pp. 19272–19286, 2017.
- [17] W. A. N. W. Mohamed, S. F. A. Talib, I. A. Zakaria, A. M. I. Mamat, and W. R. W. Daud, "Effect of dynamic load on the temperature profiles and cooling response time of a proton exchange membrane fuel cell," *J. Energy Inst.*, vol. 91, no. 3, pp. 349–357, 2018.
- [18] A. I. Ramadhan, W. H. Azmi, R. Mamat, K. A. Hamid, and S. Norsakinah, "Investigation on stability of tri-hybrid nanofluids in water-ethylene glycol mixture," *IOP Conf. Ser. Mater. Sci. Eng.*, vol. 469, no. 1, 2019.
- [19] S. Salman, A. R. A. Talib, S. Saadon, and M. T. H. Sultan, "Hybrid nanofluid flow and heat transfer over backward and forward steps: A review," *Powder Technol.*, vol. 363, pp. 448–472, 2020.
- [20] M. F. Nabil, W. H. Azmi, K. A. Hamid, N. N. M. Zawawi, G. Priyandoko, and R. Mamat, "Thermo-physical properties of hybrid nanofluids and hybrid nanolubricants: A comprehensive review on performance," *Int. Commun. Heat Mass Transf.*, vol. 83, pp. 30–39, 2017.
- [21] I. A. Zakaria, W. A. N. W. Mohamed, A. M. I. Mamat, K. I. Sainan, M. R. M. Nawi, and G. H. Najafi, "Numerical analysis of Al₂O₃ nanofluids in serpentine cooling plate of PEM fuel cell," *J. Mech. Eng.*, vol. 5, no. Special issue1, pp. 1–13, 2018.
- [22] K. S. Arjun and K. Rakesh, "Heat transfer enhancement using alumina nanofluid in circular micro channel," *J. Eng. Sci. Technol.*, vol. 12, no. 1, pp. 265–279, 2017.

Optimization of Machining Parameters using Taguchi Coupled Grey Relational Approach while Turning Inconel 625

Chinmaya Padhy*, Pariniti Singh

Center for Manufacturing Excellence, Dept. of Mechanical Engineering,
School of Technology, GITAM University,
Hyderabad, 502329, India.
*padhy.gitam@gmail.com

ABSTRACT

In manufacturing industries preparation of quality surfaces is very important. The surface roughness will influence the quality and effectiveness of the subsequent coatings for protection against corrosion, wear resistance etc. For achieving desired surface roughness, factors like cutting force (N) and material removal rate (mm^3/sec) plays an important role towards final product optimization. This study helps to determine the contribution of each machining parameters [cutting speed (v), feed rate (f) and depth-of-cut (d)] and their interaction to investigate their optimum values during dry turning of Inconel 625 with the objective of enhancing the productivity (optimum production) by minimizing surface roughness (R_a), cutting forces (F_c), whereas maximizing material removal rate (MRR). This kind of multi response process variable (MRP) problems usually known as multi-objective optimizations (MOOs) are resolved with the help of Taguchi and Grey relation approach (T-GRA). As a result, the attained optimum cutting parameters are viz. cutting speed (60 m/min), feed rate (0.3 mm/rev), depth-of-cut (0.25 mm) lead to value of desired variables - cutting forces (340 N), surface roughness (0.998 μm) and material removal rate (0.786 mm^3/min).

Keywords: Cutting force; Cutting parameters; Dry turning; Material removal rate; Minitab 17; Optimization; Surface roughness

Introduction

The level of roughness on surface finishing has an important role in the efficiency and quality of succeeding surface coatings for any material [1]. Among various existing methods to prepare the metal surfaces, the machining is the one of the most used and allow low levels of surface roughness [2], which can be achieved values like approx. to 50 nm for optical applications [3]. However, the economic factors have a strong demand in today's machining processes shouting a higher productivity, flexibility of the production systems, reduction of costs and obtaining manufactured parts with better surface and dimensional quality [4].

Productivity of a manufacturing operation is significantly contingent on set of input machining parameters. Hence, optimization of cutting parameters relates to optimizing the input factors which leads to improved machining performances. In this regard, optimization techniques offer new prospects in achieving better optimization solutions for manufacturing problems by helping to arrive at optimal set of input machining parameters which in turn result in enhancing the productivity of machining operation.

Turning is a versatile machining operation in industries and requires suitable selection of required set of cutting parameters for improved productivity. There are many statistical models which show the relationship between input factors like cutting parameters and output responses-performance parameters [5]. But for analysis of above relationship requires number of experimental trials. Further, machining with inappropriate machining parameters adds to low productivity and low machining performance [6]-[8]. So, to reduce this monotonous task and find appropriate machining parameters, the current study employed design of experiments (D-O-E) technique using *T-GRA* to combine the multi response variables into a single output in terms of ranks and delineates the optimal machining parameters. Many researchers in the recent past have done ample of work for optimizing the process machining parameters with aim of attaining improved performance response variables for different metals and alloys. For example, Shrikant and Chandra [9] investigated the optimization of machining parameters using Taguchi based L9 Orthogonal array method for turning of Inconel 781. The process parameters for the design of experimental were speed (s), feed (f) and temperature (T). The response variables - MRR and surface roughness were analysed for good surface machining quality with low tool wear. In another study Satyanarayana et al. [10] presented an optimum process for high speed dry turning of Nickle alloy (Inconel 718) with parameters (speed, feed and depth of cut) to minimize the machining force, surface roughness and tool flank wear using Taguchi-Grey relational analysis. The optimal process parameters were achieved (60 m/min for speed, 0.05 mm/rev for feed and 0.2 mm for depth of cut) from the selected range of L9 orthogonal

array. Parthiban et al. [11] employed Taguchi grey relational analysis for estimating the impact of turning Inconel 713C alloy with different tools (WC-Co tool and cryogenically treated and oil-quenched WC-Co tools). The analysis was performed with L27 orthogonal array with operating parameters (cutting speed, feed rate, and depth of cut) for recognizing the components influencing surface roughness. The Taguchi-GRA combinatorial approach were also applied for various machining operations viz. milling, grinding, drilling and turning to evaluate multi-objective optimization machining parameters [12]-[15]. Here, from the past literatures its very well illustrated that the Taguchi-Grey technique has emerged out as a successful optimization technique to solve various machining problems. The use of Taguchi Grey optimization technique is mostly done as multi optimization technique for turning of many materials works pieces but there are very few studies with hard material machining parameter optimization such as Inconel 625. Also, this optimization is mostly performed with response variables surface roughness and Material removal rate. Whereas in this study an additional performance factor is taken which is cutting force and is an essential criteria in deciding process parameters in machining. With this notion this study aims to investigate the optimum values of machining parameters required namely – cutting speed (v), feed rate (f) and depth-of-cut (d) during dry turning of Inconel 625 with the objective of enhancing the productivity by minimizing surface roughness (R_a), cutting forces (F_c), whereas maximizing material removal rate (MRR).

This work aims at finding the optimal cutting parameters in dry machining of Inconel 625 (Ni based alloy), with Taguchi-Grey relational analysis(T-GRA). Inconel 625 has its varied application in marine, aerospace, space, nuclear and manufacturing industries with high-temperature applications [16-17]. Taguchi design was used for designing trial steps and further, grey relation was done to combine multi response outcomes into a single response. The experimental outcomes were studied to achieve optimal cutting force (F_c), surface roughness (R_a) and material removal rate (MRR).

Experimental Approach

Materials and method

Inconel 625 with properties like high temperature mechanical strength and improved resistance to corrosion make its application viable in aerospace and marine sector. Inconel 625 with work hardening property is hard to machine and generates high machining temperature during machining. Table 1 shows the chemical composition details and Table 2 gives the details of physical properties of Inconel 625. Figure 1(a) shows the schematic experimental layout of the dry turning performed. For the equipment used for measuring the desired

output variables, i.e. measuring material removal rate (MRR)- weight scale device is used, refer Figure 1(b). For measuring surface roughness-Mitutoyo surface roughness tester is used, refer Figure 2(a) and for measurement of cutting forces-lathe tool dynamometer is used, refer Figure 2(b).

Table 1: Chemical Composition (wt %) of Inconel 625 [18]

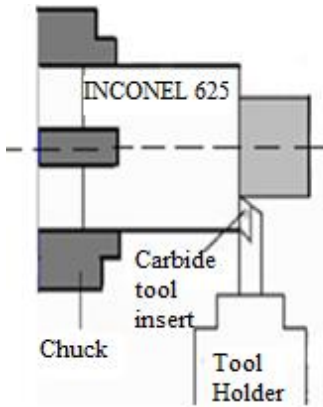
C	Mn	S	Si	Cr	Fe	Mo	Co-Ta	Ti	Al	P	Ni
.05	.30	.003	.25	20-23	4	9	3.5	.30	.30	.15	Balance

Table 2: Physical Properties of Inconel 625 [18]

Alloy	Density	Melting Point	Tensile Strength	Brinell Hardness
Inconel 625	8.4 g/cm ³	1290 – 1350 OC	760 N/mm ²	240 HB

The experiment was conducted on Inconel 625 work piece of dimensions [diameter (\varnothing)-40 mm, length (L)-350 mm], purchased from Mishra Dhatu Nigam Ltd., on NAGMATI 175 model lathe with maximum cutting speed 1200 rpm, 3HP motor, along with Korloy insert -model: PC9030 carbide tool inserts, designation: CCMT09T308.

The study optimizes the machining parameters- speed (v), feed (f) and depth-of-cut (d) with T-GRA. Each parameter has three levels – namely low, medium and high, respectively. According to the Taguchi method, if three parameters and 3 levels for each parameters L9 orthogonal array should be employed for the experimentation. The optimization parameters are designed for maximizing MRR and for minimizing the surface roughness and cutting forces. Figure 3 shows procedural steps used to follow for T-GRA [19]. The selected levels of machining parameters and attained experimental test results for corresponding set of arrays are tabulated in Table 3 and Table 4 respectively.



(a)



(b)

Figure 1: (a) Schematic experimental layout for dry turning, (b) weighing machine used for measurement of material removal rate.



(a)



(b)

Figure 2: (a) Surface roughness test meter (b) dynamometer used for measurement of cutting forces.

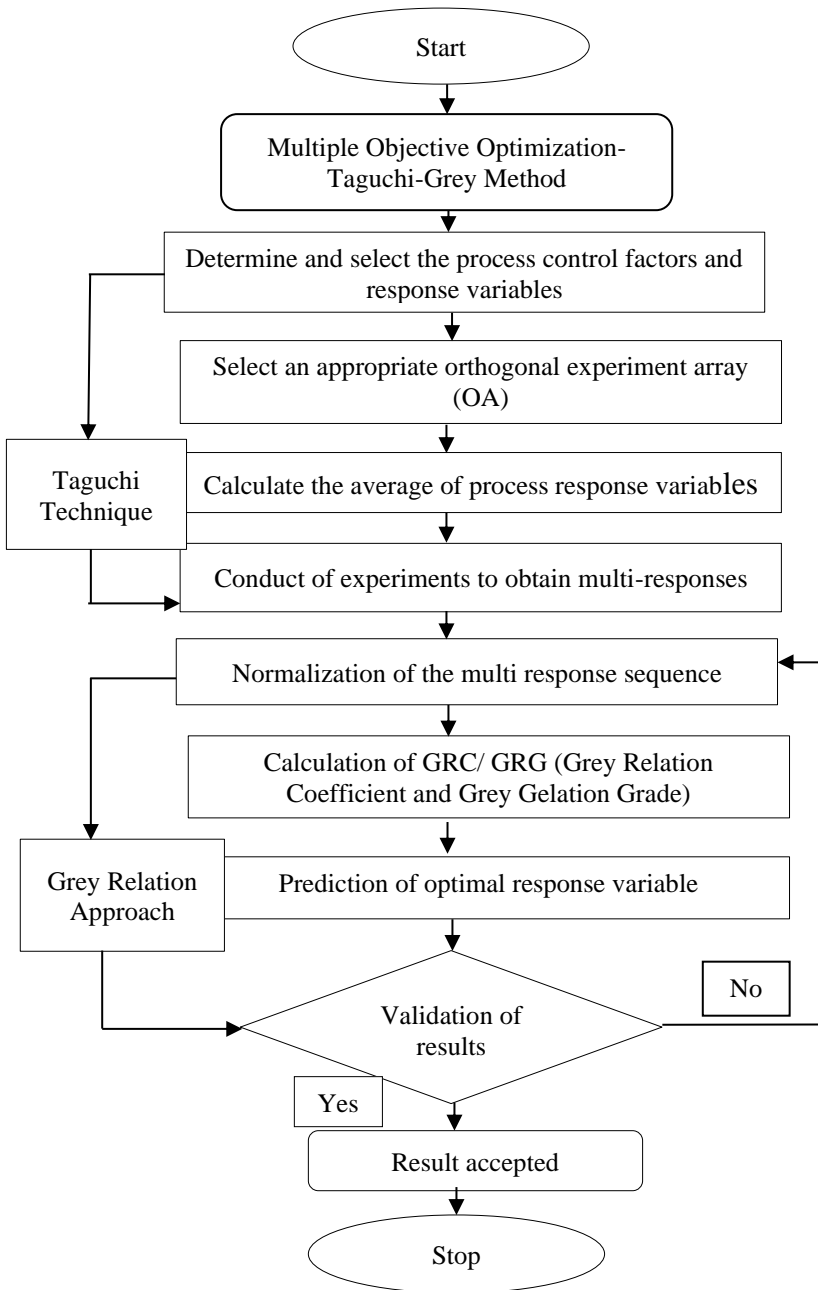


Figure 3: Flow chart of Taguchi-Grey relation method [19].

Table 3: Input parameters with Taguchi design

Machining Parameters	Levels of Parameters		
	1 (low)	2 (medium)	3 (high)
Cutting speed (v) m/min	42	60	108
Feed rate (f) mm/rev	0.1	0.2	0.3
Depth-of-cut (d) mm	0.25	0.5	0.75

Evaluation of optimal cutting parameters

Taguchi and Grey relational analysis (T-GRA)

Taguchi design of experiments is a process of optimization which deals with eight steps of planning, conducting and evaluating matrix experiments to determine the best level of control factors. Whereas, Taguchi robust design finds the appropriate control factor levels to give a robust experimental design approach. There are many factors which affect the performance parameters among which few can be controlled and are called control factors and rest are impossible control and are called “noise factors”. This experimental approach leads to the development of designs with enhanced quality and shorter design and cost. They allow to understand and provide the interaction of factors affecting the output parameters. Taguchi analysis uses orthogonal array (OA) of experiments that give set of appropriate number of experimental trials. Taguchi design gives well defined standard orthogonal arrays which are made for a precise level of independent designs. These orthogonal arrays reduce the number of trial experiments. In current study the machining parameters- speed (v), feed (f) and depth-of-cut (d), each parameter has three levels – namely low, medium and high, respectively. According to the Taguchi method, if three parameters and 3 levels for each parameters L9 orthogonal array should be employed for the experimentation. Further, on coupling with Grey relation a multi response optimization gets converted into a single response optimizing problem. S/N (signal to noise ratio) for each machining parameter level is evaluated for each performance function and the highest S/N ratio indicates an optimal level of machining. Multi response is associated with more than one performance criteria/responses (surface roughness, material removal rate, tool wear, cutting forces) simultaneously. These responses follow either larger the better equations such as for material removal rate, or for some characteristics are required to be less and are followed as smaller the better. Figure 4 shows detailed experimental stages for T-GRA used during this study [20].

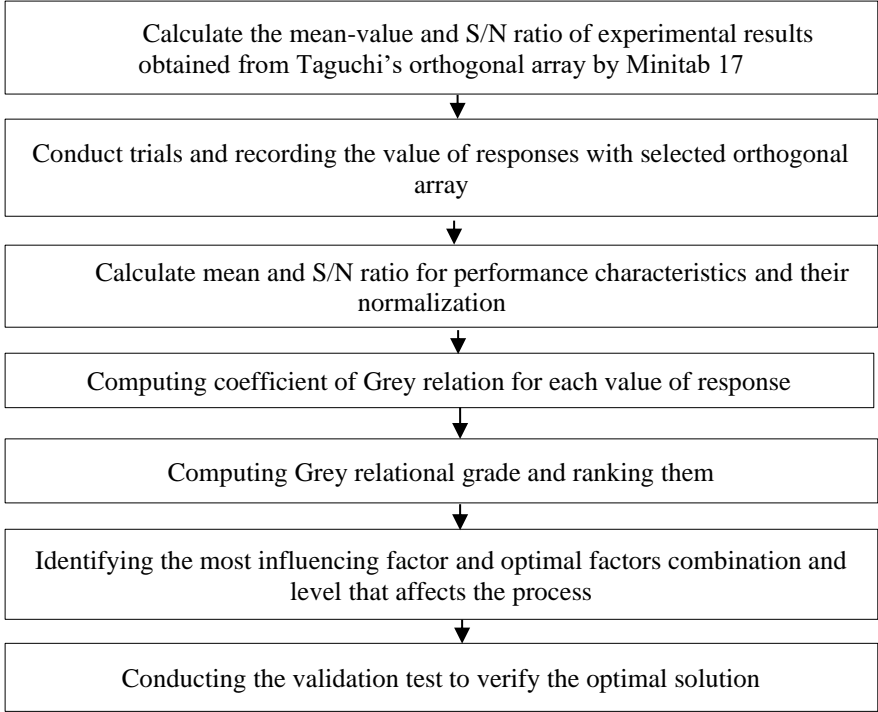


Figure 4: Steps for grey relational approach used in this study [20].

For evaluating optimal solution by grey relational, S/N ratio – signal (mean) to noise (standard deviation) ratio is considered as performance parameter to measure deviation from the desired results. For reducing noise or the effects of uncontrolled parameters, higher S/N ratios values are ideal [21]. For present study, initially the experimental outputs (cutting force, surface roughness, material removal rate) were normalized i.e., converted from random data to comparable form and then from attained normalized readings the grey relational coefficient was obtained. The linear normalized ratio has its value between zero and one, known as grey relational generation [22]. To improve a machining it is essential that the cutting force and surface roughness values are low i.e., “smaller the- better” (SB) whereas, material removal rate should be high, “larger-the-better” (LB), the grey model was evaluated by using Equation (1) and Equation (2) respectively [10].

$$\frac{S}{N} = -10 \log \frac{1}{n} \left(\sum_{i=1}^n 1/y_{ij}^2 \right) \quad (1)$$

$$\frac{s}{N} = -10 \log \frac{1}{n} (\sum_{i=1}^n y_{ij}^2) \quad (2)$$

where, y_{ij} is recorded experimental, n is the trial number. Next the Grey Relational Coefficient (GRC) is calculated from Equation (3) [10],

$$\gamma(x_0(k), x_i(k)) = \frac{(\Delta_{min} + \xi \Delta_{max})}{(\Delta_{oi} k + \xi \Delta_{max})} \quad (3)$$

where, Δ_{min} - lowest value of $\Delta_{oi}(k)$

Δ_{max} - corresponds to the highest value of $\Delta_{oi}(k)$.

The ζ which lies in between zero to one is the distinguishing coefficient [23], and is taken as 0.5 for the current study to give equal weight to the responses. Further GRG- grey relational grade (γ) is calculated which is the mean of total grey relational coefficients refer Equation (4) [17]. For present experiment the maximum value of grey relation grade corresponding to trial 6 with input parameters cutting speed (v) as 60 m/min, feed (f) as 0.3 mm/rev and depth-of-cut (d) as 0.25 mm respectively (refer Table 6). The overall GRG is represented graphically in Figure 8.

$$\gamma(x_0, x_i) = \frac{1}{m} \gamma(x_0(k), x_i(k)) \quad (4)$$

Result and Discussion

For analyzing effects of input machining parameters on response variables during machining Taguchi L9 orthogonal array was designed refer Table 4. Table 5 shows S/N ratio with its corresponding normalized S/N ratio for response variables- cutting force, surface roughness and material removal rate respectively. Figure 5, 6 and 7 (achieved by Minitab 17 software) show the output characteristics (mean S/N) of response variables. From attained mean values grey scale coefficient and then grey relational grade was calculated. From the GRG, the rank of each set of trial is assigned (refer Table 6). The maximum value of GRG shows the set of parameters for optimal condition. Hence, maximum value of GRG (.742) is assigned as rank 1 in series for set of input parameters.

Table 4: Taguchi 'L9' array with corresponding response variables

Trial No.	Input Machining Parameters			Average Response Values		
	Cutting Speed (m/min)	Feed Rate (mm/rev)	Depth-of-Cut (mm)	Cutting Forces (N) as (SB)	Surface Roughness (μm) as (SB)	Material Removal Rate (mm^3/min) as (LB)
1	42	0.1	0.25	230	1.63	0.126
2	42	0.2	0.5	195	1.25	0.252
3	42	0.3	0.75	300	1.13	0.270
4	60	0.1	0.5	240	1.01	0.380
5	60	0.2	0.75	220	0.663	0.712
6	60	0.3	0.25	340	0.998	0.786
7	108	0.1	0.75	215	1.255	0.860
8	108	0.2	0.25	265	0.865	0.918
9	108	0.3	0.5	235	0.834	1.14

Table 5: The S/N ratio for the set of experimental results

Machining Parameters(Speed (m/min)/Feed (mm/rev)/Depth of Cut(mm))	S/N ratio for Cutting Force	S/N ratio for Surface Roughness	S/N ratio for Material Removal Rate
42/.1/.25	-47.2	-4.24	-17.9
42/.2/.5	-45.8	-1.93	-11.9
42/.3/.75	-49.54	-1.06	-11.3
60/.1/.5	-47.6	-0.08	-8.4
60/.2/.75	-46.8	3.6	-2.9
60/.3/.25	-50.6	0.01	-2.09
108/.1/.75	-46.6	-1.97	-1.3
108/.2/.25	-48.4	1.25	-0.74
108/.3/.5	-49.0	1.57	-1.13

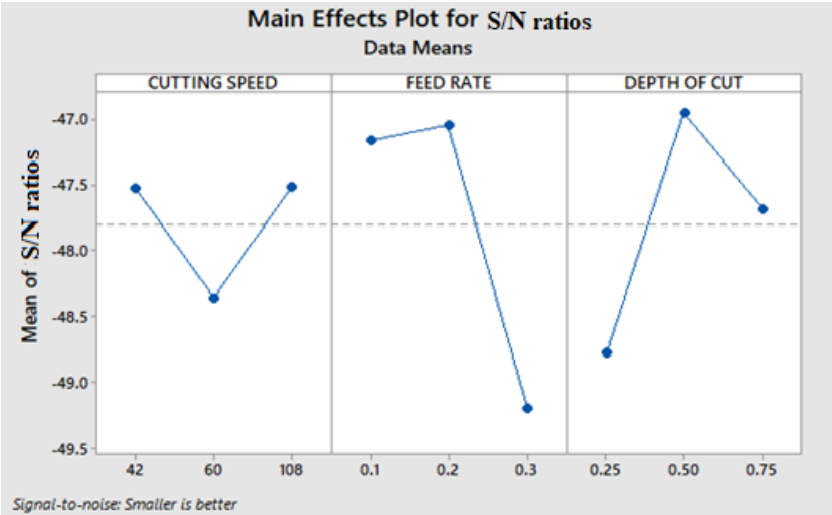


Figure 5: Plot for mean S/N ratios for cutting force.

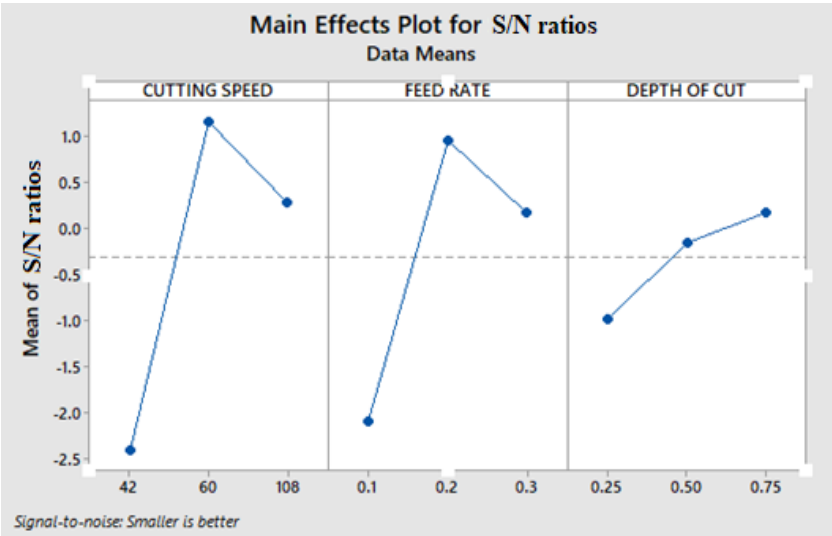


Figure 6: Plot for mean S/N ratios for surface roughness.

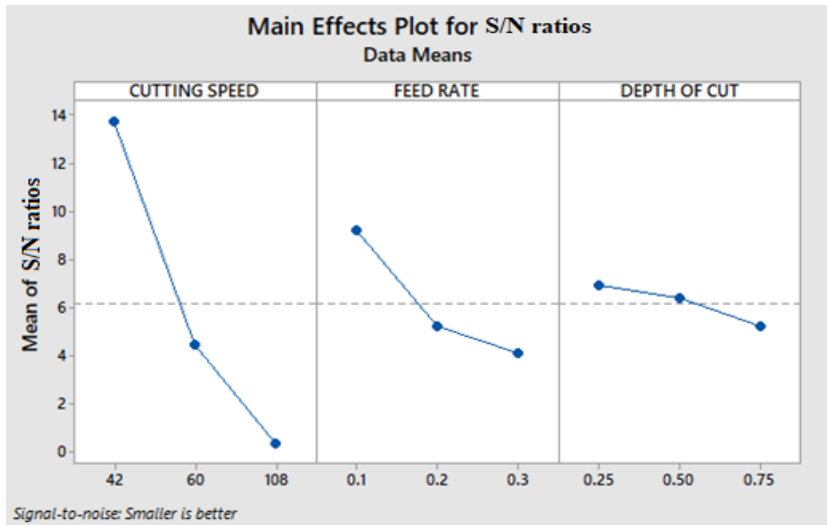
Figure 7: Plot for mean S/N ratios for material removal.

Table 6: Grey relational coefficients (GRC) and grade (GRG)

Machining Parameters(Speed (m/min)/Feed (mm/rev)/Depth of Cut (mm))	GRC Cutting Forces	GRC Surface Roughness	GRC Material Removal Rate	Grey Relational Grade (GRG)	Rank
42/.1/.25	0.413	1.00	0.332	0.581	5
42/.2/.5	0.333	0.476	0.436	0.415	9
42/.3/.75	0.694	0.398	0.450	0.514	7
60/.1/.5	0.444	0.335	0.539	0.439	8
60/.2/.75	0.387	0.766	0.822	0.658	3
60/.3/.25	1.00	0.33	0.897	0.742	1
108/.1/.75	0.377	0.480	0.833	0.563	6
108/.2/.25	0.528	0.445	0.956	0.602	4
108/.3/.5	0.606	0.440	1	0.682	2

Figure 10 shows graphical representation between number of experimental trials and corresponding highest grey relation grade (.742). The parameters from experiment no. 6 with cutting speed (v) of 60 m/min, feed rate (f) of 0.3 mm/rev and depth-of-cut (d) of 0.25 mm were the attained optimal

input machining parameters. Similar approach was used by Parthiban et al. [11], Vasudevan et al. [24], Pedkarand and Karidkar [25], Pawade and Joshi [26] and obtained results with their study were found to be in good agreement with experimental results attained in this study.

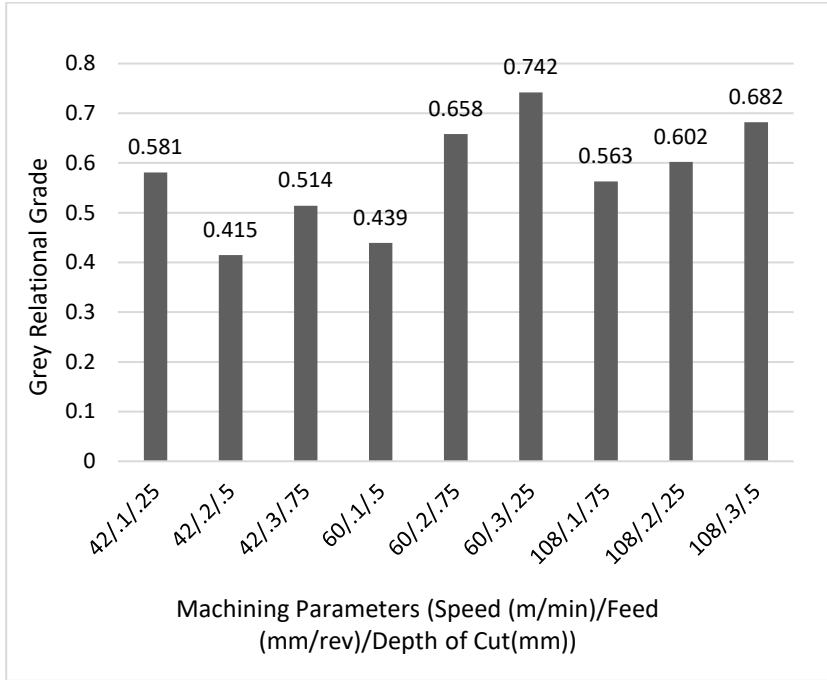


Figure 8: Grey relational grade for corresponding set of input parameters.

Conclusion

This study successfully investigates the dry turning of Inconel 625, a multi response process parameters problem, with the use of Taguchi - Grey relational approach (T-GRA) for identifying the set of optimal machining parameters. The T-GRA approach combines the design of orthogonal array for design of experiments with grey relational analysis. Grey relational theory is aims to determine the optimal process parameters that give low magnitude of cutting forces as well as surface roughness but larger amount of material removal rate. The response table and the grey relational grade graph for each level of the machining parameters have been established in order to minimize - cutting forces (F_c) and surface roughness (R_a) along with the maximizing of material

removal rate (MRR). Grey relation analysis is applied to the results obtained from Taguchi technique for establishing process parameters which provide optimal solution between the multi performance responses. Based on the experimental analysis, the results obtained for optimal machining conditions were found out viz. (i) cutting speed (v) as 60 m/min, (ii) feed (f) as 0.3 mm/rev and (iii) depth-of-cut (d) as 0.25 mm respectively. Hence, this study concludes that turning with these set of combinations maximizes the performance of response variables (F_c , R_a , MRR), ultimately which increases the overall machining efficiency (machinability) of Inconel 625. The machining parameters obtained can be used further for analyzing the machining performances (with different lubricating environment) at this optimal machining conditions, which can be extended for surface engineering study of Inconel 625.

References

- [1] T. Thomas, 2014. "Roughness and function. Surface Topography", *Metrology and Properties*, vol. 2, 014001
- [2] P. Benardos, G. Vosniakos, "Predicting surface roughness in machining: a review", *International Journal of Machine Tools and Manufacture*, vol. 43, pp. 833-844, 2003.
- [3] K. Guenther, P. Wierer, J. Bennett, "Surface roughness measurements of low-scatter mirrors and roughness standards" *Applied Optics*, vol. 23, pp. 3820–3836, 1984.
- [4] G. Besseris, "Product Screening to Multicustomer Preferences: Multiresponse Unreplicated Nested Super-ranking", *International Journal of Quality, Statistics, and Reliability*, pp. 1-16, 2008.
- [5] D. P. Selvaraj, "Optimization of cutting force of duplex stainless steel in dry milling operation", *Materials Today: Proceedings*, vol. 4, no. 10, pp. 11141–11147, 2017.
- [6] Julie Z. Zhang, Joseph C. Chen, E. Daniel Kirby, "Surface roughness optimization in an end-milling operation using the Taguchi design method", *Journal of Materials Processing Technology*, vol. 184, pp. 233-239, 2007.
- [7] Muammer Nalbant, Abdullah Altin, Hasan Gokkaya, "The effect of coating material and geometry of cutting tool and cutting speed on machinability properties of Inconel 718 super alloys", *Materials and Design*, vol. 28, pp. 1719-1724, 2007.
- [8] S.M. Darwish, "The impact of tool material and cutting parameters on surface roughness of supermet 718 nickel super alloy, s", *Journal of Materials Processing Technology*, 97, pp 10-18, 2000.
- [9] V. Srikanth, M. K. Chandra, "Parametric Optimization of Inconel 718

- With Carbide Inserts in Turning Using Taguchi L-9 Orthogonal Array Method”, *COJ Tech Sci Res*, vol. 1, no. 4, COJTS.000521, 2019.
- [10] Satyanarayana, B. Janardhana, G. Ranga Rao, D. Hanumantha, “Optimized high speed turning on Inconel 718 using Taguchi method based Grey relational analysis”, *IJEM*, vol. 20, no. 4, pp. 269-275, 2013.
- [11] V. Parthiban, S. Vijayakumar, M. Sakthivel, “Optimization of high- speed turning parameters for inconel 713C based on Taguchi grey relational analysis (TGRA)”, *Transactions of the Canadian Society for Mechanical Engineering*, vol. 43, no. 3, pp. 0221, 2019.
- [12] E. Kuram, B. Ozcelik, “Multi-objective optimization using Taguchi based grey relational analysis for micro-milling of Al 7075 material with ball nose end mill”, *Measurement*, vol. 46, pp. 1849–1864, 2013.
- [13] M. Kurt, S. Hartomac, B. Mutlu, U. Köklü, “Minimization of the Surface Roughness and Form Error on the Milling of Free-Form Surfaces using a Grey Relational Analysis”, *Mater. Technol*, vol.46, pp. 205–213, 2012.
- [14] S.J. Raykar, D.M.D. Addona, A.M. Mane, “Multi-objective optimization of high speed turning of Al 7075 using grey relational analysis”, *Procedia CIRP*, vol. 33, pp. 293–298, 2015.
- [15] S. Pariniti P, Chinmaya “Influence of nano (h-BN) cutting fluid on machinability of Inconel 625”, *Jour. of physics: conf. series*, vol. 1355, (012033), pp. 1-7, 2019.
- [16] A.N., Siddiquee, Z.A. Khan, Z. Mallick, “Grey relational analysis coupled with principal component analysis for optimization design of the process parameters in in-feed centerless cylindrical grinding”, *Int. J. Adv. Manuf. Technol*, vol. 46, pp. 983–992, 2010.
- [17] I.A. Choudhury, M.A. El-Baradie, “Machinability of nickel-base super alloys: a general review”, *Journal of Materials Processing Technology*, vol. 77, pp. 278-284, 1998.
- [18] C. V. Yıldırım, T. Kivak. M. Sarıkaya, S. Sirin, “Evaluation of tool wear, surface roughness/topography and chip morphology when machining of Ni-based alloy 625 under MQL, cryogenic cooling and CryoMQL”. *Journal of Materials Research and Technology*, vol. 9, no. 2, p. 2079–2092, 2020.
- [19] M. Mathew, P. K. Rajendrakumar, “Optimization of process parameters of boro-carburized low carbon steel for tensile strength by Taguchi method with grey relational analysis”, *Materials & Design*, vol. 32, no. 6, pp 3637–3644, 2011.
- [20] R.S. Pawade, S.B. Bhosele, “Grey Relation Parameter Optimization in ultrasonic machining of ceramic composite ($\text{Al}_2\text{O}_3/\text{ZrO}_2$)”, *Journal of the Association of Engineers*, vol. 83, no. 2, pp. 63-77, 2013.
- [21] F. Puh, Z. Jurkovic, M. Perinic, M. Brezocnik, S. Buljan, “Optimization of machining parameters for turning operation with multiple quality characteristics using Grey relational analysis”, *Tehnički vjesnik*, vol. 23,

- no. 2, pp. 377-382, 2016.
- [22] Nihat Tosun, "Determination of optimum parameters for multi-performance characteristics in drilling by using grey relational analysis", *International Journal of Advanced manufacturing Technology*, vol. 28, pp. 450-455, 2006.
- [23] K.W. Ng David, "Grey system and grey relational model", *ACM SIGICE Bulletin*, vol. 20, no. 2, pp.1-9,1994.
- [24] H. Vasudevan, R. Rajguru, M. Shaikh, & A. Shaikh, "Optimization of Process Parameters in the Turning Operation of Inconel 625". *Materials Science Forum*, vol. 969, pp. 756-761, 2019.
- [25] Pooja Petkar, S. S. Karidkar, "Optimization of Machining Parameters for Turning on CNC Machine of Inconel-718 alloy", *International Journal of Engineerig Research and Technology*, vol. 08, pp. 06, 2019.
- [26] Pawade, R. S., & Joshi, S. S., "Multi-objective optimization of surface roughness and cutting forces in high-speed turning of Inconel 718 using Taguchi grey relational analysis (TGRA)", *The International Journal of Advanced Manufacturing Technology*, vol. 56, pp. 47-62, 2011.

Effect of Fiber Misalignment on Mechanical and Failure Response of Kenaf Composite under Compressive Loading

M. F. Razali, S.A.H.A. Seman*, T. W. Theng
School of Mechanical Engineering, Engineering Campus,
Universiti Sains Malaysia,
14300 Nibong Tebal, Pulau Pinang, Malaysia
*sarehaiman@usm.my

ABSTRACT

The use of kenaf fibres has grown unexpectedly in the world as they help to establish green materials in automobile, sports and food packaging industries. Over the past few decades, unidirectional fiber-reinforced composites have been extensively used in industry due to their high specific strength characteristics. During manufacturing process, several defects especially fiber misalignment might exist in the unidirectional composite structure. This kind of deviation from its optimal parallel packing in a unidirectional fibre reinforced composite would influence its overall load-bearing efficiency. Performance data of kenaf composite due to this imperfection, however, is very limited in the literature. In this regard, the effects of fibre misalignments on the unidirectional kenaf composite compressive reaction have been studied. For this reason, pultruded kenaf composite specimens with different fibre alignment from 0^0 to 2^0 at 2.1 and 8.4 mm/s strain rates were subjected to a range of compression measures. The findings revealed that, the failure strain seems to be almost constant at value of 0.05 and 0.063 while the failure stress decreases from 140Mpa until 120MP when the fibre alignment increases when loaded within a range of $2.1\sim 8.4s^{-1}$. Additionally, under increased fiber misalignment and strain rate, fibre plastic microbuckling, fibre breakage, fibre splitting and fibre matrix debonding was progressively formed on the specimen.

Keywords: Kenaf composite; Fiber misalignment; Damage behavior

Introduction

The researchers have been especially interested in kenaf fibre composite in recent years and are becoming popular in a variety of applications including construction [1, 2], sports and the car industry [3, 4] due to its overall results, recyclability and sustainable properties [5]. More recently, the rising need for light-weight vehicles that meet strict fuel economy and safety criteria has encouraged the application in the automotive industry of the kenaf composite [6]. Low manufacturing costs and rapid production processes, resulting in small angle fibre misalignments within any structure, are important to compete in this industry [7, 8]. Worse still, it may be the greatest hurdle in this industry for kenaf composite widespread use.

In unidirectional (UD) high-performance composites, misaligned fibres are inevitably present. The fibre misalignment in UD composite is used to express the deviation of the fibres, which is not totally in parallel. This production-related imperfection [9] would control the mechanism of compressive failure, as it was loaded, called the localised plastic microbuckling [10] which is generally accepted as the dominant failure mode in UD fiber composite [11].

Composite material should have no flaws in order to serve the particular application well, especially fibre misalignment that govern during the production process, as it affects the structure's overall performance [12, 13]. The mechanical properties of the carbon fiber composite laminates with fibre misalignment angles of 0 to 40° in single ply samples and of 0 to 90° in one ply for two-ply samples have been investigated by Yang et al. [14]. They have observed that fibre misalignment noticeably reduces strength and elastic modulus of the carbon fiber composite.

Werken et al. [15] has also studied the fibre-alignment effects on the mechanical properties of recycled carbon fibre composites. The degree of alignment has been shown to have the most important effect on the composite strength and elastic modulus. The aligned composite showed an improvement of 100% and 137% in normalised tensile strength and module of recycled carbon fibre composites.

Several finite element analyses (FEA) have also been conducted to understand the effect of fiber misalignment on composite performance. For example, carbon fibres composite, although the angles of 0.25° were small, were predicted to decrease from 2720 MPa to 1850 MPa as reported by Wisnom [16]. Song et al. [17] performed a comparison between experiments and the FEA to study the influence of the original fibre alignment on the mechanical characteristics of GMT composites. The findings demonstrate that the initial orientation of the fibres in the first GMT sheets plays an important role on the finished part's structural properties.

In addition, the presence of fiber misalignment on composite material may lead to some damage such as fiber breakage and fiber-matrix debonding when loaded [18]. Hillig [19] stated that high-fibre misalignment regions of glass fibre composite can serve as nucleation points for instability-failure processes, for example buckling and shear-induced delamination. To date, there are only a few researches on the effects of fibre misalignment on kenaf composite. Static compression tests for kenaf composite material were therefore conducted to detect the effect of fiber misalignment on mechanical properties, in particular on failure stress and failure strain as well as subsequent damages.

Methodology

Specimen preparation

The pultruded kenaf composites with 60% fiber volume fraction used in this study were made of kenaf fiber with tex number 2200 and unsaturated polyester that were produced through pultrusion process with a diameter of 14 mm. Kenaf composite with a combination of 60% fiber volume fraction and tex number 2200 has been chosen as it has a good compressive strength as reported by Zamri et al. [20]. Other mixtures for resin such as benzoyl peroxide (BPO) as initiator, calcium carbonate (CaCO_3) as filler and the release agent powder were also used.

Based on ASTM E9-89a (2000) designation, 18 specimens were produced using the metallurgical specimen cutter and milling machine with length/diameter (L/D) of 1.5 and 3 different alignment angles of 0° , 1° and 2° as illustrated in Figure 1. For each strain rate and fiber misalignment tested, 3 samples have been used. The fiber angle was selected between 1 - 2° because it was the most commonly reported misalignment angle for pultruded parts as reported by Yurgartis [21]. The fiber alignment was examined in which specimens were cut into two separate parts through the fiber direction and then placed below the SEM. During the cutting process, lubricant which act as coolant was used to help the dissipate heat in order to prevent over heating which might cause changes in morphology of kenaf fiber composite material. Parallel contact surfaces were prepared by grinding for maximum contact and removing possible bending moment.



Figure 1: Specimens with different angles.

Mechanical testing

The static compressive tests were conducted to identify the mechanical properties of the kenaf composites using the universal testing machine (UTM) at two different strain rates of 2.1 s^{-1} and 8.4 s^{-1} . This strain rate which corresponds to crosshead speed of 1mm/s and 2.5mm/s was appropriate to show the effect of strain rate on compressive properties and failure behaviour of kenaf composite under low strain rate range. The specimen is positioned centrally between the two compression plates, so that the travelling head centre is vertically above the specimen centre as shown in Figure 2. During the compression testing, the end friction between the sample and compression plates was reduced by means of a lubricant in the contact field. An appropriate preload was added where the crosshead travels to load the specimen to a specified value before a test becomes reliable. The specimens were tested until failure up to a maximum load of 17 kN to attain strain values and load carrying capacity. Stress-strain curves for each of the specimens were then plotted based on the data obtained as shown in Figure 3 and Figure 4.

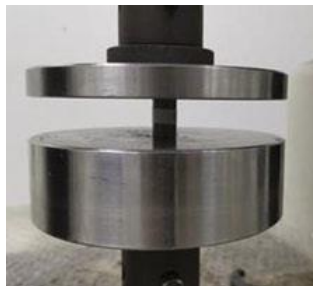


Figure 2: Position of specimens during compression test using UTM.

Failure observations

Microscopic photographs of all damage specimens have been taken with the Hitachi S-3700N scanning electron microscopic (SEM) to achieve resolution of up to 500 μm in order to find various post-compression failures. Before the SEM process was carried out, the specimens were covered with carbon layer using the sputter coater. For macroscopic images, the damage behaviour of the kenaf composite was identified in three different fibre alignments value and strain rates using an optical camera.

Results and Discussion

Mechanical properties

In the fibre direction of the composites, uniaxial compressive experiments have been carried out. Stress-strain curves with a strain rate of 2.1/s and 8.4/s are shown in Figure 3 and Figure 4 for the specimens with 3 different degree of alignment. Based on Figure 3 and Figure 4, as the fibre misalignment increased from 0° to 2° , it did not generally affect the form of the stress-strain curves. The initial straight section of the curve up to the yield point represents the specimen's elastic responses. The yield point signals the beginning of inelastic behaviour, where the curve then displays stress hardening before its maximum stress is reached. The highest stress on the graph is the ultimate stress when the specimen collapsed after the maximum load-bearing capacity was surpassed. Strain softening then took place up to the residual strength of the specimen. Similar stress-strain curve which showed elastic brittle behavior has also been reported by Dewan et al. [22] for natural jute/polyester composite.

On top of that, under different strain rates loading, the initial straight section of the stress-strain curves up to the yield point was not significantly changed. However, rate of strain softening which took place up to the residual strength of the specimen was fairly decreased as strain rates increased. Strain softening which is deterioration of material strength with increasing strain was decreased since the cumulative damage at certain stresses was much smaller under a slightly high strain rate. Hence, the residual stress of the specimen can withstand considerably more load at high strain rates and deform much longer.

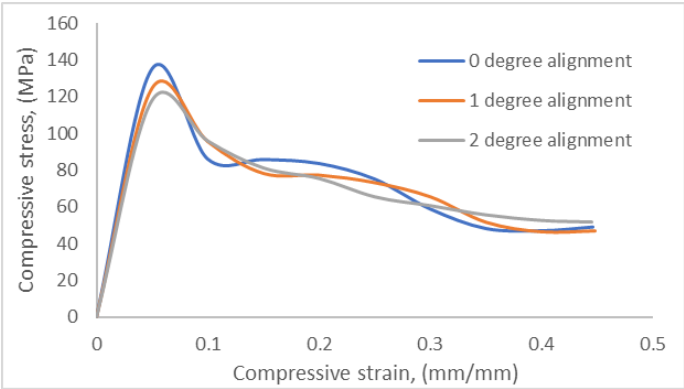


Figure 3: Stress-strain curves of kenaf composite under strain rates of 2.1/s.

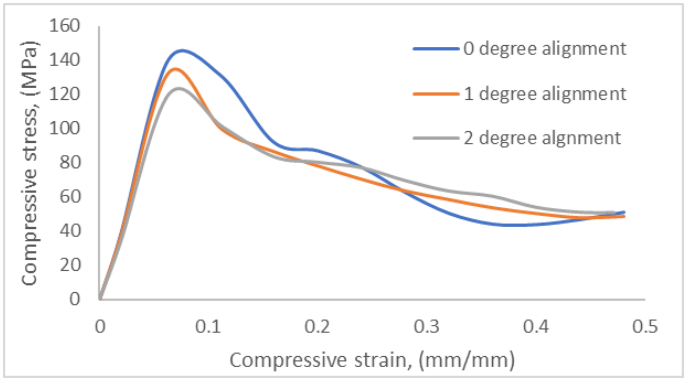


Figure 4: Stress-strain curves of kenaf composite under strain rates of 8.4/s.

The mechanical properties for sets of samples of kenaf composite materials are presented in Figure 5, Figure 6 and Table 1. Figure 5 shows the average failure stress of the kenaf composite as a function of fibre alignment under two different strain rates. Generally, as the fibre alignment increased from 0^0 to 2^0 , a maximum of 14% reduction in compressive failure stress was observed. However, under difference strain rates, the percentage of reduction was different. At strain rate of 2.1/s, failure stress was decreased from 140 Mpa to 120 MPa while at 8.4/s, failure stress was decreased from 136 Mpa to 119 MPa. Similar reduction in performance has also been reported by Yang et al. [14] and Werken et al. [15] when fiber alignment introduced in the carbon fiber composites.

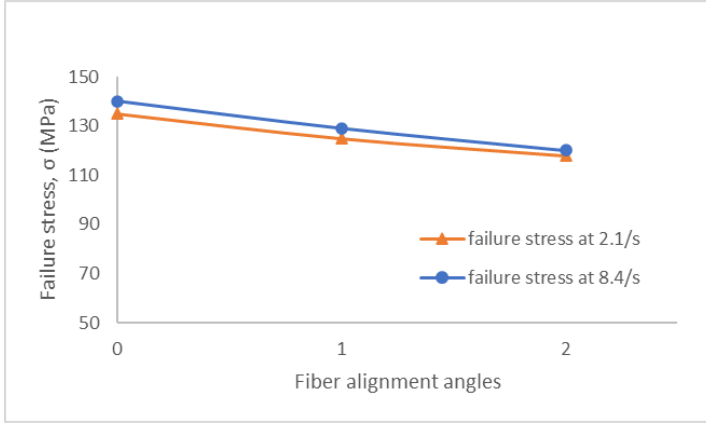


Figure 5: Failure stress vs fiber alignment angles.

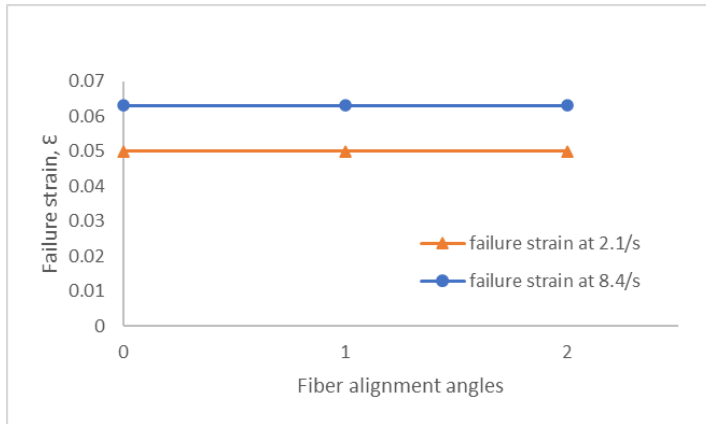


Figure 6: Failure strain vs fiber alignment angles.

Table 1: Compressive failure stress and failure strain of kenaf composite

Fiber alignment angle	Failure stress (MPa)		Failure strain	
	2.1 mm/s	8.4 mm/s	2.1 mm/s	8.4 mm/s
0°	136	140	0.05	0.063
1°	128	132	0.05	0.063
2°	119	120	0.05	0.063

Figure 6 shows the failure strain of the kenaf composite as a function of fibre alignment under two different strain rates. As the fibre alignment increased from 0^0 to 2^0 , the failure strain seemed almost constant at a fixed value. However, different value of failure strain was observed under different strain rates. At strain rate of 2.1/s, value of failure strain is 0.05 and when loaded under strain rates of 8.4/s, the failure strain is 0.063 which was increased by 26%.

Azizan et al. [23] explained the cause of failure stress reduction where the existence of fibre misalignment created an additional bending stress on the overall stress that broke the composite much earlier before its compressive strength was achieved. As shown in Table 1, only failure stress was affected by the change of fiber alignment. However, both the failure strain and failure stress were affected by the change of strain rate as they were slightly increased. Change of mechanical properties value even under low strain rate region was also reported by Hao et al. [24] when they tested nonwoven kenaf composite under tensile loading.

Damage behaviors

Microscopic observations showed that fibre matrix debonding and matrix cracking were observed on the top and bottom surfaces of each specimen with 3 different alignment angles tested under 2 different strain rates, without any fibre pull-out and fibres breaking as shown in Figure 7. Fiber matrix interface degradation was reported to generate considerable degradation in the composite's transverse response resulting in the premature degradation of the stress-strain curve [25], followed by other failures due to continuous compression of the specimens.

Macroscopically, the fibre misalignment played a major role in determining failure behaviours as shown in Table 2. With the degree of alignment increased, fibre breaking, fibre splitting and fibre matrix debonding were much more progressive than specimens with ideal parallel packaging. In addition, most of the failures that have been mentioned above were more noticeable at the middle region of the specimen with increasing fibre misalignment. Table 3 shows that most failure occurred only in half portion of the lower region in relation to the fibre misalignment of 1^0 and 2^0 in the top view of a failed kenaf composite, as compared with an ideally aligned specimen where a bottom zone failure was equally distributed.

Optical sample observations also show that an angle fracture plane occurred as a result of shear failure (Table 2). Generally, micro buckling of fibre was resulted from the process of shear instability in the matrix material that is caused by the plastic yielding at higher strains. The presence of fibre misalignment defects in a longitudinal direction, while compressing, is supposed to lead to kinks in a localised region. This eventually leads to the creation of fibre kink-bands and compressive kink failure [26]. It is important

to note that fibre misalignment is very sensitive to kinking stresses. Outcome of this study are in line with what reported by where the $0.8\text{--}2.3^\circ$ angle of misalignment was sufficient to cause a kink [27].

As shown in Table 2 and Table 3, the failure progression of the specimens with higher fiber misalignment is gradual compared to ideally aligned specimens. As previously discussed, main failure under compression loading of unidirectional composites was plastic kinking due to the existence of fiber misalignment and subsequent occurrence of matrix's shear instability. In Table 2, fiber kinking was a first failure initiated and visible prior to an inclined shear crack and fiber splitting. However, for specimens of high fibre misalignment, the gradual formation of the kink band and the associated fibre kink failure mode are more obvious.

Decohesion at the interface and shear band formation in the matrix are the two dominant damage mechanisms in controlling the composite strength [28]. In condition where decohesion is constricted, matrix's shear bands would occur at angle of $\pm 45^\circ$ from the compression axis [29]. The angle between the failure plane and the in-plane load direction is slightly higher than 45° and typical values are reported between $50\text{--}56^\circ$ for certain composites which may be more susceptible to shear bands formation [30]. For kenaf composite's compressive strength reported here, it was controlled by the visible decohesion of fiber and matrix at the interface as no shear bands failure occurred. As fiber misalignment increased, decohesion of fiber and matrix at the interface was more obvious (Table 2 and Table 3) which contribute to the reduction of compressive strength.

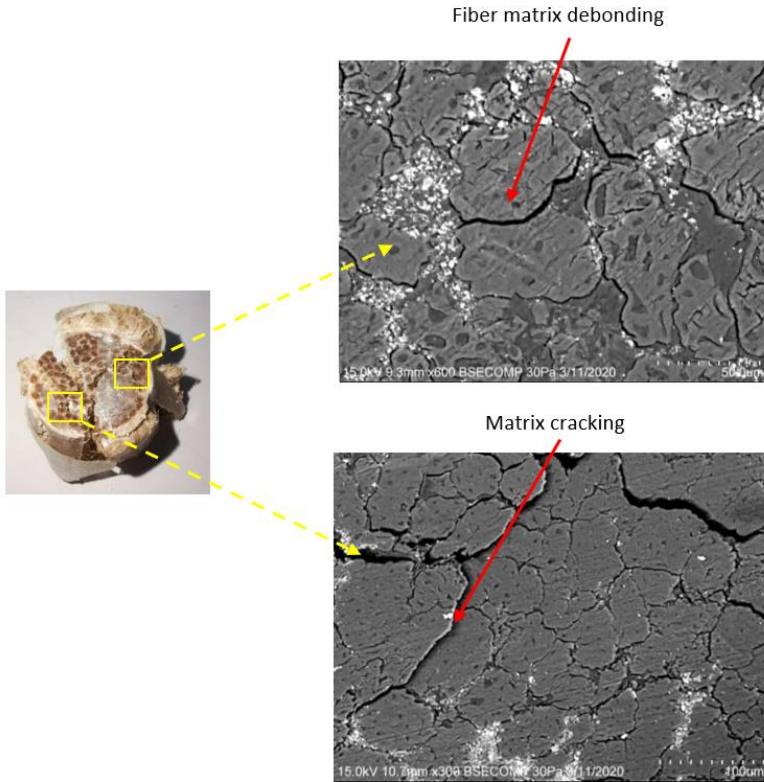


Figure 7: Top surfaces of kenaf composite.

Regarding this phenomenon, because fibre misalignment has increased, the specimen was subject to a much greater extra bending stress, thus leading to progressive damage. The kenaf composite was also gradually deteriorated as the strain rate increased, as shown in Table 2 and Table 3. This happened since the accumulated damage in certain stresses was much lower under a slightly high stress rate. Hence, the material can withstand substantially greater load with minimal damage at high strain rates and deform much longer until it fails [31].

Table 2: Side views of kenaf composite













Alignment Angle	2.1/s	8.4/s
0°		
Longitudinal splitting		
1°		
Fibers breakage		
2°		
Fibers plastic microbuckling		

Table 3: Top views of kenaf composite

Alignment Angle	2.1/s	8.4/s
0°		
1°		
2°		

Conclusions

This study has been performed with 3 different misalignment angles and loaded under two different strain-rate conditions to identify the effect of fibre misalignment on the mechanical properties and on the damage behaviour of kenaf composites. With a mean value of 0.05 and 0.063, the failure strain seems to be almost constant while the failure stress decreases from 140 Mpa until 120 MP when the fibre alignment increased when loaded within a range of 2.1~8.4/s. Fiber matrix debonding and matrix cracking have been typical failures, when loaded longitudinally, on top and bottom surfaces of every specimen. However, when the fibre alignment angle was increased, plastic microbuckling, fibre breakage, the fibre splitting and the fibre matrix debonding was progressively formed. In addition, the failure stress of kenaf composite was slightly increased by a maximum of 3% and a more progressive damage was observed as strain rate increased from 2.1~8.4/s.

References

- [1] A. Elsaid, M. Dawood, R. Seracino, and C. Bobko, "Mechanical properties of kenaf fiber reinforced concrete," *Construction and Building Materials*, vol. 25, no. 4, pp. 1991-2001, 2011.
- [2] C. Zhou, L. Cai, Z. Chen, and J. Li, "Effect of kenaf fiber on mechanical properties of high-strength cement composites," *Construction and Building Materials*, vol. 263, no. 1, pp. 121007, 2020.
- [3] N. Saba, M.T. Paridah, and M. Jawaid, "Mechanical properties of kenaf fibre reinforced polymer composite: A review," *Construction and Building Materials*, vol. 76, no., pp. 87-96, 2015
- [4] M.F. Omar, H. Jaya, and N.N. Zulkepli, "Kenaf Fiber Reinforced Composite in the Automotive Industry", In *Encyclopedia of Renewable and Sustainable Materials*. Elsevier, Oxford, 2020. pp. 95-101.
- [5] V. Fiore, G. Di Bella, and A. Valenza, "The effect of alkaline treatment on mechanical properties of kenaf fibers and their epoxy composites," *Composites Part B: Engineering*, vol. 68, no., pp. 14-21, 2015.
- [6] H.T. Sreenivas, N. Krishnamurthy, and G.R. Arpitha, "A comprehensive review on light weight kenaf fiber for automobiles," *International Journal of Lightweight Materials and Manufacture*, vol. 3, no. 4, pp. 328-337, 2020.
- [7] L.T. Harper, T. Turner, J.R.B. Martin, and N. Warrior, "Fiber Alignment in Directed Carbon Fiber Preforms — A Feasibility Study," *Journal of Composite Materials* vol. 43, no. 1, pp. 57-74, 2009.
- [8] K. Potter, B. Khan, M. Wisnom, T. Bell, and J. Stevens, "Variability, fibre waviness and misalignment in the determination of the properties of composite materials and structures," *Composites Part A: Applied Science and Manufacturing*, vol. 39, no. 9, pp. 1343-1354, 2008.
- [9] G.M. Martinez, M.R. Piggott, D.M.R. Bainbridge, and B. Harris, "The compression strength of composites with kinked, misaligned and poorly adhering fibres," *Journal of Materials Science*, vol. 16, no. 10, pp. 2831-2836, 1981.
- [10] K.K. Kratmann, M.P.F. Sutcliffe, L.T. Lilleheden, R. Pyrz, and O.T. Thomsen, "A novel image analysis procedure for measuring fibre misalignment in unidirectional fibre composites," *Composites Science and Technology*, vol. 69, no. 2, pp. 228-238, 2009.
- [11] B. Budiansky, and N.A. Fleck, "Compressive failure of fibre composites," *Journal of the Mechanics and Physics of Solids*, vol. 41, no. 1, pp. 183-211, 1993.
- [12] Y. Li, B. Stier, B. Bednarczyk, J.-W. Simon, and S. Reese, "The effect of fiber misalignment on the homogenized properties of unidirectional fiber reinforced composites," *Mechanics of Materials*, vol. 92, no., pp. 261-274, 2016.

- [13] S.C. Barwick, and T.D. Papathanasiou, "Identification of fiber misalignment in continuous fiber composites," *Polymer Composites*, vol. 24, no. 3, pp. 475-486, 2003.
- [14] X. Yang, A. Nanni, S. Haug, and C. Sun, "Strength and Modulus Degradation of Carbon Fiber-Reinforced Polymer Laminates from Fiber Misalignment," *Journal of Materials in Civil Engineering* vol. 14, no., 2002.
- [15] N. Werken, M.S. Reese, M.R. Taha, and M. Tehrani, "Investigating the effects of fiber surface treatment and alignment on mechanical properties of recycled carbon fiber composites," *Composites Part A: Applied Science and Manufacturing*, vol. 119, no., pp. 38-47, 2019.
- [16] M.R. Wisnom, "The effect of fibre misalignment on the compressive strength of unidirectional carbon fibre/epoxy," *Composites*, vol. 21, no. 5, pp. 403-407, 1990.
- [17] Y. Song, U. Gandhi, A. Koziel, S. Vallury, and A. Yang, "Effect of the initial fiber alignment on the mechanical properties for GMT composite materials," *Journal of Thermoplastic Composite Materials*, vol. 31, no. 1, pp. 91-109, 2017.
- [18] H. Ahmadian, M. Yang, A. Nagarajan, and S. Soghrati, "Effects of shape and misalignment of fibers on the failure response of carbon fiber reinforced polymers," *Computational Mechanics*, vol. 63, no. 5, pp. 999-1017, 2019.
- [19] W.B. Hillig, "Effect of fibre misalignment on the fracture behaviour of fibre-reinforced composites," *Journal of Materials Science*, vol. 29, no. 2, pp. 419-423, 1994.
- [20] M.H. Zamri, H.M. Akil, and Z.A. MohdIshak, "Pultruded Kenaf Fibre Reinforced Composites: Effect of Different Kenaf Fibre Yarn Tex," *Procedia Chemistry*, vol. 19, no., pp. 577-585, 2016.
- [21] S.W. Yurgartis, "Measurement of small angle fiber misalignments in continuous fiber composites," *Composites Science and Technology*, vol. 30, no. 4, pp. 279-293, 1987.
- [22] M.W. Dewan, M.K. Hossain, M. Hosur, and S. Jeelani, "Thermomechanical properties of alkali treated jute-polyester/nanoclay biocomposites fabricated by VARTM process," *Journal of Applied Polymer Science*, vol. 128, no. 6, pp. 4110-4123, 2013.
- [23] A. Azizan, H.A. Israr, and N. Tamin, "Effect of Fiber Misalignment on Tensile Response of Unidirectional CFRP Composite Lamina," *Journal of Advanced Research in Applied Sciences and Engineering Technology*, vol. 11, no. 1, pp. 23-30, 2018.
- [24] A. Hao, H. Zhao, W. Jiang, L. Yuan, and J.Y. Chen, "Mechanical Properties of Kenaf/Polypropylene Nonwoven Composites," *Journal of Polymers and the Environment*, vol. 20, no. 4, pp. 959-966, 2012.

- [25] W.S. Johnson, S.J. Lubowinski, and A.L. Highsmith, "Mechanical Characterization of Unnotched SCS 6 /Ti-15-3 Metal Matrix Composites at Room Temperature", In. ASTM International, West Conshohocken, PA, 1990. pp. 193-218.
- [26] B. Budiansky, and N.A. Fleck, "Compressive Kinking of Fiber Composites: A Topical Review," *Applied Mechanics Reviews*, vol. 47, no. 6S, pp. S246-S250, 1994.
- [27] J. Lee, and C. Soutis, "A study on the compressive strength of thick carbon fibre–epoxy laminates," *Composites Science and Technology*, vol. 67, no. 10, pp. 2015-2026, 2007.
- [28] S. Ghaffari, A. Makeev, G. Seon, D.P. Cole, D.J. Magagnosc, and S. Bhowmick, "Understanding compressive strength improvement of high modulus carbon-fiber reinforced polymeric composites through fiber-matrix interface characterization," *Materials & Design*, vol. 193, no., pp. 108798, 2020.
- [29] C. González, and J. Llorca, "Mechanical behavior of unidirectional fiber-reinforced polymers under transverse compression: Microscopic mechanisms and modeling," *Composites Science and Technology*, vol. 67, no. 13, pp. 2795-2806, 2007.
- [30] M.M. Shokrieh, M.A. Torabizadeh, and A. Fereidoon, "Progressive failure analysis of glass/epoxy composites at low temperatures," *Strength of Materials*, vol. 44, no. 3, pp. 314-324, 2012.
- [31] S. Abrate, "Impact on Laminated Composite Materials," *Applied Mechanics Reviews*, vol. 44, no. 4, pp. 155-190, 1991.

Flexible Pavement Crack's Severity Identification and Classification using Deep Convolution Neural Network

A. Ibrahim*, N. A. Z. M. Zukri, B. N. Ismail

Faculty of Civil Engineering, UiTM Cawangan Pulau Pinang, Malaysia

*ceanas@uitm.edu.my

M. K. Osman, N. A. M. Yusof, M. Idris

Faculty of Electrical Engineering, UiTM Cawangan Pulau Pinang, Malaysia

A. H. Rabian

THB Maintenance Sdn. Bhd. Malaysia

I. Bahri

Unitec Institute of Technology, Auckland, New Zealand.

ABSTRACT

Effective road maintenance program is vital to ensure traffic safety, serviceability, and prolong the life span of the road. Maintenance will be carried out on pavements when signs of degradation begin to appear and delays may also lead to increased maintenance costs in the future, when more severe changes may be required. In Malaysia, manual visual observation is practiced in the inspection of distressed pavements. Nonetheless, this method of inspection is ineffective as it is more laborious, time consuming and poses safety hazard. This study focuses in utilizing an Artificial Intelligence (AI) method to automatically classify pavement crack severity. Field data collection was conducted to allow meaningful verification of accuracy and reliability of the crack's severity prediction based on AI. Several important phases are required in research methodology processes including data collection, image labelling, image resizing, image enhancement, deep convolution neural network (DCNN) training and performance evaluation. Throughout the analysis of image processing results, the image output was successfully classified using MATLAB software. The good agreement between field measurement data and DCNN prediction of crack's severity proved the

reliability of the system. In conclusion, the established method can classify the crack's severity based on the JKR guideline of visual assessment.

Keywords: Road maintenance; DCNN; Crack severity; Flexible pavement

Introduction

Road networks are crucial infrastructures that provide transport services, and a catalyst for the economic development of a nation. A large part of the current road infrastructure is approaching the end of its service life, which is placing even more pressure on the budgets in the coming years [1]. Road maintenance involves monitoring road performance and repairing defects such as potholes, pavement cracks and rutting. Some examples of pavement defect treatments are pothole patching, crack sealing, mill and pave and road reconstruction [2]. Manual pavement distress survey is inefficient and lead to low productivity in road maintenance. For example, one pavement inspector can only inspect less than 10 km per day [3]. The goal of this study is to improve pavement maintenance survey using an AI by measuring the level of severity of distressed pavement. AI is an area of computer science that accentuates the development of smart machines that function and respond like humans. AI performs frequent, high-volume, computerized tasks reliably and without fatigue rather than automating manual tasks. This work introduces a customized image processing algorithm for high-speed, real-time inspection of pavement cracking [4]. Traditionally, it requires engineers working on busy roads, which is dangerous, costly, time-consuming, and inefficient [5]-[7].

Several attempts have been made in the past to automate the pavement distress survey using image processing techniques. Among them are based on image segmentation [8], seed growing [9], local optimal thresholding [10] and matched filtering algorithm [11]. However, these methods suffer from problem of intensity variation in pavement images due to shadow, oily, complex, and rough pavement surfaces. To overcome these problems, recent researches have integrated artificial intelligence such as random decision forest [12], support vector machine (SVM) [13]-[14], artificial neural network [14]-[15] and fuzzy inference system [16]. This study utilises MATLAB software to develop an AI system based on deep convolutional neural network to analyse pavement distress images automatically. The AI system will automate the classification of crack severity of flexible asphalt pavement. To further advance the system, the automated crack detection was moved to the next stage of computer vision where utilizing machine learning approach that can be found in many studies. Machine learning is a subset of AI, where it uses algorithms to analyse and learn from a sample dataset, and then decide or make new predictions about other datasets. This is compatible with the objective of machine learning which

is to allow the system to learn automatically without human intervention. Consequently, the main aim of this project is to develop an intelligent system based on DCNN to detect and classify pavement cracks of asphalt pavement. To achieve that, this project focuses on developing an AI system for flexible pavement crack's severity classification. The system is then tested using field datasets to verify its accuracy and reliability.

Research Methodology

The methodology adopted in this project involves four major steps starting with the data collection, image processing and labelling, Deep Convolution Neural Network (DCNN) training and evaluation of the system's performance. The prediction data of pavement crack's severity will be compared with the field measurement data to ensure its accuracy and reliability of the AI system.

Data collection of pavement crack and its severity

The images of asphalt pavement crack were acquired from various location in Penang and Terengganu. Generally, there are three main types of pavement cracks which are longitudinal, alligator and transverse cracks. For this study, the focus is on pavement cracks with various level of severity. Photos were taken using a mobile phone camera with its optical perpendicular to the road surface. The data collection can be carried out with any device that can take pictures downwards [17]. The camera is mounted on a phone holder with a consistent height of 100 cm from the pavement surface to achieve accurate, reliable, and efficient image collection. For every captured image, Vernier calliper is used to directly measure the width of the crack for field data collection

Image labelling, resizing, and enhancing

Pavement crack images obtained from field were labelled based on the measurement of the average width of the pavement's crack. Images will be classified into low, moderate, and high severity of crack based on [18] guideline of visual assessment of flexible pavement surface condition as shown in Figure 1. Low severity of asphalt pavement crack's width is below than 6 mm, moderate severity's width is between 6 mm to 19 mm, and high severity's width is 19 mm and above.

Resizing images is compulsory because if the size is too big, it will slow down the process in training process in Deep Convolutional Neural Network operation. For this research, 64 x 64 is found to be the optimal image size. For resizing images, using photoshop is preferred and easier method.



Figure 1: Classification of crack's severity from low, moderate to high (left to right).

Image enhancing is performed to increase the number of images. To achieve this, images were edited into 90° anti-clockwise, 90° clockwise, perpendicular, and vertical rotation form. Higher number in images from data collection will allow better accuracy in the training process of DCNN system.

DCNN data training and testing

The network prepares two sets of training and testing dataset: types of crack classification consists of transverse, longitudinal and alligator [19]. To achieve the objective, Deep Convolutional Neural Network (DCNN) must be train first. Divide the data into datasets for the testing and validation. Using 70% of the photos for processing, and 30% for validation. After succeeding with the when training the coding in MATLAB, run the other codes to test the pavement crack images. When running the codes, it will ask to input the images we want to test. After selecting the image, MATLAB will state the severity of pavement cracks in the images.

Performance evaluation

The performance of the DCNN was tested based on testing patches that have not been used in the training process. The value of prediction and actual labels in this study uses of matrix analysis which is called confusion matrix. Figure 2 shows that the confusion matrix represents all the parameters that have been mention before. The predicted labels are relayed on the horizontal axis while for the actual labels is relayed on the vertical axis. Usually, training data has higher accuracy than the validation data. For this research, confusion matrix shows the accuracy for each classified data which are low, moderate, and high data.

		Target class			
		High	Low	Medium	
Output class	High	80 (19.2%)	0 (0%)	0 (0%)	100%
	Low	0 (0%)	80 (19.2%)	0 (0%)	100%
	Medium	0 (0%)	0 (0%)	256 (61.5%)	100%
		100%	100%	100%	
		Training			

		Target class			
		High	Low	Medium	
Output class	High	14 (13.5%)	0 (0%)	0 (0%)	100%
	Low	0 (0%)	19 (18.3%)	0 (0%)	100%
	Medium	6 (5.8%)	1 (1%)	64 (61.5%)	90.1%
		70%	95%	100%	93.3%
		Validation			

Figure 2: Training confusion matrix (left) and validation confusion matrix (right).

Result and Discussion

The results of prediction from DCNN and validation based on field data collection were discussed to ensure the main objective of this study is achieved. This project aims to have an AI that will enable auto classification of crack's severity of flexible pavement.

Flexible pavement crack's severity using artificial intelligence system result

Figure 3 shows the training process for DCNN. Deep learning models of the neural network learn to map inputs to outputs given an example collection of training data. The training method includes finding in the network a set of weights that proves to be sufficient or sufficient to solve the problem. A validation set is used to evaluate the model during the training [20]. The developed system managed to achieve 93.27 % accuracy for all data.

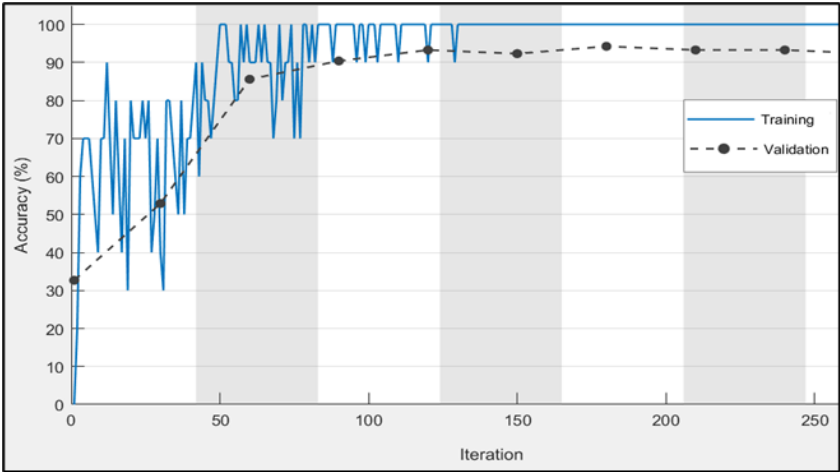


Figure 3: Training confusion matrix (left) and validation confusion matrix.

Crack’s severity prediction based on field data comparison


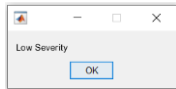

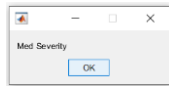
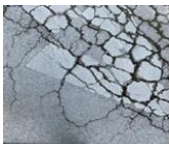
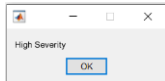
Prediction results using AI must be validated with the field data that were acquired from field works on selected roads. Table 1 presents the comparison of predicted and measured data of crack’s severity level. Original images show cracks at various severity and measurement was taken to obtain average width of the crack. The prediction results using AI are tabulated on the right column to show the comparison between prediction and field results.

To evaluate this proposed DCNN model, three (3) different datasets were used which are low, medium, and high severity of pavement crack. The selection of dataset is based on the JKR guideline in the visual assessment of flexible pavement functional surface. Another reason for using three (3) different datasets is to study whether the size of the patch used to train and test if the model will affect the model or vice versa. Low, medium, and high datasets contain identical size of patches which is 64 x 64 pixels. After determining the most ideal characteristics for the proposed DCNN model, it is tested on real data which are images that have been developed during this study and the structure of the pavement image represents the general pavement condition in Malaysia.

The evaluation result obtained is quite good with an accuracy of 93.27% and very low loss of only 20 epochs. The complete training and test process took about 1 minute and 29 seconds which is relatively short. This is due to the small dataset used, with a total of 520 input data and 64 x 64 patch size. The output of DCNN prediction of crack severity shows promising results, allowing fast evaluation of flexible pavement crack severity, and eliminating

the hazard of conducting visual road assessment manually on the field. Improving field images acquisition in future works will allow higher quality and better consistency of pavement distress images analysis. Thus, the need to develop a system and hardware that can control the environment conditions will enhance the efficiency and reliability of images analysis using the AI system.

Table 1: Comparison between prediction using AI and field data

No	Image	Crack's severity of field data				Crack's severity prediction using AI	
		Width		Average			Severity
1		2.66	2.43	2.96	2.68	Low	
2		5.06	6.02	8.04	6.37	Medium	
3		58.42	40.92	43.94	47.76	High	

Conclusion

In conclusion, the prediction of crack severity using DCNN could be effectively conducted without relying on operator judgement on the field assessment. Throughout the analysis of processing images, the objectives were successfully achieved using MATLAB software with excellent accuracy of output data. The predicted results using the developed system indicated a good agreement with the field data, which proved the reliability of the system.

Acknowledgement

The authors would like to thank to all parties that support and involve directly or indirectly into this research especially to Advanced Rehabilitation Engineering in Diagnostic and Monitoring Research Group (AREDiM), Universiti Teknologi MARA, Pulau Pinang and Universiti Teknologi MARA, Shah Alam. This research is supported by the Fundamental Research Grant Scheme (FRGS), Grant No: FRGS/1/2019/TK04/UITM/02/30. Also, appreciation goes to the Ministry of Higher Education (MOHE) for giving great privilege in providing scholarship as inspiring encouragement for the success of this research.

References

- [1] R. Salini, B. Xu and P. Paplauskas, "Pavement distress detection with picucha methodology for area-scan cameras and dark images," *Civ. Eng. J.*, vol. 1 no. 1 pp. 34 - 45, April 2017.
- [2] A. Cubero-Fernandez, F. J. Rodriguez-Lozano, R. Villatoro, J. Olivares and J. M. Palomares, "Efficient pavement crack detection and classification," *EURASIP Journal on Image and Video Processing*, vol. 39, June 2017.
- [3] N. D. Hoang, "An artificial intelligence method for asphalt pavement pothole detection using least squares support vector machine and neural network with steerable filter-based feature extraction," *Advances in Civil Engineering*, pp. 1 – 12, June 2018.
- [4] Y. Huang and B. Xu, "Automatic inspection of pavement cracking distress," *Journal of Electronic Imaging*, vol. 15, no. 1, January 2006.
- [5] M. A. Qurishee, "Low-cost deep learning UAV and Raspberry Pi solution to real time pavement condition assessment," Department of Civil and Chemical Engineering, University of Tennessee, 2019.
- [6] S. Bhat, S. Naik, M. Gaonkar, P. Sawant, S. Aswale, and P. Shetgaonkar, "A Survey on Road Crack Detection Techniques," *2020 International Conference on Emerging Trends in Information Technology and Engineering (ic-ETITE)*, Vellore, India, pp. 1-6, 2020.
- [7] C. O. Tayo, N. B. Linsangan and R. V. Pellegrino, "Portable Crack Width Calculation of Concrete Road Pavement Using Machine Vision," *2019 IEEE 11th International Conference on Humanoid, Nanotechnology, Information Technology, Communication and Control, Environment, and Management (HNICEM)*, Laoag, Philippines, pp. 1-5, 2019.
- [8] Y. C. Tsai, V. Kaul, and R. M. Mersereau, "Critical Assessment of Pavement Distress Segmentation Methods," *J. Transp. Eng.*, vol. 136, pp. 11-19, 2010.

- [9] Q. Li, L. Zou, D. Zhang and Q. Mao, "FoSA: F* Seed-growing Approach for crack-line detection from pavement images," *Image and Vision Computing*, vol. 29, no. 12, pp. 861-872, 2011.
- [10] S. Wang, and W. Tang, "Pavement Crack Segmentation Algorithm Based on Local Optimal Threshold of Cracks Density Distribution," In: Huang D.S., Gan Y., Bevilacqua V., Figueroa J.C. (eds) *Advanced Intelligent Computing. ICIC 2011, Lecture Notes in Computer Science*, vol. 6838. Springer, Berlin, Heidelberg.
- [11] A. Zhang, Q. Li, K. C. P. Wang and S. Qiu, "Matched Filtering Algorithm for Pavement Cracking Detection," *Transportation Research Record*, vol. 236, no. 1, pp. 30-42. 2013.
- [12] L. Cui, Z. Qi, Z. Chen, F. Meng and Y. Shi, "Pavement Distress Detection Using Random Decision Forests," In: Zhang C. et al. (eds) *Data Science. ICDS 2015, Lecture Notes in Computer Science*, vol. 9208.
- [13] G. M. Hadjidemetriou, P. A. Vela and S. E. Christodoulou, "Automated Pavement Patch Detection and Quantification Using Support Vector Machines," *Journal of Computing in Civil Engineering*, vol. 32 no. 1, pp. 1-11, 2018.
- [14] N. D. Hoang and Q. L. Nguyen, "A novel method for asphalt pavement crack classification based on image processing and machine learning," *Engineering with Computers*, vol. 35, pp. 487-498, 2019.
- [15] N. D. Hoang, "An Artificial Intelligence Method for Asphalt Pavement Pothole Detection Using Least Squares Support Vector Machine and Neural Network with Steerable Filter-Based Feature Extraction," *Advances in Civil Engineering*, vol. 2018.
- [16] M. Abambres and A. Ferreira, "Application of ANN in pavement engineering: State-of-Art," *SSRN Electronic Journal*, 2017.
- [17] Pavement Research Unit, "A Guide to the Visual Assessment of Flexible Pavement Surface Conditions," Jabatan Kerja Raya Malaysia, JKR 20709-2060-92, 1992.
- [18] A. Ibrahim, M. K. Osman, N. A. Yusof, K. A. Ahmad, N. H. Harun, and R. A. Raof, "Characterization of cracking in pavement distress using image processing techniques and k-Nearest neighbour," *Indonesian Journal of Electrical Engineering and Computer Science*, vol. 14, no. 2. 2019.
- [19] R. Yamashita, M. Nishio, R. K. Do and K. Togashi, "Convolutional neural networks: an overview and application in radiology, Insights into imaging," vol. 9, issue 4, pp. 611-629, 2018.
- [20] A. T. Azeez and N. Anupama, "Crack Pavement Detection Utilizing Fuzzy Inference System," *Int. Journal of Scientific Engineering and Technology Research*, vol. 5, no. 7, pp. 1400-1404, 2016.

Severity Effect of Methanol Toxicity from High Pressure Reactor

Z A Rashid*, M A Subri, M A Ahmad, M F I Ahmad Fuad, N S Japperi
Faculty of Chemical Engineering, Universiti Teknologi MARA,
40450 Shah Alam, Selangor, Malaysia
*zulkifli466@uitm.edu.my

ABSTRACT

CO₂ hydrogenation to methanol synthesis is one of the effective solutions to mitigate the climate changes and the greenhouse gas emissions. However, the drawbacks of this process needed it to operate at high pressure condition where the possibility of leakage and fatality occur is possible. The simulation of this process was simulated using Aspen HYSYS, ALOHA and Google Earth to analyse the methanol toxicity severity from the high-pressure reactor. The probit will determine the level of the severity. It shows that higher pressure with bigger leakage size may experience high severity for the methanol is achieved the highest severity at 400 bar with the bigger leakage size. As the leakage size and pressure is increasing the exposure of the chemical is increasing, thus increasing the severity to the surrounding.

Keywords: Risk Assessment; Severity; Consequence Modelling; Toxicity

Introduction

Methanol has a characteristic which are very toxic and very flammable. Methanol is toxic when it enters the body by ingestion, inhalation, or absorption through the skin and can be fatal due to depression of the central nervous system which can lead to decreased respiratory rate, decreased heart rate, and suppressed brain activity [1]. Methanol has colourless appearance, hygroscopic and methanol is miscible or mixable with water completely. The demand of methanol has increasing as fuel at global competition where the needs to search the new alternatives of producing the chemical bulk is varied [2]. Methanol is a feasible substitute for the energy source which offering a suitable solution on large scale for the efficient energy storage, while it plays a significant part in economy and sustainability by captured the carbon dioxide from power plant and convert it into the methanol [3]. One of the alternatives

is the methanol synthesis from hydrogen (H_2) and carbon dioxide where carbon dioxide is hydrogenated to methanol which has greater attention recently because of the global warming such as greenhouse gas emission from the industrial activities [4]. The importance of CO_2 hydrogenation to methanol was highlighted in the work using electricity and electrolysis for methanol production [5], and study on power to fuel technologies [6].

Since 1920's until 1960's the methanol synthesis from syngas was operated at pressure range from 250 bar to 350 bar and 320 °C to 450 °C. Then, at 1970 the reaction operating condition switched to 50–100 bar and 200–300 °C due to present catalyst that more active [7]. However, the methanol conversion percentage is still low (less 60%). Recently, advantage of using high pressure has been discovered by several researchers [8]–[11]. In 2016, based on experiment done by Gaikward *et. al.*, have shown that under high-pressure condition above a threshold temperature, the reaction overcomes kinetic control, entering thermodynamically controlled regime. 90% CO_2 conversion and >95% methanol selectivity was achieved with a very good yield (0.9–2.4 gMeOH gcat⁻¹h⁻¹) at 442 bar [10]. In view of this fact, it can be concluded that CO_2 hydrogenation methanol synthesis process introduced is operated at the high-pressure condition which is more than 100 bars, when the experimental results show a 76.4 bar with recycle pressurized CO_2 hydrogenation reactor, at a temperature of 288 °C, is able to produce a conversion to methanol product of 24%. This methanol conversion percentage increased to 35% (200 bar), 54% (300 bar), 87% (400 bar) and exceeded 90% (500bar). However, this condition is possibly can lead to the leaking of the reactor due to the high-pressure condition [12]. Furthermore, high temperature combine with high pressure have more energy, lead to higher risk compare to lower pressure [13]. The exposure of chemical from the reactor such as methanol may lead to fatality to the human and environment. Based on past incident, methanol has poison effect that can cause severe metabolic disturbances, loss of sight, permanent neurologic dysfunction and also lead to death [14]. This study aims to analyse the leakage from CO_2 hydrogenation to methanol synthesis reactor that operating at high pressure and determine the severity effect from the CO_2 hydrogenation to methanol synthesis process which is methanol toxicity. The risk assessment analyses the severity of the incident towards the human and environment if the methanol leakage occurred in the plant. Currently, only few author works on high-pressure methanol plant such as study on fatalities comparing pressure 76 bar and 442 bar [15], work using artificial intelligent to predict percentage fatalities for methanol jet fire [16], where other works not focus on risk assessment study for CO_2 hydrogenation to methanol such as study on energy analysis for methanol plant up to 950 bar and 1000 bar [17, 18], study on the thermodynamic equilibrium using high-pressure methanol process [19], design and simulation CO_2 hydrogenation to produce methanol for CO_2 capture and energy analysis [20],

works on CO₂ and H₂ different ratio to produce high yield methanol [21, 22], works on CO₂ and H₂ 1:3 ratio at high-pressure as high as 442 bar to produce more methanol [10] [23].

Methodology

The assessment is focussed on severity effect of methanol plant in high pressure condition. The reactor of the methanol is modelled to determine the methanol produce based on 100, 200, 300, 400 and 500 bar. The volume of reactor used was 7.6 m³, refer to the work by Mar Perez-Fortes et al. [24]. In this study, mass flow rate into reactor was 91,500 kg/h, combining 80,500 kg/h of CO₂ and 11,000 kg/h of H₂, while simulation study by Mar Perez-Fortes et al. used 91,500 kg/h at inlet combined with recycle flow rate of 376, 200 kg/h, to have 467,600 kg/h flow rate into reactor. Mar Perez-Fortes et al. using 42 m³ to contain 515 gas hourly space volume (GHSV), then this GHSV value was used to get reactor volume of 7.6 m³ for this study. The severity effects of methanol are determined based on the leakages and pressure simulations.

Modelling simulation

The study is conducted by using the computer aided such as Aspen HYSYS, ALOHA and Google Earth. The suitable fluid package for carbon dioxide (CO₂) process used is The Peng-Robinson equation of state. Peng Robinson equation is suitable for mixtures of nonpolar and slightly polar compounds and most widely used thermodynamic package as it applies to all applications involving hydrocarbons [25]. The ALOHA is simulated to determine the radius affected and downwind concentration which the location is located at Port Kalama, WA. The coordinate location is 46° 01' 18" N 122° 51' 30.07" and has elevation about 8 meters. The windspeed modelled is 1.6 m/s, temperature is 51.5 °F, surface roughness is 1 meter, class B, no inversion and humidity level at 71%. All these data extracted from QRA report on Methanol Plant produced by AcuTech Consulting Group [26]. The Google Earth is applied in order to get affected mapping areas from consequence simulation. Figure 1 shows the process diagram of reactor modelled in this analysis.

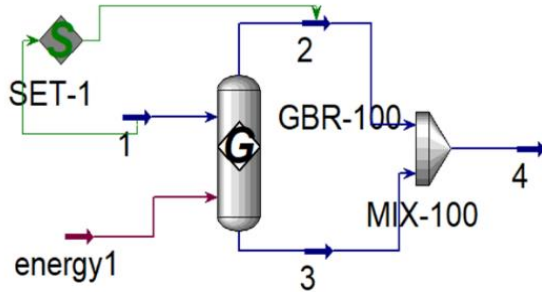


Figure 1: Reactor's process flow diagram.

Release rate formulation

The choked pressure is the maximum downstream pressure resulting in maximum flow through the hole or pipe.

$$\frac{P_{choked}}{P_1} = \left(\frac{2}{\gamma+1}\right)^{\gamma/(\gamma-1)} \quad (1)$$

Where P_{choked} is maximum downstream pressure resulting in maximum flow, P_1 is upstream pressure (bar abs) and k is heat capacity ratio (1.2 for methanol).

$$Q_{m,choked} = C_o A P_o \sqrt{\frac{\gamma g_c M}{R_g T_o} \left(\frac{2}{\gamma+1}\right)^{(\gamma+1)(\gamma-1)}} \quad (2)$$

Where $Q_{m,choked}$ is gas discharge rate, choked flow (kg/s), C_o is discharge coefficient (approximately 1.0 for gases), A is hole cross-section area (m^2), P_o is upstream pressure (N/m^2), M is molecular weight ($kg/kg\text{-mol}$) (for methanol 1.2), R_g is gas constant ($8314 J/kg\text{-mole}/^\circ K$) and T is upstream temperature (K). Equation (1) and Equation (2) is referred in published Purple book [27].

$$Y = K_1 + K_2 \ln V \quad (3)$$

Where V is dose and Y is probit variable. Equation (3) provided by author in QRA book [28].

Results and Discussion

Methanol vapour discharge rate

Simulation of methanol plant was conducted using HYSYS software, where density of mixture in reactor was increase with 30, 71, 148, 387 and 433 kg/m³ for plant 100, 200, 300, 400 and 500 bar respectively. The simulation also observed increasing of weight fraction for methanol which were 0.14, 0.29, 0.44, 0.59 and 0.61 for plant 100, 200, 300, 400 and 500 bar respectively. The increasing of density and weight fraction lead to increasing mass of methanol in the reactor, which were 32, 155, 492, 1753 and 1990 kg for plant 100, 200, 300, 400 and 500 bar respectively. The increasing amount of methanol mass cause increasing amount of mass release when subjected to leakage, thus, higher discharge rate was observed. Figure 2 shows the gas discharge rate (mchoked) in relation with the pressure operated for methanol at opening of 10 mm, 25 mm and 160 mm with different pressures of 100, 200, 300, 400 and 500 bar. The lowest gas discharge rate is at pressure 100 bar for all leakages. As the pressure increases, the gas discharge rate increases and the highest mchoked is at 500 bar. The mchoked values for leak sizes are 5.45×10^{-5} kg/s (10 mm), 0.000341 kg/s (25 mm) and 0.0139 kg/s (160 mm). The leak sizes affect the gas discharge rate (mchoked) where the larger the leak size, the higher the gas discharge rate (mchoked). Gas discharge rate (mchoked) will determine the radius of areas affected. The choked pressure is the maximum downstream pressure that will results in maximum flow through the leakage and caused the choked flow or sonic flow.

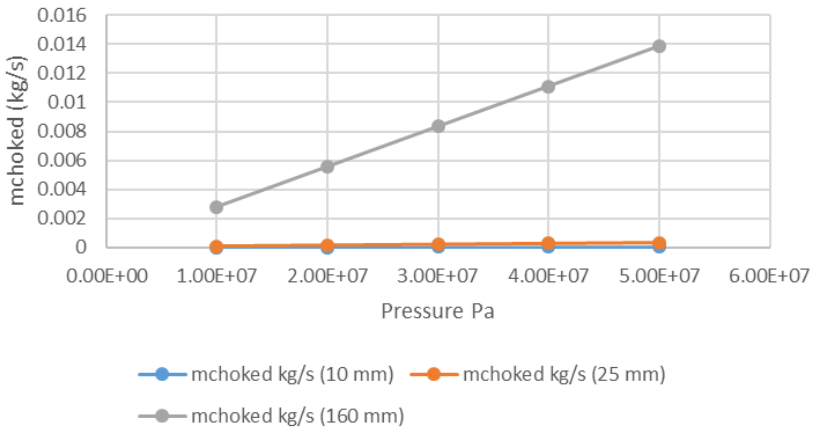


Figure 2: Methanol vapour discharge rate.

Consequence analysis

Figure 4 - 8 show the areas affected by methanol dispersion at 10 mm leakage size where the operating pressures are varied from 100 bar to 500 bar. Wind speed is simulated at 1.6 m/s with three wind directions, which of NNW, NW, and WNW. The duration simulated is 60 minutes, which is the maximum duration of release. Figure 3 shows the dispersion areas at a pressure of 100 bar, which has the lowest distance of area affected. The affected areas are at 34 yards (red zone), 64 yards (orange zone), and 128 yards (yellow zone). Figure 7 shows that at 400 bar of pressure, yield the highest distance where the red zone is affected at 58 yards, the orange zone at 108 yards, and the yellow zone is affected at 216 yards. Figure 8 shows the affected area at 500 bar of pressure yields the highest gas discharge rate but has a lower distance. The affected areas are at 56 yards (red zone), 103 yards (orange zone), and 205 yards (yellow zone). The distance of affected areas increased at 100 bar until 400 bar and decreasing back when the pressure reached 500 bar. At 500 bar of pressure, the affected distance is higher than 300 bar of pressure, as shown in Figure 13. The maximum area affected due to 10 mm of leak size is predicted at 400 bar, and the minimum area affected is predicted at 100 bar. In the red zone, the person exposed may have life-threatening health effects or mortality at a distance of 58 yards. In comparison, at 108 yards, the person may experience injury or disability, and at 216 yards, the person may experience discomfort or irritation of breathing.

Figure 9-13 shows that the areas affected by 25 mm leakage of the methanol reactor, where the wind speed simulated is 1.6 m/s at three wind direction of NNW, NW, and WNW. The 25 mm leakage shows the increase in distance of area affected compared to the 10 mm leakage, where the lowest area affected leakage occurs at 100 bar, as shown in Figure 8. The affected distances are 83 yards at the red zone, 154 yards at the orange zone, and 305 yards at the yellow zone. Figure 12 shows the highest area affected has occurred at 400 bar. The affected areas are at 134 yards (red zone), 249 yards (orange zone), and 474 yards (yellow zone).

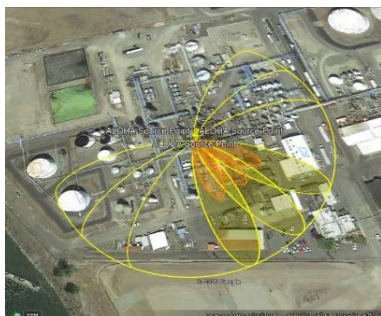


Figure 4: Area affected at 100 bar from 10 mm leakage.

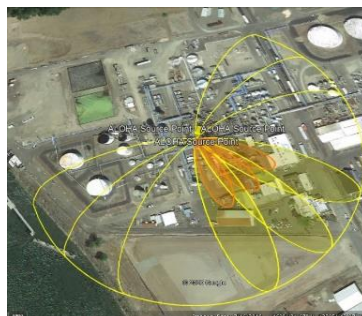


Figure 5: Area affected at 200 bar from 10 mm leakage.



Figure 6: Area affected at 300 bar from 10 mm leakage.



Figure 7: Area affected at 400 bar from 10 mm leakage.



Figure 8: Area affected at 500 bar from 10 mm leakage.



Figure 9: Area affected at 100 bar from 25 mm leakage.



Figure 10: Area affected at 200 bar from 25 mm leakage.



Figure 11: Area affected at 300 bar from 25 mm leakage.

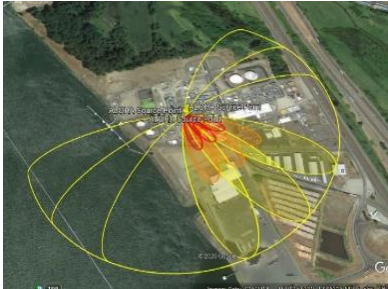


Figure 12: Area affected at 400 bar from 25 mm leakage.

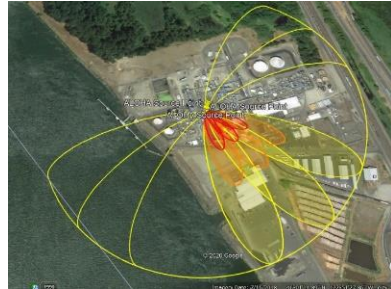


Figure 13: Area affected at 500 bar from 25 mm leakage.

Then, the affected areas are decreasing at 500 bar, as shown in Figure 13, where the red zone is at 129 yards, the orange zone at 240 yards, and the yellow zone at 458 yards. The affected areas at 500 bar are quite similar to the affected areas at 300 bar, as shown in Figure 11. The trend of affected areas at 25 mm leakage size shows the increase of the affected areas from 100 bar to 400 bar and decreasing between 400 bar and 500 bar. It is simulated at 400 bar has a higher severity followed by 500 bar, 300 bar, 200 bar, and 100 bar. At 134 yards, there will be a life-threatening effect on the person in the area distance. In contrast, at 249 yards, the person may experience severe or irreversible and long-lasting adverse health effects or an impaired ability to escape the area. At 458 yards, the person may experience the discomfort of irritation of breathing.

Figure 14 - 18 show the affected areas at 160 mm leakage of the methanol reactor. The wind speed is 1.6 m/s at three different directions: NNW, NW, and WNW. The 160 mm leakage size is simulated to yield the

highest affected areas compared to the other two leak sizes (10 mm and 25 mm). The lowest area affected is shown in Figure 14 at the distance of 137 yards for the red zone, 254 yards for the orange zone, and the 471 yards for the yellow zone. The highest affected area is shown in Figure 17 at the distance of 251 yards for the red zone, the orange zone at 440 yards, and the yellow zone is at 731 yards. It is predicted that the methanol reactor with bigger leak size may have a longer distance of area compared to the smaller leak size. The maximum pressure that yields higher severity is 400 bar for all the leak sizes. The severity percentage is calculated based on the probit percentage studied and discussed in the next section.

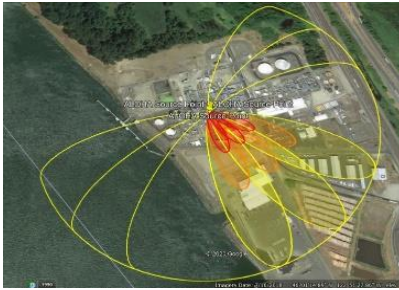


Figure 14: Area affected at 100 bar from 160 mm leakage.



Figure 15: Area affected at 200 bar from 160 mm leakage.

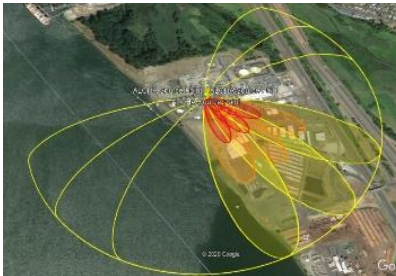


Figure 16: Area affected at 300 bar from 160 mm leakage.



Figure 17: Area affected at 400 bar from 160 mm leakage.



Figure 18: Area affected at 500 bar from 160 mm leakage.

Methanol probit toxic release

Table 1 shows the value of probit for each duration, from 10 minutes to 60 minutes, and categorized by three different types of exposure-response of Acute Exposure Guideline Levels for Airborne Chemicals (AEGL). Each level of AEGL has each concentration limit to methanol exposure, AEGL-3 at 7200 ppm, AEGL-2 at 2100 ppm, and AEGL-1 at 530 ppm. The severity of methanol from the exposure of 10 minutes is 1.1% of people will suffer to the exposure of AEGL-1, 0.3% of people will suffer to the exposure of AEGL-2, and there will be no injury or exposure to people in AEGL-3 as the probit is negative in values. At a duration of 20 minutes, the exposure from AEGL-1 will suffer about 1.5%, whereas AEGL-2 will expose the chemical to people about 0.7% and no injury or any suffering at AEGL-3. At the duration of 30 minutes, the probit percentage increases, where about 1.8% of people will suffer from exposure to AEGL-1. While 1% of people will experience at AEGL-2, and 0.08% will suffer life-threatening effects at AEGL-3. As the duration reached 40 minutes, 2% of people will suffer from AEGL-1, 1.2% will suffer from AEGL-2, and 0.3% will suffer at an exposure of AEGL-3, which can lead to mortality. In the duration of 50 minutes, the severity increases as the people will experience 2.1% from AEGL-1, 1.3% will suffer from the AEGL-2, and 0.4% will be exposed to AEGL-3. The highest score of probit will be at duration 60 minutes, where 2.3% of people will suffer irritation or discomfort of breathing, while 1.5% of people will suffer long-lasting adverse health effects or an impaired ability to escape and 0.5% of people surrounding may suffer which can lead to mortality. Figure 19 shows most of the people surrounding will have higher exposure from AEGL-1.

Table 1: Probit percentage of methanol

Duration	10	20	30	40	50	60
AEGL-1	1.079456	1.539706	1.808934	1.999955	2.148123	2.269184
AEGL-2	0.261312	0.721562	0.990791	1.181812	1.329979	1.451041
AEGL-3	-0.65289	-0.19264	0.076585	0.267606	0.415774	0.536835

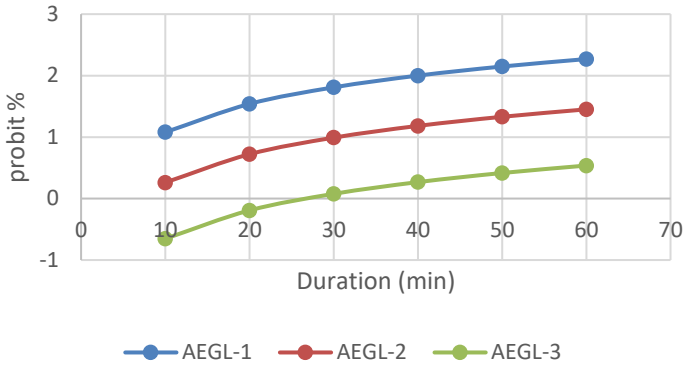


Figure 19: Duration vs probit for Methanol.

Conclusion

This study analyses the severity of methanol with various high pressure and three different leakages. The gas release from methanol is causing the severity of such toxicity towards the surroundings. The gas discharge rate from methanol is increasing as the pressure operated is increasing. While the affected areas from methanol exposure are achieved, the highest at 400 bar for all leakages and increasing as the pressure increases for all leak sizes simulated. Probit equation is added to determine the percentage from the general population to the surrounding, which methanol yield cause bigger severity for catastrophic leakages.

Acknowledgment

The authors would like to acknowledge Faculty of Chemical Engineering, Universiti Teknologi MARA (UiTM) and the Ministry of Education (MOE) for the 600-RMI/FRGS/5/3 (0094/2016) grant, for all the funding and support given in establishing this project.

References

- [1] J. V Ashurst and T. M. Nappe, "Methanol toxicity," *StatPearls [Internet]*, 2019.
- [2] R. Kajaste, M. Hurme, and P. Oinas, "Methanol-Managing greenhouse gas emissions in the production chain by optimizing the resource base," *AIMS Energy*, vol. 6, no. 6, pp. 1074–1102, 2018.
- [3] A. A. Kiss, J. J. Pragt, H. J. Vos, G. Bargeman, and M. T. De Groot, "Novel efficient process for methanol synthesis by CO₂ hydrogenation," *Chem. Eng. J.*, vol. 284, pp. 260–269, 2016.
- [4] T. Kakumoto and T. Watanabe, "A theoretical study for methanol synthesis by CO₂ hydrogenation," *Catal. today*, vol. 36, no. 1, pp. 39–44, 1997.
- [5] C. Bergins, K. C. Tran, E. I. Koytsoumpa, E. Kakaras, T. Buddenberg, and Ó. Sigurbjörnsson, "Power to methanol solutions for flexible and sustainable operations in power and process industries," *Power-Gen Eur*, 2015.
- [6] S. Schemme, R. C. Samsun, R. Peters, and D. Stolten, "Power-to-fuel as a key to sustainable transport systems—An analysis of diesel fuels produced from CO₂ and renewable electricity," *Fuel*, vol. 205, pp. 198–221, 2017.
- [7] B. Tidona, C. Koppold, A. Bansode, A. Urakawa, and P. R. von Rohr, "CO₂ hydrogenation to methanol at pressures up to 950 bar," *J. Supercrit. Fluids*, vol. 78, pp. 70–77, 2013.
- [8] R. Gaikwad, A. Bansode, and A. Urakawa, "High-pressure advantages in stoichiometric hydrogenation of carbon dioxide to methanol," *J. Catal.*, vol. 343, pp. 127–132, 2016.
- [9] S. Li, L. Guo, and T. Ishihara, "Hydrogenation of CO₂ to methanol over Cu/AlCeO catalyst," *Catal. Today*, vol. 339, pp. 352–361, 2020.
- [10] R. Gaikwad, A. Bansode, and A. Urakawa, "High-pressure advantages in stoichiometric hydrogenation of carbon dioxide to methanol," *J. Catal.*, vol. 343, no. April, pp. 127–132, 2016.
- [11] R. Gaikwad, H. Reymond, N. Phongprueksathat, P. R. von Rohr, and A. Urakawa, "From CO or CO₂?: space-resolved insights into high-pressure CO₂ hydrogenation to methanol over Cu/ZnO/Al₂O₃," *Catal. Sci. Technol.*, vol. 10, no. 9, pp. 2763–2768, 2020.
- [12] A.-M. Heikkilä, "Inherent safety in process plant design," *VTT Publ*, pp. 1–132, 1999.
- [13] R. Srinivasan and N. T. Nhan, "A statistical approach for evaluating inherent benign-ness of chemical process routes in early design stages," *Process Saf. Environ. Prot.*, vol. 86, no. 3, pp. 163–174, 2008.
- [14] N. Yayci, H. Ağritmiş, A. Turla, and S. Koç, "Fatalities due to methyl alcohol intoxication in Turkey: an 8-year study," *Forensic Sci. Int.*, vol.

- 131, no. 1, pp. 36–41, 2003.
- [15] M. Aizad and A. Rashid, “Fatality assessment for high pressure reactor of methanol production plants from CO₂ hydrogenation,” *Malaysian J. Chem. Eng. Technol.*, vol. 2, pp. 26–40, 2019.
- [16] M. A. Ahmad and Z. A. Rashid, “Adaptive neuro-fuzzy inference system prediction method for percentage fatalities of jet fire incident in methanol production plant,” *Int. J. Eng. Adv. Technol.*, vol. 9, no. 1, pp. 5766–5772, 2019.
- [17] P. R. Tidona, B., Koppold, C., Bansode, A., Urakawa, A., & von Rohr, “CO₂ hydrogenation to methanol at pressures up to 950 bar,” *J. Supercrit. Fluids*, vol. 78, pp. 70–77, 2013.
- [18] B. Tidona, “Hydrogenation of carbon dioxide in a flow microreactor at pressures up to 1000 bar.” *ETH Zurich*, 2013.
- [19] J. G. Van Bennekom *et al.*, “Methanol synthesis beyond chemical equilibrium,” *Chem. Eng. Sci.*, vol. 87, pp. 204–208, 2013.
- [20] É. S. Van-Dal and C. Bouallou, “Design and simulation of a methanol production plant from CO₂ hydrogenation,” *J. Clean. Prod.*, vol. 57, pp. 38–45, 2013.
- [21] A. B. Bansode, “Exploiting high pressure advantages in catalytic hydrogenation of carbon dioxide to methanol.” *Universitat Rovira i Virgili*, 2014.
- [22] A. Bansode and A. Urakawa, “Towards full one-pass conversion of carbon dioxide to methanol and methanol-derived products,” *J. Catal.*, vol. 309, pp. 66–70, 2014.
- [23] R. Gaikwad, “Carbon dioxide to methanol: stoichiometric catalytic hydrogenation under high pressure conditions.” *Universitat Rovira i Virgili*, 2018.
- [24] M. Pérez-Fortes, J. C. Schöneberger, A. Boulamanti, and E. Tzimas, “Methanol synthesis using captured CO₂ as raw material: Techno-economic and environmental assessment,” *Appl. Energy*, vol. 161, pp. 718–732, 2016.
- [25] R. Stryjek and J. H. Vera, “PRSV: An improved Peng—Robinson equation of state for pure compounds and mixtures,” *Can. J. Chem. Eng.*, vol. 64, no. 2, pp. 323–333, 1986.
- [26] AcuTech Consulting Group, “Quantitative risk assessment final report prepared for : NW Innovation Works, Port of Kalama,” February, 2016.
- [27] P. G. Stoffen, “Guidelines for quantitative risk assessment,” *Minist. van Volkshuisv. Ruimtelijke Ordening en Milieu. CPR E*, vol. 18, 2005.
- [28] J. Casal, 2nd Ed., *Evaluation of the effects and consequences of major accidents in industrial plants*. Amsterdam: Elsevier, 2017.

Artificial Neural Network Predictive Modelling of Laser Micro- Grooving for Commercial Pure Titanium (CP Ti) Grade 2

Sivaraos, A.K Zuhair, M.S. Salleh, M.A.M. Ali*
Faculty of Manufacturing Engineering,
Universiti Teknikal Malaysia Melaka (UTeM), Malaysia
**sivaraos@utem.edu.my*

Kadiringama
Faculty of Engineering Technology Mechanical and Automotive,
Universiti Malaysia Pahang, Malaysia

U.K. Dubey
Amity University, Uttar Pradesh, India

Satish Pujari
Lendi Institute of Engineering and Technology,
Vizianagaram, Andhra Pradesh, India

L.D. Sivakumar
Faculty of Mechanical Engineering,
Universiti Teknikal Malaysia Melaka (UTeM), Malaysia

ABSTRACT

Grooving is the process of making a narrow channel on a surface of flat or cylindrical workpiece. Groove is precisely made to parts used in automotive, biomedical, and electronics industries. In automotive industries, groove plays an important role especially on mechanical parts to precisely locate seal (o-ring) to prevent gas/oil leakage between dynamic mating parts. On the other hand, artificial neural network (ANN) has been widely used in developing predictive models of various manufacturing processes to save huge amount of production time and money for industries. Unfortunately, very limited research has been investigated on micro groove quality employing ANN predictive models. Therefore, this research work presents on how the Artificial Neural Network (ANN) predictive model has been established, optimised and utilised

to predict the laser micro-grooving quality of commercial pure titanium grade 2 material. A 3KW CO₂ laser cutting machine was employed considering laser power, gas pressure, cutting speed, depth of cut and focal distance as the design parameters for modelling. On the other hand, three significant responses namely groove depth, groove width and groove corner radius were investigated. Experimental results were fed to establish the ANN predictive model, which then its parameters were optimized to gain high level prediction accuracy. The predicted results of ANN model presented the mean absolute percentage error for groove depth, groove width and groove corner radius at about 7.29%, 10.93% and 11.96% respectively. The obtained predictive results were found quite promising with the average of mean absolute percentage error (MAPE) for quality predictions which falls between 10 to 15%, concluding the validity of the developed ANN predictive model.

Keywords: ANN predictive modelling; CO₂ laser cutting; Micro-grooving; Commercial pure titanium (CP Ti)

Introduction

In today's world of revolutionising industry, most of the mechanical parts are required to be manufactured with tight tolerances without having to go through secondary processes. As such, micro-groove is in demand for super-hard rods in providing precise seats to locate seals, where it is a popular geometric feature especially in the area of precision machining. Micro groove is widely used in critical industries such as automotive, biomedical, aerospace, and microelectronics as sealant sittings, mechanical splitters, rotatable locating rings, micro-sprue actuators, etc. [1]. Gachot et al. [2] revealed that, micro-groove is very helpful in maintaining the performance of lubrication such as in wet sliding conditions to ensure coefficient of friction and wear between the mating parts are maintained. In biomedical field, micro-groove is becoming much crucial for dental implantation ensuring soft tissue formation to prevent the biological adverse effect. Rapidly growing hard-to-machine engineering materials such as titanium is being challenged to be processed by conventional machining. Thus, laser grooving being the non-contact advanced machining process, is mostly preferred by many precision industries as it stands the ability of net production, even for rods with greater length to diameter ratio.

In fact, the superiority of commercial pure (CP) titanium together with micro-groove as initiated by [22] is now in the raise of various applications including dental implants, turbocharger, and valve system. Generally, laser cutting machine which falls under the family of advanced machine tool is capable of cutting almost all kind of materials regardless of material rigidity, flexibility, metallic, non-metallic, malleability, or literally anything under the

sky for the matter. Thus, laser cutting is often used as precision machining preference which is also able to produce micro level grooves, holes, and corners with tight tolerances due to its excellent kerf width and narrower heat affected zone [3]. But then, practical applications of the laser advancements by newly exploring industries often spend huge amount of production time and materials which leads into unnecessary money spending before arriving at the final decision of the process parameters setting. In conjunction to that, the machinability investigation of titanium alloy (Ti-6Al-4V) using laser machining has been successfully performed by controlling the material removal rate to attain desired surface roughness [4]. The micro grooving of Ti-6Al-4V alloys conducted by [5] reveals that, a good quality of 8-12 μm groove depth and width was achieved by controlling the pulse frequency, scan speed, and focal length which have direct control over the laser spot size. Taweeporn et al. [6] performed underwater laser micromachining of titanium alloy with different sets of temperatures. It was found that, the effect of laser power, traverse speed and numbers of laser passes are much significant for deep grooving. In fact, to have the laser processing phenomenon be well understood, [7] has modelled the micro-grooving process by employing Artificial Neural Network (ANN).

ANN multi-objective model was developed to optimize the process parameters of yttrium aluminium garnet (YAG) laser for minimum depth investigation of micro-turning by [8]. ANN model developed by [9] was capable to accurately predict the surface quality of CNC turning processes as compared to Taguchi model. Sathish et al., [10] investigated the ANN predicted of methane yield by different parameters selection and the model was proven to be efficient within the settings of feed forward network (FFN) with one hidden layer was a better approach over other common types for methane content prediction. Ming-Jong [11] has investigated the cut quality measurements of Quad Flat Non-lead (QFN) package which is depth of cutting line, width of heat affected zone, cutting line of epoxy, and copper-compounded using back propagation neural network model. On top of that, four algorithms including broyden fletcher goldfarb shanno quasi-newton (BFG), scaled conjugate gradient (SCG), gradient descent (GD), and lavenberg-marquardt (LM) were also used to simulate the model. Ming-Jong concluded that, LM algorithm is an optimal algorithm which yields much lower error predictions as compared to other optimised algorithms.

On the other hand, optimization of surface roughness has been studied and modelled employing ANN by [12]. The model shows that, 4-7-1 structure predicts best cut quality of surface roughness with properly controlled three design parameters which are cutting speed, power, and assist gas pressure. It has been summarised that, cutting speed plays an important role as compared to other tested parameters. The optimized model of hybrid Taguchi artificial

neural network hybrid with genetic algorithm based model was developed by [13] to predict the CO₂ laser cut quality. The model succeeded to predict the cut quality accuracy with the prediction error of not more than 10%. ANN modelling is able to reduce the production cost particularly in precision industries which often waste a lot of experimental time and raw materials to arrive into the optimal settings, especially if it involves new material or new processing [15]. Properly designed ANN model architecture with optimised parameters will be powerful enough to capture the relationship between input and output parameters. The pattern learning ability of ANN makes it a very powerful predictive modelling tool. In other words, artificial neural network can be classified as a black box model which provides information behind the processing physics explicitly [16].

ANN model is often adopted for prediction and optimization of many processes including laser micro-grooving process as it has the ability to compute the very non-linear process phenomenon including laser machining. According to [17], the artificial neural network model can be simplified using mathematical expression as shown in Equation (1).

$$y(k) = F\left(\sum_{i=0}^m w_i(k) + b\right) \quad (1)$$

where;

$x_i(k)$ is input value in discrete time k where i goes to 0 to m

$w_i(k)$ is weight value in discrete time k where i goes from 0 to m

b is bias

F is a transfer function

$y_i(k)$ is output value in discrete time k

As to achieve the primary objective of this research which is to predict laser grooving quality of commercial pure titanium grade 2, various critical steps have been performed towards developing a sound ANN model to ensure that the attainable values are within desired values.

Experimental setup and procedures

The aim of this experimental based modelling research is to develop, optimise and validate ANN model to predict and experimentally validate micro-groove quality of laser processed commercial pure (CP) titanium grade 2 rods. The material was selected based on high demand of wide applications in the area of aerospace, architecture, power generation, medical industry, hydro-carbon processing, marine industry and so on [27]. The CP titanium grade 2 is well

known for its superior formability, corrosion resistance and strength where, it offers minimum yield strength of 275 MPa as shown in Table 1.

Table 1: Properties and composition of CP titanium grade 2 [14]

Properties	Value
Yield Strength	275 - 410 MPa
Modulus of Elasticity	105 GPa
Density	4.51 g/cc
Specific Heat Capacity	0.523 J/g-°C
Melting Point	Max 1665 °C
Shear Modulus	45 GPa

The specifications of 3-kilowatt carbon dioxide (CO₂) laser cutting machine employed for experimentation in this research are shown in Table 2.

Table 2: Specification of CO₂ laser cutting machine

Laser	Specification
Manufactured by	LVD, Belgium
Brand	LVD Helius
Model	Helius-2513
Maximum laser power	3 kW
Maximum speed	250 mm/s
Envelope	2.50 x1.25 m

On the other hand, Table 3 shows the selected laser machining process parameters. Out of 14 laser processing parameters, five (5) significant ones were selected upon conducting preliminary research. Namely, they are power (P), gas pressure (G), cutting speed (V), depth of cut (d) and focal distance (F).

Table 3: Laser processing parameters

Parameters	Unit	Low	Medium	High
Power (<i>P</i>)	watt	1500	1650	1800
Gas Pressure (<i>G</i>)	bar	170	180	190
Cutting Speed (<i>V</i>)	mm/min	700	800	900
Depth of Cut (<i>d</i>)	mm	0.25	0.48	0.7
Focal Distance (<i>F</i>)	-	-2	-1	0

The specimens used in this experimental work were of the commercially available in the market with 5mm diameter and 130mm in length. Considering five (5) process parameters with three (3) different levels, a total of 32 experiments were designed. For data reliability, three (3) replications were conducted for each experiment which sums into the total 96 experimental runs. The Design of Experiment (DoE) run matrix was established using commercially available statistical package called Minitab employing response surface methodology (RSM) tool by selecting faced cantered central composite design (CCD).

The entire research was carefully design and conducted based on the research methodology established as shown Figure 1. All primary activities were strictly followed accordingly.

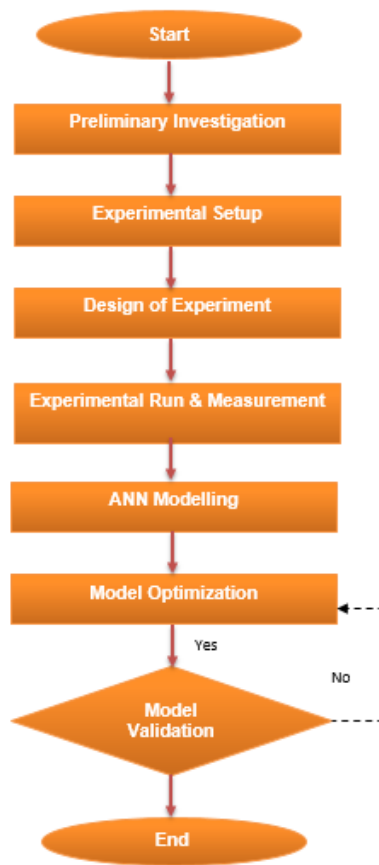


Figure 1: Research methodology flowchart.

The laser grooving process was performed onto the CP titanium grade 2 rod(s) by securing within a three-jaw chuck attached onto a specially designed speed-controlled spinning device. The spinner was properly aligned in the transverse direction laser beam to provide lathe alike interaction. Figure 2 shows how the spinner was mounted and used for laser grooving. The laser machine used in the experimental work was a 2.5 x 1.25 meter flatbed where the interaction of the linearly moving bed axes with spinning speed controllable device enabled the development of a cost effective 3D laser grooving possibility.

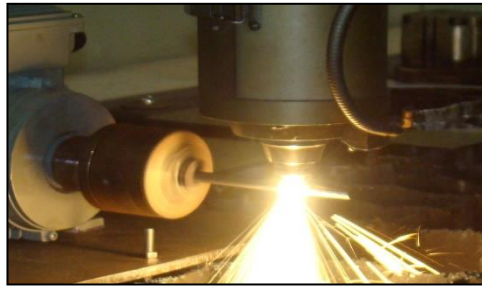


Figure 2: Flatbed Laser with integrated spinner chuck.

The depth, width, and corner radius of the produced micro-groove by laser machine was precisely measured using 20-4600 series model optical comparator made by Scherr-Tumico as shown in Figure 3.

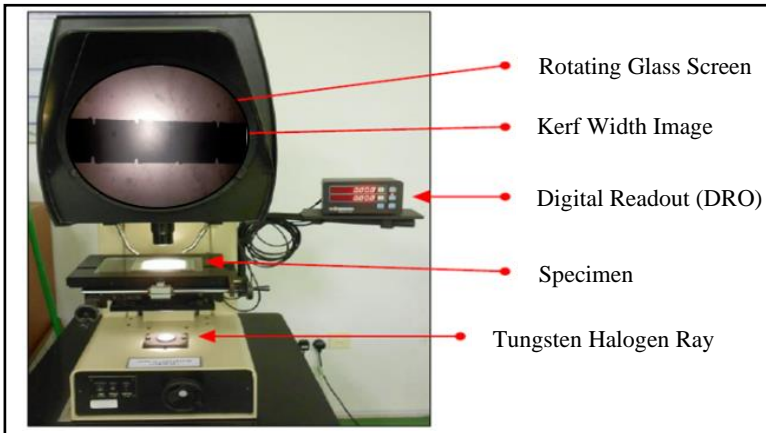


Figure 3: Measuring of micro-groove with optical comparator.

The optical comparator allows precise measurements to be captured with the ability of magnifying the image up to 50X larger with high degree of accuracy even for a very tiny part or groove in this matter. The measurements were taken at three different points along the circumference with 120° each point. The average of these three readings was considered as the values of the micro-groove profile. The measurement and observation of the grooves were performed based on ISO 5346 standard. Figure 4 shows the schematic drawing of how the groove depth, width and corner radius were observed as per ISO 5346 standard.

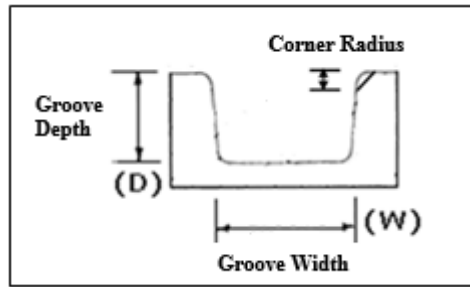


Figure 4: Schematic diagram of groove observations.

ANN Modelling of Micro Grooving

In this model, a three layer ANN network architecture consists of input layer, hidden layer, and output layer as shown in Figure 5 was utilised. The input layer of the architecture consists of five (5) neurons indicating the number of input process parameters. On the other hand, the output layer consists of three neurons, which are also the predictive responses namely, groove depth, groove width and groove corner radius. In the middle of the architecture there is a hidden layer with number of neurons which are considered as crucial element to determine the prediction. Therefore, the appropriate selection of neuron numbers is very important in order to establish excellent predictions with minimal number of iterations in ensuring the network processing speed and accuracy. Every model is evaluated based on how accurate can the predictions be made. Means, smaller the prediction error value, more accurate and robust the model is to be. The prediction error can be calculated or defined based on Equation (2).

$$\text{Prediction error (\%)} = \frac{\text{Exp. results} - \text{Pred. results}}{\text{Exp. result}} \times 100\% \quad (2)$$

After a serious study, a feed forward back-propagation network was finalised for the ANN model development. The training and testing of datasets have been performed using neural network algorithms under commercially available Mat lab software. From the total of 96 experimental datasets, 85% of them were used for training and the rest were used for the testing of ANN network.

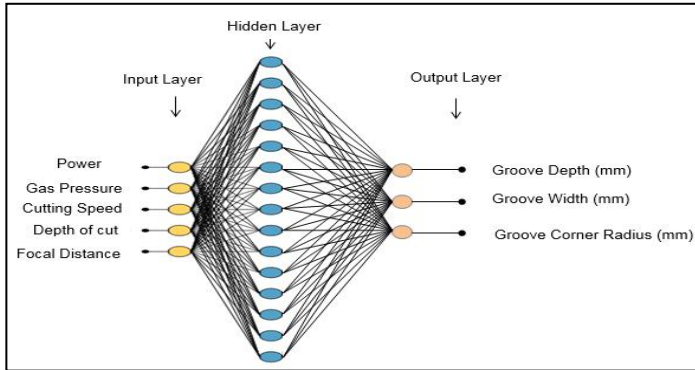


Figure 5: ANN 5-15-3 architecture with 5 inputs, 1 hidden layer and 3 outputs.

Through a thorough investigation, the neuron numbers of hidden layers were determined as in the ANN architecture. The predicted results of ANN model were evaluated by considering the minimum percentage of prediction error. There are six (6) design parameters of ANN that was considered for modelling which are namely; network algorithm, training function, transfer function and adaption learning, hidden layers, error goal and neuron numbers. In order to obtain precise predictions without having to go through trial-and-error methods, the established ANN model was optimized for its attributes and parameters within as shown in Table 4.

Table 4: ANN Attributes and optimized parameters.

ANN Attributes	Optimized parameters
Network algorithm	Feed-forward BP
Training function	Levenberg–Marquardt
Transfer function	Hyperbolic tangent
Number of hidden layer	One (1)
Error goal	0.0001
Number of neuron	15

Results and Discussion

The entire experimental results gained for the total number of 96 experimental runs against their respective responses are as shown in Table 5.

Table 5: Experiment results – responses over the experimental runs

No.	GD (mm)	GW (mm)	CR (mm)	No.	GD (mm)	GW (mm)	CR (mm)
1	0.16	0.34	0.12	49	0.65	0.16	0.22
2	0.39	0.20	0.15	50	0.45	0.18	0.17
3	0.66	0.18	0.26	51	0.42	0.17	0.18
4	0.41	0.18	0.23	52	0.72	0.24	0.27
5	0.12	0.15	0.12	53	0.25	0.32	0.10
6	0.43	0.20	0.15	54	0.49	0.19	0.15
7	0.44	0.14	0.14	55	0.64	0.09	0.19
8	0.44	0.15	0.28	56	0.26	0.28	0.08
9	0.45	0.16	0.11	57	0.72	0.17	0.19
10	0.69	0.15	0.13	58	0.59	0.20	0.10
11	0.23	0.24	0.14	59	0.61	0.24	0.13
12	0.73	0.20	0.27	60	0.63	0.21	0.22
13	0.48	0.18	0.17	61	0.22	0.27	0.08
14	0.20	0.24	0.06	62	0.20	0.23	0.15
15	0.68	0.08	0.14	63	0.23	0.29	0.17
16	0.24	0.26	0.19	64	0.48	0.17	0.12
17	0.49	0.14	0.16	66	0.49	0.21	0.12
18	0.66	0.13	0.29	66	0.24	0.26	0.11
19	0.46	0.18	0.17	67	0.64	0.14	0.14
20	0.13	0.29	0.15	68	0.48	0.20	0.15
21	0.39	0.22	0.19	69	0.51	0.20	0.16
22	0.35	0.25	0.17	70	0.30	0.29	0.08
23	0.44	0.21	0.20	71	0.69	0.22	0.16
24	0.20	0.33	0.11	72	0.41	0.21	0.12
25	0.13	0.30	0.12	73	0.16	0.28	0.07
26	0.51	0.19	0.18	74	0.23	0.23	0.10
27	0.52	0.17	0.13	75	0.25	0.27	0.09
28	0.18	0.29	0.13	76	0.64	0.13	0.19
29	0.46	0.18	0.15	77	0.21	0.26	0.08
30	0.71	0.21	0.23	78	0.66	0.16	0.14

31	0.73	0.14	0.24	79	0.67	0.12	0.18
32	0.44	0.21	0.15	80	0.20	0.25	0.08
33	0.41	0.22	0.12	81	0.48	0.23	0.10
34	0.21	0.31	0.10	82	0.49	0.24	0.11
35	0.15	0.27	0.14	83	0.49	0.20	0.12
36	0.40	0.13	0.15	84	0.23	0.26	0.10
37	0.22	0.37	0.15	85	0.17	0.21	0.10
38	0.72	0.12	0.14	86	0.7	0.17	0.16
39	0.37	0.19	0.17	87	0.66	0.15	0.14
40	0.61	0.18	0.24	88	0.52	0.16	0.15
41	0.22	0.35	0.15	89	0.50	0.23	0.19
42	0.38	0.26	0.16	90	0.71	0.14	0.16
43	0.43	0.19	0.22	91	0.48	0.19	0.13
44	0.58	0.14	0.16	92	0.44	0.20	0.10
45	0.43	0.19	0.14	93	0.65	0.20	0.13
46	0.40	0.19	0.13	94	0.47	0.22	0.14
47	0.48	0.22	0.14	95	0.49	0.17	0.15
48	0.47	0.21	0.16	96	0.60	0.15	0.16

Based on the experimental results, ANN model with multiple outputs has been developed. Various architectures were designed, optimised and tested where in this case, 5-15-3 architecture was seen to be fitting best and therefore it is selected for this modelling process. Table 6 shows the optimised neural network parameters within the 5-15-3 network architecture.

Table 6: ANN parameters for 5-15-3 architecture

ANN Parameter	Value
Network Architecture	5-15-3
Training/Testing Data	83/13
Network	Feed forward back Propagation
Performance	MSE
Training Function	Trainlm
Transfer Function	Tansig/Tansig
Learning Function	LearnGDM

Figure 6 shows the performance simulation of the developed model for training environment. The ANN model training performance was determined based on the lowest Mean Square Error (MSE) gained. The training curve

mean square error (MSE) was seen decreasing with the increase of the epoch number till it reaches 12. If the test curve increases significantly before the validation curve increased, it is then possible that some over-fitting to have occurred. At this point, the curve remained constant and therefore the value of 0.00079511 is considered best for training, and model validation performance was observed to be epoch number 6.

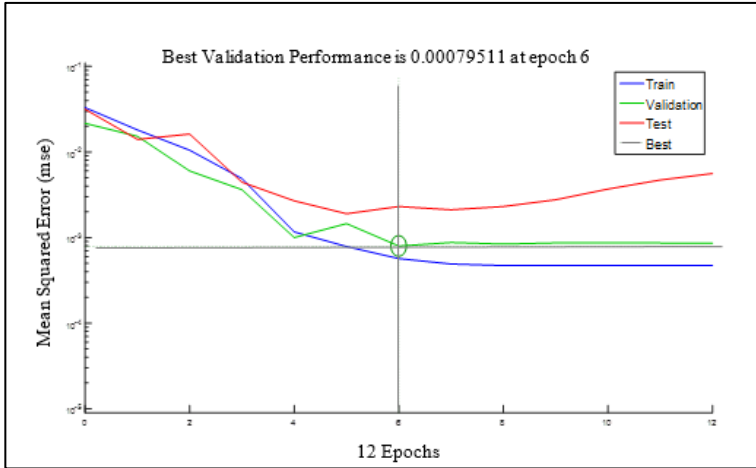


Figure 6: Performance simulation plot of 5-15-3 network.

The decreasing of training mean square error indicates that the training was almost perfect. The validation and test curves gained shows similarity in performance trend of the work performed by [18], which proves the model development coherence between both types of research work.

As for the ANN architecture validation, regression analysis was established in order to analyse the ANN model network outputs and the targets. Figure 7(a) shows the correlation of regression coefficients for training pattern with 0.98981 being the regression value. On the other hand, Figure 7(b) and Figure 7(c) show the regression correlation for validation and testing pattern with 0.98977 and 0.95605 of their respective regression values. The correlation coefficient of regression for total corresponding response is observed to be 0.98469 as shown in Figure 7(d).

Thus, the value of regression coefficient is very close to one which indicates the established and optimised ANN model predictions matches very well as compared to experimental results.

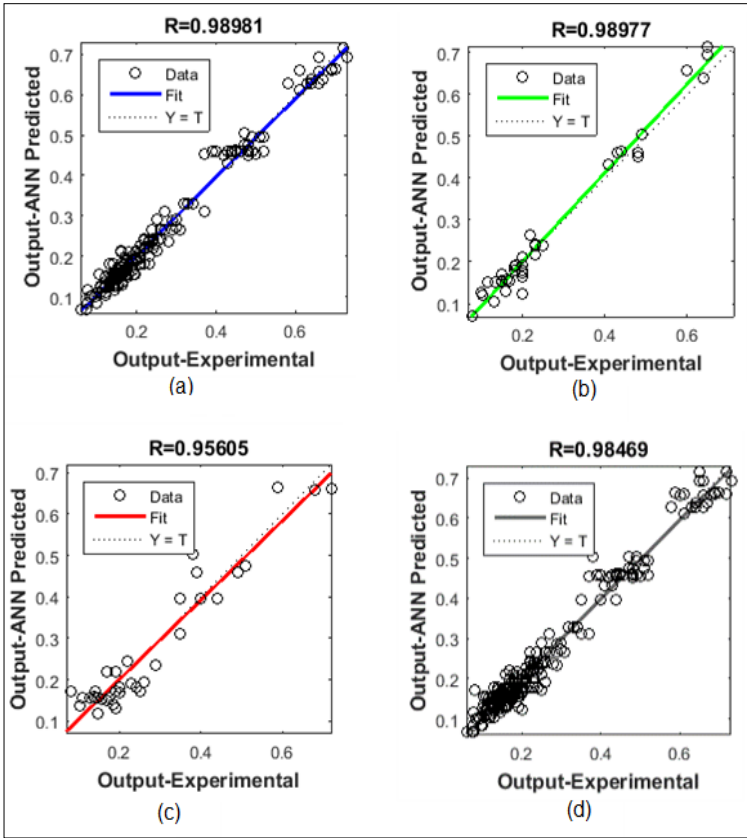


Figure 7: Regression coefficient of 5-15-3 ANN model: (a) training (b) validation (c) testing, and (d) overall data sets.

Table 7 shows the mean absolute percentage error (MAPE) of neural network training for 5-15-3 network architecture which was the main measure of model efficiency. The overall percentage of prediction error for 5-15-3 model architecture is 10.06% which indicates that, the data training for 5-15-3 architecture possesses good model training which yields the accuracy beyond 85% (15% error). In this context, the predictions made by the established ANN model can be considered highly accurate based on MAPE prediction categories made by [19]. He mentioned that the predictions can be classified into four different categories namely, below 10% as highly accurate prediction, 10-20% as good prediction, and 20-50% as reasonable prediction and 50% and above is inaccurate prediction.

Table 7: MAPE error of 5-15-3 architecture

Response	MAPE (%)	Average MAPE (%)
Groove Depth	7.29	
Groove Width	10.93	10.06
Groove Corner Radius	11.96	

The predictions by the ANN model were then experimentally validated for selected sets or runs. The comparative scatter plot of 5-15-3 architecture between experimental and predicted for groove depth, groove width and groove corner radius are shown in Figure 8, Figure 9, and Figure 10, respectively.

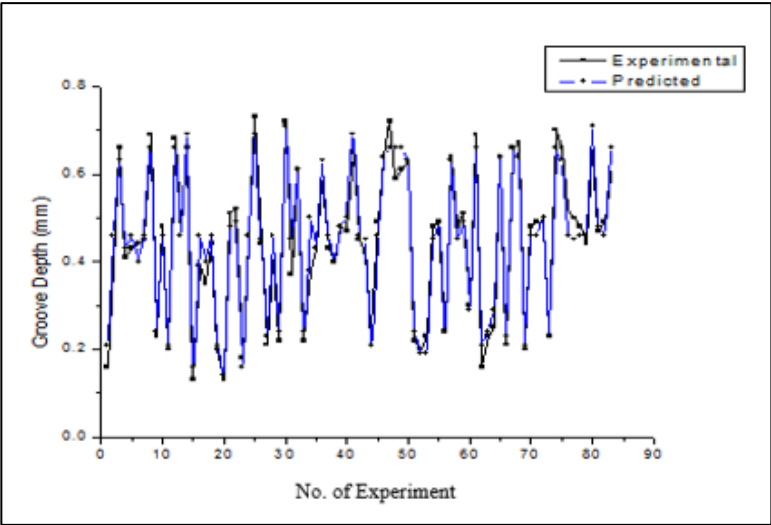


Figure 8: ANN predicted versus experimental for groove depth.

It is very clear that, the comparative scatter plot between experimental and predicted by the established ANN model with 5-15-3 architecture for groove depth, width and radius provided very promising results. Similar work on ANN modelling has been conducted by [20, 21] and the researchers found that, the ANN model utilised in their research has successfully made close predictions to the experimental results where the error was within 15%.

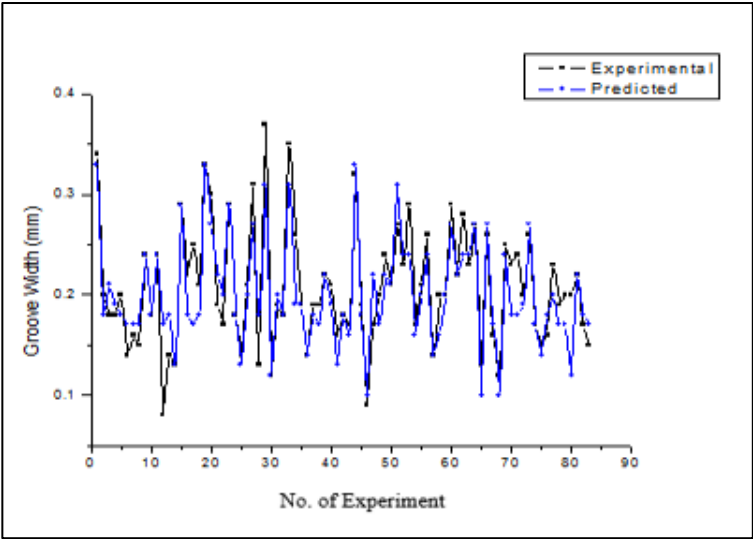


Figure 9: ANN predicted versus experimental for groove width.

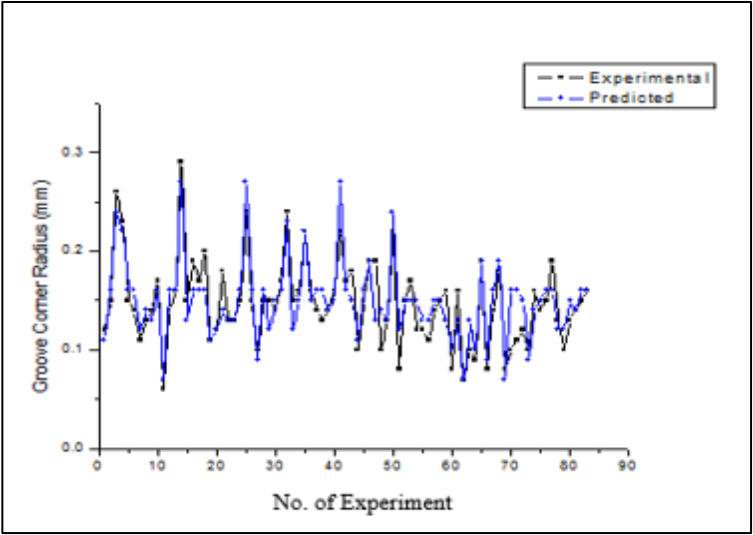


Figure 10: ANN predicted versus experimental for groove corner radius.

The exact overlapping of almost 85% of the signature graph spikes between experimental and predicted values proves that, a properly designed and optimised ANN model is capable of capturing the pattern and processing behaviour of even a complex and non-linear parametric relationship, in this case even for non-linear laser machining process.

Conclusions

Developing an artificial intelligence neural network model to understand the phenomena of a complex and non-linear laser processing to predict micro-grooving quality of CP Titanium Grade 2 has been successfully conducted besides attaining efficient predictions. Perhaps, a flatbed laser machine was modified by integrating a controllable spinning device to perform laser micro-grooving on a cylindrical part. Transforming the flat to 3D machining is primary contribution of this work where, it would be a cost effective solution for most precision metal machining industries. Secondly, the developed and optimised ANN model with 5-15-3 architecture was able to precisely predict the machining accuracy and cut geometry quality. The model stands to contribute in terms of cost and time saving to most industries employing laser lathing as their primary businesses. As to improve the parameter selection of laser cutting accuracy, an effective ANN model selection has been developed in this research to model the experiment before bringing it into actual environment. The results show that, the ANN model was able to predict the desired responses; groove depth, groove width, and corner radius. The achieved mean absolute percentage error (MAPE) for groove depth, width and corner radius was about 10% in average, where each of them yields with 7.29%, 10.93% and 11.96% respectively. This indicates the model robustness allowing the predictions to achieve as high as 90% in accuracy. As overall, the development of ANN model and the validation between predictive model and experiment shows an excellent agreement. To move forward and explore ahead within the field and further enhance the prediction accuracy, it is strongly recommended to develop Adapted Neuro-Fuzzy Inference System (ANFIS) predictive model where the attained results can be directly compared with the attained results.

Acknowledgement

The authors would like to thank the top management of Universiti Teknikal Malaysia Melaka, as well as Faculty of manufacturing Engineering for their continuous support in having this research completed as scheduled.

References

- [1] C. Chen, J. Li, S. Zhan, Z. Yu, and W. Xu, "Study of micro groove machining by micro ECM," *Proc. CIRP*, vol. 42, pp. 418-422, 2016.
- [2] C. Gachot, A. Rosenkranz, S.M Hsu, and H.L Costa, "A critical assessment of surface texturing for friction and wear improvement," *Wear* vol. 372-373, pp. 21-41, 2017.
- [3] S. Sivarao, P. Brevern, N.S.M El-Tayeb, and V.C Vengkatesh, "GUI based mamdani fuzzy inference system modeling to predict surface roughness in laser machining," *Int. J. of Elec. & Comp. Sci. IJECS-IJENS*, vol. 09, no. 09, pp. 37-43, 2009.
- [4] N. Ahmed, S. Ahmad, S. Anwar, A. Hussain, M. Rafaqat, M. Zaindin, "Machinability of titanium alloy through laser machining: material removal and surface roughness analysis," *Int. J. Adv. Manuf. Technol.*, vol. 105, pp. 3303-3323, 2019.
- [5] A.Y. Fasasi, S. Mwenifumbo, N. Rahbar, J. Chen, M. Li, A.C. Beye, C.B. Arnold, W.O. Soboyejo, "Nano-second UV laser processed micro-grooves on Ti6Al4V for biomedical applications," *Mat. Sci. and Eng. C*, vol. 29, pp. 5-13, 2009.
- [6] W. Taweeporn, T. Viboon, D. Chaiya, "Laser micromachining of titanium alloy in water with different temperatures," *Key Eng. Mat.*, vol. 777, pp. 333-338, 2018.
- [7] M.F.M Yunoh, S. Abdullah, M.H.M Saad, Z.M Nopiah, M.Z Nuawi, A. Ariffin, "Classification of fatigue damaging segments using artificial neural network," *J. of Mech. Eng. SI* 5, no. 3, pp. 61-72, 2018.
- [8] G. Kbrial, B. Doloi, and B. Bhattacharyya, "Modelling and optimization of Nd:YAG laser micro-turning process during machining of aluminum oxide (Al₂O₃) ceramics using response surface methodology and artificial neural network," *Manuf. Rev.*, vol. 1, no. 12, pp. 1-8, 2014.
- [9] V.C Boppana, J. Riaz, A. Fahraz, G. Trishel, "Optimisation of surface roughness when CNC turning of Al-6061: application of taguchi design of experiments and ANN algorithm optimization," *J. of Mech. Eng.*, vol. 16, no. 2, pp. 77-91, 2019.
- [10] S. Sathish A. Parthiban, R. Balakrishna, and R. Anandan, "Development of ANN models for optimization of methane yield from floating dome digester," *Int. J. of Eng. & Technol.*, vol. 7, no. 2.21, pp. 316-318, 2018.
- [11] T. Ming-Jong, L. Chen-Hao, and C. Cheng-Che, "Optimal laser cutting parameters for QFN packages by utilizing artificial neural networks and genetic algorithm," *J. of Mat. Proc. Technol.*, vol. 208, pp. 270-283, 2008.
- [12] B.J Ranaganth, and G. Viswanath, "Application of artificial neural network for optimising cutting variables in laser cutting of 304 Grade stainless steel," *Int. J. of Appl. Eng. and Technol.*, vol. 1, no. 1, pp. 106-112, 2011.
- [13] Y. Nukman, M.A Hassan, and M.Z Harizam, "Optimization of prediction

- error in CO₂ laser cutting process by Taguchi artificial neural network hybrid with genetic algorithm,” *Appl. Math. & Info. Sci.*, vol. 7, no. 1, pp. 363-370, 2013.
- [14] *Titanium Grade 2*, Aerospace specification metals Inc., n.d. [Online] Available at <http://asm.matweb.com/search/SpecificMaterial.asp?bassnum=MTU020>.
- [15] K.D Chinmay, and S. Abdulhafiz, “Prediction of depth of cut for single-pass laser micro-milling process using semi-analytical, ANN and GP approaches,” *Int. J. Adv. Manuf. Technol.*, vol. 60, pp. 865–882, 2012.
- [16] I.T Moghaddam, M. Ayati, A. Taghavipour, J. Marzbanrad, “Modeling and prediction of driver-vehicle-unit velocity using adaptive neuro-fuzzy inference system in real traffic flow,” *J. of Mech. Eng.*, vol. 16, no. 3, pp. 105-122, 2019.
- [17] *Introduction to the Artificial Neural Networks, in Artificial Neural Networks*, Methodological Advances and Biomedical Applications, 2011. [Online]. Available: <http://www.intechopen.com/books/artificial-neural-networks-methodological-advances-and-biomedical-applications/introduction-to-the-artificial-neural-networks>
- [18] W. Saleem, M. Zain-ul-abdein, H. Ijaz, A.S Abdullah Salmeen Mahfouz, A. Ahmed, M. Asad, T. Mabrouki, “Computational analysis and artificial neural network optimization of dry turning parameters-AA2024-T351,” *Appl. Sci.*, vol. 7, pp. 1-21, 2017.
- [19] A. Gokhan, K. Izzet, H. Coskun, “Artificial neural network and regression models for performance prediction of abrasive waterjet in rock cutting,” *Int. J. Adv. Manuf. Technol.*, vol. 75, pp. 1321–1330, 2014.
- [20] D. Dhupal, B. Doloi, B. Bhattacharyya, “Optimization of process parameters of Nd:YAG laser micro-grooving of Al₂TiO₅ ceramic material by response surface methodology and artificial neural network algorithm,” *Proc. of the Inst. of Mech. Eng. Part B: J. of Eng. Manuf.*, vol. 221, pp. 1341-1351, 2007.
- [21] G. Kibria, B. Doloi, B. Bhattacharyya, “Modelling and optimization of Nd:YAG laser micro-turning process during machining of aluminum oxide (Al₂O₃) ceramics using response surface methodology and artificial neural network,” *Manuf. Rev.*, vol. 1, no. 12, pp. 1-8, 2014.
- [22] Yoji Kosaka, Stephen P. Fox, Kurt Faller, “Recent Development of Titanium and Its Alloys in Automotive and Motorcycle Applications,” *Titanium Science and Technology, The Japan Institute of Metals*, pp. 1383-1386, 2007.